Multiscale impact of the addition of a coating layer on the color of halftone prints

Fanny Dailliez

▶ **To cite this version:**

Fanny Dailliez. Multiscale impact of the addition of a coating layer on the color of halftone prints. Optics / Photonic. Université Grenoble Alpes [2020-..], 2023. English. NNT : 2023GRALI080 . tel-04414909

HAL Id: tel-04414909
https://theses.hal.science/tel-04414909

Submitted on 24 Jan 2024

HAL is a multi-disciplinary open access archive for the deposit and dissemination of scientific research documents, whether they are published or not. The documents may come from teaching and research institutions in France or abroad, or from public or private research centers.

L'archive ouverte pluridisciplinaire **HAL**, est destinée au dépôt et à la diffusion de documents scientifiques de niveau recherche, publiés ou non, émanant des établissements d'enseignement et de recherche français ou étrangers, des laboratoires publics ou privés.

THÈSE

Pour obtenir le grade de

DOCTEUR DE L'UNIVERSITÉ GRENOBLE ALPES

École doctorale : I-MEP2 - Ingénierie - Matériaux, Mécanique, Environnement, Energétique, Procédés, Production
Spécialité : MEP - Mécanique des fluides Energétique, Procédés
Unité de recherche : Laboratoire de Génie des Procédés pour la Bioraffinerie, les Matériaux Bio-sourcés et l'Impression Fonctionnelle

Impact multi-échelle de l'addition d'une couche transparente sur la couleur d'une impression en demi-ton

Multiscale impact of the addition of a coating layer on the color of halftone prints

Présentée par :

Fanny DAILLIEZ

Direction de thèse :

Anne BLAYO Enseignant-chercheur (Ingénieur HDR), Université Grenoble Alpes	Directrice de thèse
Lionel CHAGAS Enseignant-chercheur, Université Grenoble Alpes	Co-encadrant de thèse
THIERRY FOURNEL PRF UNI 2C, Université Jean Monnet Saint-Etienne	Co-directeur de thèse
Mathieu HEBERT PROFESSEUR DES UNIVERSITES, Université Jean Monnet	Co-encadrant de thèse

Rapporteurs :

Carinna PARRAMAN
FULL PROFESSOR, University of th West of England Bristol
Romain PACANOWSKI
CHARGE DE RECHERCHE HDR, Inria centre Bordeaux Sud-Ouest

Thèse soutenue publiquement le **12 octobre 2023**, devant le jury composé de :

Anne BLAYO INGENIEURE HDR, Grenoble INP	Directrice de thèse
Carinna PARRAMAN FULL PROFESSOR, University of th West of England Bristol	Rapporteure
Romain PACANOWSKI CHARGE DE RECHERCHE HDR, Inria centre Bordeaux Sud-Ouest	Rapporteur
Clotilde BOUST INGENIEURE DE RECHERCHE, Centre de Recherche et de Restauration des Musées de France	Examinatrice
Evelyne MAURET PROFESSEURE DES UNIVERSITES, Grenoble INP	Présidente
Thierry FOURNEL PROFESSEUR DES UNIVERSITES, Université de Saint-Etienne - Jean Monnet	Co-directeur de thèse

Invités :

Lionel CHAGAS
INGENIEUR, Université Grenoble Alpes
Mathieu HEBERT
PROFESSEUR DES UNIVERSITES, Université Jean Monnet

Acknowledgements

Dear reader, welcome to this thesis manuscript. As you may know it has required quite some work. Fortunately, I have been very well surrounded during this time, for which I would like first to thank my wonderful supervisors, Anne Blayo, Lionel Chagas, Thierry Fournel, and Mathieu Hébert. Thank you for your careness, your pedagogy and rigor, your trusting, your help at any time, your sharing of your tremendous scientific knowledge, your support, and your enthusiasm. It has been a great pleasure and honor to work with you.

I would also like to acknowledge my jury members, thank you Carinna Parraman and Romain Pacanowski for your time reading this thesis and your guidance. Thank you Clotilde Boust for accepting to be examiner and Evelyne Mauret for presiding the defense. I really appreciated our discussion.

During this work I had the opportunity to meet Hano Hoffstadt and Julia Mäder from GMG Color, thank you for the interesting talks and the fruitful collaboration.

Thank you very much Lionel Simonot for your scientific support, your rigorous proofreading and for being part of my CSI. Thank you as well Raphaël Passas for your time on the microscope and for accepting to be a CSI member.

Many thanks to the students I had the chance to work with, especially to Léo Condamine for his patient and meticulous work on the microscope.

During my time at LGP2, I have had the great pleasure to meet amazing colleagues and friends, among whom Khawla Bouzidi, Amélie Brogly, Maxime Faureau-Tellier, Erwan Troussel, Loreleï Douard, Florian Le Gallic, Karine Janel, Lorette Brault, João Conceição, Marlène Saulais, Mathieu Loste Berdot… and so many others. Thank you Bertine Khelifi for the good chats at the microscope.

Thank you, Vincent Duveiller, my friend and co-PhD student from the Laboratoire Hubert Curien, for your companionship during this thesis. The motivation and the scientific rigor you shared with me had a significant impact in this work. Many thanks to my family for the support, interest, and help they give for all my projects. Last but not least, thank you, my boyfriend, fiancé, and now fabulous husband, Baptiste Lefaucher, for the wonderful support you gave me during this work, the countless scientific discussions, the oral repetitions, the help you provided me with at any time, and for being who you are.

I hope you enjoy reading this!

Abstract

The addition of a transparent coating layer over a halftone print can significantly change its color, even if the layer is perfectly clear and of similar roughness as the uncoated print. The objective of the present work was to understand, model, and evaluate the impact of the optical phenomenon at the origin of this color change for color management purposes in the printing industry.

This color change is caused by the interreflections of light in the coating layer between the diffusing substrate and the coating-air interface. This lateral light propagation has a very specific ring-shaped point spread function caused by the angular dependency of the Fresnel reflectance at the interface between the coating layer and air. This ring-shaped lateral propagation enables light to meet various inked areas of the printed halftone pattern and be absorbed by them, which induces a darkening and a saturation of the color which can be seen as an additional optical dot gain for coated prints. We proposed a reflectance model for this optical phenomenon (that we have called *halation phenomenon*) which relies on multiple convolutions between the ring-shaped point spread function, function of the thickness of the coating layer, and the spatial and spectral intrinsic reflectance of the non-coated print.

Two macroscale experiments were performed for verification of the model: the reflectance factor of centimetric and millimetric printed halftone patterns coated with various coating thicknesses were measured. These experiments enabled to validate the theory behind the halation phenomenon, both in the spectral and in the spatial dimensions.

Simulations with the multi-convolutive model allowed to evaluate the impact of various printing parameters in the color change caused by the addition of a coating layer. In particular, simulations through a microfacet-based BRDF showed that the roughness of the coating-air interface had almost no impact on the halation phenomenon. The multi-convolutive model may then be applied to both glossy and matte coatings by adjusting, for each surface roughness, a parameter in the model which accounts for the light portion externally reflected by the interface towards the sensor.

The halation phenomenon has been studied at the microscale for electrophotographic and inkjet prints. At this scale, the intrinsic reflectances of prints are impacted by mechanical and optical dot gains. To calibrate the multi-convolutive model, an apparatus was developed to measure the spatial and spectral reflectance factor of the prints: a multispectral microscope. This microscope captured pictures through rather small wavelength bandpass optical filters (25 nm), allowing to characterize the prints both spectrally and spatially. This apparatus was calibrated to find an agreement between microscale measurements, performed with the multispectral microscope, and macroscale ones, performed with a spectrophotometer.

This setup allowed to calibrate the multi-convolutive model and to evaluate its accuracy for microscale prints coated with a 25 μm-thick lamination layer. The color difference between the

predictions given by the model and the reflectance factor measurements of coated prints was in average $\Delta E_{00}^{*} = 0.95 \pm 0.39$ for electrophotographic prints and $\Delta E_{00}^{*} = 0.68 \pm 0.28$ for inkjet prints. These fairly accurate results make the multi-convolutive model a rather promising tool for color management in the printing industry. As the multispectral microscope used to calibrate the multi-convolutive model is a rather rare instrument, preliminary simulations are presented which attempt to use classical RGB microscopic measurements to calibrate the model.

Knowing how the halation phenomenon impacts the color of various halftone patterns also paves the way towards security applications. An application is presented where it is shown that images can be hidden and revealed only by adding or removing a clear coating layer.

Résumé

Ajouter une couche transparente (vernis, ou pellicule) sur un imprimé en demi-ton peut changer sa couleur, et ce même si cette couche est non-absorbante et de même rugosité de surface que l'imprimé sans couche transparente. L'objectif est de comprendre, de modéliser, et d'évaluer l'impact du phénomène optique à l'origine de ce changement de couleur afin d'améliorer la gestion de la couleur en impression.

Notre théorie est que ce changement de couleur est dû à des interréflexions de la lumière au sein de la couche transparente, entre le support imprimé diffusant et l'interface avec l'air. Cette propagation latérale a une fonction d'étalement de point (PSF) très spécifique en forme d'anneau causée par la dépendance angulaire de la réflectance de Fresnel à l'interface. Elle permet à la lumière de se propager d'un motif imprimé à un autre et augmente la probabilité que la lumière soit absorbée par de l'encre. Ce phénomène, que nous avons appelé *halation*, sature et assombrit les couleurs de l'imprimé et peut être vu comme un dot gain optique additionnel causé par la couche transparente. Nous proposons un modèle optique permettant de prédire le facteur de réflectance d'un imprimé couvert d'une couche transparente prenant en compte ce phénomène. Il repose sur des convolutions multiples entre la PSF en forme d'anneau, qui dépend de l'épaisseur de la couche transparente, et sur la réflectance intrinsèque spatiale et spectrale de l'imprimé qui peut être évaluée avant ajout de la couche transparente.

Deux expériences ont été réalisées à l'échelle macroscopique pour valider la théorie du phénomène de halation et sa modélisation multi-convolutive à la fois spatialement et spectralement. Elles ont consisté à mesurer le facteur de réflectance de motifs de demi-tons larges pour différentes épaisseurs de couche transparente.

Des simulations via le modèle multi-convolutif ont permis d'estimer l'influence de différents paramètres d'impression sur le changement de couleur causé par l'ajout d'une couche transparente. Il a été en particulier établi que la rugosité de surface de la couche transparente n'avait pratiquement aucun impact sur le phénomène de halation et qu'ainsi le modèle multi-convolutif peut s'appliquer aussi bien à des couches brillantes qu'à des couches mattes.

Ce phénomène de halation a été étudié à l'échelle microscopique pour des impressions électrophotographiques et en jet d'encre. A cette échelle les réflectances intrinsèques des impressions sont impactées par le dot gain optique et mécanique. Pour calibrer le modèle multi-convolutif un instrument a été développé pour mesurer le facteur de réflectance spatial et spectral des impressions : un microscope multispectral. Celui-ci prend des photos à travers des filtres optiques colorés de faible bande passante spectrale (25 nm). Il a été calibré de façon à avoir un accord entre les mesures microscopiques du microscope et celles macroscopiques d'un spectrophotomètre.

Cet instrument a permis de calibrer le modèle multi-convolutif et d'évaluer ses performances sur des impressions de dimensions microscopiques pelliculées avec une couche transparente de 25 µm d'épaisseur. La différence de couleur entre les prédictions du modèles et les mesures était en moyenne $\Delta E_{00}^{*} = 0.95 \pm 0.39$ en électrophotographie, et $\Delta E_{00}^{*} = 0.68 \pm 0.28$ en jet d'encre. Ces résultats relativement précis font du modèle multi-convolutif un outil prometteur pour la gestion des couleurs en impression. Comme le microscope multispectral est un instrument rare, des simulations préliminaires sont présentées pour essayer de calibrer le modèle à partir de mesures microscopiques RGB classiques.

Les connaissances sur le phénomène de halation et sur son impact sur les couleurs de différents motifs de demi-ton imprimés pourraient amener à de nouvelles solutions anti-contrefaçon. Une application est présentée montrant que des images peuvent être cachées ou révélées simplement en ajoutant ou en enlevant une couche transparente sur une impression.

Table of contents

Chapter 1. Introduction

The color of a print usually appears uniform to the naked eye, yet it is usually produced by small inked dots of primary colors printed on a substrate, which blend together when viewed at a reading distance. To reach accurate colors with given materials, the printers have to control the size and distribution of the printed dots, called *halftone pattern*. This can be difficult due to the *dot gain* phenomenon: the printed dots usually appear larger than what was commanded to the printer (i.e., they appear larger than the nominal halftone pattern). This phenomenon has two origins: the ink-paper interactions can lead to an ink distribution on paper usually larger than the nominal one (which is called *mechanical dot gain*) [1], and the light propagation within the substrate tends to optically blur the boundaries between the inked areas (which is called *optical dot gain*) [2]. Color management solutions have been developed to reach accurate colors in spite of dot gain and these solutions can be based on optical models. As the printing field continues to expend [3], research on color management solutions in the printing industry continues to play an important role.

Figure 1. Picture printed in inkjet on a glossy photo paper. The left part is non-coated, the middle part is coated with a matte-finishing layer, and the right part is coated with a glossy-finishing layer.

When adding a clear layer in contact on a print, a color change can easily be observed. If the clear layer is smooth, with a glossy finishing, the print usually becomes glossier, and its colors become deeper. If the clear layer is rough, i.e., with a matte finishing, the colors usually become

less saturated. This can be observed in the picture in Figure 1, where a printed picture has been coated with a matte layer on the middle area, and with a glossy one on the right area. It can, for instance, be noticed that the bushes in the foreground are lighter on the matte-coated area than on the non-coated one and that the sky, ocean, and sand have darker and more saturated colors in the glossy-coated area than on the non-coated one. This can be rather easily observed at home on book covers for instance, or by adding a tape layer on halftone-printed paper.

Even if this color change can be exploited to generate fancy effects on prints, it can be problematic for color reproduction in the printing industry. Indeed, the printers are usually calibrated to produce accurate colors on uncoated prints and the color change induced by the addition of a coating layer can have a negative impact on the accuracy of the color rendering.

The reason behind this color change is rather unknown: it can come from differences in the surface topology with and without coating, reflecting light in different directions, yet Hoffstadt also showed that it depended on the surface coverage and period of the halftone patterns composing the prints [4]. He referred to this color change as an additional dot gain induced by the coating layer and suggested that it may come from light propagation within the transparent layer.

Figure 2. Photography of The Milky-Way & Nubeculae, Henry Chamberlain Russell, Sydney Observatory, 1890. Collection: MAAS [5].

In 2018, Simonot and co-workers have shown that when a transparent layer is in optical contact with a uniform substrate, light propagates inside the transparent layer in a specific manner: the internal reflections inside the coating layer are halo shaped [6]. This halo-shaped propagations had already been described by astronomers in the late 19th century as the photographs were made of a diffusing photosensitive layer in contact with a transparent plate: a halo appeared

around the brightest stars [7], as can be seen in Figure 2. It could be possible that such a halo-shaped light propagation occurs within the coating layer above a print.

Therefore, the objectives of this work are:

- to understand if this halo-shaped light propagation could impact the color of a non-uniform substrate coated with a transparent layer in the case of prints,
- to be able to predict the color change induced by the addition of a transparent coating layer,
- to evaluate its impact with different printing parameters,
- to exploit it for applications.

The scientific background for color reproduction, the scientific tools towards it, and the chosen approach are detailed in Chapter 2. The optical phenomenon at the origin of the color change when a print is coated with a transparent layer and the model we have issued from it are presented in Chapter 3. This chapter contains experimental validations of this theory and of its modelling, as well as simulations of the impact of various parameters on the color change induced by the addition of a coating layer. Chapter 4 deals with the predictions of the color change due to the addition of a coating layer for "real-life" halftone prints which are impacted by the optical and mechanical dot gain at the microscale. An inverse approach for color prediction, a visual application to this color change, and the conclusions are detailed in Chapter 5.

Chapter 2. Color management in printing

The objective of this chapter is to describe the problematic at stake, the state of the art on the subject, to explain the chosen approach, and the theoretical and experimental tools associated to it. The first section deals with color reproduction, which is at the heart of the printing industry, and the problematic associated to it when it comes to coating a layer over a print. The second section presents the theoretical tools associated to the chosen optical approach, and the third section presents the experimental tools enabling the optical approach.

2.1 Color reproduction

Color reproduction aims at reproducing the colors of a scene on a support. The basics of color and colorimetry can be found in Appendix I. Apart from the numerical devices such as screens, the physical supports for such a reproduction are various: canvas for paints, tapestries, paper, plastic, or metals for prints, gelatine films (collotypes) for photography, cave walls in the case of parietal paintings, or interwoven polymer filaments for 3D prints. On such various supports and color reproduction devices a problematic is often to reach the same color between the reproduced objects and the real objects. Various technics, methods, and colorants have been investigated in each field to reach such a goal. For instance, to obtain an accurate skin tone in *Mona Lisa*, Leonardo Da Vinci used a glazing technic, where layers of very low concentration of umber pigment were successively applied over a base of 99% lead white and 1% vermilion [8]. Among the various applicative fields of color reproduction, this work focuses on the printing area. Indeed, even with the expansion of digitalisation, it remains an important sector with applications in various domains: art, press, security, and packaging for instance. In Europe, the printing market was worth €159.2 billion in 2022 according to Smithers [3]. The packaging market is also expected to grow from $473.7 billion in 2022 to $551.3 billion in 2027, with a growth rate of 3.1% [9]. This worldwide growing need for prints requires an increasing control in color reproduction, a demand which can be problematic in the case of prints coated with a transparent layer.

Color reproduction in the printing industry is difficult as the appearance of prints relies on numerous parameters, the most significant of which are introduced here: the halftoning method, the distortions and colors induced by the printing process, and the optical properties of the prints. The last paragraph details color management methods and the problems of color reproduction induced by the addition of a coating layer over a print.

2.1.1 Halftoning

The most usual painting techniques and the first color photographs have in common that the reproduced colors can vary continuously in the spatial dimension: they are directly dependent of the pigment blending and paint spreading on the canvas in the case of paintings, and of the amount of light reaching the photosensitive layers in the case of collotype photography [10] p.67, [1] p.90. Such continuous tones (or *contone*) are difficult to perform in the printing domain as it is complex to make the ink layer characteristics (such as its thickness or colorant concentration) vary locally.

The method patented by George Meisenbach in 1882 to generate color gradients with a limited number of primary colors is to generate a discontinuous tone (called *halftone*) from the continuous one, which is printed at a small scale [11]. This method relies on the limited acuity of the human eye: small discontinuous printed dots blend together when viewed from a reading distance and appear as a continuous tone [12] p.925. A similar technic exists in painting, called *pointillism*, where dots of pure color where applied on the canvas, trusting the visual system to blend colors together [13]. The French painter Georges Seurat was a pioneer of this technic during the XIX^{e} century, one of his artworks is displayed Figure 3.a. The visual perception of paints based on this technic relies on the optical additive color mixing: light rays of juxtaposed areas of the paint reach the retina where they are mixed, similarly to the working principle of LCD displays. In the case of halftone prints, as light can propagate laterally in the print, the visual perception relies both on the additive color mixing and on the subtractive one, where colors are obtained by absorption through superimposed color filters made of ink [14].

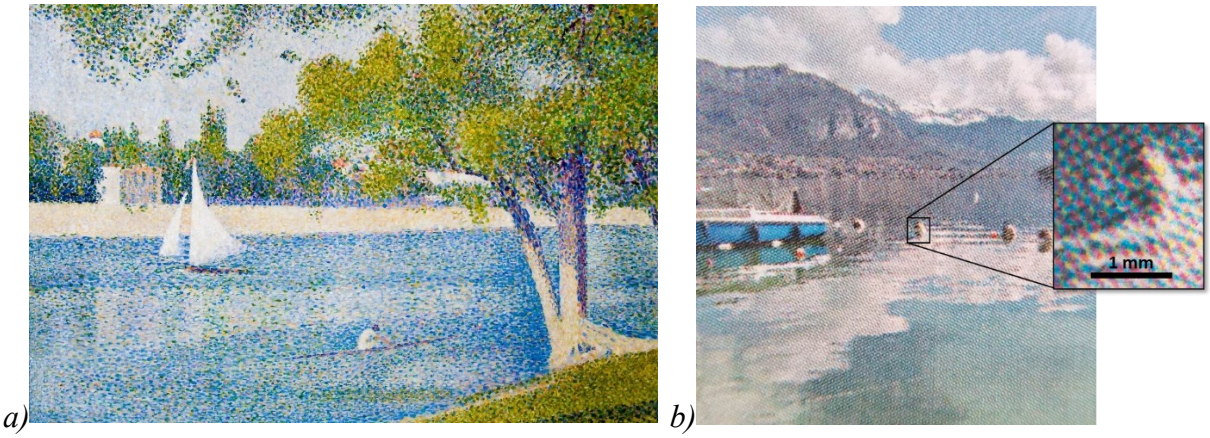

Figure 3. a) George Seurat, La Seine à la Grande Jatte, 1888, Royal Museums of Fine Arts of Belgium, Brussels. b) Halftone print.

Observed with a microscope, a halftone print is composed of small areas of various colors, as shown Figure 3.b. Their shape and distribution are selected during the halftoning process where the continuous tone of the image is transformed into a discontinuous one. Performed originally through optical methods (analog or photographic halftoning), halftoning (also called *dithering)* is nowadays usually performed digitally: an original image, usually in RGB, is converted thanks

to an algorithm into one binary image for each color channel of the printer (called a *bitmap*) where "on" generates a printed dot and "off" leads to an unprinted one. This process is usually performed through a raster image processor (RIP) integrated in the printing device.

There are two main types of halftone dot distributions: frequency modulated (FM), and amplitude modulated (AM). In the case of FM halftones, the area of the printed pattern is constant, and the spatial frequency of the pattern varies spatially. The concentration of printed patterns varies then spatially to generate the color gradients, as shown in figure 4.c. The first FM halftoning techniques were not visually appealing as uniform areas comported visible artifacts once printed.

In the case of AM halftones, the color gradients are obtained through spatial variations of the printed area of the pattern at a given spatial frequency, as shown in figure 4.b. More precisely, the area of the print is divided into cells evenly distributed according to the halftone screen. Each cell is composed of printable dots, the number of which depend on the printing resolution and on the screen spatial frequency. The spatial resolution of the screen, called *line screen ruling* or *screen frequency*, is usually expressed in line per inch (lpi), where one inch corresponds to 24.5 mm. The printing resolution, usually presented in dot per inch (dpi), can be identical or smaller than the printer resolution. The number of tints which can be obtained from one color channel of the printer directly depends on the number of printable dots per cell. It is equal to $\left(N_{dpi}/N_{lpi}\right)^2 + 1$, where N_{dpi} is the number of dpi, and N_{lpi} is the number of lpi. For instance, images encoded within 8 bits present 256 tone per color channel, each cell should then contain 16×16 printable dots to adequately reproduce each channel. For a given number of dpi, decreasing the number of lines per inch leads to larger cells so a higher range of tints. However, large cells can become discernible by the eye at a viewing distance, a compromise needs then to be reached between the range of colors and the spatial perception of the cells.

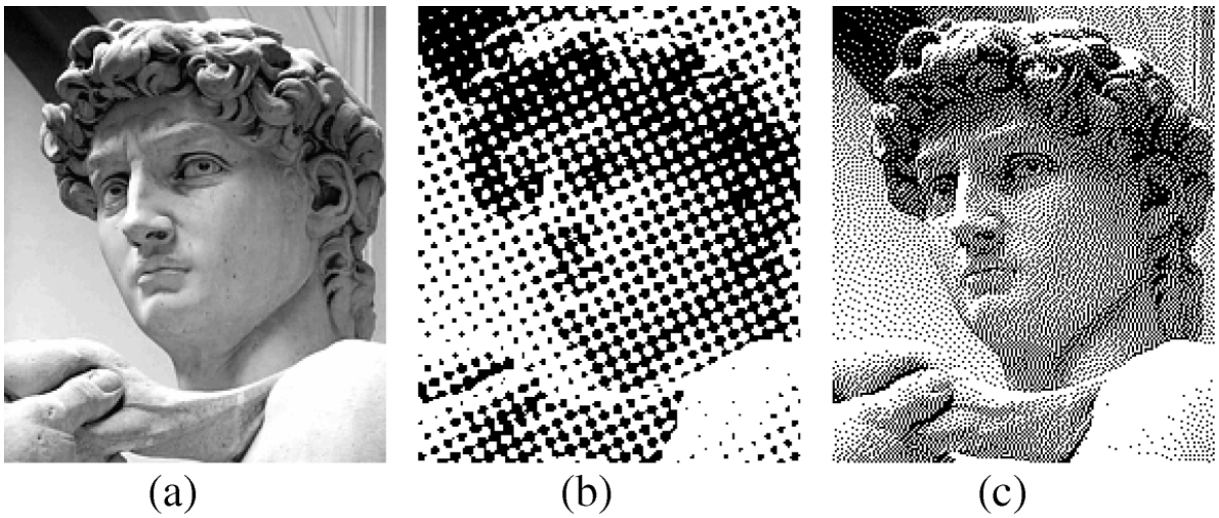

Figure 4. Figure extracted from [15], a) original image, b) AM halftone (clustered dot halftoning), c) FM halftone (Floyd-Steinberg error diffusion).

As FM techniques have appealing appearance for details in images and AM techniques for uniform areas, hybrid halftoning techniques have also been developed [16], some of them can even take into account the structure of the objects in images. Both FM and AM halftoning technics can present clustered or dispersed printed dot [17], [18], where the printed dots are respectively grouped and dispersed. The percentage of the area of a print which is covered by ink during the printing process is called the *surface coverage*. It takes values between 0%, for which the substrate is not printed, and 100%, for which the print is completely covered by ink, which is called a *fulltone*.

In the case of color printing, the halftone pictures from each color channel of the printer are printed in overlays. The printed color dots can be superimposed (*dot-on-dot* printing), juxtaposed (*dot-off-dot* printing), or can partially overlap [19]; these different distributions have an influence on the resulting color. In any case, if there is a slight misalignment between the printed dots of the different color layers, it can lead to *moiré* effects: an overall structure appears of spatial frequency smaller than the one of the halftone screen. *Moiré* can be seen for instance when superimposed line patterns of period p are slightly tilted, at an angle α, as can be seen in Figure 5.a, the period of the *moiré* is then $p/(2\sin(\alpha/2))$, p.334 of [20].

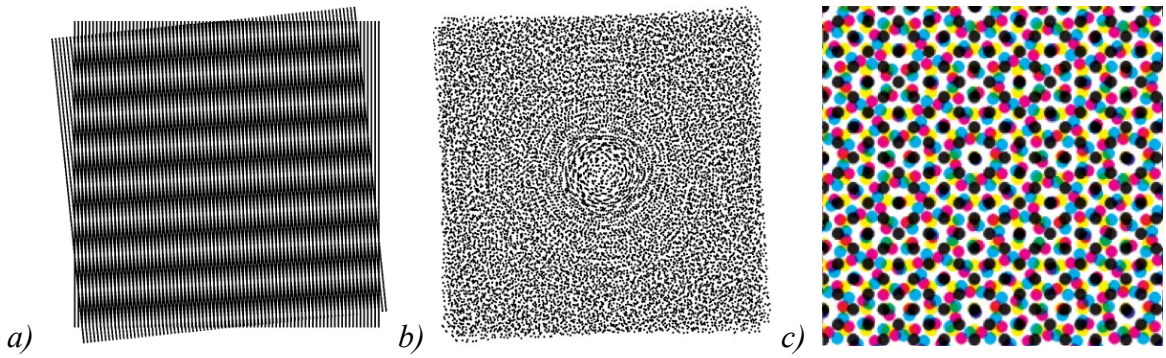

Figure 5. a) Moiré pattern resulting from the superimposition of two line halftones slightly tilted. b) Glass pattern resulting from the superimposition of two identical aperiodic halftones, slightly tilted. A) and B) were extracted from [21]. c) Rosette pattern.

Moiré effects can occur both for AM and FM halftones, they are often considered less visible for FM halftones. If the differently colored layers of FM halftones are correlated they can still produce a *moiré* visual effect called *Glass* patterns, visible in figure 5.b [21]. For AM halftones, in the case of four primary color printing (cyan, magenta, yellow, and black, which is the most common) a way to minimize the *moiré* effect is to rotate the different channels at different angles. As the perception is less sensitive for 45°, the darkest color, black, is usually oriented at 45°, cyan at 15°, magenta at 75° and the lighter color, yellow, is oriented at 0°, angle at which the eye is the most sensitive [12]. The flower-like pattern resulting from these different orientations is called a *rosette*, displayed in Figure 5.c. Halftones with a low screening frequency are less subject to *moiré* effect [16]. For printers with more colour channels, it is complex to find adequate orientations preventing *moiré*, FM halftones are then preferred. The

objective is to get uncorrelated superpositions of the different color layers, this is called a *moiré* free superposition. Blue noise halftoning algorithm, in particular, gives uncorrelated superposition and minimizes the halftone visibility, p239 of [16], p233 [22]. Yet, dispersed dot halftones require a precise printer able to reproduce accurately single dots. Even if inkjet printers are accurate enough for single dots printing, it is not possible for some printing processes such as the electrophotographic one, for which clustered dot AM halftones are thus still used.

2.1.2 Printing processes: mechanical dot gain and color gamut

As the printing application fields are various, the printing processes are multiple, and each induces different deformations between the nominal halftone and the printed result which have an impact on the printed colors. These deformations usually cause an increase of the size of the printed pattern with respect to the digital one, which is called *mechanical dot gain*. The properties of the printing process impacting dot gain and colors are briefly presented in this part. Further explanations on the different printing processes are described in [1].

Conventional printing is mainly composed of four technologies: letterpress (among which flexography), gravure printing, lithography (among which offset), and screen printing. They all require a printing master (e.g., a printing plate) locally transferring ink to the substrate. This printing master can be difficult to produce, but it can offer a good reproducibility between prints once set. These printing processes are then usually used when many copies are needed, such as for packaging applications, or for specific uses (like screen printing for printed electronic). They rely on the fact that the printing plate is partially covered by ink according to the halftone bitmap: through raised or hollow elements for letterpress and gravure printing respectively, through ink-repellent element for lithography or through a mesh and stencil for screen printing [1].

Due to these intrinsic differences, the different printing technologies distort the nominal halftone in different manners which can help to identify the type of printer [23]. Examples are shown in Figure 6: in letterpress technology, there is more ink at the edges of the printed patterns, in gravure printing the cell structure of the plate is visible in the prints, in the screen-printed print the mesh can be visible. For each printing process individual characteristics of the printer have an influence on the mechanical dot gain, such as: the printing speed, the printing pressure, the ink viscosity, its rheological properties and chemical characteristics, the surface properties of the substrate and the inking plate, the thickness of the ink layer on the plate (or the depth of the cell for gravure printing), the geometry of the printer, the temperature [1]. Depending on the different ink-substrate interactions, ink can for instance penetrate and spread differently on the substrate, causing different mechanical dot gains and thus different overall colors.

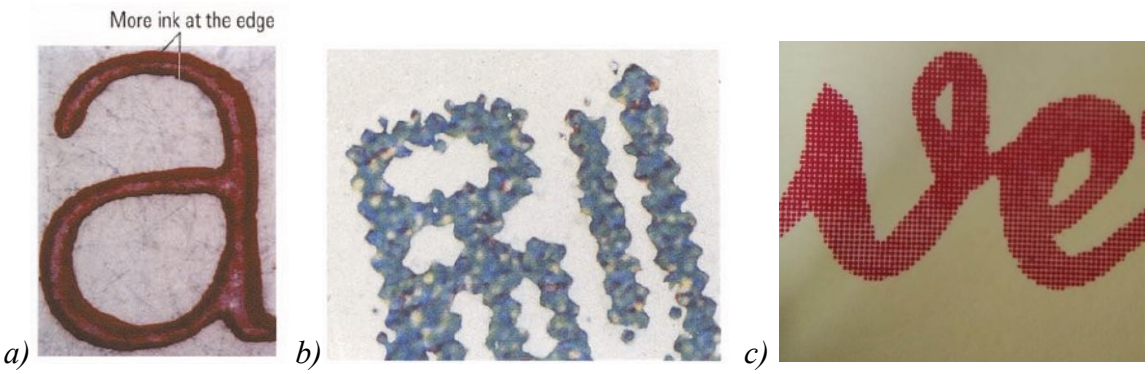

Figure 6. Mechanical dot gain of various printing processes: a) letterpress, b) gravure, c) screen printing, a) and b) are extracted from [1].

Non-conventional or non-impact printing processes (NIP) do not use printing masters, they allow having a new printed content for each print. This adaptability was at the origin of their development and wide spread use. They now show similar accuracy as offset printers. The two main non-impact technologies are electrophotography and inkjet. As they are rather accurate and have a good printing versatility, these printing processes were selected for experiments in this work and are further detailed. Their respective schemes, extracted from [1] are displayed in Appendix II.

In electrophotography a photoconductor drum is charged with a corona and some charges are locally removed by exposure to a controlled light beam (laser or LED), according to the halftone. The toner, containing pigments in powder (solid form) or embedded in a liquid (liquid form), has a charge so that it sets on the charged areas of photoconductor drum. The toner is then transferred to the paper by contact between the paper and the photoconductor drum (or through an intermediate one) and by generating an electrostatic force with a corona. The toner is then melted and anchored to the substrate with a fusing roll. During this step, it can spread on the substrate and usually remains mainly on its surface. If the temperature of the fusing roll is inadequate, the toner can stick to it, which can generate ghost images, p.770 [12]. After the toner transfer, the photoconductor drum is cleaned of the remaining toner particles and of the remaining charges. If the toner cleaning is imperfect, especially for powder toner, the prints can be contaminated by remaining particle, which is called *dusting*, visible in Figure 7.a. Furthermore, the electrostatic and electrodynamic forces applied to the toner particles can have an impact on their adhesion and cohesion which can generate misplaced toner particles, called *satellites*, visible in figure 7.b, reducing the print quality [24]. This technology has a resolution of 1200 dpi (dot size of 21.1 µm). As this process is not accurate enough to generate single dots and as it is not robust to distortions, clustered dot AM halftones are usually preferred, pp. 239-241 [16].

Inkjet is a second non-impact printing technology. In this process, liquid ink is stored in the reservoir of a printhead which deposit ink droplets where it is needed on the substrate, according to the halftone image. Droplets can be generated continuously, for instance with a piezo crystal inside the cavity of the printhead, and the needlessly generated droplets are deflected into a

gutter. Droplets can also be generated on demand where needed. The resolution of this process can be of 1440 dpi (dot size of 17.5 µm) with a thickness below 0.5 µm [1], [25]. The printer resolution is fundamentally limited by the volume of the droplets. The ink droplets impact the substrate, spread on it, and set. As the ink is rather liquid, it can penetrate into the substrate and needs to dry, this can cause bleeding and coalescence in the inked areas for aqueous inks, p.903 [12]. The size and shape of the printed ink dots depend on multiple parameters among which: the nozzle shape and dimension, the viscosity of ink, the ink-paper interactions, the signal addressed to the piezo electric, the drop volume, the number of drops, the velocity and the height of the drop fall, the drop trajectory, the drop break off characteristics, p.882 [12]. The colorants in inkjet inks can be soluble dyes or pigments. In Figure 7.c can be seen the printed drops composing lines of an inkjet print. The visual quality of prints lays in the consistent positioning of the ink drops: if it is inconsistent, they can become visible. For visual applications with a high viewing distance, this dot visibility can be improved by using larger dots with lower colorant concentration, light color primaries can then be used, p.884 [12].

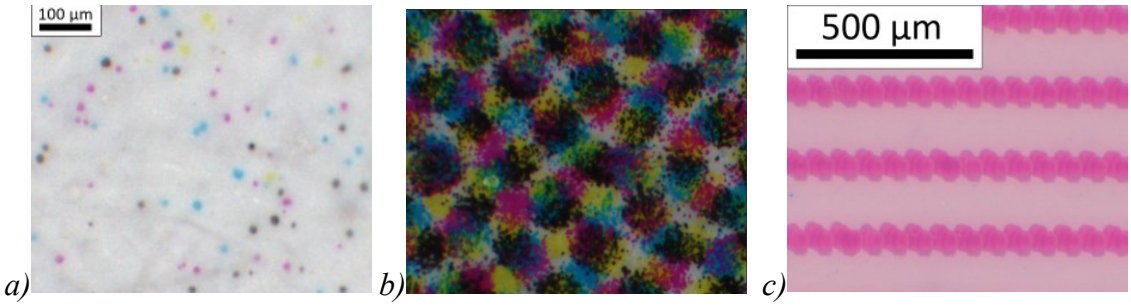

Figure 7. Mechanical dot gain in electrophotography: a) dusting, some toner particles may remain on the drum after the cleaning step and contaminate the print; b) satellites around the printed dots; c) mechanical dot gain in inkjet: the shape of the printed dots are visible in printed the line patterns.

To generate multicolor prints, the different printing technologies usually rely on processed color: the target colors are printed by using a combination of few primaries, usually cyan, magenta, yellow, and black, (CMYK). This enables printers to generate a wide range of colors with only a few printing units, each one successively printing one primary. The range of colors which can be printed by a device is called a *gamut*. It is usually represented in 3D colorspaces such as the CIE1976 L*a*b* colorspace, (further details on this colorspace can be found in Appendix I). To maximize the range of reproducible colors, the volume of the gamut needs to be maximized, the choice of primaries is then crucial as the gamut is usually limited by their number and by their color. The black primary in CMYK printers is not compulsory as black can be obtained by superimposing cyan, magenta, and yellow inks. The black primary is however useful to get a better color reproduction as the CMY superimposition can be brownish. For dark colors, the CMY superimposition can then be replaced by black ink through a process called *undercolor removal* (UCR). Black ink is also usually cheaper than the other primaries

and can be used to save ink in color prints through a *grey component replacement* process (GCR), and by using it for texts.

Each primary acts as an absorbing filter which can be combined with others by juxtaposition, playing on the additive color rendering, and by superimposition, playing on the subtractive color rendering. Three chromatic primaries are sufficient to reproduce a maximal number of colors with a minimal number of primaries. Their spectrum is not perfectly selective which tend to reduce the range of reproducible color and complexify color management. Inkjet, as it is not limited by the *moiré* caused by clustered AM halftoning, and as it does not necessarily rely on printing units, can deal with more color primaries to increase the color gamut. For the other printing processes, in the case where a color outside the gamut needs to be printed (for instance the Pantone specific color of a brand logo) spot colors can be used, associated to a dedicated color unit [26], [27]. Other processed colors can also be added, such as orange, green, and violet. To print color gradients of good quality light primaries can also be added. The color primaries have a significant impact on colors, but the result also depends on the substrate and its finishing. The main paper finishing consists in *coating*: applying a layer composed of pigments, vehicles, and additives over the plain paper. The paper can then be calendered between rollers to get the final texture: matte, glossy or satin. These finishing step have an impact on the color, on the printability, on the optical properties, and on the texture of the substrate [1].

2.1.3 Optical properties of prints and optical dot gain

Color reproduction is impacted by the color dot distribution, selected in the halftoning process, by the distortions which can modify the dots during the printing process, i.e. the mechanical dot gain, and by the choice of primaries which has an impact on the range of reproducible colors. The optical properties of the print have also a significant impact on color reproduction, mainly due to an effect called *optical dot gain* which is qualitatively detailed in this paragraph. Further explanations on the modelling of this phenomenon are exposed in Section 2.2.

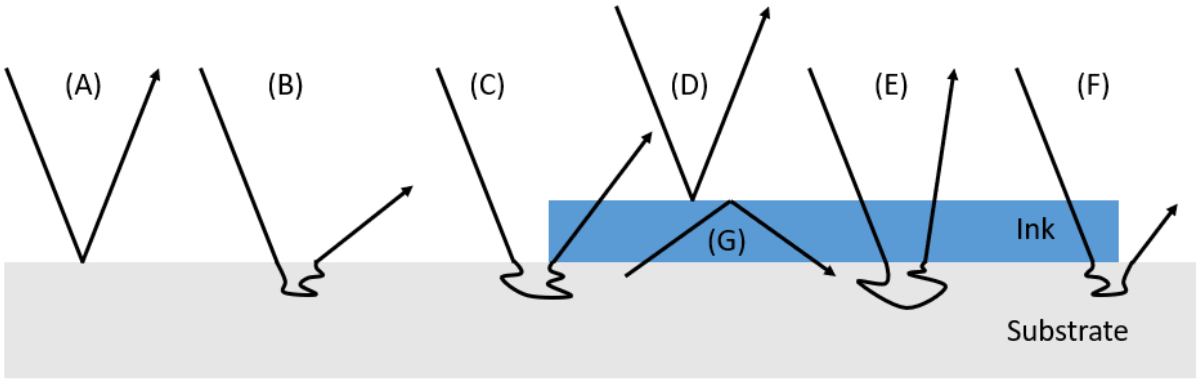

Figure 8. Light interactions with prints, inspired from [25].

In Figure 8 are displayed various paths which can be taken by light when meeting a print composed of a substrate and inked areas. Paths (A) and (D) describe a surface reflection: light is partially reflected at the interface between air and the material, i.e. substrate or ink, due to the difference of optical index between air and the material. Ink and substate are usually of similar optical index, the ink-substrate interface is then optically neutral. Usually achromatic, the surface reflected light can sometimes be colored with a metallic sheen if the ink is highly absorbing, a phenomenon called *bronzing* [28], illustrated in Figure 9. b. The angle of reflection of the light is identical to the incident one, with respect to the normal of the material surface. If the interface is planar with a directional illumination, all the light reflected at the interface has a unique direction, called *specular direction*, pictured in Figure 9.a. If the interface is rough, light is reflected in several directions depending on the local slopes, it is a *diffuse surface reflection*.

The portion of light which is not reflected at the interface is refracted in the matter, where it can be: transmitted, absorbed, or scattered. For instance, if the substrate is scattering and non-absorbing, light can propagate within the substrate before exiting the print at a different point than the entry one, as illustrated by path (B). If the print has some optical brighteners agents (OBA), light may not only by scattered but also absorbed and reemitted at longer wavelengths through a fluorescence phenomenon such as the one displayed in Figure 9.c.

Let us now consider path (E), supposing the ink is non-scattering, light is then partially absorbed and partially transmitted by the ink, after which it is reflected by the substrate through a bulk reflection before propagating again through the ink layer. Light is then affected two times by the absorption of the ink layer. In the cases of paths (C) and (F), the distance of propagation of light within the substrate enables light to propagate from a non-inked area to an inked one (i.e., path (C)) and conversely (i.e., path (F)). The light is then impacted by the absorption of the ink layer only once. This scattering within the substrate optically blurs the inked area boundaries, which tend to increase the apparent area of the inked dots, a phenomenon called *optical dot gain*.

The internal reflection caused by the interface with air, featured by path (G), also contributes to this effect by trapping light within the print. This phenomenon, depicted in Figure 9.D, depends on the perimeter of the printed area and the scattering properties of the materials and cannot be easily separated from the mechanical dot gain [29]. Both the optical and the mechanical dot gains have an effect on the printed pattern at the microscale, which can significantly impact the color of the print at a reading distance [30].

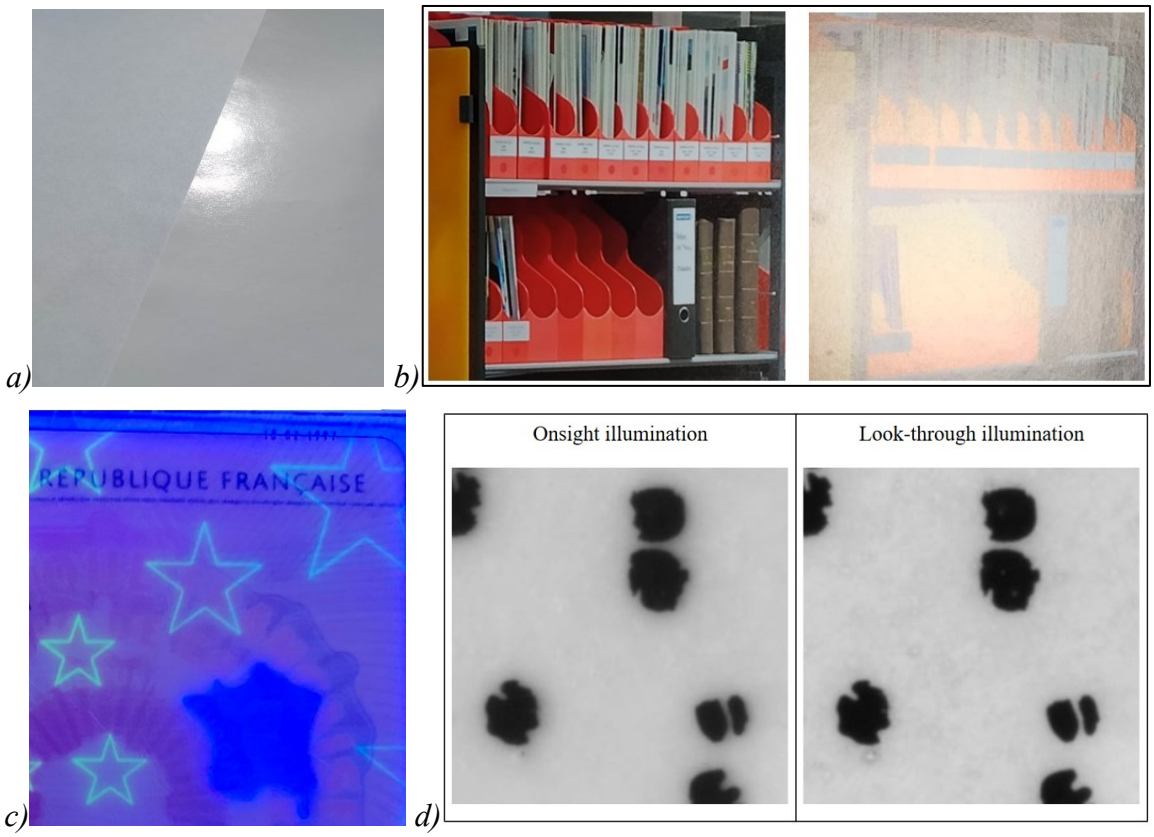

Figure 9. a) Effect of the paper surface finishing on the surface reflection: plain office paper on the left, glossy coated paper on the right, captured in the specular direction. b) Bronzing effect, left: inkjet print captured in the non-specular direction, right: same print captured in the specular direction. The print has a metallic sheen. c) Effect of fluorescence: driving licence observed under UV light: fluorescent stars are revealed. d) Effect of optical dot gain on plastic print, extracted from [29], left: print captured in reflection mode, the optical dot gain generates a color gradient between the inked dots and the non-inked areas; right: print captured in transmission mode, the optical dot gain is reduced in comparison with the left pictures as it is mainly due to internal reflections (path (G)) and much less on scattering than in the reflection mode (paths (C) and (F)).

2.1.4 Coating processes and impact on color

Various application fields of the printing industry require the prints to be overlaid with a transparent coating layer (e.g., a varnish or lamination layer). This coating layer can improve the resistance of the print to scratches or liquid penetration, improve its surface properties, or enhance its appearance. In the packaging industry for instance, the substrate of the package may need to be protected from moisture or grease with a coating layer [31]. Book covers or identity cards are subject to a lot of abrasion and scratches and require a protection [32], this layer can also prevent forgery for secured documents [33]. Some processes also require specific surface friction coefficients, to stack the products or to fold them for instance, which can be obtained through a coating process. Some coatings can also make the product less inflammable when needed [1].

There are two main types of coating materials: varnishes and lamination films. Varnishes are usually water-based, acrylic or photo-curable varnishes [34], [35], they can be printed, applied through a varnishing unit directly implemented in the printer, or independently, off-line, after the printing process. According to their composition, drying process, and interactions with the substrate, various thicknesses can be obtained. Except for the UV varnish for which high thicknesses can be obtained, the lamination layers are usually thicker than the ones obtained with a varnish coating. Laminates can be composed of PET, PE, or PP [36], [37] and can be thermally applied to the prints, extruded, calendered, or applied with adhesives [1], [33].

Various studies have shown that adding a coating layer on a print modifies the color of the prints [27], [38], [39]. For a smooth one, the colors have more depth (darker and more chromatic) when a coating layer is added [1], [4], for a matte one it can decrease the saturation of the colors [39], [40]. These color differences by addition of a coating layer were first studied in the case of paintings [41]–[43]. They come from a modification of the surface topology [44] and have an impact on the glossiness of the print [37], [39], [45]–[49]. Indeed, adding a coating layer can smoothen the surface of the material and reduce light scattering on it [50], [51], or, on the contrary, increase the surface scattering in the case of a matte finishing [52].

Berns and de la Rie mentions the impact of the optical index of the varnish on interreflections within the varnish in the case of paintings [42], a phenomenon also taken into account for modelling by Simonot and Elias in [43]. The optical index of the coating layer can also modify the color of the surface reflection of the prints if they are subject to bronzing.

Moreover, several studies show that the coating layer induces an additional dot gain which is dependent on the surface coverage (or tone value) of the halftone print [4], [31], [40], [53], [54]. According to Cigula and co-workers, the tonal value increase is higher for UV varnish than for water-based and offset varnishes [53]. This can be caused by the fact that the UV varnish layer, which was applied off-line, was thicker than the other varnish layers, which were applied on-line. It can also be caused by the fact that the optical brighteners embedded inside the substrates were less activated with the UV varnish, which acts as a filter, than with the other ones. This could also be caused by absorption by the coating layer, an effect also mentioned in [48]. The study presented by Hoffstadt in 2004 shows that not only the additional dot gain seems to be dependent on the coating layer, but also on the size of the printed pattern, in terms of lineature for AM halftoning and in terms of dot size for FM halftoning [4]. Intermediate screening, 120-150 lpi are more impacted by the additional dot gain than higher lpi. The additional dot gain also varies as a function of the surface coverage and shows a peak for smaller coverages than the ones obtained for traditional dot gain. For fulltones, no color change was obtained, therefore, the color changes are not due to absorption by the coating layer. In the case of processed colors, it showed that the addition of a coating layer could induce a significant hue change in the print. Furthermore, apart from the surface reflection, similar results were obtained for matte and glossy coatings.

To conclude, the colors obtained in prints depend on many parameters: the halftoning method, the printer characteristics (e.g., the mechanical dot gain), the optical properties of the print (e.g., the optical dot gain), and the surface finishing of the print. In this work, the microscale deformations of the print due to mechanical and optical dot gains had a significant impact on the measurement methods as these deformations needed to be accounted for. To accurately reproduce targeted colors, reproduction devices require management methods, which are detailed in the following subsection.

2.1.5 Color management

Color reproduction requires color management methods. This subsection describes the main principles of color management, the workflow and approaches towards it; the specific case of color reproduction with coated prints is presented.

Principles

Color is a visual sensation generated by the brain from the light signals reaching the eye. Colorimetry aims at linking the visual sensation with the physical properties of the light signal. It usually represents colors in a 3D space such as the CIE1976 L*a*b* color space. The objective of color management is to be able to accurately reproduce similar color sensations through different color reproduction devices. In other words, the objective can be simplified to generate colors of similar L*a*b* coordinates with various devices. The target colors are called *device-independent colors*. The challenge lays in the fact that each color reproduction device has its own way of generating colors: through the deposition of CMYK ink dots in the case of a printer, through the enlightenment of RGB LEDs for a display, etc. Each device can then describe colors according to its own *device-dependent colorspace* (e.g., CMYK for a four-color printer).

One color management method which is widely spread consists in linking the device-dependent colors with the device-independent ones. It can be performed by characterizing each color reproduction device through an ICC profile, with ICC denoting the *International Color Consortium* which promotes and defines specifications for color management [55]. Through the ICC profiles, several color reproduction devices can communicate through a *profile connection space* (PCS), corresponding to the device-independent colorspace, to enable the reproduction of device-independent colors. For instance, if a picture of a scene is captured with a camera and printed, the original colors of the scene can be retrieved from the RGB values captured by the camera by using the ICC profile of the camera. Consequently, the original colors can be printed by deducing the corresponding CMYK values from the ICC profile of the printer.

Unfortunately, color reproduction devices have a limited gamut. The gamuts of different devices are usually different, for instance, the gamut of a printer is usually smaller than the one of a display as inks absorb a less monochromatic signal than the one which is emitted by the LEDs of a display. Therefore, it becomes necessary to perform some gamut mapping to manage

the colors which are outside of the gamut, and to ensure the best color reproduction. This gamut mapping can be performed differently according to the color rendering intents. There are four main color rendering intents: the perceptual one, the relative and absolute colorimetric ones and the saturation one.

With a *perceptual intent*, the objective is to perceive in the reproduction similar color variations as the ones occurring within the original piece, the colors of the original piece are then modified and mapped into the reproduction-device gamut. This type of mapping is commonly used when printing a camera picture where the objective is to reproduce the overall perception with the color variety and their gradient, the true colors of the scene are less important in this case.

On the contrary, with a *colorimetric intent* the objective is to reproduce as accurately as possible the colors of the original piece. For instance, the colors outside of the reproduction-device gamut can be clipped to the boundaries of the gamut of the device. With a relative colorimetric intent, the white reference of the original piece is identical to the white reference of the reproduction device. An absolute colorimetric intent requires the color of the white reference of the original piece to be mapped inside the reproduction-device gamut. For instance, the reproduction of logos usually has a colorimetric intent: the colors of the logo have to be identical whatever the reproduction device.

The *saturation intent* involves mapping all the colors of a piece at the boundaries of the reproduction-device gamut in order to have the most vibrant color at the expense of the color gradients. This is performed mostly for the reproduction of graphs [56].

Workflow and approaches

There are three main steps to make a device capable of color reproduction, steps described as "the three *C*s" in [56]: Calibration, Characterisation and Conversion.

Calibration consists in setting the parameters of the device to make it stable and its results reproducible. For printers, this step can include the choice of ink quantity for the fulltones, the choice of halftoning method, the choice of inking limit per channel and the total area coverage, and a color linearisation. For each color channel, this linearisation consists in determining a tonal value correction to obtain a linear relation between the print surface coverages (i.e., its tonal value) and the color difference between the print and the substrate. This calibration may include setting the printer to standard requirements such as the ones described by ISO 12647, which ensures a standardisation of the printed colors, [57].

The second step aims at *characterising* the device to derive its ICC profile. If the printer has been set to a standard and representative of the process, this step is sometimes not mandatory as the standard ICC profile are publicly available [58]. ICC profile can also be provided by the device manufacturers, but it is usually more accurate to generate a custom profile. There are two main approaches to characterise the printer: through numerical characterization or through optical modelling. The numerical approach consists in printing a great number of color patches by using a color chart and characterizing their color with a spectrophotometer. The profile is

then derived by interpolating, by fitting the data, or by using a neural network. The color chart needs to be detailed enough to accurately describe the gamut, and the spatial distribution of the patches may need to be considered in the case of a printer spatially inconsistent. The problem of this method is that the number of required patches can be very high and increases significantly for each supplementary ink. For instance, the ECI 2002 test chart developed to characterize CMYK printers consists in 1485 patches [59], whereas the "idealliance" ECG test chart enabling the characterisation of 7-color printers (CMYKOGV, with O = orange, G = green and V = violet) consists in 4340 patches [60], both test charts are presented in Figure 10. Yet, the increase of the number of inks seems to become more common as it allows a larger gamut which can prevent the use of spot colors. This growing demand is illustrated by the project no. 32.176 from Fogra, which should be released in August 2023 and aims at standardising 7-color printing for offset printers [61]. The other method is through optical modelling. This requires less measurements than for the numerical approach as the color rendering is calculated through optical models. Hybrid techniques have also been developed by calibrating optical models on a large number of patches.

The last step for color management is the *conversion*: it enables to link in the forward and the backward ways the device-dependent and the device-independent colorspaces. This is usually performed by a color management module (CMM), through inversing the optical models, interpolating or fitting the ICC profile [10]. For standardised printing devices, the performances of the color management can be evaluated by printing a control strip composed of a few color patches of known device-independent color.

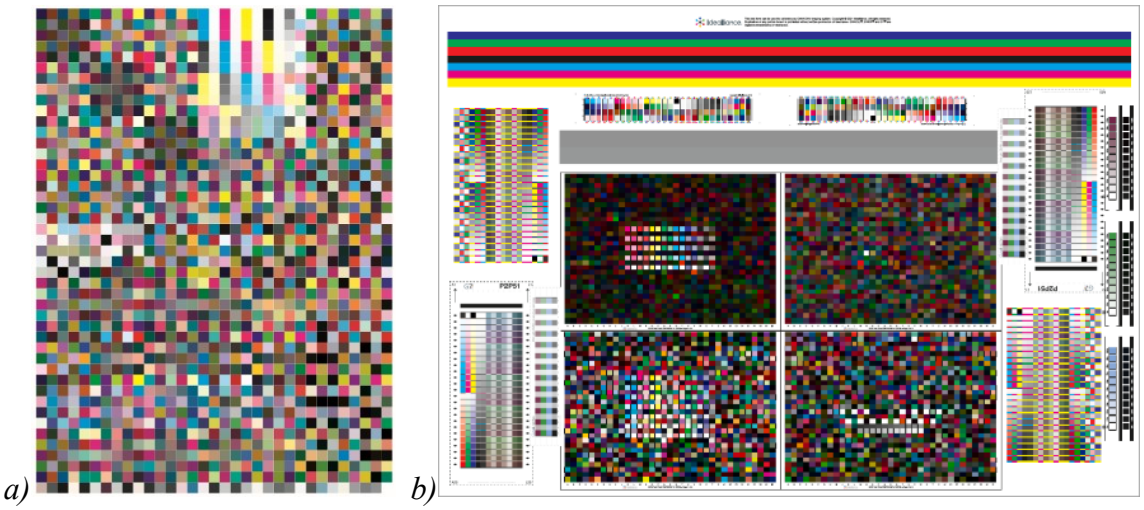

a) b)

Figure 10. a) ECI2002 test chart for CMYK printers (1485 patches) [59], b) ECG idealliance test chart for CMYKOGV printers (4340 patches in the central part used for characterisation), Image provided courtesy of Idealliance [60].

2.1.6 Color management when prints are coated

When the coating process is independent from the printing one, color management is usually performed on uncoated prints. Yet, various studies have shown that adding a coating layer over

prints induces significant color change which would need to be taken into account in the characterisation step for an accurate color management [53].

Hoffstadt presents an empirical solution to predict the effect of a coating layer on an ICC profile by adding a correction on the tonal value of each color channel of the profile of the uncoated prints, and by adding a 2% stray light contribution within the calculation of the measured XYZ values to predict the effect of a matte coating [4]. The maximal tonal correction was a tonal value increase of 6% of and the correction resulted in a color difference ΔE_{94}, presented in Appendix I, between 1.4 and 1.7, depending on the coating. This study states that it could be better to include micrometric measurements for color prediction, to better anticipate the effect of the additional dot gain linked with the interreflections within the coating layer. Österberg opted for a similar empirical solution through a compensation of the tonal value for each channel and found that the correction as a function of the input tonal value could be fitted with a polynomial function [31].

In the end, a collaboration between ECI (European Color Initiative), Fogra, and BVDM released in 2012 profiles characterising the printed colors coated with matte and glossy OPP layers, FOGRA49 and FOGRA50 respectively [62], which were generated with a printer of standard unlaminated profile corresponding to FOGRA39. However, it is mentioned that it is only to get a preview of the color changes and suggests to make custom profiles, especially for varnishes which were not considered [63].

The patent in [54] presents a method to predict the color change by using Kubelka-Munk model to characterise the coating layer, and by evaluating empirically the additional dot gain it induces on the print. Therefore, it seems that there is currently no optical approach which allows to predict the color changes induced by a coating layer.

To conclude this section, reproducing colors with a printer requires a strong color management to get consistent and reproducible colors. The reproduction is difficult due to multiple artifacts occurring at the microscale which have an impact on the colors perceived at a viewing distance. These artifacts include the halftoning method, the mechanical dot gain and the optical dot gain. Adding a coating layer over the print also induces a color change even if the layer is perfectly clear, especially if the coating layer is thick. This addition of a coating layer induces an additional dot gain which needs to be taken into account during the generation of the ICC profile of the printer. This could be performed numerically, by measuring a great number of patches, or optically, which is the approach that we chose to develop as it can be applied to any printing materials and requires few measurements. Such an optical approach to predict the appearance of coated prints requires theoretical and experimental tools which are detailed in a second part.

2.2 Optical models for color reproduction

In this section are described the main optical models for color reproduction which can be found in the literature. A table summarising the notations is available at the end of the manuscript in Appendix X.

Light is an electromagnetic radiation of wavelengths comprised inside the visible range [400; 800 nm], or the nearly visible range (ultraviolet and infrared wavelengths). In this document, the dimensions and conditions are such that light can be described by the geometrical optics: it is assumed that light propagates along rays and is not impacted by diffraction or interference phenomena.

2.2.1 Notions of radiometry

Light can be described by its power, called *flux* (in W). Its flux in one direction, described by a solid angle, is called *intensity* (density of flux per unit solid angle, in $W.sr^{-1}$). An *isotropic* source is a punctual source of constant intensity for any emission direction. The flux received by a surface can be described with a quantity called *irradiance* (density of received flux per unit area, in $W.m^{-2}$). Equivalently, *exitance* describes the flux emitted by a surface, per unit area (in $W.m^{-2}$). The *radiance* describes the flux emitted or received by a surface in one direction, described with a solid angle. It is then a density of flux per unit geometrical extent (in $W.sr^{-1}.m^{-2}$). All units can be converted into visual units accounting for the spectral sensitivity of the human eye, or to photon units accounting for photon energy [64].

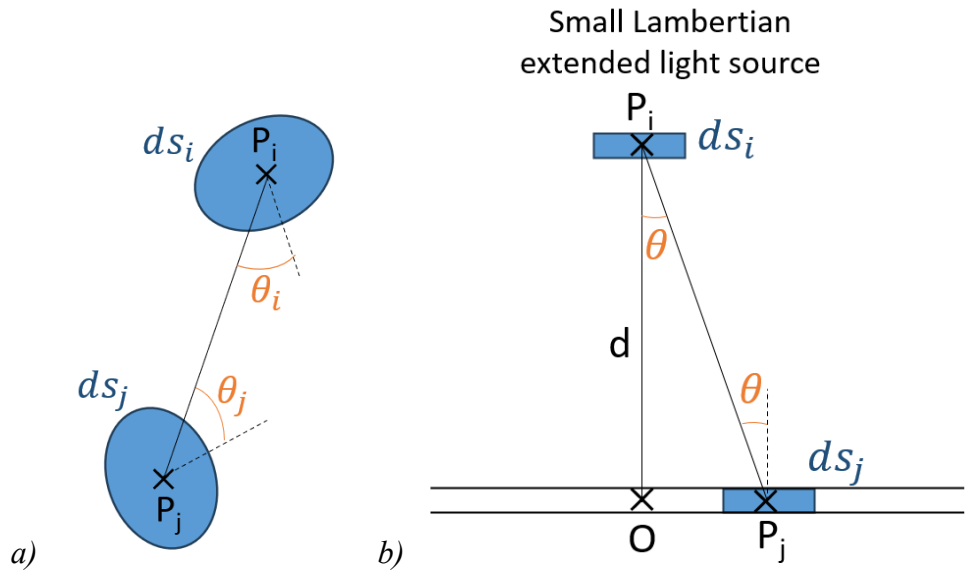

Figure 11. a) Geometrical extent between two surfaces; b) Small Lambertian extended light source illuminating a planar surface. Both schemes are adapted from [64].

The elementary geometrical extent (in m².sr) between two elementary surfaces around points P_i and P_j represented in Figure 11.a is:

$$d^2G(P_i,P_j) = \frac{1}{P_iP_j^2}(ds_i \cos\theta_i)(ds_j \cos\theta_j) \quad 1$$

where ds_i is the elementary area around P_i and ds_j is the elementary area around P_j. The normal of the surface around P_i is directed at an angle θ_i from $\overrightarrow{P_iP_j}$, and the normal of the surface around P_j at an angle θ_j.

An extended light source of radiance independent of the direction is called *Lambertian*. Similarly, a surface diffusing light constantly in any direction is a *Lambertian surface*. If the small surface around a point P_i is Lambertian of exitance $M(P_i)$, it emits an equal radiance in every direction:

$$L(P_i) = \frac{M(P_i)}{\pi} \quad 2$$

The irradiance at the elementary surface around P_j coming from the small surface around P_i is:

$$E(P_j) = \frac{d^2G(P_i,P_j)L(P_i)}{ds_j} = \frac{1}{P_iP_j^2}(ds_i \cos\theta_i)(\cos\theta_j)L(P_i) \quad 3$$

Let us now consider a very small Lambertian extended source around a point P_i illuminating a planar surface placed at a distance *d*, as depicted in Figure 11.b. The point O is the nearest point from the plane to point P_i. For any point P_j of the plane $\theta_i = \theta_j = \theta$ and the distance between P_i and P_j is $P_iP_j = d/\cos\theta$. Therefore, the irradiance on a small area around P_j is:

$$E(P_j) = \frac{1}{d^2}\cos^4\theta \, dsi \, L(P_i) = \cos^4\theta \, E(O) \quad 4$$

where $E(O)$ is the irradiance from the small extended light source at a small area around point O.

Therefore, it can be noted that if a very small Lambertian light source enlightens a flat surface, its irradiance at the surface varies according to a $\cos^4$ law [64].

2.2.2 Light-matter interactions

In Section 2.1.3 on the optical properties of prints, the main light interactions with prints were qualitatively described. This paragraph aims at providing adequate theoretical tools and models to describe quantitatively the different interactions between light and matter in the case of prints. Optical models for prints, based on these tools, are described in next paragraphs.

Reflectance describes the ratio between the incident flux and the reflected one. Reflectance can depend on the angle of measurement, especially if the surface is not Lambertian. Bidirectionnal Reflectance Distribution Function (BRDF) characterizes the variations of reflectance as a

function of the angles of illumination and measurement. Volume scattering and internal reflection inside the material can allow light to propagate inside the material and exit it at a point at a non-negligible distance from the illumination point. The probability for light to escape at a given distance is described by the Point Spread Function (PSF) of the material. To fully characterize the way light is reflected by an object, Bidirectional Scattering-Surface Reflectance Distribution Function (BSSRDF) measurements would be needed [65]. The radiometric definitions of BRDF, PSF, and BSSRDF are available in [64]. In the printing industry, characterising and predicting the reflectance is usually enough to have a good print quality. Reflectance can be converted to color information through mathematical transformations described by the CIE. The transformations which were used during this study to obtain CIE1931 XYZ tristimulus values, L*a*b* coordinates and estimate the color differences are presented in Appendix I.

Let us first consider surface reflection. A light ray propagating in a medium of optical index n_0 and meeting the smooth surface of a medium of optical index n_1 can be both reflected and refracted through this interface according to Snell-Descartes Law. If $n_0 > n_1$, there is a limit angle above which light is totally reflected by the interface, there is no refracted ray. This limit angle is equal to $\arcsin(n_1/n_0)$. The amount of light reflected by the interface can be characterised by the reflectance. According to Fresnel's formulae, the reflectance, R_{01}, at an interface depends on the incidence angle, θ_0, the ratio $n_{01} = n_1/n_0$, and the light polarization. If light is unpolarized or at normal incidence, and with $n_0 < n_1$, the reflectance at the interface is:

$$R_{01}(\theta_0) = \frac{1}{2}\left[\left(\frac{n_{01}^2 cos\theta_0 - \sqrt{n_{01}^2 - sin^2\theta_0}}{n_{01}^2 cos\theta_0 + \sqrt{n_{01}^2 - sin^2\theta_0}}\right)^2 + \left(\frac{\sqrt{n_{01}^2 - sin^2\theta_0} - cos\theta_0}{\sqrt{n_{01}^2 - sin^2\theta_0} + cos\theta_0}\right)^2\right] \quad 5$$

At normal incidence, with $n_1 = 1.5$ and $n_0 = 1$, $R_{01}(0°) = 0.04$. The ratio between the refracted flux and the incident flux is called transmittance, denoted T_{01}. As all the light is either reflected or transmitted by the interface, it is equal to:

$$T_{01}(\theta_0) = 1 - R_{01}(\theta_0) \quad 6$$

In the case where light comes from the medium of index n_1, at an angle $\theta_1 = \arcsin(n_0 \sin(\theta_0/n_1))$, the reflectance, R_{10}, at the interface with the medium of optical index n_0 is: $R_{10}(\theta_1) = R_{01}(\theta_0)$ and the transmittance is: $T_{10}(\theta_1) = T_{01}(\theta_0)$. At normal incidence, with $n_1 = 1.5$ and $n_0 = 1$, $R_{01}(0°) = 0.04$.

It can be noted that the surface reflection can be partially or totally polarized (even if the incident light might not be polarized). Thus, observing a material through a polarizer can remove the specular reflection, leading to different measurements from unpolarized ones [66]. For instance, sunglasses are often polarized to better see the road or the bottom of the sea. In the case of a totally polarized incident light, the surface reflection stays similarly polarized. It can also be noted that a very absorbing medium can have a complex optical index, $\hat{n}_i = n_i +$

$i\kappa_i$ where the imaginary part κ_i is linked with the material absorption coefficient, α, at the wavelength λ with: $\alpha(\lambda) = \frac{4\pi\kappa_i(\lambda)}{\lambda}$. In this case the surface reflection can be colored [28]. Some material can have an optical index varying with the wavelength, e.g., water or glass. The angle of the refracted ray can then vary according to the wavelength. This is called *dispersion* and is at the origin of rainbows. In the case where the material is rough, its surface can be seen as a composition of multiple microfacets, each oriented differently, reflecting the incident light in various directions. The material appears matte and its surface scattering can be described using a microfacet-based BRDF model, [67], [64].

Inside a medium, light can be transmitted, absorbed, or scattered. In the case of an absorbing medium of absorption coefficient α, the light propagating for a distance, d, is transmitted to a proportion t, called *intrinsic transmittance*, described by Beer-Lambert-Bouguer law:

$$t = e^{-\alpha d} \tag{7}$$

If the material is perfectly clear, $t = 1$. It can be noted that if the light propagates in the material for a distance $k \times d$, it is transmitted to a proportion $t^k = e_i^{-\alpha k d}$.

A medium both absorbing and scattering can be described by the Kubelka-Munk model [68], [69], conceived in 1931. It derives from the radiative transfer equation in the case where two fluxes in opposite directions interact with a planar medium. This medium is considered turbid, with K its absorption coefficient and S its scattering coefficient, both in m^{-1}. By considering a material slice of infinitely small thickness dz, i the light flux oriented upward and j the light flux oriented downward with respect to the horizontal layer, the following equations can be found:

$$\begin{cases} \frac{di}{dz} = -(K+S)i + Sj \\ \frac{dj}{dz} = -Si + (K+S)j \end{cases} \tag{8}$$

The solution at the thickness z is:

$$\begin{cases} i(z) = i(0)\cosh(bSz) + \frac{1}{b}[j(0) - ai(0)]\sinh(bSz) \\ j(z) = j(0)\cosh(bSz) + \frac{1}{b}[aj(0) - i(0)]\sinh(bSz) \end{cases} \tag{9}$$

where

$$a = \frac{K+S}{S} \text{ and } b = \sqrt{a^2 - 1} = \frac{1}{S}\sqrt{K^2 + 2KS}.$$

The solution can also be written in a matrix format [12]:

$$\begin{pmatrix} j(z) \\ i(z) \end{pmatrix} = exp\left[\begin{pmatrix} -(K+S) & S \\ -S & (K+S) \end{pmatrix}(z-0)\right] \cdot \begin{pmatrix} j(0) \\ i(0) \end{pmatrix} \tag{10}$$

where the exponential matrix of a matrix M is:

$$\exp(M) = \sum_{k=0}^{\infty} \frac{M^k}{k!} \quad 11$$

Supposing that the turbid medium has no interface, has a thickness d and is only illuminated from above in the downward direction by a flux $i(0) = I_0$, the reflectance ρ_d and transmittance t_d of the layer are:

$$\begin{cases} \rho_d = \dfrac{j(0)}{I_0} = \dfrac{\sinh(bSd)}{b\cosh(bSd) + \mathrm{a}\sinh(bSd)} \\ t_d = \dfrac{i(d)}{I_0} = \dfrac{\mathrm{b}}{b\cosh(bSd) + \mathrm{a}\sinh(bSd)} \end{cases} \quad 12$$

In the case where the medium is infinitely thick, its reflectance, ρ_∞, is:

$$\rho_\infty = 1 + \frac{K}{S} - \sqrt{\left(\frac{K}{S}\right)^2 + 2\frac{K}{S}} \quad 13$$

From which can be derived:

$$\frac{K}{S} = \frac{(1-\rho_\infty)^2}{2\rho_\infty} \quad 14$$

In the case of the dyeing industry where the K/S ratio of a mix of dyes is composed of the K_i and S_i coefficients of the individual dyes, i, composing the mix [70]:

$$\left(\frac{K}{S}\right) = \frac{\sum_{i=0}^{N} c_i K_i}{\sum_{i=0}^{N} c_i S_i} \quad 15$$

where c_i is the concentration of the colorant i.

If the colorants are embedded in a support and if they have a scattering coefficient negligible with respect to the scattering coefficient of the support, Equation 15 becomes:

$$\left(\frac{K}{S}\right) = \sum_{i=0}^{N} c_i \frac{K_i}{S_0} \quad 16$$

where S_0 is the scattering coefficient of the support.

The K/S ratio of the mix can then be determined from the K/S ratio of each individual colorant embedded in the support. If the colorant is strongly scattering the K and S ratios can be deduced from measurements of the colorant in optical contact with a black substrate and with a white substrate.

One of the limitations of this model is that it does not consider the interfaces of the medium, at which light can be partially reflected. Saunderson proposed a correction [71]:

$$R = r_s + \frac{T_{in}T_{out}\rho}{1 - r_i\rho} \quad 17$$

where R is the corrected reflectance and ρ is the reflectance of the medium without interface (its intrinsic reflectance).

$r_s, r_i, T_{in}, and\ T_{out}$ characterise the light transfers at the interface with air. The reflectance r_s represents the portion of incident light externally reflected by the air-print interface and captured by the observer or the detector. The transmittance T_{in} represents the portion of light entering into the substrate. The reflectance r_i represents the portion of light internally reflected by the print-air interface, and the transmittance T_{out} represents the portion of light emerging from the substrate in direction of the observer or detector, as presented in Figure 12. These light transfers at the interface are further detailed in the Clapper-Yule and Williams-Clapper model paragraphs.

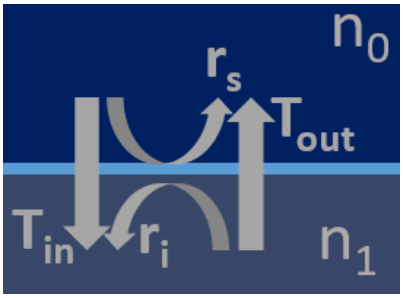

Figure 12. Light transfers at the interface between two media of optical indices n_0 and n_1.

2.2.3 Murray-Davies model

One of the first widely used optical model for prints was described in 1936 by Murray and Davies [72]. They linked the optical density of a single-ink halftone with the reflectance and surface coverage of the printed ink. The optical density, D, is defined with respect to the average spectral reflectance of a print, R, with:

$$D = -\log(R) \tag{18}$$

According to Murray and Davies work, a halftone of effective surface coverage, a, of fulltone reflectance, R_1, of substrate reflectance 1, and of optical density, D, follows the equation:

$$D = \log\left(\frac{1}{1 - a(1 - R_1)}\right) \tag{19}$$

From this equation, considering a reflectance R of the halftone print and a substrate reflectance R_0, can be derived the Murray-Davies equation:

$$a = \frac{R - R_0}{R_1 - R_0} \tag{20}$$

2.2.4 Neugebauer model

In 1937, Neugebauer enlarged this result to multi-ink halftones [73], [74]. He started by explaining that the colors displayed by a halftone not only consisted of the colors of the ink but

also their superimposition. These colors were afterward designed as Neugebauer primaries. Neugebauer gave the example of a print made of cyan, magenta and yellow inks printed on a white substrate. The Neugebauer primaries, displayed in Figure 13, are then:

- white (no ink)
- cyan, magenta, yellow (one ink superimposed with the substrate)
- blue (superimposition of cyan and magenta inks on the substrate), red (superimposition of magenta and yellow), green (superimposition of cyan and yellow)
- black (superimposition of the three inks on the substrate).

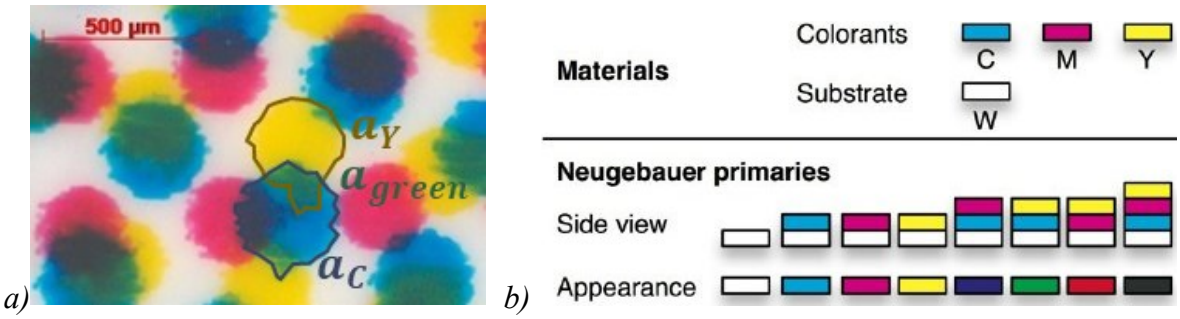

Figure 13. a) Inkjet print with cyan, magenta, and yellow inks. b) Neugebauer primaries, figure extracted and adapted from [75].

From three inks printed on a substrate are then generated eight Neugebauer primaries. The surface coverage of each Neugebauer primary, a_i, can be described as a function of the surface coverage of the different ink primaries a_{Ink} thanks to Demichel's equations [76], which are based on statistics. For a Neugebauer primary which is the superimposition of inks contained in a set *I*, it can be written:

$$a_i = \prod_{Ink \in I} a_{Ink} \prod_{Ink \notin I} (1 - a_{Ink}) \qquad 21$$

For instance, in the case of a CMY print, the surface coverage, a_{green} of the green Neugebauer primary, superimposition of cyan and yellow inks, is:

$$a_{green} = a_C a_Y (1 - a_M) \qquad 22$$

where a_C, a_M, and a_Y are respectively the surface coverages of the cyan, magenta and yellow inks.

In case of a halftone composed of *N* Neugebauer primaries, at a given wavelength, the spectral Neugebauer model describes the reflectance of the halftone *R as*:

$$R = \sum_{i=0}^{N} a_i R_i \qquad 23$$

where a_i and R_i are respectively the surface coverage and the reflectance of the Neugebauer primary i.

It can be noted that for a halftone made of only one ink of surface coverage a, the Murray-Davies equation (Equation (20)) can be retrieved, and the reflectance R predicted by the Neugebauer model is:

$$R = (1 - a)R_0 + aR_1 \quad 24$$

The model from Neugebauer proved to be efficient and gave good results according to the quality standards at the time. Its major drawback was that it did not consider the light diffusion inside the paper, the optical dot gain, which can have a significant impact on the halftone reflectance if the printed dots are small enough. This dot gain can yet be partly taken into account in the calculation of the surface coverages. In the 1950's physicists tried to remedy to this issue. There were then two approaches: improve the accuracy of the Neugebauer model or find a physical model describing the optical phenomena at stake.

2.2.5 Yule-Nielsen model

The model developed by Yule and Nielsen in 1951 [77] follows the first approach by introducing an empirical n_{YN} parameter to the Neugebauer model (Equation 23). It was generalized to spectral predictions with several primaries by Viggiano [78], [79] and is described, at a given wavelength, by:

$$R = \left(\sum_{i=0}^{N} a_i R_i^{\frac{1}{n_{YN}}} \right)^{n_{YN}} \quad 25$$

where R is the reflectance of the halftone, R_0 is the reflectance of the bare substrate, R_1 the one of the solid ink (i.e., the fulltone).

The parameter n_{YN} was evaluated empirically by fitting with measurements. Without any optical dot gain, n_{YN} is equal to 1 (it corresponds to the Neugebauer model). The parameter n_{YN} increases according to the strength of the optical dot gain effect. It was shown that if there is no diffusion inside the substrate $n_{YN} = 1$. If there is complete diffusion inside the substrate, i.e. the light entering the print propagates in a distance significantly longer than the halftone screen frequency, $n_{YN} = 2$, as shown in [2]. Experimentally, $n_{Yn} > 2$ was also found, this is due to internal reflection inside the substrate, predicted by Snells-Descartes law, as shown by Rogers in [80] , or n_{NY} can even take negative values [81]. This model was modified to account for a varying ink thickness [82], [83], and for varying effective surface coverages depending on ink superimpositions [84]. It was also applied to recto-verso prints [85].

It can be noted that if the halftone is made of one ink, the Yule-Nielsen model can be simplified to:

$$R = \left[(1 - a)R_0^{\frac{1}{n_{YN}}} + aR_1^{\frac{1}{n_{YN}}} \right]^{n_{YN}} \quad 26$$

where a is the surface coverage of the halftone, R is the reflectance of the halftone, R_0 is the reflectance of the bare substrate, R_1 the one of the solid ink (i.e., the fulltone) and n_{YN} the Yule-Nielsen parameter.

It is also possible to increase the number of Neugebauer primaries by considering intermediate surface coverages, with a model called *Cellular Neugebauer model* [86]. This model is particularly efficient if the fulltones have an ink density so important that the calibration measurements saturate, the print being too absorbing. However, it requires more calibration measurements than simpler models [87].

Callahan seems to be the first, in 1952, who followed a physical approach by considering light diffusion inside the substrate [88]. Two physical phenomena happen inside the substrate: light is scattered inside the substrate and light is partially reflected at the print-air interface, leading to internal reflections within the substrate. Unlike Callahan, Clapper and Yule noticed that this second phenomenon was far from negligible and implemented it in their phenomenological model described in the next paragraph [89].

2.2.6 Clapper-Yule model

Published in 1953, this model follows a physical approach by considering the layered structure of the printed material: the substrate, the ink layer, and the interface with air, as displayed in Figure 14.

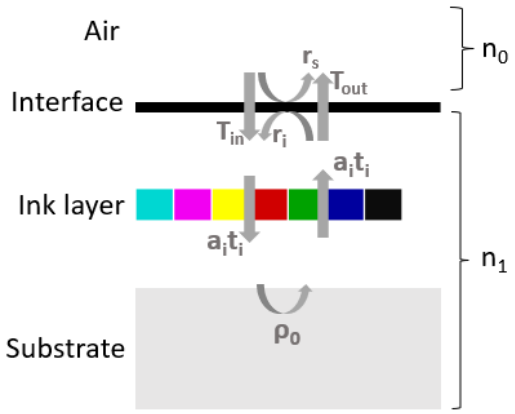

Figure 14. Scheme of the multi-layered structure considered in Clapper-Yule model.

It takes into account the portions of light transmitted and reflected at the interface between the print and air, r_s, r_i, T_{in}, and T_{out}, similarly to the Saunderson correction presented above. The light transfers at the interface can be derived from Fresnel angular reflectance and transmittance of the interface, denoted by $R_{01}(\theta_0)$, respectively $T_{01}(\theta_0) = 1 - R_{01}(\theta_0)$, when light incomes at angle θ_0 from air (labelled 0, with a refractive index $n_0 = 1$), and $R_{10}(\theta_1)$, respectively $T_{10}(\theta_1) = 1 - R_{10}(\theta_1)$, when light incomes at angle θ_1 from the coating (labelled 1, with a refractive index n_1). For a di:8° measurement geometry, they are given by:

$$r_s = \frac{1}{\pi} R_{01}(8°) \quad 27$$

$$r_i = \int_0^{\frac{\pi}{2}} R_{10}(\theta_1)\, sin(2\theta_1)\, d\theta_1 \quad 28$$

$$T_{in} = \int_0^{\frac{\pi}{2}} T_{01}(\theta_0)\, sin(2\theta_1)\, d\theta_1 \quad 29$$

$$T_{out} = \frac{T_{10}(8°)}{\pi {n_1}^2} \quad 30$$

Let us first enunciate the Clapper-Yule model for a print with one ink of surface coverage a and of intrinsic transmittance $t(\lambda)$ which corresponds to the transmittance at the wavelength λ of the layer from one end to the other end, light travelling in the direction of the normal of the layer. In case of a non-inked area or a perfectly clear layer, $t(\lambda)$ is 1 for all wavelengths. Otherwise, it relies on the Beer-Lambert-Bouguer Law described in Equation (7). The Clapper-Yule model considers the optical indices of the substrate and of the ink to be the same. It is then considered that there is no light reflection at the substrate-ink interface, this interface is optically neutral. The substrate has an intrinsic reflectance $\rho_0(\lambda)$. It is considered that light can propagate along long distances within the substrate. The light interactions are described in Figure 15.

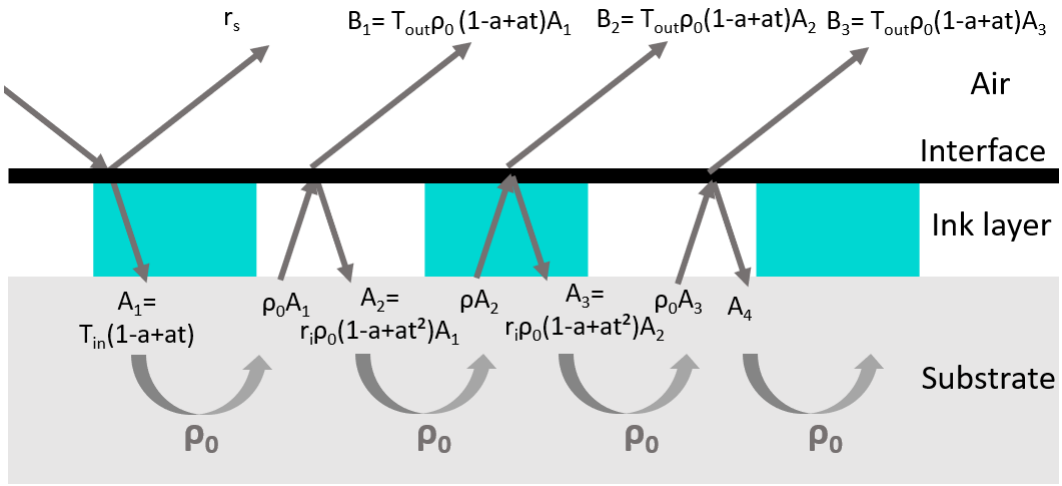

Figure 15. Scheme of the light multiple interreflections between the substrate and the interface with air described by the Clapper-Yule model, where t and ρ_0 depend on the wavelength λ.

Let us consider a light beam of wavelength λ reaching the interface between the ink layer and air with a unit flux. A light portion r_s is reflected into air and a portion T_{in} is transmitted through the interface towards the substrate. This light has a probability a of meeting an inked dot and be transmitted to a proportion $t(\lambda)$, and a probability $(1-a)$ of meeting a non-inked area and be totally transmitted. Therefore, the light portion reaching the substrate is $A_1 = T_{in}(1-a+at(\lambda))$.

It is reflected to a proportion $\rho_0(\lambda)$ by the substrate and crosses again the ink layer before meeting the interface with air where it can be either transmitted through the interface to proportion T_{out} or reflected back in the ink layer to a proportion r_i. The light issued from the substrate which is transmitted at the interface with air has crossed the ink layer once, the light portion escaping the print is then $B_1 = T_{out}\rho_0(\lambda)\big(1 - a + at(\lambda)\big)A_1 = T_{in}T_{out}\rho_0(\lambda)\,(1 - a + at(\lambda)\,)^2$. The light reflected at the interface back towards the substrate crosses the ink layer twice at the same spot, therefore the total distance travelled by light within the ink layer from the substrate and back to it is twice the thickness of the ink layer, which yields an ink transmittance $t^2(\lambda)$, as described by Beer-Lambert-Bouguer Law. The portion of light internally reflected at the interface and reaching again the substrate is $A_2 = r_i\rho_0(\lambda)\big(1 - a + at^2(\lambda)\big)A_1 = T_{in}r_i\rho_0(\lambda)(1 - a + at(\lambda)\,)(1 - a + at^2(\lambda))$

This light is once again reflected by the substrate to a proportion ρ_0, it crosses again the ink layer and meets the interface with air. The light portion transmitted into air is $B_2 = T_{out}\rho_0(\lambda)(1 - a + at(\lambda)\,)A_2 = T_{out}T_{in}r_i\rho_0^2(\lambda)(1 - a + at(\lambda)\,)^2(1 - a + at^2(\lambda))$. The light portion internally reflected into the ink layer at the interface with air is again reflected by the substrate, it crosses again the ink layer and may be transmitted by the interface, which represents a portion $B_3 = T_{out}T_{in}r_i^2\rho_0^3(\lambda)(1 - a + at(\lambda)\,)^2(1 - a + at^2(\lambda))^2$. The light internally reflected at the interface once again produces another contribution, and so on.

In the end, the light portion reflected into the air by the print, corresponding to the reflectance $R(\lambda)$ of the halftone print, is:

$$R(\lambda) = r_s + \sum_{k=1}^{+\infty} B_k = r_s + T_{in}T_{out}\rho_0(\lambda)(1 - a + at(\lambda))^2 \sum_{k=1}^{+\infty} (r_i\rho_0(\lambda)(1 - a + at^2(\lambda)))^k$$

This is a geometric series which can be simplified to:

$$R(\lambda) = r_s + \frac{T_{in}T_{out}\rho_0(\lambda)(1 - a + at(\lambda))^2}{1 - r_i\rho_0(\lambda)(1 - a + at^2(\lambda))} \qquad 31$$

This equation is the Clapper-Yule model for prints composed of one ink.

If the ink layer is composed of *N* Neugebauer primaries, the Neugebauer primary *i* having a surface coverage a_i and an intrinsic transmittance $t_i(\lambda)$, the Clapper-Yule model describes the reflectance $R(\lambda)$ of the halftone print as:

$$R(\lambda) = r_s + \frac{T_{in}T_{out}\rho(\lambda)\left(\sum_{i=0}^{N} a_i t_i(\lambda)\right)^2}{1 - r_i\rho(\lambda)\sum_{i=0}^{N} a_i t_i^2(\lambda)} \qquad 32$$

The Clapper-Yule model is valid only in the case where light strongly diffuses inside the substrate with respect to the halftone screen frequency. It considers that a photon entering the substrate at a point A has a probability of exiting at a point B which is independent of the distance between A and B. The Clapper-Yule model usually applies to prints of halftone screen frequency higher than 120 lpi, or with a Yule-Nielsen n_{YN} parameter higher than 2. Rogers

generalized this model to lower diffusion by implementing a point spread function in the calculation [80]. A modification of this model was also presented in [90] to account for ink spreading on other inks, and a corrective element on the probabilities.

2.2.7 Williams-Clapper model

In the meantime, Williams and Clapper also published in 1953 a model which is very similar to the Clapper-Yule model but which was designed to predict the reflectance of photographic color print, where a transparent colored gelatine overlays a white scattering substrate [91]. The substrate and the transparent coating are uniform and in optical contact, as shown in Figure 16. The major difference from the Clapper-Yule model is that this model takes into account the angle of incidence of light in the evaluation of the transmittance inside the transparent coating. Indeed, a ray of light having a high incidence angle to the normal of the layer crosses a longer path inside the transparent layer than a ray of light having a normal incidence, it is then more absorbed by this layer. The Williams-Clapper model was at first designed for a 45°:0° geometry, it was generalized in 2001 to other geometries by Shore and Spoonhower [92] and by Elias and coworkers [93].

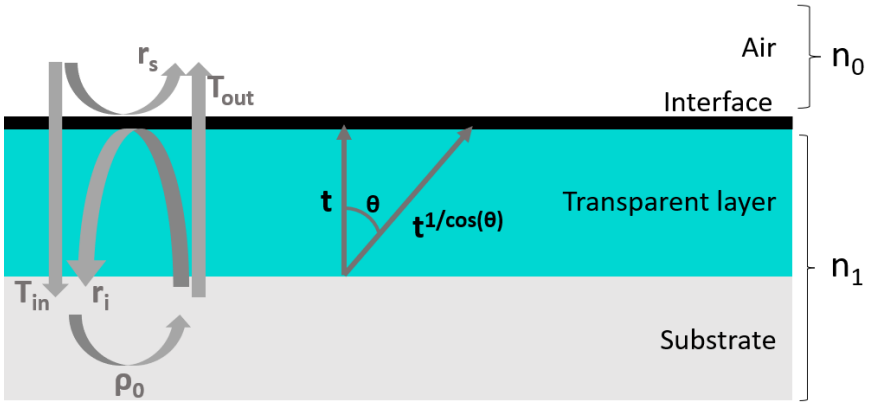

Figure 16. Scheme of the multi-layered material considered in the Williams-Clapper model.

The transmittance of the coating is taken into account in the calculation of the light transfers at the interface between the print and air, r_s, r_i, T_{in}, and T_{out}. For a di:8° geometry at a wavelength λ they are:

$$r_s = \frac{1}{\pi} R_{01}(8°) \quad 33$$

$$r_i(\lambda) = \int_0^{\frac{\pi}{2}} R_{10}(\theta_1) t^{2/\cos(\theta_1)}(\lambda)\, \sin(2\theta_1)\, d\theta_1 \quad 34$$

$$T_{in}(\lambda) = \int_0^{\frac{\pi}{2}} T_{01}(\theta_0) t^{\left[1-\sin(\theta_0/n_1)^2\right]^{-\frac{1}{2}}}(\lambda)\, \sin(2\theta_0)\, d\theta_0 \quad 35$$

$$T_{out}(\lambda) = \frac{T_{01}(8°)t(\lambda)}{\pi {n_1}^2} \quad 36$$

where $t(\lambda)$ is the intrinsic transmittance of the transparent coating, and n_1 is its optical index.

The Williams-Clapper model describes the reflectance R of the photography as:

$$R(\lambda) = r_s + \frac{T_{in}(\lambda)T_{out}(\lambda)\rho_0(\lambda)}{1-r_i(\lambda)\rho_0(\lambda)} \quad 37$$

where ρ_0 is the intrinsic reflectance of the bare substrate. It can be demonstrated in a similar manner as the Clapper-Yule model by considering a surface coverage equal to 0 and r_s, r_i, T_{in}, and T_{out} dependant of the intrinsic transmittance of the transparent coating.

This model was generalized to halftone prints for highly diffusive substrates by Hébert and Hersch [94], where the transparent layer is composed of colored inks. In this case of high diffusion within the substrate (which can be obtained with high lpi halftone screens), the intrinsic transmittance of the ink layer can be considered as the weighted average of the intrinsic transmittance of each colorant composing the halftone print. Equations 33-36 can then be written as a composition of each colorant:

$$r_s = \frac{1}{\pi} R_{01}(8°) \quad 38$$

$$r_i(\lambda) = \sum_{i=0}^{N} \left(a_i \int_0^{\frac{\pi}{2}} R_{10}(\theta_1) {t_i}^{2/cos(\theta_1)}(\lambda) sin(2\theta_1)\, d\theta_1 \right) \quad 39$$

$$T_{in}(\lambda) = \sum_{i=0}^{N} \left(a_i \int_0^{\frac{\pi}{2}} T_{01}(\theta_0) {t_i}^{\left[1-sin(\theta_0/n_1)^2\right]^{-\frac{1}{2}}}(\lambda)\, sin(2\theta_0)\, d\theta_0 \right) \quad 40$$

$$T_{out}(\lambda) = \frac{T_{01}(8°)\sum_{i=0}^{N} a_i t_i(\lambda)}{\pi {n_1}^2} \quad 41$$

The reflectance of the halftone is then described by Equation (37) but taking as parameters the ones defined in Equations (38-41).

2.2.8 Berns model

The Williams-Clapper model was also simplified by Berns [64], [95], by considering the transmittance of the coating layer independently from the angle incidence of the light rays within the layer, similarly to the Clapper-Yule model. In this case, the intrinsic transmittance can be separated from the integral terms in the calculations of the light transfers at the interface with air, $r_i(\lambda)$, $T_{in}(\lambda)$,, and $T_{out}(\lambda)$,described in Equations (34-36), which become:

$$r_i(\lambda) = t^2(\lambda) r_i \quad 42$$

$$T_{in}(\lambda) = t(\lambda) T_{in} \quad 43$$

$$T_{out}(\lambda) = t(\lambda)T_{out} \quad 44$$

where r_i, T_{in},, and T_{out} are only related to the interface, as defined by Saunderson.

With this simplification, Equation (37) of the Williams-Clapper model becomes:

$$R(\lambda) = r_s + \frac{T_{in}T_{out}\rho_0(\lambda)t^{2(\lambda)}}{1 - r_i\rho_0(\lambda)t^2(\lambda)} \quad 45$$

It can be noted that this Berns equation is identical to the Clapper-Yule model for a fulltone (of surface coverage equal to 1).

2.2.9 Intrinsic parameters estimation

If the transparent layer (coating or ink layer) is perfectly clear, $t(\lambda) = 1$ for all wavelengths, Clapper-Yule, Williams-Clapper, and Berns models (Equations (32), (37), and (45)) yield the same reflectance:

$$R_0(\lambda) = r_s + \frac{T_{in}T_{out}\rho_0(\lambda)}{1 - r_i\rho_0(\lambda)} \quad 46$$

where r_i, T_{in},, and T_{out} are only related to the interface, as defined by Saunderson. As the transparent layer and the substrate have the same optical index, these parameters remain identical whether the substrate is coated with a transparent layer or not. Therefore, the uniform substrate reflectance $R_0(\lambda)$ is identical whether it is covered, or not, by a clear layer. By inverting this equation and measuring the reflectance factor of a bare substrate (or one coated with a perfectly clear layer), one can evaluate its intrinsic reflectance $\rho_0(\lambda)$:

$$\rho_0(\lambda) = \frac{R_0(\lambda) - r_s}{T_{in}T_{out} + r_i[R_0(\lambda) - r_s]} \quad 47$$

Once the intrinsic reflectance of the substrate, $\rho_0(\lambda)$, is known, if the substrate is coated with a uniform transparent layer, (e.g., a fulltone if the transparent layer is ink), one may deduce its intrinsic transmittance $t(\lambda)$ from the reflectance factor measurement $R(\lambda)$ of the coated substrate according to Berns'Law:

$$t(\lambda) = \sqrt{\frac{R(\lambda) - r_s}{\rho_0(\lambda)\left[T_{in}T_{out} + r_i[R(\lambda) - r_s]\right]}} \quad 48$$

This estimation of *t* is approximative as it does not take into account the change of absorptance of the layer according to the angles of the light rays inside it. This equation can also be expressed by:

$$t(\lambda) = \sqrt{\frac{\rho(\lambda)}{\rho_0(\lambda)}} \quad 49$$

where $\rho(\lambda)$ is the intrinsic reflectance of the system composed of both the substrate and the transparent layer, it can be estimated with Equation (47) by replacing $R_0(\lambda)$ by $R(\lambda)$.

Another way is to fit $t(\lambda)$ within the Williams-Clapper model so that the modelled reflectance matches with the measured one. This fitting method is more complex but may result in a more rigorous estimation of this parameter.

2.2.10 Modeling optical dot gain

Point spread functions (PSF) were originally used to characterize the precision of an optical instrument, it corresponds to the response of a system to an infinitely thin pencil of light. In the case of prints, the PSF of the substrate is a way to characterize light diffusion inside the substrate. It characterizes the probability for a photon entering the substrate at a point A to exit the substrate at a point B.

PSF have been used inside optical models to account for light diffusion inside the substrate, a hypothesis lacking in the Neugebauer model. Callahan [88], Lehmbeck, Yule [96], Ruckdeschel and Hauser [97] and Rogers [2] gradually developed the model as:

$$R(x,y,\lambda) = R_0(\lambda)T(x,y,\lambda)[T * H](x,y,\lambda) \qquad 50$$

where $R_0(\lambda)$ is the reflectance of the substrate, $T(x,y)$ is the ink transmittance at the point (x,y) (equal to 1 if there is no ink at (x,y)), H is the point spread function of the substrate, it is normalized to unity. Often described as a Gaussian, the PSF is subject to a significant number of studies about its mathematical shape and its experimental characterisation [25], [96]–[99]. As this model does not take into account separately the effects of the interface, as was considered in all models issued from Saunderson's correction (Clapper-Yule, Williams-Clapper, and Berns models), the ink transmittance T is different from the ink intrinsic transmittance t. It can be estimated through reflectance factor measurement $R_1(\lambda)$ of a fulltone:

$$T(\lambda) = \sqrt{\frac{R_1(\lambda)}{R_0(\lambda)}} \qquad 51$$

In 1999 Rogers took into account the interface and distinguished the internal reflection it generates from the scattering within the substrate. This model featured multiple convolutions and was called *Generalized Clapper-Yule model* [80]. A similar modelling approach was followed in this work.

Huntsman, Arney, Yang, and coworkers, also developed a model which can account for low scattering mediums [100]–[106]. This model is based on the probabilities for light to propagate from an inked area to a non-inked one, and conversely. These probabilities might yet be difficult to evaluate [12]. Rogers showed that they can be derived from the substrate PSF [2].

Various theoretical tools and optical models have been developed towards an optical prediction of the colors of halftone prints. These models require calibrations and measurements through experimental tools.

2.3 Measurement setups for color reproduction

This subsection presents the main experimental tools which have been used during this work. It describes the principles of spectrophotometers, photography, multispectral and hyperspectral imaging, and microscopy.

2.3.1 Spectrophotometer

Traditionally, optical measurements were performed with densitometers which allowed to measure the ink optical densities. In the 1980's, devices were developed allowing colorimetric measurements: spectrophotometers. They allow to measure the spectral reflectance factor of prints over the visible wavelengths, and from there deduce the CIE1976 L*a*b* values of the prints. They are often used to characterize, control, and correct the printed colors for color management purposes, [1] p305.

The measurements are performed by emitting light in the direction of the print, the light reflected by the print is captured by a spectrometer through a diffraction grating by a row of photodiodes. The diffraction grating and the row of photodiode enable to spatially sample the spectral signal and capture the spectrum on small wavelength bands. Typically, spectrophotometers have bandwidths of 10 nm over the visible range. The captured spectrum is converted into a reflectance factor by taking into account the captured spectrum of a perfect white diffuser under the same measurement conditions.

Spectrophotometers can have various measurement geometries which, except in the case of perfectly Lambertian surfaces, have an impact on the measured reflectance factors. In the printing industry two main geometries are used: 45°:0° spectrophotometers illuminate the samples at 45° from the normal of the surface, either with a punctual source or with an annular one, and measure the reflected light in the direction of the normal of the measured surface, and d:8° spectrophotometers illuminate the samples diffusely from every direction of the hemisphere thanks to an integrating sphere, and measure the reflected light at an angle of 8° from the normal of the sample.

In a d:8° spectrophotometer the light specularly reflected by the surface of the sample can be included, denoted di:8° measurement geometry or SCI for specular included component, or excluded, denoted de:8° or SCE. The exclusion can be performed numerically by comparing two measurements performed with different light sources, as presented in Figure 17. In this example, the light source 1 is used for all measurements, and the light sources 2 enables to characterise the specular reflection, [107]. In other spectrophotometers, there can be a hole in the integrating sphere at point A to remove the specular component, [64]. An issue in both de:8°

and 45°:0° measurements is that the surface reflection might not be well managed in the case of non-glossy samples for which the diffuse surface reflection may not be entirely excluded. To avoid this issue, the measurements presented in this study were performed with a di:8° geometry.

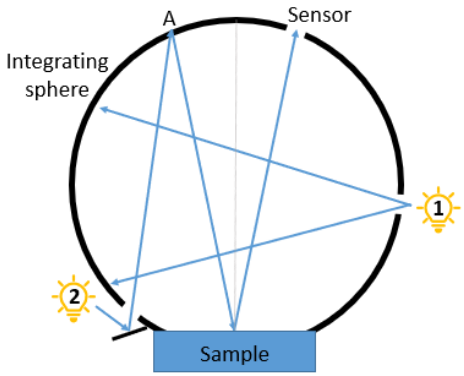

Figure 17. Measurement principles of a d:8° spectrophotometer, adapted from [107].

According to ISO 13655, some spectrophotometers have standard illuminations, respectively condition M0, M1, M2, or M3. In condition M0, the light source have an illuminant spectral distribution similar to the one of illuminant A defined by the CIE (Commission Internationale de l'Eclairage). This mode is not recommended for fluorescent samples as the amount of UV light is not well controlled.

In condition M1, the spectral density of the light source is similar as the one of illuminant D50 defined by the CIE. In condition M2, the measurements are performed with a UV cut. In condition M3, the measurements include a polarization filter.

2.3.2 Photography, multispectral and hyperspectral imaging

Photography is the art of capturing the light from the scene to generate a long-lasting picture of this scene. It is widely used for scientific purposes and came as a key characterising system during this work, its main principles are thus presented here. There are two main technologies: analogic photography, where the light sensor is a photosensitive film which darkens when exposed to light, and digital photography where the light sensor converts the light signal into an electrical signal which can then be digitally computed to generate the picture of the scene. Both photographic systems depend on the same principles and parameters:

The sensor (or film) can be overexposed: the sensor receives so much light that it reaches a threshold over which light variations can no longer be recorded. In a similar manner, it can be underexposed: the amount of light reaching the sensor is not enough to generate a response. Over-exposure or under-exposure can be prevented by adjusting several settings of the camera.

It can first be prevented by adjusting the light sensitivity of the film, called *ISO*. Easily adjusted in a digital camera, this can be more complex for analogic photography as the film sensitivity

depend on its chemical composition. Another parameter to avoid mis-exposition of the picture is the *exposure time*: the time during which the sensor is exposed to light. This can be set by controlling the opening and closing of a shutter placed in front of the sensor. Over or under exposure can also be prevented by adjusting the *aperture* of the camera. It usually consists in a diaphragm whose diameter can be controlled, a small aperture restricts the amount of light reaching the sensor, in comparison with a large aperture.

The aperture also plays a role in the *depth of field*: the maximal distance between two objects in the scene, in the camera direction, for which both objects appear sharp in the picture. A large aperture induces smaller depth of field than a small aperture. The sharpness of an object at a certain distance in a scene can be controlled by adjusting the focus of the camera, i.e. by adjusting the distance between the sensor and a lens in the objective of the camera.

In digital photography, the light-sensitive element of a camera is its sensor, which is usually of type CMOS (Complementary Metal-Oxyde-Semiconductor) or CCD (Charged Coupled Device). They convert light into an electric signal encoding the irradiance each pixel received in a certain number of bits. To capture the colors of a scene, red, green, and blue optical filters are set in front of the pixels of the sensor. They are usually arranged in a specific order called Bayer matrix, shown in Figure 18.a. A Bayer matrix contains two times more green filters than red or blue ones to adapt to human light sensitivity which is higher in the green. This color recording is similar to analogic processes (Autochrome Lumière, Lumicolor, Dufraycolor, Finlay [108]) designed in the early years of the 20th century. Yet, the microscopic scale of digital sensors rendered this process far more performing than the analogic one.

Digital imaging has the advantage of enabling rather easily High Dynamic Range photography (HDR): if a scene has light intensities in such a large range that even with the best parameters, a part of the image is under-exposed and another part is overexposed, HDR consists in taking several pictures of the same scene with different exposure parameters. The different pictures are then combined to produce a picture avoiding saturation.

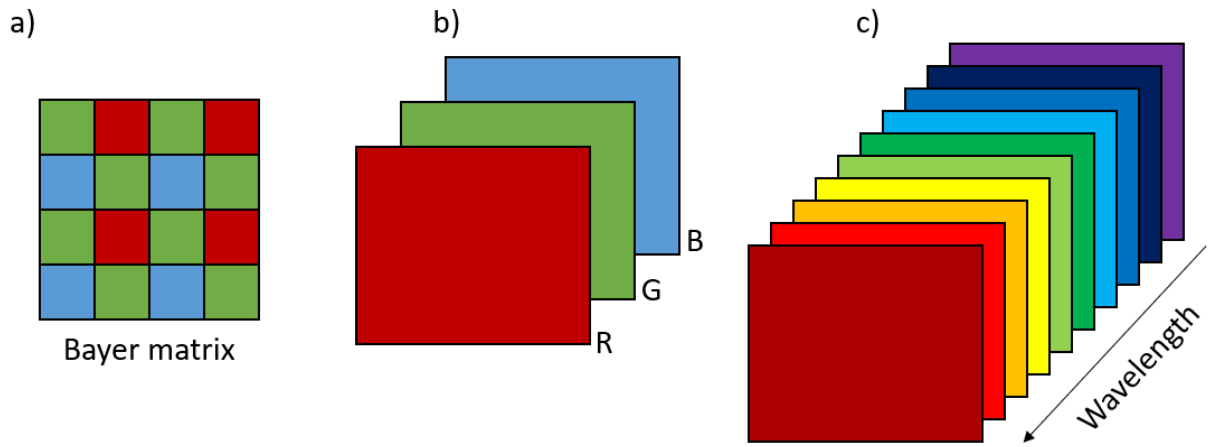

Figure 18. a) Bayer matrix with a pattern GRBG, b) RGB image, c) Multispectral image.

The possibility to associate a camera with a microscope, a telescope, a spectrograph, and so on, has set photography, and more generally imaging, as a major tool for scientific purposes. Nowadays a major example of the possibilities of scientific photography lays within the James Webb telescope, which allies astronomy, imaging, and spectroscopy to capture never seen before astronomic objects and deduce their composition. This combination of imaging and spectroscopy, also called *multispectral* or *hyperspectral imaging*, consists in measuring the local spectrum for each pixel of a picture [109]–[111]. Multispectral and hyperspectral imaging only differ in the spectral resolutions: multispectral imaging usually consists in evaluating the spectral information on 7 to 15 wavebands whereas hyperspectral imaging has a better spectral resolution. The measured data are 3-dimensional, with two spatial dimensions and one spectral dimension, a type of data which is also called a *hypercube*, as shown in Figure 18. C. Various approaches exist to perform multispectral imaging, [109] denotes four of them.

The first one, called *staring approach*, consists in scanning on the spectral dimension: the selected wavelength bandpass vary over time and for each one a picture is captured. The wavelength bandpass can be selected through optical filters, which can be set for instance on a filterwheel [112], or by illuminating the sample with small band light sources such as LEDs [113].

A second approach consists in scanning on one of the spatial dimensions. This approach, also called *pushbroom*, relies on similar measurement methods as single-point spectrometers as it is based on diffraction by a prism or a grating. The spectra of each line of the picture can be captured in one shot, the lines of the pictures are then captured successively.

The third method is based on a time scan and on interferometry and requires a mathematical transform such as the Fourier transform to retrieve the hypercube. The last approach encompasses all the method reaching a compromise between the spectral and the spatial resolutions to get fast measurements. One of these methods consists in implementing additional color filters in the Bayer matrix.

The two first methods are the most common, the staring approach has the advantage of providing images instantly which enable to set the aim and focus, it is then well adapted for flat and inert objects as for microscopic applications [110], but its spectral resolution is usually poorer than the pushbroom approach as it can be limited by physical components such as the size of the filterwheel [111].

2.3.3 Microscopy

Spectrophotometers enable to characterize the color of prints at a macroscale, the measured reflectance factor being averaged over all the measured area. Yet, as presented in Section 2.1, the color of prints depends on microscale characteristics, namely the halftone pattern, and the physical and optical dot gains. Various studies have then used microscopic imaging to characterize prints at the microscale[25], [29], [99], [114]–[117]. These studies often aim at separating the optical dot gain from the physical one, which is a complex task as the reflectance

of the edges of the printed dots vary continuously from the inked area to the non-inked one. The objective is usually to better account for dot gains for color prediction purposes, or for forensic applications. They present methods to characterize the paper MTF and to better manage the optical dot gain.

2.4 Conclusions

The printing industry continues to grow, especially as paper-based packaging is replacing fossil-based ones. For an adequate color reproduction, the printers require a strong color management. Indeed, various parameters have an influence on the resulting color of the prints: the microscale structure of the print, i.e. the halftone image, has a strong impact on the macroscale color, this halftone image is distorted during the printing process due to the mechanical dot gain which tends to increase the size of the printed pattern, and the optical properties of the print can also make the microscale patterns appear bigger than they actually are, a phenomenon designed as optical dot gain. It was also shown that adding a coating layer over the print can induce significant color changes, even if the layer is perfectly clear. All the microscale characteristics of the prints have a strong impact on the color perceived at a viewing distance. To manage the resulting colors, the printer needs to be characterised. This can be performed numerically by printing and characterising the colors of a great number of patches, or by calibrating and using optical models, which requires fewer measurements. This second approach is particularly efficient in the case of printers relying on a large number of inks, which seems to be a rising tendency. Except for the Williams-Clapper model which allows to predict the spectral reflectance factor of a uniform substrate overlaid with a transparent layer, there is, to our knowledge, no optical model which allows to do color management in the case where prints are coated with a transparent layer. This work aims at contributing to solve this problematic. It relies on scientific concepts, optical models, and experimental tools which have been presented in this chapter. Starting on the subject, the first question which arose was: how does a clear coating layer modify the appearance of a coated print? Question which is treated in the next chapter.

Chapter 3. Coated prints: color prediction by optical approach

Adding a transparent coating over a printed surface significantly changes its color. If the coating has a smooth finishing, the print color usually becomes darker and more saturated than the one of the uncoated print, even when the coating is perfectly clear. If the layer has a rough finishing, the color becomes brighter and less saturated. As far as we know, there is currently no optical approach allowing to predict this color change, and the reasons behind it are rather unclear. Hoffstadt suggested that light propagation within the coating layer could be at the origin of the color change [4]. Simonot et al. investigated the lateral propagation of light within a smooth transparent layer in optical contact with a highly scattering uniform substrate [6]. The latter study and the optical phenomenon that it describes, presented in Section 3.1, were at the origin of an optical model that we developed for halftone prints coated with a transparent layer, detailed in Section 3.2. Its calibration and computation are described in Section 3.3 and its experimental validation in Sections 3.4 and 3.5. Simulations of the impact of various model parameters on the color changes are exposed in Sections 3.6, 3.7, and 3.8. In this chapter, prints and coating layers are assumed to have an identical optical index and to have a glossy finishing, i.e., a smooth interface with the surrounding air, except in Section 3.8 where the case of a matte finishing, i.e., a rough coating-air interface, is considered.

3.1 Halo effect on uniform coated substrates

Interactions between light and a uniformly colored substrate coated with a transparent layer are very peculiar. They were first described at the end of the 19th century as they caused imaging issues, which is detailed in Section 3.1.1. This intriguing phenomenon was then studied to generate a BSSRDF model for uniform substrates coated with a transparent but possibly absorbing layer, detailed in Section 3.1.2. The phenomenon and model presented in this section laid the foundation for the optical model we developed.

3.1.1 Photographic halo, halation ring

Let us consider a Lambertian diffusing substrate coated with a transparent (i.e., non-diffusing) layer. The coating can be absorbing, which can provide a coloration to the coated substrate if the absorption of light by the transparent layer depends on the wavelength, (if the layer is clear, its absorptance is null). The phenomenon that we will fully study later is related to the multiple reflections of light between the diffusing substrate and the coating-air interface. It occurs whichever the absorptance of the coating layer and it is linked with the lateral propagation of light inside the coating layer during the multiple reflection process (an effect which was not considered in the Williams-Clapper model). It is particularly visible when the substrate is

illuminated with a thin light beam. This thin light beam can be generated for instance with a laser, or from the light coming from a small bright and distant object in photographs. The phenomenon was particularly depicted at the early age of photography as photographs were made of a glass plate coated with a white photosensitive emulsion. Bright punctual objects such as stars appeared surrounded by a bright ring, a curious phenomenon causing a loss of the contrast of the edges, referred to as "halo", "halation", "blurring", "nubation", or "auréoles" in French in the first publications on the subject [118]–[121]. Exploring observatory archives, various astronomical pictures depict such a halo, as shown in Figure 19.

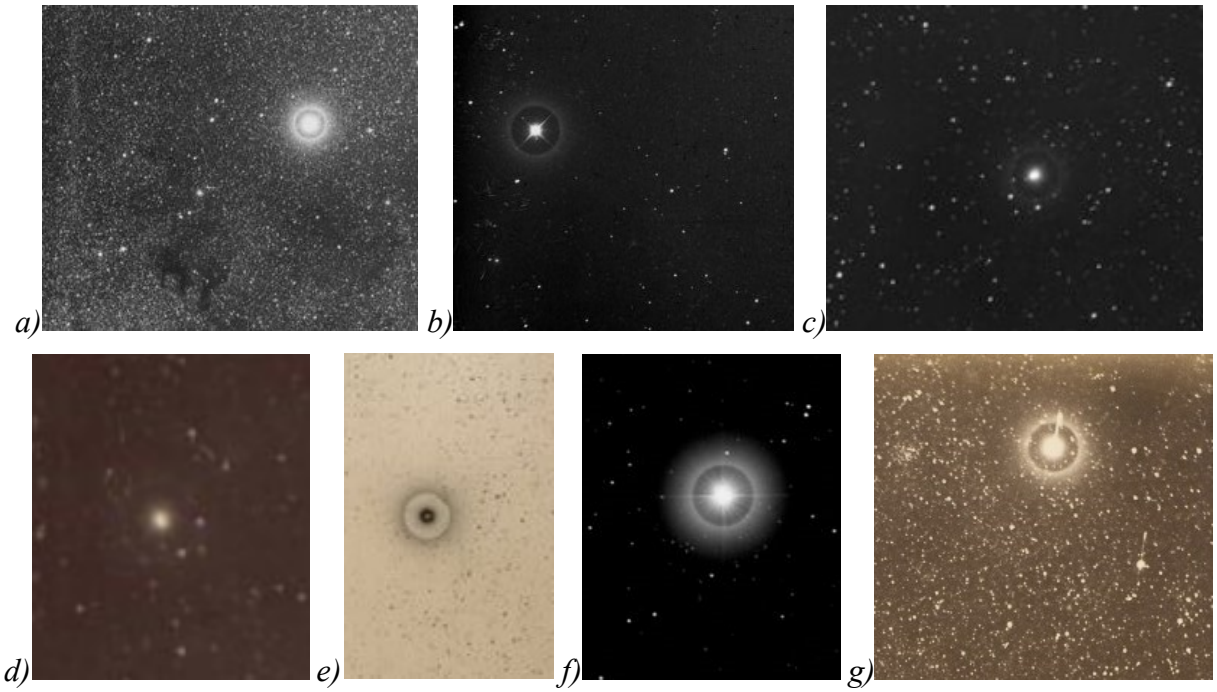

Figure 19. Patchwork of halos around stars extracted from astronomical photographs from the archives of the Lick and Sydney observatories. a) [122]; b) [123]; c) [124]; d) [125]; e) [126]; f) [127]g)[128].

Russel and Sutton seem to have been the first astronomers in the 1860's to emit a theoretical explanation to this phenomenon [120]. In 1890, Cornu explicitly detailed and validated this theory through experimentation and suggested an efficient method to get rid of this halo [7]. According to Cornu, the halo is due to an internal reflection of light at the glass-air interface at the back of the photographic plate, as displayed in Figure 20.a: the light reaching the photosensitive layer (acting like a diffusing substrate in Figure 20.a) is scattered in every direction, a part of which towards the glass plate (acting as a transparent coating layer in Figure 20.a). The light propagating in the glass plate propagates along straight lines as the glass plate is non-diffusive and it reaches the interface between glass and air with various incidence angles. This interface reflects light in proportions depending on these incidence angles, according to Fresnel reflectance at the glass-air interface. The Fresnel reflectance, described in Equation (5), is displayed in Figure 20.b for a material of optical index of 1.5 as a function of the relative

position *x/d,* where *d* is the thickness of the transparent layer, and *x* is the lateral distance from the incident-beam impact point, (at a relative distance *x/d*, the incidence angle at the interface is $\arctan(x/d)$). As displayed in Figure 20.b , the Fresnel reflectance is rather weak for a small angle of incidence, the light rays are then mainly refracted at the glass-air interface. The Fresnel reflectance becomes 1 beyond the critical angle of incidence which is:

$$\theta_c = \arcsin\left(\frac{n_0}{n_1}\right) \qquad 52$$

where n_0 is the optical index of air, $n_0 = 1$, and n_1 is the optical index of the transparent layer, usually around 1.5 for a glass plate. This critical angle is equal to 41.8° for such optical indices. Therefore, the light reaching the glass-air interface with an angle of incidence higher than θ_c is completely reflected towards the photosensitive layer, enlightening it in a ring shape. The diameter of the halo ring, Φ, is given by:

$$\Phi = \frac{4d}{\sqrt{n_1^2 - 1}} \qquad 53$$

The light reaching again the photosensitive layer is then depicted in the pictures and generate the halo shape around the stars. This light can also be reflected once again in every direction, it propagates again with various incidence angle towards the substrate and can generate secondary internal reflections meeting the photosensitive layer, and so on. This light also participates in the halo shape visible around the stars.

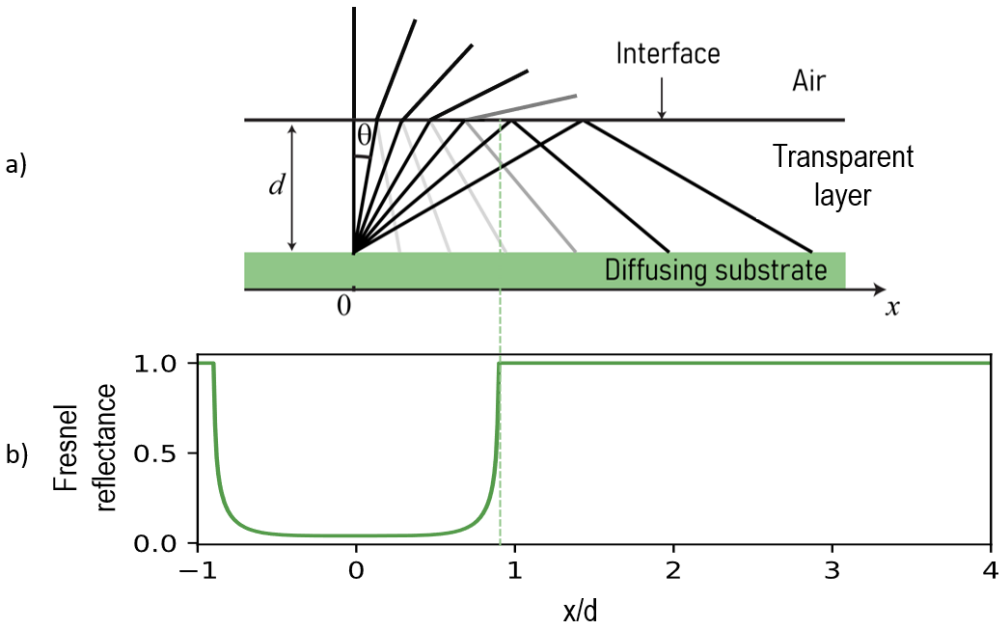

Figure 20. a) Transmission and internal reflections at the glass-air interface of the light issues from a point of the substrate, the darker the color, the stronger the transmission and reflection; b) Fresnel reflectance at the interface at a relative position x/d where d is the thickness of the transparent layer, and x is the lateral distance from the original point source on the substrate.

The solution described by Cornu to prevent these unwanted internal reflections causing the halo and a blurring of the pictures, was to apply an absorbing coating at the glass-air interface. He specified that this coating should have the same optical index as the coating layer for this interface to become optically neutral. The ring-shaped internal reflection phenomenon, described afterwards as *halatio*n or *halation ring* in literature and analogic photographic books [129]–[135], seem to have been rather forgotten or mingled with other optical phenomena causing a blur in images in the 20th century [136]–[141]. Recently, a study conducted by Simonot and co-workers has revived the interest in the subject through a BSSRDF model taking into consideration this halo-shaped light propagation [6].

3.1.2 BSSRDF model for uniform substrates in optical contact with a transparent layer

This 2018 study by Simonot *et al.* [6] takes into account the lateral propagation of light within a transparent layer on top of a uniform Lambertian substrate in order to determine the BSSRDF of the system. It considers a transparent layer, i.e., a non-diffusing but possibly absorbing material, of optical index n_1, one side of which is in contact with air, of optical index 1. This interface is assumed to be flat and can be considered as a specular reflector. The other side of the layer is in contact with a very diffusing material behaving like a Lambertian reflector of intrinsic reflectance denoted ρ_0. The Lambertian reflector and the transparent layer are in optical contact, i.e., there is no air or specular interface between them. The transparent layer has a thickness d and it is considered to be transparent (i.e., non-diffusing) and potentially absorbing, with an intrinsic transmittance t_c along its normal direction. If the layer is perfectly clear, $t_c = 1$. The system is similar as the one considered in the Williams-Clapper model, which allows to determine its reflectance, but the light-matter interactions are taken into account more thoroughly than within the Williams-Clapper model. The BSSRDF model considers three different contributions to the BSSRDF: the light externally reflected by the interface with air (i.e., the specular reflection), the light bouncing once on the substrate, and the light bouncing multiple times due to internal reflections between the substrate and the coating-air interface.

The phenomenon can be described by an analytical model, the system is presented in Figure 21. Let us consider an external irradiance E_i of incidence angle θ_i on the air-transparent layer interface. The contribution to the BSSRDF of the light externally reflected by the interface is easily evaluated with the Fresnel reflectance at the air-coating interface, described in Equation (5), a proportion denoted r_s in the Williams-Clapper model (Equation (33)). The light refracted at the interface with air is transmitted into the transparent layer to a proportion $T_{01}(\theta_i)$ given by the Fresnel formulae. It propagates in the transparent layer of optical index n_1 in a distance $dn_1/\sqrt{n_1^2 - \sin^2(\theta_i)}$ (derived from Snells-Descartes law) before meeting the substrate on a small area A_O around a point O with an irradiance:

$$E_0(O) = T_{01}(\theta_i) t_c^{\,n_1/\sqrt{n_1^2 - \sin^2(\theta_i)}} E_i \qquad 54$$

The exponent $n_1/\sqrt{n_1^2 - \sin^2(\theta_i)}$ on the intrinsic transmittance t_c is proportional to the path length in the transparent layer, according to Beer's Law described in Equation (7).

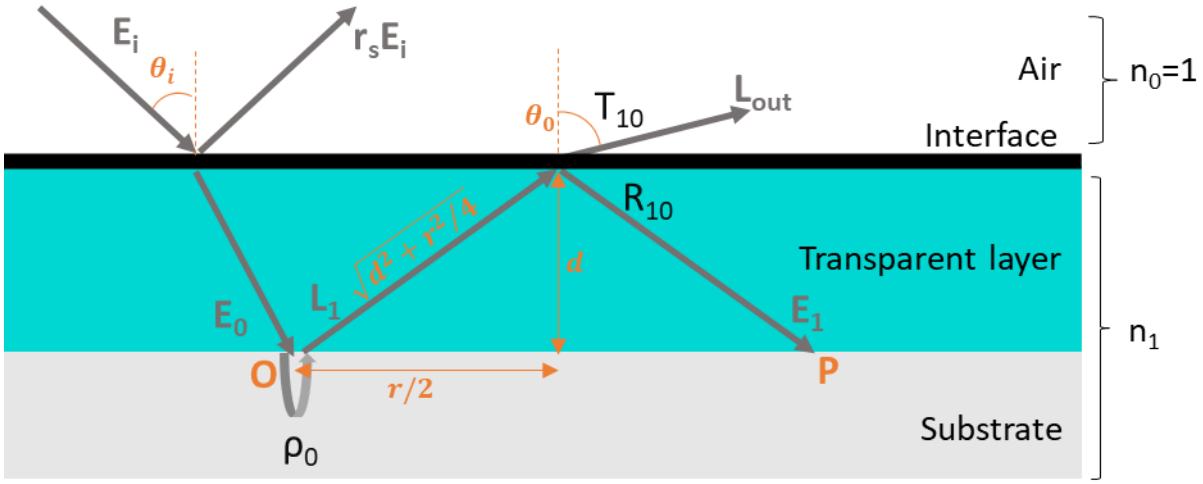

Figure 21. Light interactions within the transparent layer over a uniform substrate.

The light meeting the substrate is diffused in a Lambertian manner: an equal radiance flows in each direction in the coating:

$$L_1(O) = \frac{\rho_0}{\pi} E_0(O) \qquad 55$$

with an exitance:

$$M_1(O) = \pi L_1(O) \qquad 56$$

This light propagates within the transparent layer and meets the interface with air where it is refracted into air or reflected, with a total reflection in the case of high angles of incidence, as presented in Figure 20.a.

The light refracted into air from point O at an angle in air θ_0 has a radiance:

$$L_{out}(O, \theta_0) = \frac{T_{01}(\theta_0)}{n_1^2} t_c^{\,n_1/\sqrt{n_1^2 - \sin^2\theta_0}} L_1(O) \qquad 57$$

The factor $1/n_1^2$ comes from the increase of geometrical extent passing from the transparent layer into air. The exponent $n_1/\sqrt{n_1^2 - \sin^2\theta_0}$ on the intrinsic transmittance t_c is proportional to the path length in the transparent layer, which is $dn_1/\sqrt{n_1^2 - \sin^2\theta_0}$.

The light reflected at the interface with air propagates back towards the Lambertian reflector. At a point P of the substrate, the irradiance due to the light internally reflected at the interface is:

$$E_1(P) = h(O, P) M_1(O) A_O \qquad 58$$

where function h gives, for a given coating thickness d, the light portion propagating from a point P_i to a point P_j on the substrate, separated by a distance $r = P_iP_j$:

$$h(P_i,P_j) = \frac{4d^2R_{10}\left(\arctan\left(\frac{r}{2d}\right)\right)t_c^{\sqrt{4+\frac{r^2}{d^2}}}}{\pi(r^2+4d^2)^2} \qquad 59$$

This proportion depends on:

- the geometrical extent between the small area around P_i and around P_j, which is proportional to $4d^2/(r^2+4d^2)^2$;
- the Fresnel reflectance at the interface, which depends on the incidence angle at the interface: $\arctan(r/2d)$;
- the intrinsic transmittance of the transparent layer for a propagation distance equal to $d\sqrt{4+\frac{r^2}{d^2}}$.

When light comes only from the origin O of the Lambertian surface, the irradiance map on the Lambertian surface after one reflection of light at the interface draws a ring-like halo around point *O*, displayed in Figure 22.a for a coating of optical index n_1 = 1.5. The irradiance of each point of the substrate depends on the distance *r* separating the considered point from point *O*, the irradiance profile is then radially symmetric around *O* and is also displayed in Figure 22.a. The dark disk in the middle of the halo pattern corresponds to a low irradiance of the substrate produced by the small amount of light internally reflected by the interface at law incidence angles, according to the Fresnel formulae. The bright ring is produced by the rays totally reflected by the interface because their incidence angle is higher than 42°. The ring has a diameter $\Phi = 4d/\sqrt{n_1^2-1}$, according to Equation (53), and fades in a $\cos^4$ similarly to the irradiance of a small extended light source on a plane, as explained in Section 2.2.1.

Each point of the Lambertian reflector thus reilluminated becomes a new point source and generates a similar ring-like halo, and this occurs multiple times. This gives, at the end of the multiple reflection process, another ring-like halo illustrated by Figure 22.b also visible in the astronomical pictures in Figure 19. This ring-like halo is a PSF (Point Spread Function); if the substrate is uniform, the irradiance map on the substrate caused by external illumination convolved with this PSF gives the total irradiance map on the substrate. Therefore, this PSF is visible whenever a Dirac illumination beam meets a diffusing background covered by a clear layer. If the illumination is uniform and of infinite area, the total irradiance is also uniform: all the halos induced in each point of the illuminated substrate mingle with each other and they become indiscernible.

These multiple interreflections can be modelled either through a multi-convolution process or through a matrix system, as presented by Simonot and coworkers [6]. Dolin further developed modelling for bathymetry applications by considering the impact of light scattering and absorption inside the transparent layer and the impact of the incident beam diameter on the resulting halo image [142], [143].

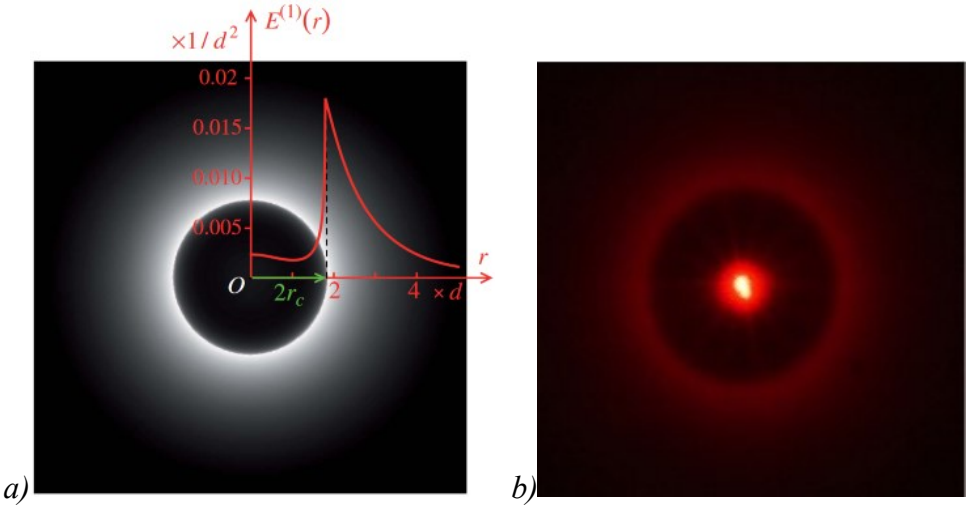

Figure 22. a) Irradiance map on the substrate of the light diffused by point O of the substrate and reflected at the interface with air, extracted from [6]; b) Picture of a uniform diffusing substrate covered with a clear layer, as displayed when illuminated with a red laser beam.

The model presented in this subsection describes the light lateral propagation in a transparent layer in optical contact with a uniform substrate, and the interreflections occurring between the substrate and the interface with air. It is the basis of the model which we developed to predict the color of coated halftone prints.

3.2 Halation model for halftone prints

A halftone print is composed of various-inked areas, which make the spectral reflectance of the print vary spatially. If the print is in optical contact with a transparent layer (non-scattering but possibly absorbing layer), the lateral propagation of light within the transparent layer may increase the probability for light to be absorbed by an inked area, a phenomenon similar to the optical dot gain within the substrate. Indeed, the light internally reflected at the interface between the transparent layer and air meet again the printed substrate in a ring-shaped halo, pictured in Figure 23. This light may be absorbed by an inked area of the print which may darken and saturate the print in comparison with the non-coated print, an optical effect called *halation phenomenon* in the following.

As shown in the previous section for a uniform substrate, the specific halo-shaped PSF due to the lateral light propagation within the transparent layer has a diameter proportional to the thickness of the coating layer. There are then two limit cases for which the reflectance of the coated prints can be predicted without considering the halo-shaped PSF: the first one is met when the transparent layer is infinitely thin compared to the spatial variations of the substrate spectral reflectance, and the other one when the transparent layer is infinitely thick compared to the spatial variations of the substrate spectral reflectance.

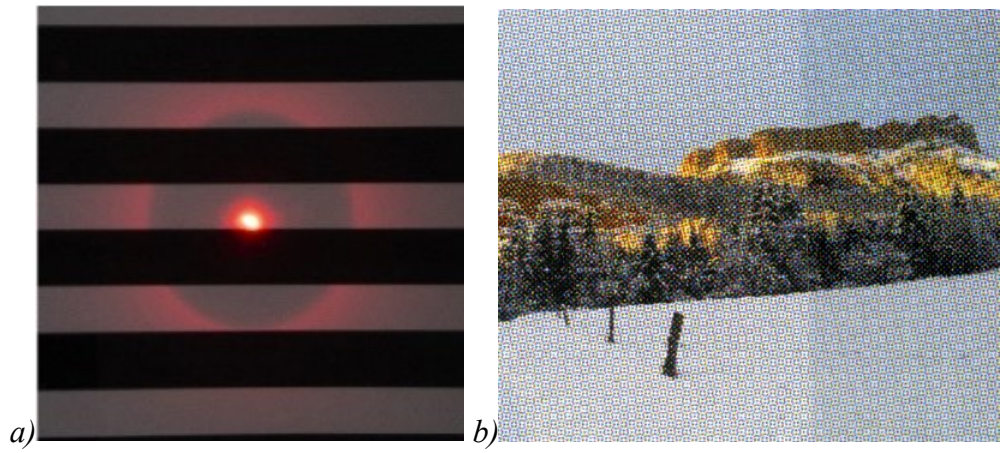

Figure 23. a) Halo on a non-uniform substrate. b) Printed and scanned image, the right side was coated with a glossy tape layer.

3.2.1 Limit cases

In the first case, the transparent layer is so thin compared to the spatial variations of the substrate spectral reflectance that light cannot propagate from an inked area to another area. The overall reflectance of the print is then the arithmetic average of the reflectance of the variously colored areas over the spatial dimension. If the coating layer is non-absorbing, this overall reflectance can then be estimated for instance with the Neugebauer model if the substrate is highly diffusing (i.e., if there is no optical dot gain within the substrate), Equation (23), or for instance with the Yule-Nielsen modified spectral Neugebauer model if there is optical dot gain within the substrate, Equation (25). It can also be estimated using the Williams-Clapper model, especially if the coating layer is absorbing. In this case, the overall reflectance can be estimated by spatially averaging the reflectance predicted by the Williams-Clapper model (Equation (37)) for each differently colored area of the print. If there is no optical dot gain within the print and if the print is composed of N Neugebauer primaries of intrinsic reflectance ρ_i and surface coverage a_i, the averaged Williams-Clapper model yields:

$$\mathrm{R}(\lambda) = \mathrm{r_s} + \sum_{i=0}^{N} a_i \frac{\mathrm{T_{in}}(\lambda)\mathrm{T_{out}}(\lambda)\rho_\mathrm{i}(\lambda)}{1 - \mathrm{r_i}(\lambda)\rho_\mathrm{i}(\lambda)} \qquad 60$$

where $\mathrm{R}(\lambda)$ is the reflectance of the print at wavelength λ. The absorptance of the coating layer is taken into account in the estimation of the light fluxes at the interface with air, r_s, $r_i(\lambda)$, $T_{in}(\lambda)$, and $T_{out}(\lambda)$, which are detailed in Equations (33-36) for a di:8° measurement geometry. If the transparent layer is perfectly clear, this equation is identical to the Neugebauer model. The intrinsic reflectances ρ_i can be estimated using Equation (47) by replacing in this equation the reflectance of the substrate $R_0(\lambda)$ by the reflectance of the non-coated fulltone of the considered Neugebauer primary. If the spatial intrinsic reflectance $\rho(x, y, \lambda)$ over a significant area A of the halftone print is known, Equation (60) may also be written:

$$\mathrm{R}(\lambda) = \mathrm{r_s} + \frac{1}{\mathrm{A}} \iint\limits_{(x,y)\in A} \frac{\mathrm{T_{in}}(\lambda)\mathrm{T_{out}}(\lambda)\rho(\mathrm{x},\mathrm{y},\lambda)}{1 - \mathrm{r_i}(\lambda)\rho(\mathrm{x},\mathrm{y},\lambda)} dxdy \qquad 61$$

The second limit is met when the transparent layer is thick compared to the spatial variations of the substrate spectral reflectance. In this condition, the lateral propagation of light within the layer is so large that we can assume that there is no correlation between the inked areas that light meets successively during the multiple reflection process. In this case, the printed area can be considered as a uniform area with respect to the thickness of the coating and the reflectance of the coated print can be estimated with the Williams-Clapper model:

$$\mathrm{R}(\lambda) = \mathrm{r_s} + \frac{\mathrm{T_{in}}(\lambda)\mathrm{T_{out}}(\lambda)\bar{\rho}(\lambda)}{1 - \mathrm{r_i}(\lambda)\bar{\rho}(\lambda)} \qquad 62$$

where $\overline{\rho}$ is the spatial average of the intrinsic spectral reflectance of the print at wavelength λ, if the print is composed of N Neugebauer primaries of intrinsic reflectance ρ_i and surface coverage a_i, it is:

$$\overline{\rho}(\lambda) = \sum_{i=0}^{N} a_i \rho_i(\lambda) \qquad 63$$

And if the spatial intrinsic reflectance $\rho(\mathrm{x},\mathrm{y},\lambda)$ over a significant area A of the halftone print is known, it can be written in this way:

$$\overline{\rho}(\lambda) = \frac{1}{\mathrm{A}} \iint\limits_{(x,y)\in A} \rho(\mathrm{x},\mathrm{y},\lambda)\,\mathrm{dxdy} \qquad 64$$

3.2.2 General case

If the inked patterns and the coating thickness have similar sizes, the halation phenomenon involving the halo-shaped PSF cannot be discarded anymore. A new reflectance model has thus been developed considering this halo-shaped light diffusion on a non-uniform printed substrate. Let us first describe the system: the coating is a smooth transparent layer of thickness d and of intrinsic transmittance $t_c(\lambda)$ along the normal of the layer at wavelength λ. It is in optical contact with the printed substrate, which is supposed to be perfectly diffusing, i.e., Lambertian. The printed substrate and the coating layer have an optical index n_1, the interface between them is optically neutral, and the surrounding air has an optical index $n_0 = 1$. There is therefore an interface between the coating layer and air which induces light flux transfers r_s, $r_i(\lambda)$, $T_{in}(\lambda)$, and $T_{out}(\lambda)$, as defined by the Williams-Clapper model (Equations (33-36)), which depend on the intrinsic transmittance of the coating layer $t_c(\lambda)$. The bare substrate (i.e., non-printed substrate) has an intrinsic reflectance $\rho_0(\lambda)$, and the printed substrate has a spatial intrinsic reflectance $\rho(x,y,\lambda)$ depending on the position (x,y) on the print. This spatial intrinsic reflectance $\rho(x,y,\lambda)$ can be derived from the spatial reflectance of the non-coated print, $R_{NC}(x,y,\lambda)$, by using the inverse Williams-Clapper model, described in Equation (47),

by replacing $R_0(\lambda)$ by $R_{NC}(x,y,\lambda)$ in the equation. Using Berns model (described in Section 2.2.8), the spatial intrinsic reflectance $\rho(x,y,\lambda)$ of the printed substrate and the intrinsic transmittance of the bare substrate $\rho_0(\lambda)$ enable to retrieve the spatial intrinsic transmittance of the ink layer:

$$t_i(x,y,\lambda) = \sqrt{\frac{\rho(x,y,\lambda)}{\rho_0(\lambda)}} \qquad 65$$

The system and the light interactions described by the equations of the model are displayed in Figure 24.

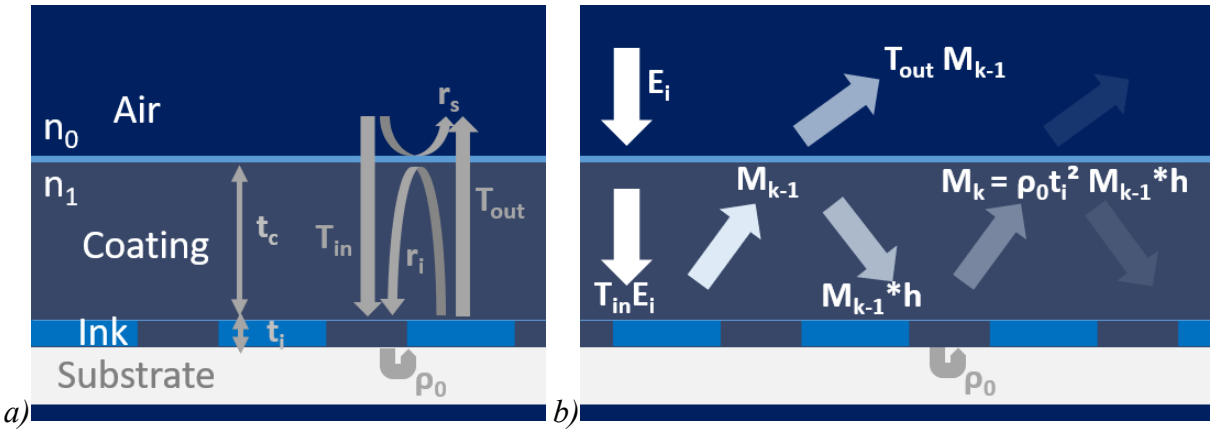

Figure 24. a) Scheme of the coated halftone print and of its optical properties; b) scheme of the flux transfers within the coated halftone.

Let us describe the analytical model for halftone prints coated with a transparent layer, based on the flux transfers shown in Figure 24.b. The coating layer is illuminated with a uniform irradiance $E_i(\lambda)$ at normal incidence. Light is partially reflected by the air-coating interface to a proportion denoted r_s. The light transmitted across the interface crosses the transparent layer to a proportion $T_{in}(\lambda)$ which is dependent of the intrinsic transmittance of the coating layer, $t_c(\lambda)$, and reaches the inked support. It is partially absorbed by inked areas and transmitted through it into a proportion $t_i(x,y,\lambda)$ towards the substrate. The substrate reflects light into a proportion $\rho_0(\lambda)$, yielding the same radiance in all directions since the substrate is a Lambertian reflector. The light emerging from the substrate is attenuated once again by a factor $t_i(x,y,\lambda)$ due to absorption by the ink layer and emerges from the printed substrate with a radiance L_1 (dependency on wavelength will be omitted in the following equations):

$$L_1(x,y) = \frac{T_{in}t_i^2(x,y)}{\pi}\rho_0 E_i \qquad 66$$

and an exitance:

$$M_1(x,y) = \pi L_1(x,y) \qquad 67$$

The light emerging from the substrate and reaching the coating-air interface is either transmitted through the interface to an extent $T_{out}(\lambda)$ (depending on the intrinsic transmittance of the coating layer) and can be captured by the sensor, or it is reflected towards the halftone to an extent $r_i(\lambda)$. Yet, this reflection on the coating-air interface is halo-shaped, as presented in Figure 22.a in Section 3.1.2, which has an impact on the spatial and overall reflectance of the coated halftone. The irradiance map of the halo emitted by a point of coordinates (0,0) is described by the function *h* given by Equation (59), which can be written in this way according to the position (x, y) on the substrate:

$$h(x,y) = \frac{4d^2 R_{10}\left(arctan\left[\frac{\sqrt{x^2+y^2}}{(2d)}\right]\right) t_c^{\sqrt{4+\frac{x^2+y^2}{d^2}}}}{\pi(x^2+y^2+4d^2)^2} \quad 68$$

It is verified that light is reflected at the interface to the same extent with the halo function as with $r_i(\lambda)$:

$$\int_{-\infty}^{\infty}\int_{-\infty}^{\infty} h(x,y)\,dxdy = r_i \quad 69$$

The light reflected towards the halftone after reflection on the coating-air interface and absorption by the ink layer produces an irradiance E_1 of the substrate in each point (x,y):

$$E_1(x,y) = \mathrm{t_i}(x,y)[\mathrm{M_1} * h](x,y) \quad 70$$

where symbol $*$ denotes the 2D spatial convolution operator. Indeed, as each initially illuminated point (x, y) of the substrate produces a halo described by function *h*, the irradiance after reflection on the coating-air interface rely on a convolution operation, as featured in Figure 25.

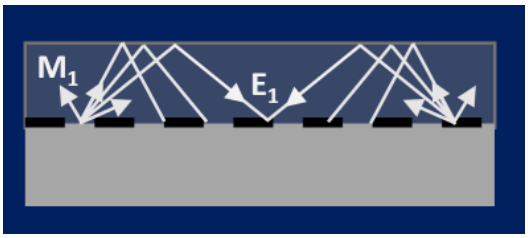

Figure 25. Scheme of the interreflections within the coating layer.

This light meeting again the substrate is reflected into a proportion $\rho_0(\lambda)$ in a Lambertian manner and produces an exitance after absorption by the ink layer:

$$M_2(x,y) = \rho_0 \mathrm{t_i}(x,y)\mathrm{E_1}(x,y) = \rho_0 \mathrm{t_i^2}(x,y)[\mathrm{M_1} * h](x,y) \quad 71$$

which is equivalent to:

$$M_2(x,y) = \rho(x,y)[\mathrm{M_1} * h](x,y) \quad 72$$

and it produces an equal radiance in every direction:

$$L_2(x,y) = \frac{M_2(x,y)}{\pi} \quad 73$$

It produces again a halo reilluminating the substrate, and so on. The successive exitances of the printed substrate, $M_k(x,y)$, satisfy the recursive equation:

$$M_k(x,y) = \rho_0 t_i^2(x,y)[M_{k-1} * h](x,y) \quad 74$$

which can also be written in this way:

$$M_k(x,y) = \rho(x,y)[M_{k-1} * h](x,y) \quad 75$$

We can show that beyond $k = 10$, the exitance $M_k(x,y)$ is close to zero and the total exitance which is the sum of all exitances $M_k(x,y)$, can be approximated by the corresponding truncated sum.

Each time the light meets the interface, a part of the light is reflected in a halo shape described by function h, and the other part is refracted through the interface with a factor $T_{out}(\lambda)$ depending on the intrinsic transmittance of the coating layer, $t_c(\lambda)$. Therefore, the total radiance $L(x,y)$ observed from a certain direction, after crossing the interface, is given by:

$$L(x,y) = \frac{1}{\pi} T_{out} \sum_{k=1}^{10} M_k(x,y) \quad 76$$

The spatial reflectance factor of the coated print is the external reflectance r_s of the upper interface —equal to zero in the specular excluded configuration—, plus the internal contribution given by the spatial value of radiance $L(x,y)$, divided by the radiance $1/\pi$ scattered by a perfect white diffuser in same direction and under unit irradiance [144]:

$$R(x,y) = r_s + \pi L(x,y) = r_s + T_{out} \sum_{k=1}^{10} M_k(x,y) \quad 77$$

This equation (77) gives the model predictive spatial reflectance factor of the print when it is coated with a clear layer at a given wavelength. The overall reflectance factor of the print over an area A can be retrieved by calculating the spatial average of the reflectance factor:

$$R = r_s + \frac{T_{out}}{A} \iint_A \sum_{k=1}^{10} M_k(x,y)\, dxdy \quad 78$$

It can be noted that in the case where the uncoated print has a uniform reflectance, i.e. the substrate is non-printed or is a fulltone, this model gives identical results as the Williams-Clapper model, as presented in the limit cases in Section 3.2.1.

3.2.3 Discussion and addition of a parameter in the model

The underlaying assumptions under the use of the spatial intrinsic reflectances in the multi-convolutive model, Equation 75, is that the light propagation inside the substrate, causing optical dot gain, does not vary whether the substrate is coated or not. In other words, it implies that the interface between the halftone and air has no impact on the substrate point spread function (PSF), and that the halation phenomenon and optical dot gain within the substrate are two independent phenomena. This is a strong assumption but some more complex simulations including the paper PSF that we have tested have not shown any improvement over the hereby presented multi-convolutive model.

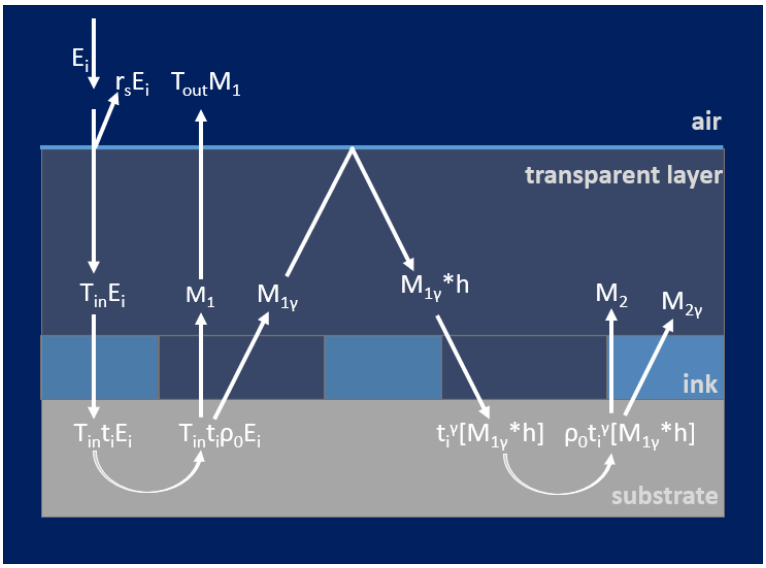

Figure 26. Introduction of the γ parameter in the intrinsic transmittance of the ink layer for light rays of high angle of incidence.

During some experiments (detailed in Section 4.3.1), it was observed that the multi-convolutive model failed to accurately take into account the absorptance of inked areas of some printed halftone patterns. This might be due to the fact that the light emerging from the substrate with a high angle of incidence travels a longer path in the absorbing ink layer than light with a small angle of incidence, which results in a higher absorption by the ink layer. These light rays of high angle of incidence are also totally internally reflected at the coating-air interface, before propagating once again within the ink layer with the same high angle of incidence, as presented in Figure 26.

This can be taken into account in the presented multi-convolutive model by introducing a free parameter, γ, representing the ratio between the path length in the ink layer of high angle of incidence and the one along the normal of the print. The intrinsic transmittance of the ink layer for high angle of incidences then becomes t_i^γ, according to Beer's Law, Equation (7). In the model, a distinction is made between the light exiting the substrate with a low angle of incidence, which is transmitted by the ink layer into a proportion t_i, and which is mostly

transmitted at the coating-air interface, and the light exiting the substrate with a high angle of incidence which is transmitted by the ink layer into a proportion t_i^{γ} and which is mostly internally reflected at the coating-air interface, as described by the following equations.

In Equation 67 of the multi-convolutive model, $M_1(x,y)$ then only describes the exitance for light rays propagating along the normal of the print, and the exitance for light emerging with a high angle of incidence is then:

$$M_{1_\gamma}(x,y) = T_{in} t_i^{1+\gamma}(x,y)\rho_0 E_i = t_i^{\gamma-1} M_1(x,y) \quad 79$$

Most of the light coming back towards the substrate after reflection on the coating-air interface has an angle of incidence higher than 42°, it is thus subject to high absorption by the ink dots. Therefore, the irradiance on the substrate after reflection on the coating-air interface originally described by Equation 70 becomes:

$$E_1(x,y) = \mathrm{t_i^{\gamma}}(x,y)\left[\mathrm{M_{1_\gamma}} * h\right](x,y) \quad 80$$

After reflection on the substrate, the exitance along the normal of the print (at small angles) is:

$$M_2(x,y) = \rho_0 t_i^{\gamma+1}(x,y)\left[M_{1_\gamma} * h\right](x,y) \quad 81$$

and $M_{2\gamma}$, the exitance at high angles, is:

$$M_{2_\gamma}(x,y) = \rho_0 t_i^{2\gamma}(x,y)\left[M_{1_\gamma} * h\right](x,y) = t_i^{\gamma-1}(x,y) M_2(x,y) \quad 82$$

It produces again a halo reilluminating the substrate, and so on. The successive exitances along the normal of the print $M_k(x,y)$ satisfy the recursive equation:

$$M_k(x,y) = \rho_0 t_i^{\gamma+1}(x,y)\left[M_{k-1_\gamma} * h\right](x,y) = \rho_0 t_i^{\gamma+1}(x,y)\left[t_i^{\gamma-1} M_{k-1} * h\right](x,y) \quad 83$$

From this equation, the predicted reflectance factor of the coated print can be evaluated with Equations (77) and (78) by replacing $M_k(x,y)$ by the expression described here.

The introduction of the γ parameter allows, to a small extent, to account for a modification of the substrate optical dot gain PSF by addition of a coating layer. This parameter can be estimated trough a fitting of the multi-convolutive model predictions with the experimental results. An attempt at estimating its theoretical value is described in Appendix III, it was found to be around 2. However, this theoretical estimation omits the fact that the intrinsic transmittance of ink (along the normal of the ink layer) can be overestimated as it accounts partly for light rays having a high angle of incidence. Thus, when γ is above 1, the prediction given by the multi-convolutive model tend to misevaluate the reflectance of fulltones, which should be theoretically unimpacted by the addition of a coating layer. The default value for this parameter is then 1 and it can be fitted for finer predictions.

The multi-convolutive model requires the calculation of 10 convolutions between the halftone print intrinsic reflectance, $\rho(x,y)$ and the halo function, $h(x,y)$. Yet, it is probable that after a certain number of convolutions, the halo shape does not impact the final reflectance factor anymore. In this case, the convolution can be approximated by a multiplication between $\rho(x,y)$ and r_i, the portion of light internally reflected at the interface, which can simplify the model.

Let us consider that after the i^{th} reflection on the support ($i \geq 1$), the convolution can be approximated. The exitance after the $i+1$ reflection is:

$$M_{i+1} = r_i \rho(x,y) M_i(x,y) \tag{84}$$

and for any positive integer k, the $i+k$ reflection becomes:

$$M_{i+k} = \left(r_i \rho(x,y)\right)^k M_i(x,y) \tag{85}$$

The spatial reflectance factor under unit irradiance becomes:

$$R_{approx}(x,y) = r_s + T_{out}\left(\sum_{k=1}^{\mathrm{i}-1} M_k(x,y) + \sum_{k=0}^{\infty} M_{i+k}(x,y)\right) \tag{86}$$

$$R_{approx}(x,y) = r_s + T_{out}\left(\sum_{k=1}^{\mathrm{i}-1} M_k(x,y) + \frac{M_i(x,y)}{1 - r_i \rho(x,y)}\right) \tag{87}$$

It can be noted that if $i = 1$, the Williams-Clapper model is retrieved (as $\sum_{k=1}^{\mathrm{i}-1} M_k(x,y) = 0$ and $M_1 = T_{in}\rho(x,y)$). Simulations displayed in Appendix IV show that $i = 5$ yields a rather good estimation. This approximation was not used during this work, but it might facilitate calculations in the future.

Last but not least, it can be noted that the multi-convolutive model relies on two spatial parameters: the thickness of the coating layer, *d*, and the print spatial and spectral intrinsic transmittance, ρ. As long as the proportion between both spatial parameters remains constant, the multi-convolutive model predictions remain constant. Thus, if the intrinsic reflectance is periodical, of period *p*, the model results only depend on the ratio *d/p* in the spatial dimension. This information can be useful to extrapolate the results: as long as the optical characteristics of the materials remain similar, the spatial scale of an experiment has no importance.

3.3 Model calibration and computation

In this section are detailed the calibration and computation methods for the optical multi-convolutive model presented in the previous section.

3.3.1 Calibration

The multi-convolutive model relies on a rather limited number of parameters: the light fluxes at the interface with air, r_s, r_i, T_{in}, and T_{out}, the spatial and spectral reflectance factor of the halftone print, R_{NC}, the thickness of the coating layer, d, and potentially the spectral reflectance factor of the substrate, R_0 with and without coating if the coating layer is absorbing, and the γ parameter. The multi-convolutive model also relies on the optical indices of the print and of the coating layer, which are close from each other, and considered to be equal to 1.5.

The flux transfers at the interface with air can be determined by considering the measurement geometries and the optical index of the print, thanks to Fresnel formulae, Equation (20). Their values for various geometry are displayed in Table 1 for a clear layer of optical index equal to 1.5. It can be noted that for a sensor in the normal direction of the sample, r_s is equal to 0 if the specular component is not detected by the sensor, otherwise it is 0.04. As long as the substrate is a Lambertian reflector, the light portion internally reflected at the interface with air, r_i, is independent of the measurement geometry. The factor $1/\pi$ in T_{out} was omitted as it cancels when the radiance measured from the sample is divided by the radiance $1/\pi$ measured from a perfect white diffuser (illuminated with an irradiance unity) in order to obtain the reflectance factor [64]. If the coating layer is not absorbing, these parameters are identical whether the print is coated or not. If the coating layer is absorbing, its intrinsic transmittance should be taken into account in the estimation of these parameters.

	Measurement geometry			
	di:8°	de:8°	45°:0°	0°:0°
r_s	0.040	0	0	0.04
r_i	0.596	0.596	0.596	0.596
T_{in}	0.908	0.908	0.950	0.960
T_{out}	0.427	0.427	0.427	0.427

Table 1. Light fluxes at the interface with air for various measurement geometries and for a material of optical index equal to 1.5.

The multi-convolutive model also relies on the spatial and spectral intrinsic reflectance of the halftone print, ρ, which can be determined from the spatial and spectral reflectance factor of the print, R_{NC}, through the inverse Williams-Clapper model, described in Equation (47). The spectrophotometers usually used in the printing industry allow to measure the spectral reflectance factor of prints averaged over the measurement area. Therefore, they are usually

insufficient to characterise spatially the reflectance factor of a print due to optical and mechanical dot gains impacting the reflectance factor of the print at the microscale. A solution to measure the spatial and spectral reflectance factor of prints at the microscale is presented in Section 4.1. However, if the print is not subject to optical dot gain and its reflectance factor follows a binary distribution between inked and non-inked areas, it is possible to model the spatial and spectral intrinsic reflectance of the print from the spectral measurement factor measurements of inked and non-inked areas performed with a spectrophotometer. For instance, let us consider a halftone print composed of a periodic pattern of inked and non-inked lines of which the relative widths are proportional to the surface coverage of the halftone print, as displayed in Figure 27. At a given wavelength, the intrinsic reflectance ρ of the halftone varies only along the x-axis and can be described as:

$$\rho(x,y) = \begin{cases} \rho_1 \text{ when } jp \le x < jp + ap \text{ with } j \in \mathbb{Z} \\ \rho_0 \text{ otherwise} \end{cases} \quad 88$$

where p is the period of the halftone, a is the surface coverage, and the intrinsic reflectance ρ_0 for non-inked areas and ρ_1 for inked areas can be determined from the reflectance factor of the uncoated fulltone and substrate respectively. The surface coverage can be determined by imaging the halftone print, or by applying the Murray-Davies equation on the reflectance factor measurement of the uncoated halftone print, Equation (20).

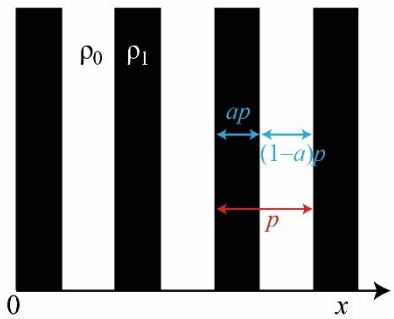

Figure 27. Line halftone pattern with a binary reflectance distribution: the black areas are inked and the white ones are non-inked.

The thickness of the coating layer, d, can be determined by evaluating the thickness difference between the coated and the uncoated print. This method relies on the assumption that the coating process has no impact on the thickness of the printing support without coating. It can be performed with a micrometer for instance. With micrometer measurements, the surfaces must be clean as dusts can induce imprecisions. Other optical methods can be used, for instance by evaluating the difference of position in the z-axis of the sample plate of a microscope when the focus is on the air-coating interface and when it is on the substrate surface. This method is painstaking and has been only used to confirm the micrometer measurements at the beginning of this work. Another method, if the coating layer is large, consists in measuring the diameter

of the halo produced by illuminating the coated substrate with a thin light beam such as a laser, by inverting Equation (53).

The multi-convolutive model can also rely on the intrinsic transmittance of ink layers and of the transparent coating layer. In this case the spectral reflectance factor of the substrate with and without the ink or absorbing layer needs to be determined. There are then two methods which can be used to estimate the intrinsic transmittance of the layer: the first one consists in using Berns approximation (Equation (45)) after having determined the intrinsic reflectance of the substrate with and without the transparent layer as presented in the previous paragraph. This method was used to determine the ink intrinsic transmittance. The second method, which is more tedious, consists first in generating a two-entry lookup table for the Williams-Clapper model: one of the entry is a range of intrinsic transmittances of the transparent layer and the other entry consists in a range of intrinsic reflectances of the print. The reflectance factor predicted by the Williams-Clapper model estimated by considering each entry is stored within the lookup table. For each wavelength, knowing the intrinsic reflectance of the substrate and the reflectance factor of the substrate with the absorbing layer, the intrinsic transmittance of the layer can be retrieved. This method has been used to determine the intrinsic transmittance of the coating layer.

The γ parameter, described in Section 3.2.3, has a default value of 1 and can be fitted either by minimizing the color difference between the predicted reflectance results and the measured ones, or by minimizing the root mean square error (RMSE) between both reflectance factors. In our work, the first option was chosen to get the best colorimetric results.

This multi-convolutive model aims at predicting the additional dot gain caused by a transparent layer on coated halftone prints. It can thus come as a complement to already existing models predicting the appearance of uncoated halftone prints. Compared to the calibration of classical models, the presented multi-convolutive model requires additional specific inputs: the spatial reflectance factors of the uncoated prints and the thickness of the coating layer.

3.3.2 Computation methods

The computations were performed in Python with Numpy. It can be noted that in the case of a halftone print of spatial reflectance factor varying only along one dimension, *x*, line halftones like in Figure 27, the multiple convolutions inside the model can be performed in one dimension, which greatly reduce the algorithm complexity. In this case, the halo function h in Equations (74) and (83) can be replaced by a function $h_{integrated}$ corresponding to the integral of h in the *y*-dimension:

$$h_{integrated}(x) = \int_{-\infty}^{+\infty} h(x,y)dy = \int_{-\infty}^{+\infty} \frac{4d^2 R_{10}\left(arctan\left[\frac{\sqrt{x^2+y^2}}{(2d)}\right]\right)}{\pi(x^2+y^2+4d^2)^2}dy \qquad 89$$

In Figure 28 are displayed the 2D halo along the x-dimension at position $y = 0$ corresponding to the centre, and the halo integrated along the y-dimension. Due to the integration, the two profiles are different, but the two-peak shape of $h_{integrated}$ remains very specific and characteristic of the halo-shaped light reflections at the interface.

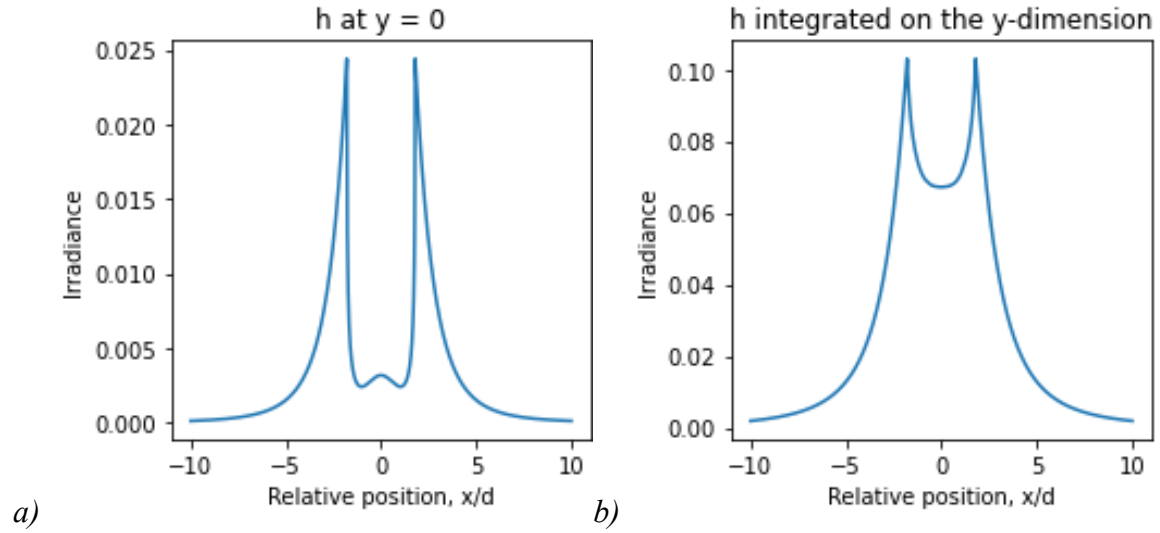

a) *b)*

Figure 28. a) Profile of the halo at its center; b) $h_{integrated}$.

An equality, which proved important to verify, is that the overall spatial integral of h (or $h_{integrated}$ in one dimension) is equal to r_i (equal to 0.5963 for a clear coating of optical index $n_1 = 1.5$), as mentioned in Equation (69) :

$$\int_{-\infty}^{\infty}\int_{-\infty}^{\infty} h(x,y)\,dxdy = \int_{-\infty}^{+\infty} h_{integrated}(x)dx = r_i$$

which can be written, for a discrete function, h as:

$$\Delta x\,\Delta y \sum_{x_i=x_1}^{x_2}\sum_{y_i=y_1}^{y_2} h(x_i,y_i) = r_i \qquad 90$$

where Δx is the spatial resolution on the x-axis, Δy is the spatial resolution on the y-axis, and x_1, x_2, y_1, y_2 are the limits on which h is defined. This requires h (or $h_{integrated}$) to be defined on a large number of points in the algorithm. The ring shape needs to be well resolved, and the area on which it is defined needs to be large enough to also account for the "tail" of the halo shape (ideally it would be defined on an infinite plane). The resolution we basically used for $h_{integrated}$ was 10 000 points, and it was usually defined for $x \in [-50; 50]$, with d = 1. For h, as the multi-convolutive process has a high computational complexity, the size was limited to 501 × 501 points, h was usually defined on $x, y \in [-346.6; 346.6]$, with d around 20. As the multi-convolutive model spatially depends only on the ratio between d and the spatial resolution of the intrinsic reflectance ρ, the computations can be performed with relative spatial

dimensions and no unity is given here for d nor for (x, y). The only important constraint is to guarantee that h and ρ are defined on the same spatial scale by images with same resolution.

In our verifications, even with a good resolution for h (or $h_{integrated}$), there remained a small error to obtain the equality described by Equation (90). This error, caused by the discrete computation, was estimated and compensated in each pixel of h by adding a small component:

$$e/(|\mathrm{x}_2 - \mathrm{x}_1||y_2 - y_1|) \qquad 91$$

where e is the estimated overall error:

$$e = \Delta x\, \Delta y \sum_{x_i=x_1}^{x_2} \sum_{y_i=y_1}^{y_2} h(x_i, y_i) - r_i \qquad 92$$

The multi-convolutive model relies on multiple spatial convolutions and multiplications between h and the print intrinsic reflectance ρ. During the numerical convolution process, edge effects can have a strong impact on the results, especially if the convolution process relies on zero padding where the area outside the defined intrinsic reflectance area are filled with zeros, leading to dark edges.

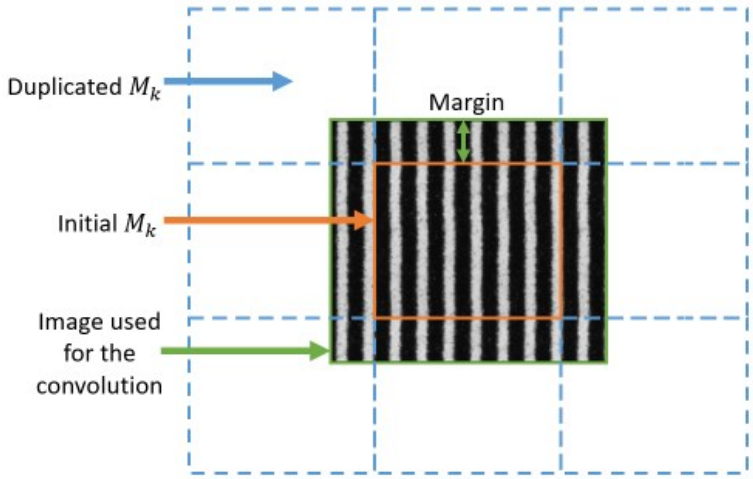

Figure 29. Method to prevent edge effect: generate a margin for each convolution.

A way to prevent edge effect is to originally define a large initial intrinsic reflectance image and crop, at the end of the process, the predicted spatial reflectance matrix given by Equation (77) to the area unaffected by the edge effect. However, this method can be unreliable as it depends on the dimensions of h and on the number of convolutions which are performed; it also requires a strong calculation capacity as the convolutions are performed with large dimension images. The preferred method to prevent edge effects consisted, for each matrix M_k given by Equations (74) and (83), in duplicating it in the two spatial dimensions until a margin of size at least equal to half the size of the matrix h in each dimension could be cropped around the initial matrix M_k, illustrated in Figure 29. The image issued from the convolution was cropped

back to the original size of M_k to retrieve the contribution M_{k+1} to the final predicted reflectance. This matrix M_{k+1} was duplicated again to get a margin for the next convolution and so on. This method requires the initial intrinsic reflectance matrix ρ to contain an integer number of halftone patterns, or a number of patterns high enough to be able to proceed statistically. This method also requires the intrinsic reflectance matrix ρ to be periodical along the x and y dimension to prevent misalignments with the margins in the convolution process.

3.4 Experimental validation of the model: large scale halftone patterns

The objective of this section is to validate experimentally the optical multi-convolutive model proposed in Section 3.2.2, and to observe the halation phenomenon. Two experiments were performed, and the results were compared to the model prediction. The first experiment was at a large scale with a centimetric halftone screen and with a perfectly clear layer, it is detailed in this section. The second experiment was at a smaller scale with millimetric halftone screens and a transparent but absorbing coating layer, it is presented in Section 3.5. Both experiments aimed at validating the theory of the light lateral propagation inside the coating layer and to evaluate the darkening it induces for various sizes of halftone patterns with respect to the thickness of the coating layer. To avoid any confusion with other optical phenomena, the halftone screens had a size such that optical dot gain within the substrate was negligible.

We chose a configuration where the halftone patterns are very large in comparison to the significant size of the substrate point-spread function to avoid any confusion between this effect and dot gain due to light diffusion within the substrate. In this experiment, the line halftone pattern had a period of 33.3 mm, composed of large black and white lines. The support had to be waterproof and of significant scale. It was thus conceived by sticking alternatively black and white parallel tape bands over a white Teflon plate. The Teflon plate was 0.46 m long and 0.33 m wide. The tapes were electrical insulation tapes. The black tape was from BizLine and had an original width of 19 mm. The white tape was from McKenzie and had an original width of 15 mm. Even if the underneath Teflon plate was white, the white tape was used to ensure that the lines were regularly spaced and to increase the diffusivity of the white areas.

The halftone was placed at the bottom of a transparent basin. It was set horizontally on the ground with a bubble level. A white Lambertian diffuser, a spectralon, was placed next to it to be used as a white reference. The clear liquid which was poured over the halftone was a blend of water and sugar at saturation. The liquid is considered to have an optical index of 1.5.

To generate multiple thicknesses of clear coating layers, a clear liquid was gradually poured on the support. For each coating thickness, the halftone was captured by a camera. Each thickness was derived from the size of the halo generated by a laser beam and captured with a handheld camera. The experimental setup and a typical example of captured picture are displayed in Figure 30.

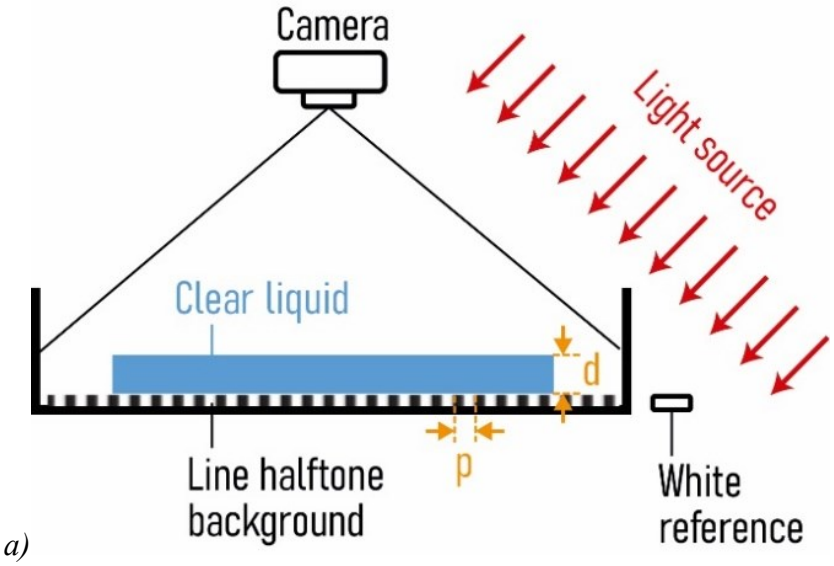

a)

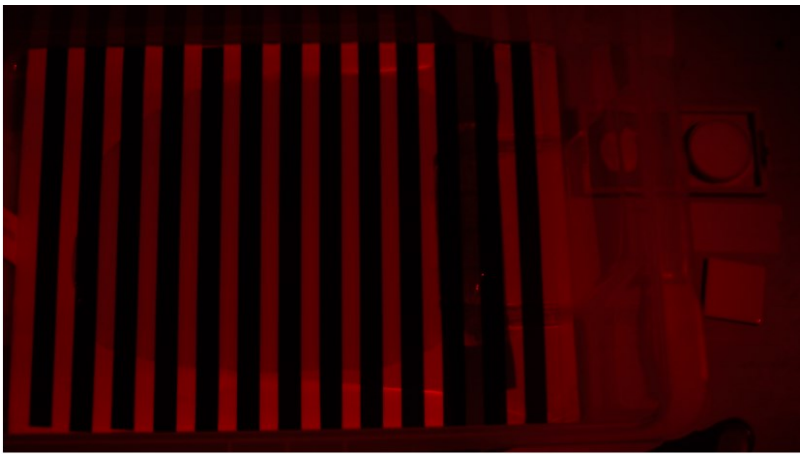

b)

Figure 30. a) Experimental setup. b) One of the captured pictures, the white reference was the round diffusing spectralon on the right, a dark area caused by clear liquid is visible in the central part of the halftone area.

The support and its surroundings were illuminated by a punctual light source set at 1.35 m from the middle of the halftone in the horizontal direction, and 1.5 m high. It thus formed an angle of 42° from the normal of the centre of the halftone. The light source was composed of two optical fibres without collimator linked to the same generator (from Micro-contrôle 154, division Nachet). A red filter inside the generator provided a light of bandpass higher than 650 nm, measured by a goniospectrophotometer (Eta Optik CG100 Goniometric Color Measurement System).

The halftone area was captured with a camera Sony α6000 which was set at 0.3 m from the middle of the halftone in the horizontal direction, and at 1 m in the vertical direction. It thus formed an angle of 16.7° with the normal at the middle of the halftone. The camera was set, in the azimuth plan, perpendicularly to the direction of the light from the source to prevent capturing diffuse surface reflection on the halftone. The parameters of the camera were: ISO 400, completely open diaphragm, 8 s exposure time, focus around 1.7 m, zoom at 35, RAW

picture format. The sensor had a 14-bit encoding. The linearity of the sensor with exposure time was verified by capturing an area with various exposure times. The average pixel value as a function of the exposure time is displayed in Figure 31.a for the red channel. The values given by the sensor of the camera in the complete darkness were captured through 11 pictures, their mean values were calculated to get the black frame picture. As the illuminating light is red, only the red channel of the Bayer matrix of the camera was considered. Its sensitivity was considered to be low above 720 nm, thus the wavelength bandpass of the system was considered to be between 660 and 720 nm. For each measurement on the halftone, two pictures were taken and the mean of them was used in the data treatment. An illumination map was also captured by imaging with the camera the same area as for the halftone but with a uniform paper substrate.

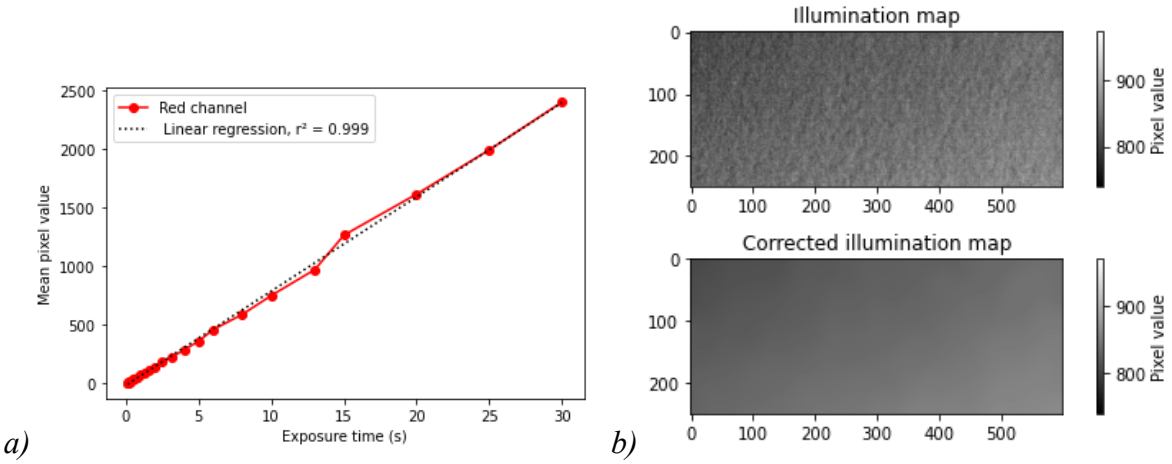

Figure 31. a) Pixel value of the red channel as a function of the exposure time; b) Illumination map on the area of the halftone. A convolution with a gaussian kernel was used to remove the noise caused by the graininess of the uniform paper.

For each coating thickness, a data treatment was made to retrieve, from the pixel values of the camera, the reflectance factor of the halftone. First, all the pictures from the camera were cropped to put the focus on two zones of the pictures: the halftone and the white reference. The halftone zone was delimitated to have a zone with an integer number of periods, completely covered by coating (except in the first picture without coating), and where the illumination is regular (in the middle of the halftone and with a small number of periods). The white reference zone was as large as what was allowed by the captured circular spectralon. The illumination map and the black frame were also cropped according to these two zones. The cropped pictures from the illumination map were blurred to remove the noise induced by the grain of the paper used as uniform substrate, as shown in Figure 31.b. The blur was made through a convolution with a Gaussian function. The pixel values of the halftone and of the white reference were calibrated with considerations to the black frame and the illumination map with:

$$V_{c_h} = \frac{(V_h - V_{k_h})}{(V_{i_h} - V_{k_h})} \qquad 93$$

$$V_{c_w} = \frac{(V_w - V_{k_w})}{(V_{i_w} - V_{k_w})} \quad 94$$

where V_{c_h} denotes the calibrated pixel values in the halftone area, V_h the pixel values of the halftone, V_{k_h} the pixel values of the black frame in the halftone area, V_{i_h} the pixel values of the blurred illumination map in the halftone zone. The same operation was performed for the white reference zone, with V_{c_w} the calibrated pixel values of the white reference area, V_w the pixel values of the white reference, V_{k_w} the black frame pixel values in the white reference area and V_{i_w} the pixel values of the blurred illumination map in the white reference area.

From these calibrated values, we can deduce the reflectance factor of the halftone for each pixel position with:

$$R = \overline{R_w}\frac{V_{c_h}}{\overline{V_{c_w}}} \quad 95$$

where R is the reflectance factor of the halftone at each pixel position, V_{c_h} the calibrated pixel values in the halftone zone, $\overline{V_{c_w}}$ the average calibrated pixel value over the white reference zone and $\overline{R_w}$ the average reflectance of the white reference over the range of wavelengths (660–720 nm). This reflectance was measured with the spectrophotometer CM-2600d from Konica Minolta (geometry: de:8°, 8 mm aperture, without UV cut-off filter), it is displayed in Figure 32.a, we found $\overline{R_w} = 0.747$.

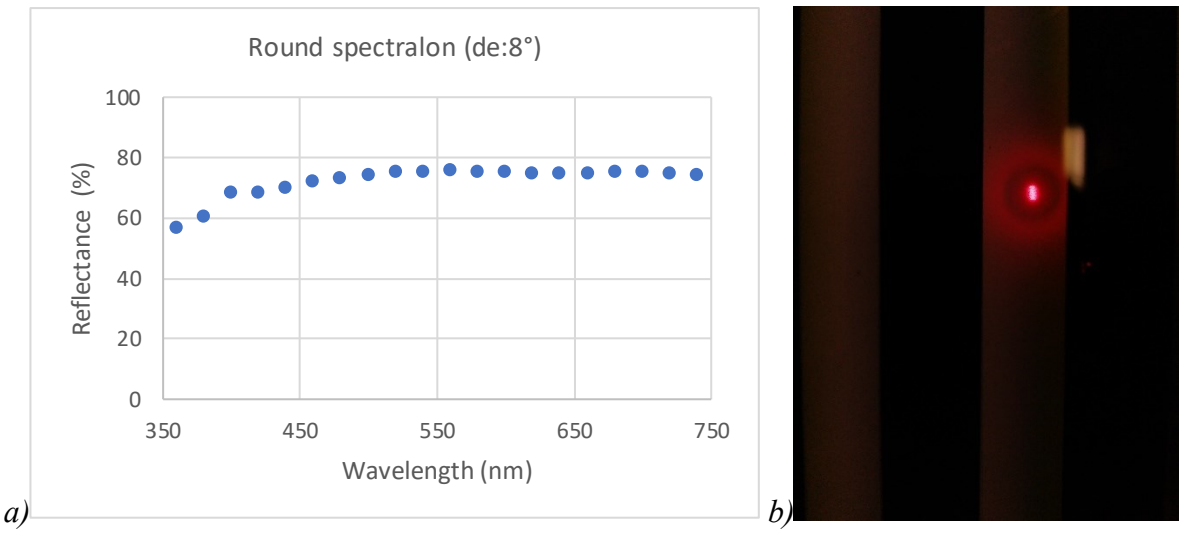

Figure 32. a) Spectral reflectance factor of the white reference measured with a de:8° geometry. b) Exemple of a captured picture used to determine the thickness of the clear layer. Specific care was taken to adapt the illumination and the exposure time to capture both the halo and the halftone lines which were used to scale the image.

The model was calibrated as follows. The surface coverage, a, of the halftone was first determined. It was measured on pictures of the halftone with ImageJ software by measuring the width of the black tape, in number of pixels, and dividing it with the width of the period. Eleven

measurements were performed and the results is $a = 0.551 \pm 0.011$. This surface coverage matches the one determined by thresholding the reflectance picture of the halftone zone without coating. The period of the halftone was measured over nine periods, and we determined that $p = 33.3 \pm 0.2$ mm. The intrinsic reflectances of the white tape, ρ_0, and of the black tape, ρ_1, were fitted from the measured spectral reflectance factors of respectively, the white and the black tapes without coating captured with this setup, they were found to be $\rho_0 = 0.932$ and $\rho_1 = 0.04$. From these different parameters, the spatial intrinsic reflectance of the halftone zone was retrieved from Equation (88).

The thickness of the clear layer was determined by measuring the diameter of the dark disk in the halo in images: for each thickness, a picture was taken of the halo generated by a thin laser beam, as shown in Figure 32.b. The scale of each picture was determined in the ImageJ software using the averaged size of one period (in pixel) over five measurements near the halo region. The area of the dark circle A of the halo was measured on the scaled image with ImageJ software. From this area, and considering the optical index of the clear layer to be $n_1 = 1.5$, we determined the thickness d thanks to the following formula issued from Equation (53):

$$d = \frac{\sqrt{A/\pi} \times \sqrt{n_1^2 - 1}}{2} \qquad 96$$

This was repeated twice and the considered result was the average of the two values obtained for d. The measured thicknesses were: 1.9, 1.2, 1.5, 2.5, 3.2, 2.0, 2.4, 3.7, 2.8, 2.7, 5.3, 6.5, and 8.2 mm.

The coating layer was considered to be perfectly clear ($t_c = 1$) and with an optical index of 1.5. Parameters r_s, r_i, T_{in}, and T_{out}, were estimated for the specific geometry of the experiment: directive illumination with an angle of 42°, and directive measurement with an angle of 16.7°. They were equal to: $r_s = 0$, $r_i = 0.596$, $T_{in} = 0.953$, and $T_{out} = 0.427$. The γ parameter was 1 (the black tape was opaque).

We compared the reflectance factors measured for each coating thickness with the ones predicted by the multi-convolutive model for the same thickness. Some of the experimental spatial reflectance factors are displayed in Figure 33.a. It can be seen that as d/p increases (d thickness of the coating layer, p period of the halftone which is constant), the reflectance of the white bands decreases. Pictures also look blurrier when a coating layer is applied.

The decrease in reflectance of the samples due to the coating layer can be seen in the diagram of Figure 33.b showing the average reflectance factor over the picture as a function of the d/p ratio. The vertical error bars represent the mean standard deviation of each spatial reflectance factors calculated for each column over all the lines, for each measurement. The predictions given by the multi-convolutive model are also plotted (except for $d/p = 0$ for which the model is not defined). The experimental and theoretical reflectance factor values match rather well and show the darkening effect due to the diffusion of light inside the coating layer. This diffusion allow light to propagate from clear areas to dark ones, where it is absorbed. As the

halo size increases with the thickness of the coating layer, the thicker the clear layer, the stronger the darkening. The darkening reaches a plateau for high thicknesses as the light internally reflected has the same probability (weighted by the surface coverage) to reach a dark as a white area. In this condition, the limit described by the Williams-Clapper model is reached. Even though we took care in the experiment to verify the assumptions on which the multi-convolutive model relies, real materials hardly meet the ideal properties that the model considers: the substrate was probably not a perfectly Lambertian reflector, and the optical index was close to 1.5 but maybe not precisely this value.

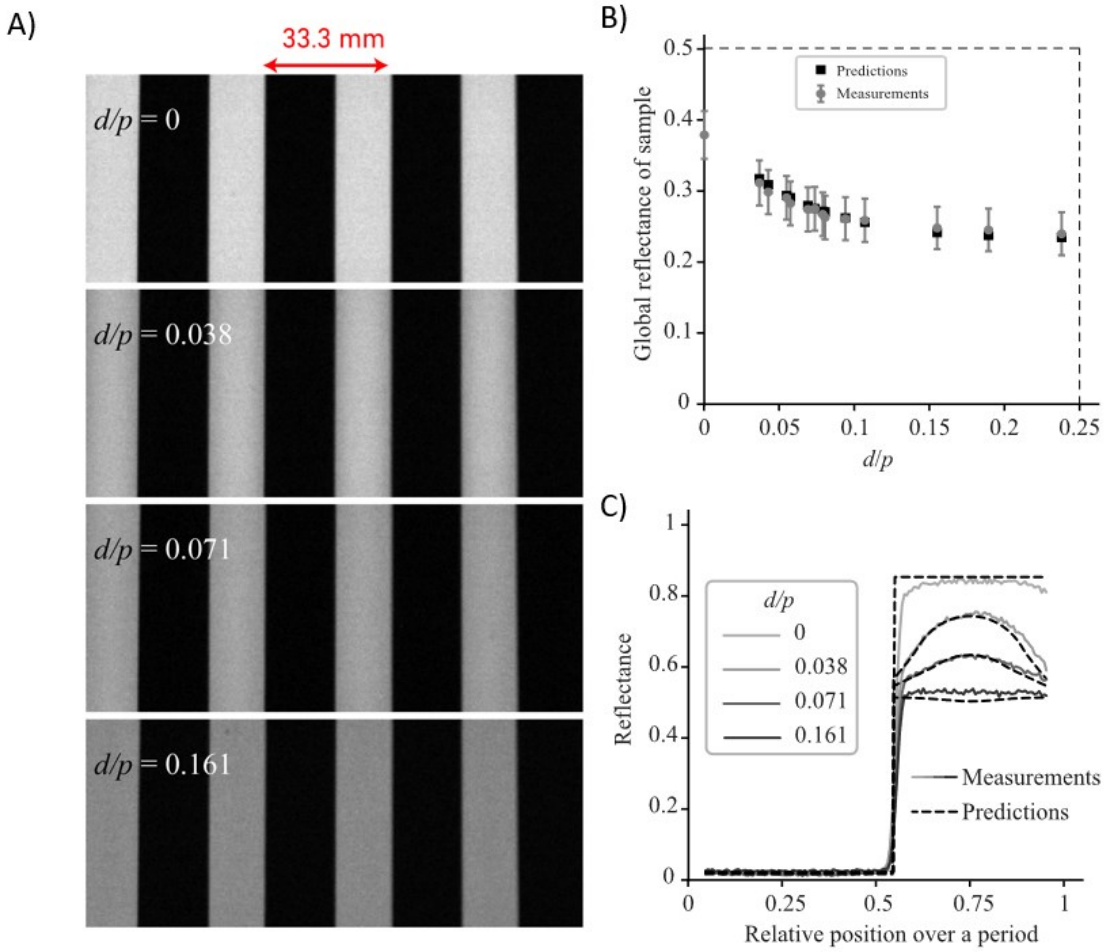

Figure 33. a) Pictures of the halftone pattern when uncovered and covered by a layer of clear liquid (optical index of 1.5) with increasing thickness, yielding four different d/p ratios. b) Comparison between measured and predicted reflectances of the coated support for different d/p values. The error bars correspond to the mean standard deviation of the reflectance along the strips in each captured image. c) Reflectance profiles for the different d/p values over one stripped pattern period from the pictures displayed in a). The measured curves are represented in solid lines, and the predicted curves in dashed lines.

The large-scale experiment allows us to detect the effects of a coating layer on the reflectance factor spatial distribution of the halftone area. Experimental and theoretical reflectance factor profiles of the halftone are thus plotted in Figure 33.c. The experimental profiles are the average

profile of the second left period of the pictures in Figure 33.a over 100 horizontal lines, which reduced the noise. It can be seen that the experimental and theoretical profiles match fairly well despite the differences which might exist between the ideal materials considered in the multi-convolutive model and the real ones used in the experiment. In the picture corresponding to a ratio $d/p = 0.038$, the edges between the white and black area look blurred. This blurring effect is a rather logical consequence of the halation phenomenon that we analyse, and it can be easily observed with any coated print (examples are shown in [145]); surprisingly, this blurring effect that affects every laminated print, such as ID cards, is not reported anywhere in the literature.

This experiment allowed to estimate the darkening caused by the addition of a clear layer in optical contact with a non-uniform, line-halftoned, substrate. It showed that the multi-convolutive model presented in section 2.2 gives similar results as the measurements which were performed, both for the overall reflectance factor and for in the spatial profiles. This experiment was yet performed with materials and conditions far from the ones encountered in the printing domain. Another experiment was then performed at a smaller scale with materials showing variations in the spectral dimension.

3.5 Experimental validation of the model: small scale printed halftone patterns, and comparison with classical models

A second experiment was carried out to verify the multi-convolutive model in conditions which are closer to the printing domain and to compare the multi-convolutive model predictions with other classical optical models.

Halftone line patterns were printed with magenta ink on a glossy coated paper (90g/m², Bekk smoothness of 2000 s). Seven patches, pictured in Figure 34, were considered: one patch of bare substrate, one patch of solid magenta-inked substrate, and five patches of nominal coverage 0.5 with different line periods: 1.69, 1.35, 1.02, 0.85 and 0.68 mm. The test form was printed with a Xerox printer, the Xerox Versant 180, of resolution: 1200 dpi (dot diameter of 21 µm); the printing resolution was 600 dpi.

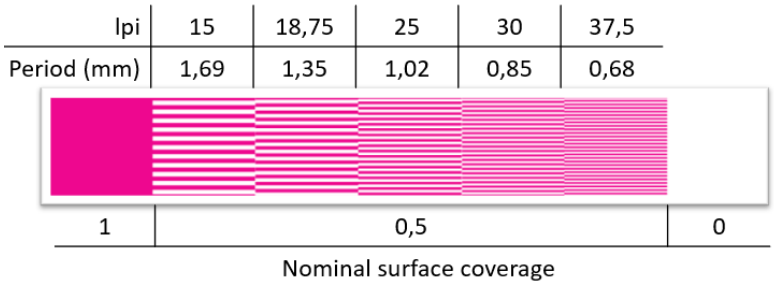

Figure 34. Test form which was printed and patches characteristics.

The corners of the sample were first pasted onto a rigid substrate to prevent bending during the coating process. It was then coated with one to three layer(s) of varnish. The varnish was a UV curing varnish (Vernis Sérigraphie, Omniplus UL, UL360, Application varnish, e 5 kg 54 BN777642, UN 3082, Fujifilm, Broadstairs, United Kingdom). It was applied with a thread bar (Mayer bar n°4, black handle, made for 40 µm deposit) from K control coater. The Mayer bar was at maximal speed and the coater was calibrated for twice the thickness of the sample, to ensure that the varnish layers were of significant thicknesses and had a flat surface. Each coating layer was polymerised with a conveyor from Distrilampe illuminating the sample with UV light.

Before coating and after each varnish layer deposition, the thickness of each patch was measured, including the rigid substrate, and the reflectance of each patch was measured twice. The reflectance measurements were performed with the spectrophotometer CM-2600d from Konica Minolta, based on the di:8° measurement geometry, delivering spectral reflectance from 400 to 730 nm in steps of 10 nm. There was a UV cut-off filter to prevent any fluorescence effect as there were optical brighteners in the substrate. The thickness measurements, performed with a micrometer from Adamel Lhomargy (m120, 15 mm-diameter probe), allowed to estimate the local thickness of the coating layer over each patch. The varnish thickness of each layer averaged over all the patches was, respectively: 61, 107 and 191 µm.

The measured reflectance factors were compared with the multi-convolutive model presented in Section 3.2, as well as with classical reflectance models: the spectral Neugebauer model and Yule–Nielsen modified spectral Neugebauer model presented in Equations (24) and (26) for one ink. These two models were used as a comparison to evaluate whether the halation phenomenon caused by the addition of a coating layer was similar, or not, to the optical dot gain induced by light propagation within the substrate, presented in Sections 2.2.4 and 2.2.5. If the halation phenomenon induced no additional dot gain, the spectral Neugebauer model could be applied on the coated prints. If the halation phenomenon caused a similar dot gain as the one induced by light diffusion within the substrate, the Yule-Nielsen modified spectral Neugebauer model could apply to the coated prints. In this case, the n_{YN} parameter of this model would be an indicator of the additional dot gain: equal to 1 without dot gain, its value would be superior to 1 for coated prints and would increase for thicker layers where the halation phenomenon could have more impact on the print reflectance.

We wanted to evaluate the performances of the different halftone reflectance models when the halftone is coated. To calibrate the models, the effective scalar surface coverage of each halftone, *a*, is needed. As the periods of the halftone patches are large, the optical dot gain should not impact the determination of the surface coverages. They can thus be estimated by minimizing the deviation between the measured halftone spectral reflectance factor, $R_m(\lambda)$, and the one predicted by the spectral Neugebauer model, using the following equation:

$$a = \underset{x}{argmin} \sum_{\lambda=400nm}^{730nm} \left(\frac{R_m(\lambda)}{R_0(\lambda)} - \left[(1-x) + x \frac{R_1(\lambda)}{R_0(\lambda)} \right] \right)^2 \qquad 97$$

These surface coverages are the input surface coverages of the three tested models (spectral Neugebauer, Yule–Nielsen modified spectral Neugebauer, and multi-convolutive model). The Neugebauer and the Yule–Nielsen models are based, for each layer, on the reflectance measurements of the bare substrate and solid ink covered with varnish coating. The n_{YN} parameter of the Yule–Nielsen model is fitted for each halftone reflectance measurement.

To calibrate the multi-convolutive model, the intrinsic reflectances of the bare substrate, $\rho_0(\lambda)$, and the solid magenta, $\rho_1(\lambda)$, were determined from the measured reflectance $R_i(\lambda)$ of these patches without coating by using Equation (47). In this equation r_s, r_i, T_{in}, and T_{out} were calculated for the di:8° measurements geometry of the spectrophotometer, their values are displayed in Table 1. The spatial intrinsic reflectance of the patches was simulated with Equation (88).

The coating layer was considered to have an optical index of 1.5. The varnish was rather transparent but it had a yellowish color. Its intrinsic transmittance t_c was thus evaluated with the Williams–Clapper model from the reflectance measurements of the bare substrate for each coating layer: for each wavelength, the intrinsic transmittance t_c is estimated through a linear interpolation from the 2D-lookup table of the Williams–Clapper model introduced in Section 3.3.1. The input intrinsic reflectance of the substrate and the input intrinsic transmittance of the varnish, each ranged from 0 to 1 with a 0.001 sampling step. The output of this lookup table was the reflectance factor of the coated bare substrate calculated with the Williams–Clapper model for the di:8° geometry, Equation (37). Knowing the experimental reflectance of the coated bare substrate and the experimental intrinsic reflectance of the substrate, the intrinsic transmittance of each coating layer can be deduced. The intrinsic transmittances were then estimated for the local thickness of the layer over each halftone according to Beer's law, Equation (7), their average for each layer is displayed in Figure 35.

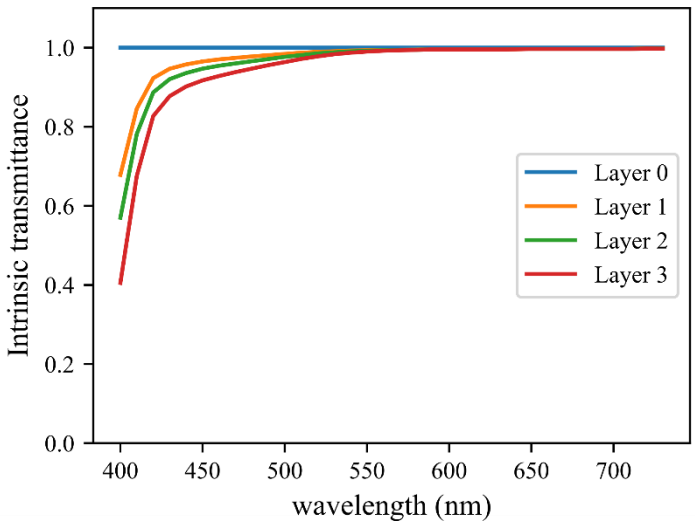

Figure 35. Intrinsic transmittance of the coating layer for each thickness, averaged over all the halftone patches.

In the multi-convolutive model, r_s, r_i, T_{in}, and T_{out} values took into account the intrinsic transmittance of the coating layer through lookup tables we had previously generated. The γ parameter was 1.

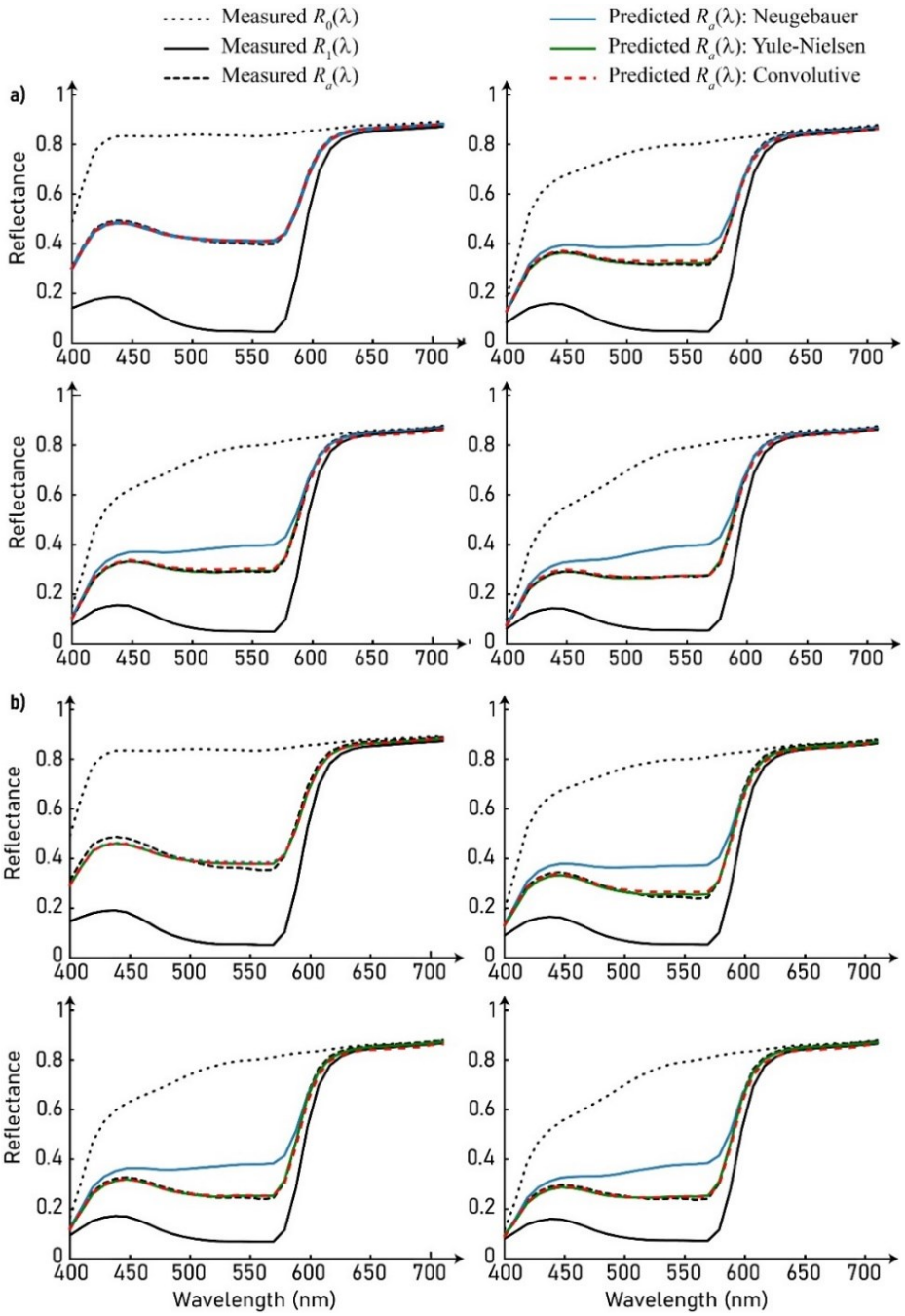

Figure 36. Measured and predicted reflectances of magenta line halftones of period a) 1.69 mm; b) 0.68 mm, with different varnish thicknesses: without varnish (top left); one layer (top right); two layers (bottom left) and three layers (bottom right).

The spectral reflectance predicted by the spectral Neugebauer, Yule-Nielsen and multi-convolutive models, as well as the measured ones, are displayed in Figure 36 for the halftone screens of period 1.69 mm and 0.68 mm. The results detailed for all periods are displayed in Appendix V.

For the uncoated patches, Figure 36.a and B (top left), the reflectances predicted by the spectral Neugebauer model matches rather well to the measured reflectances. Optical dot gain has therefore little impact on the print reflectance, and this justifies that the Neugebauer model was used to determine the surface coverage of the print.

Period (mm)	1.69	1.35	1.02	0.85	0.68
No coating	1.01	1.02	1.02	1.02	1.03
Layer 1	1.50	1.74	1.94	1.91	2.13
Layer 2	1.86	2.13	2.38	2.33	2.48
Layer 3	2.29	2.61	2.79	2.59	2.68

Table 2. Fitted n_{YN} parameter of the Yule–Nielsen model.

For the coated patches, the predicted spectral reflectances given by the Neugebauer model do not coincide with the measured one anymore. This cannot be attributed to the absorptance by the coating layer as the calibration of the Neugebauer model relies on coated primaries: the print is darkened due to lateral light propagation within the coating layer. The Yule–Nielsen modified spectral Neugebauer model is able to render this darkening thanks to the fitted n_{YN} parameter, which are detailed in Table 2 (and displayed in Figure 38.b). The darkening can thus be viewed as an optical dot gain caused by the coating layer, as described in the literature [4].

The multi-convolutive model also renders the halation phenomenon and approaches fairly well the measured spectral reflectances without any fitted parameter. The root mean square errors between predictions and measurement, given in Table 3, show that it is almost as accurate as the Yule–Nielsen model, known to be one of the most accurate reflectance prediction models for halftone prints [87]. The small spectral differences that can still be seen between the predicted and measured spectra in wavelength domain 500–600 nm are probably due to the fact that the solid magenta patch absorbs almost all the light in this spectral domain and the measured reflectance reaches a floor value. They could also be due to an effect of fluorescence by the paper.

Period (mm)		1.69	1.35	1.02	0.85	0.68
Multi-convolutive model	layer 1	0.012	0.015	0.018	0.015	0.015
	layer 2	0.011	0.012	0.014	0.012	0.014
	layer 3	0.009	0.010	0.009	0.010	0.013
Yule–Nielsen model	no coating	0.007	0.009	0.013	0.014	0.017
	layer 1	0.005	0.005	0.006	0.009	0.010
	layer 2	0.004	0.004	0.005	0.006	0.007
	layer 3	0.004	0.004	0.005	0.007	0.008
Neugebauer model	no coating	0.007	0.009	0.013	0.014	0.018
	layer 1	0.043	0.054	0.062	0.062	0.068
	layer 2	0.057	0.065	0.071	0.070	0.073
	layer 3	0.065	0.071	0.073	0.071	0.072

Table 3. Root mean square error between the models and the measurements.

On a colorimetric point of view, the darkening effect due to the coating can be observed in Figure 37 in the CIE 1976 L*a*b* color space, where the coordinates associated with the different measured spectral reflectances are represented. These color coordinates were obtained by converting each spectral reflectance as well as the spectral reflectance of the bare paper into CIE 1931 XYZ tristimulus values by considering 2° observer and an illuminant E of uniform spectral power distribution over the visible spectrum. These tristimulus values were then converted into L*a*b* color coordinates with the bare paper as white reference for the chromatic adaptation. The color of each patch is represented with one point in the a*b* plane and in the L*C* plane, with a* denoting the green to red tones, b* denoting the blue to yellow tones, L* being the lightness and C* being the chroma [146]:

$$C^* = \sqrt{a*^2 + b*^2} \qquad 98$$

It can be observed in the L*C* plane that, as the coating thickness increases, the halftone color becomes darker and more saturated, which is linked with the higher probability for light to meet a neighbouring ink pattern. The a*b* plane shows that the color of the halftones also becomes more yellowish as the varnish thickness increases, which is due to the absorptance of the varnish.

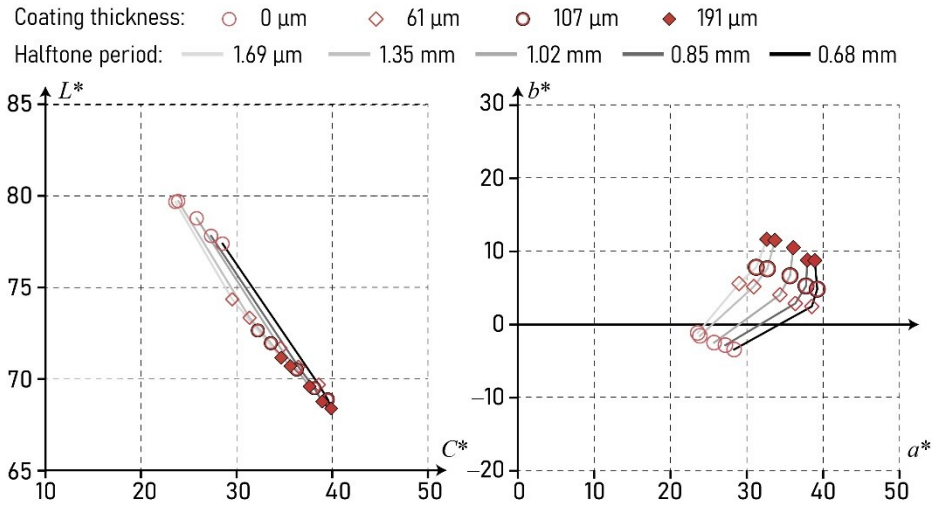

*Figure 37. CIE1976 L*a*b* colorspace.*

The halation phenomenon due to the presence of a transparent coating on top of halftone-printed diffusing support is confirmed both theoretically and experimentally, and we have shown through the example of line halftones that it is predictable.

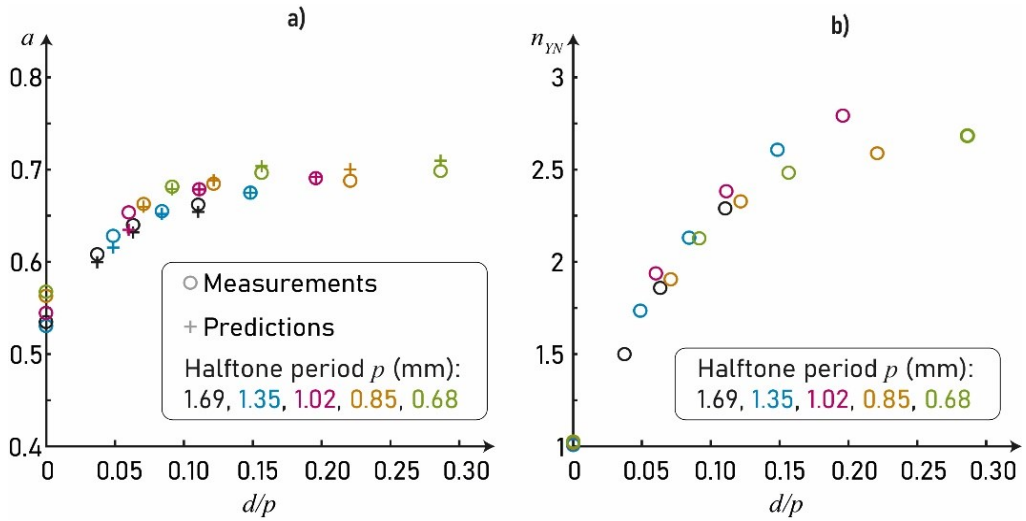

Figure 38. a) Apparent surface coverage estimated with the Murray–Davies equation; b) fitted n_{YN} parameter of the Yule–Nielsen model.

The further question that arises is the error that we can do with classical models that ignore this effect in their calibration, i.e., in the estimation of the surface coverage of the ink patterns from reflectance measurements. In Figure 38.a are displayed the apparent surface coverages of the coated halftones for various *d/p* ratios. The apparent surface coverages are estimated through the Murray–Davies equation and their average is calculated over the absorption wavelength range of the ink: between 400 and 620 nm. It can be seen that the coating layer induces an overestimation of the surface coverage, which is due to the fact that the Murray–Davies equation does not take into account the halation phenomenon. We can also verify that the

halation phenomenon can be considered as an optical dot gain effect. The parameter n_{YN} of the Yule–Nielsen model which is a marker of optical dot gain [87], [147], is displayed in Figure 38.b as a function of the *d/p* ratio of each coated patch. We observe as expected that n_{YN} increases as *d/p* increases, which corroborates the trends evocated above.

In Section 3.4 and 3.5, we have shown through experiments that the color changes occurring within a print coated with a transparent layer are due to a lateral propagation of light within the coating during the multiple reflections process that occurs between the inked diffusing substrate and the coating–air interface. The consequences on the spectral reflectance and color of halftone prints are similar to the well-known optical dot gain effect due to scattering within the diffusing substrate, even though the point-spread function associated with this the lateral propagation of light is a ring-like halo, not a Gaussian or Lorentzian-like point-spread function as usually observed in diffusing supports [148], [149]. The accuracy of the optical model taking into account the multiple convolutions between the ring-like halo and the halftone screen pattern presented in Section 2.2 was verified thanks to an experiment based on large-line halftone patterns in order to isolate the dot gain due to the coating from the dot gain due to the diffusing substrate, the latter being negligible in this case, and with a clear coating layer. A second experiment based on single-ink-line halftone prints on paper could also show the good accuracy of the multi-convolutive model.

The classical spectral Yule–Nielsen model can also provide good predictions of the spectral reflectance of the coated print, provided the coating is not absorbing too much, by means of fitting the empirical Yule–Nielsen n_{YN} often considered as a marker of lateral propagation of light within the print [29], [77], [97], [101], [105], [147], [150]–[152]. The value of this latter increases as the coating thickness increases, which confirms the idea that the halation phenomenon can be considered as an optical dot gain effect. As the multi-convolutive model and theoretical approach has been verified through the two experiments presented in this section, it may now be used to simulate the impact of various parameters on the appearance of a coated halftone.

We are now rather certain that the halation phenomenon was at the origin of a print darkening when it was coated with a transparent layer. The model and corresponding experiments were published in [153].

3.6 Impact of the optical indices on the halo: water or oil

The halation phenomenon is induced by any type of materials (water, oil, glass, PET…), as long as it is a homogenous transparent layer with smooth and plane surface and in optical contact with the scattering substrate. These materials can have various optical index which have an influence on the optical properties of the printed substrate coated with a transparent layer. The objective of this study is to observe the effect of a variation of the optical index on the

reflectance of the system composed of a transparent layer and non-uniform substrate in optical contact. Therefore, the substrate and the coating layer keep the same optical index and the interface between them is optically neutral. This study was performed in the context of a participation in a book project on the effect of water on the appearance of wet materials, which was published in 2023 [154]. This study was thus mainly performed under the prism of a non-uniform substrate covered with a liquid layer, but the results remain identical for any type of materials with the same optical indices.

Let us first simulate the impact of the index of the coating layer on the halo-shaped light propagation inside the coating layer.

To illustrate the phenomenon, approximately 10 mm of liquid (consecutively water and oil) was spread inside a container having a white bottom surface. It was illuminated with a laser beam and captured, from above, with a camera, the pictures are shown in Figure 39.

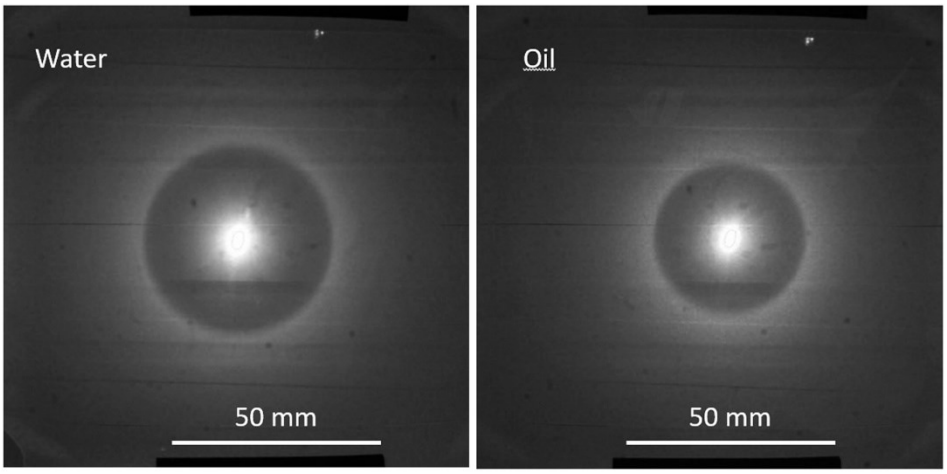

Figure 39. Picture of a laser spot on a scattering surface overlayed with a liquid layer, water on the left and oil on the right. The liquid thickness is 10 mm in both pictures, the diameter of the halo is 46 mm for the water (n = 1.33) and 36 mm for the oil (n = 1.5).

As can be seen in this figure, the halo due to the oil layer is more intense and has a smaller diameter than the halo produced by the water layer. This is due to the fact that the critical angle of incidence for total internal reflection at the liquid-air interface is lower for the oil than for the water. It is equal to 42° for oil (of optical index 1.5) and 49° for water (of optical index 1.33). A larger amount of light is thus reflected at the interface when the liquid is oil than when it is water. The critical angle also determines the halo diameter on the substrate, denoted Φ, detailed in Equation (53):

$$\Phi = \frac{4d}{\sqrt{n_1^2 - 1}}$$

where n_1 denotes the optical index of the liquid layer, and d denotes the thickness of the transparent layer.

This change of optical index has an impact on the irradiance map on the substrate caused by the internal reflection at the interface with air, described by function h in Equation (68). This halo function is displayed in Figure 40 for two optical indices: 1.5 (oil, sucrose, PET) and 1.33 (water), and a liquid layer of thickness unity (for a thickness d, all distances indicated on the graphs would be multiplied by d). The profile along the diagonal of the halo is also displayed for these two indices, as well as for two extreme, purely theoretical cases: the case where $n_1 = 1$ (the internal reflectance r_i of the interface with air is zero), and the case where n_1 tends to infinity, as if the interface were a perfect mirror of Fresnel reflectance 1 for every angle of incidence. In the latter case, h would describe a cos^4 law which is inherent to the variation of irradiance of light on a flat surface when it is enlightened by a very small, perfectly Lambertian light source, as explained in Section 2.2.1. For $n_1 = 1.5$ or 1.33, h follows the cos^4 low when the angle of incidence is higher than the critical angle and is much smaller at smaller angles of incidence.

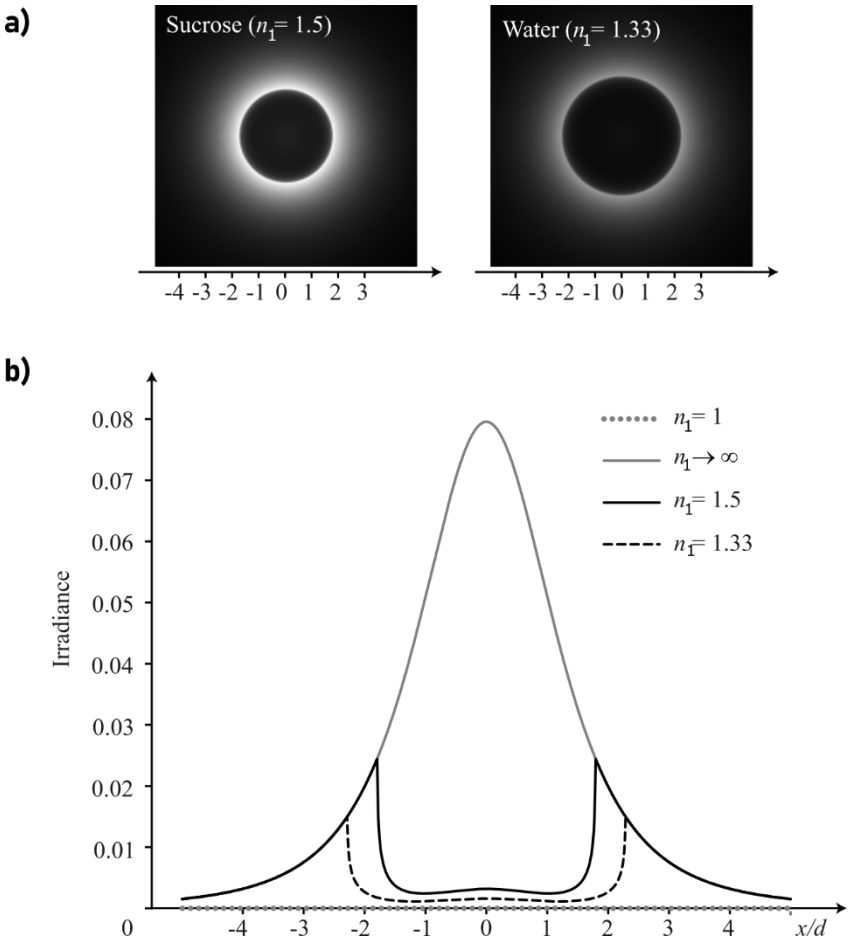

Figure 40. a) Density plots of the halo function h, for water and sucrose (displayed with the same grayscale). b) Corresponding profiles of h for various refractive indices. The abscissa denotes the ratio between length x on the substrate from the center of the halo and layer thickness d. Accordingly to Equation (53), the halo radius is greater for water ($\Phi_{1.5}/2d \cong 2.28$), than for sucrose ($\Phi_{1.33}/2d \cong 1.79$).

The multi-convolutive model enables to predict the reflectance of non-uniformly colored substrates. In the following, we focus more specifically on the case study where the substrate is composed of black and white lines of equal fractional coverage of the surface, as shown in Figure 27. The reflectance of the dark lines is 0, the reflectance of the white lines is 1 and the liquid is clear. The halation phenomenon depends on the ratio between the thickness *d* of the liquid layer and the spatial period *p* of the stripped pattern. The reflectance predicted by the multi-convolutive model is plotted as a function of the ratio *d/p* in Figure 41 for various optical indices, by considering a Lambertian illumination, an observation at 8° from the normal of the surface, and no specular reflection.

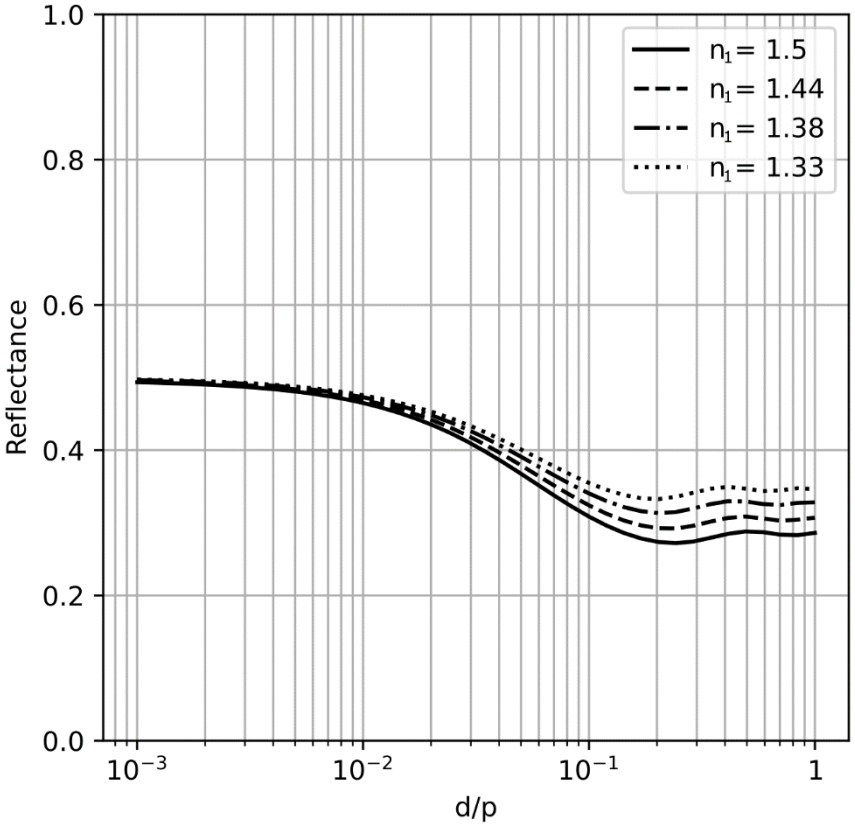

Figure 41. Predicted reflectances of a black and white stripped substrate covered by layers of light with various indices, as functions of the ratio between the liquid thickness d and the period p of the stripped pattern. The reflectance of the black strips is 0, the reflectance of the white strips is 1, and both strips have the same fractional area.

When *p* is large in comparison with the liquid thickness *d* (low *d*/*p* values), the layer has a weak impact on the reflectance: light cannot propagate from a white line to a dark one, or to a negligible extent. All curves have the same limit 0.5. This limit corresponds to the average reflectance of the substrate [73], [74].

When d is much larger than p (high d/p values), the halo is large in comparison with the pattern period and light has the same probability to meet a white area or a dark area after each internal reflection on the interface. The reflectance reaches another limit dependant on the layer optical index, which corresponds to the Williams-Clapper model, detailed in Equation (62), where the substrate intrinsic reflectance, $\overline{\rho}$, is the average reflectance of the white and black areas, i.e., 0.5. Indeed, the color variations of the substrate are negligible compared to the size of the halo and the substrate can be considered as uniformly colored. In this condition, Equation (62) applies.

The reflectance of the covered substrate decreases as the ratio d/p increases, to a different extent according to the optical index. As the optical index increases, the halo is more intense (see Figure 40), i.e., the fraction of light internally reflected by the interface is higher; this gives more chance for light to meet a dark line and to be absorbed. The global reflectance of the covered substrate is therefore lower. For each optical index value, there is a d/p value for which the reflectance is the lowest. This value is smaller for water than for sucrose. This is explained by the fact that the halo in water is larger than the one in oil or sucrose, such that dark lines are met sooner.

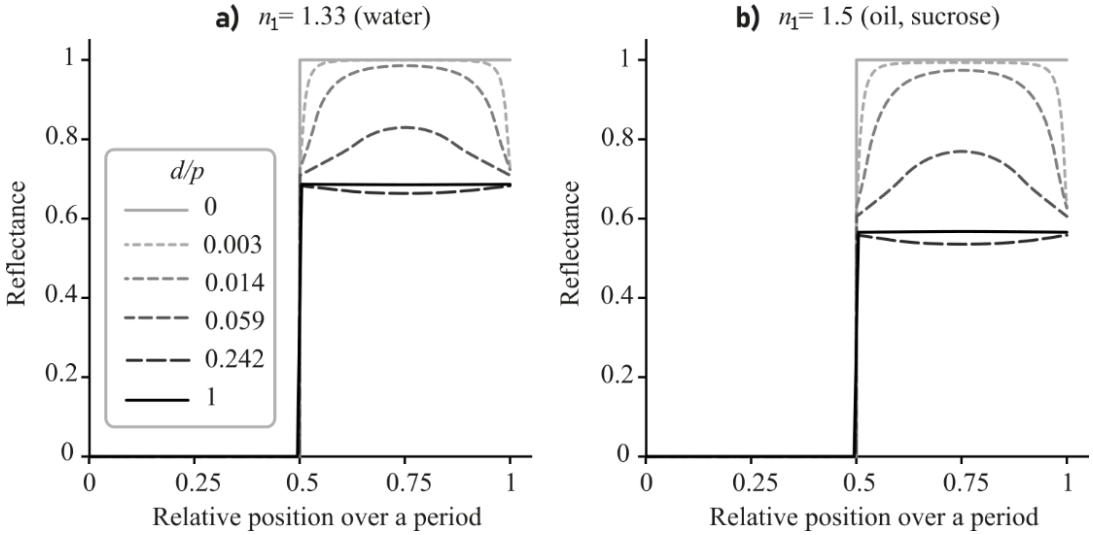

Figure 42. Simulated reflectance profiles over one period of black and white patterns for various d/p values when the substrate is covered by a clear layer of refractive index a) 1.33 or b) 1.5.

Figure 42 shows simulations given by the multi-convolutive model of the spatial reflectance of the samples over one pattern period for various d/p values when covered by water (Figure 42.a), or by oil or sucrose (Figure 42.b). The value $d/p = 0$ means that there is no liquid, and the reflectances of the white and black areas are 1 and 0, respectively. For every other d/p value, the reflectance of the black strips remains 0 since all the light falling on them is absorbed. The influence of the d/p value therefore concerns only the white areas, which are most often darker near the edges: the stripped patterns look blurry. Interestingly, there exists a d/p value, near 0.2

(the halo diameter is slightly larger than half a pattern period), for which we observe the opposite: the center of the white strips is darker than the edges. The points that would contribute most to reflect light to the center of the white strips according to the halo function are mostly black points. As the halo becomes very large (large *d/p* values), the points that contribute most to reflect light to white strips are equally white or black. The white strips are uniform, and the reflectance of the sample reach the limit mentioned in Equation (62) with the Williams-Clapper model.

Let us now consider that the dark strips are not black but grey, with various reflectance values between 0 and 1. In the printing domain, it would be equivalent to print lines with inks of various absorbance. Once again, we consider various liquid thicknesses, therefore various *d*/*p* values. The global reflectance of the samples are plotted as functions of the reflectance of the dark strips in Figure 43, again for water (n = 1.33), and oil or sucrose (n = 1.5). With $d/p = 0$, there is no halation phenomenon, and the reflectance of the substrate is a ramp between 0.5 (dark lines completely absorb light, corresponding to black) and 1 (all the lines are perfectly reflecting, corresponding to white). For other *d*/*p* values, the sample is darkened, in a non-linear way, depending on the reflectance of the dark lines. At the extreme right of the plot, where the dark lines are perfectly white, all the curves converge towards the value $T_{in}T_{out}/(1-r_i)$, which is very close to 1.

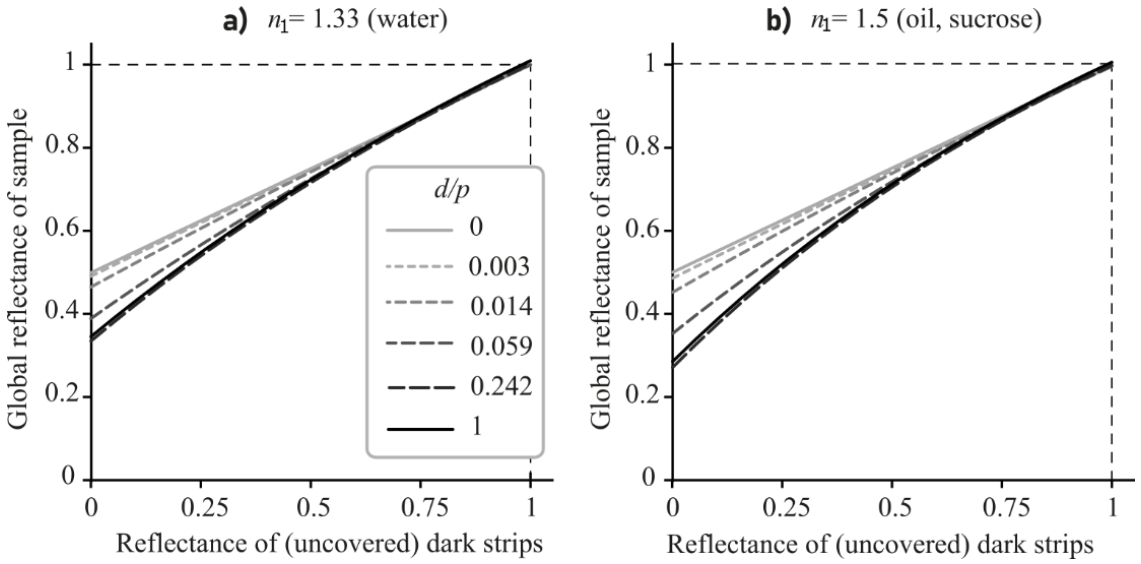

Figure 43. Global reflectances of a stripped substrate covered by a clear layer of refractive index a) 1.33 or b) 1.5, as a function of the reflectance of the uncovered dark strips, for various d/p values.

The color changes induced by a clear coating layer depend on the size of the color patterns on the support, the size of the halo (proportional to the layer thickness), and the refractive index of the coating (which determines the internal reflectance of the interface, thereby the amplitude of the halo). The halo is larger and less intense when the substrate is overlaid with water (optical index 1.33) than with oil (1.5). Predictions by the multi-convolutive model show that the

darkening is more pronounced with a liquid of high optical index (oil) than one with a lower index (water). However, the darkening reaches a minimum at a smaller liquid thickness of low optical index rather than with a high one due to the halo size difference. In the printing domain, optical indices and thicknesses could be optimized to maximize the halation phenomenon and to minimize the amount of ink required to produce a given color. Other parameters of the halftone pattern may also be optimized, which is the subject of the next subsection.

3.7 Influence of the halftone pattern

The objective of this subsection is to simulate the influence of variations in the uncoated spatial reflectance factor of halftone patterns in the halation phenomenon. The influence of the surface coverage, of 2D pattern shapes and of 1D profile shapes are presented. In these simulations, the index of the coating layer was 1.5.

3.7.1 Halftone surface coverage

The first objective is to determine the influence of the surface coverage on the color change caused by the addition of a coating layer over a print. Similarly to the simulations performed in the previous subsection, the simulated halftone pattern is composed of black and white lines of relative width depending on the surface coverage, as shown in Figure 27. The reflectance of the black lines was 0 and the reflectance of the white lines was 1. The simulations were performed with a de:8° geometry.

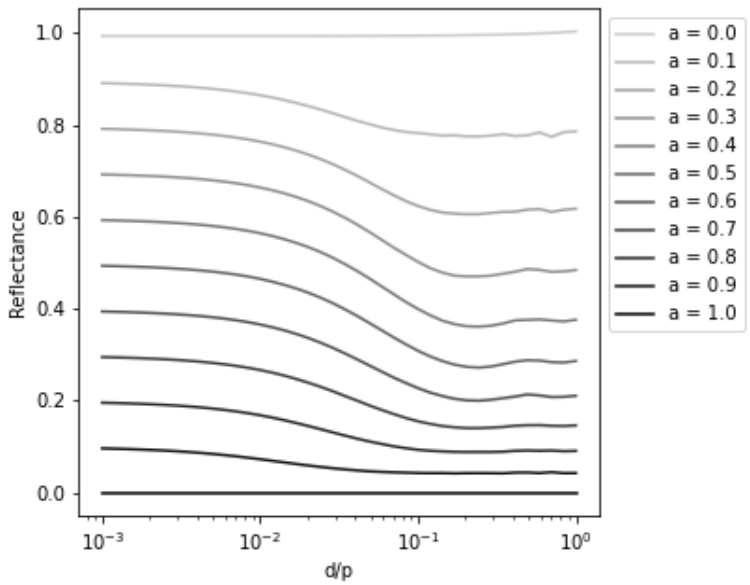

Figure 44. Reflectance of a line halftone pattern for various surface coverages, a, between 0 and 1, as a function of the d/p ratio. The reflectances of white and black lines without coating are 1 and 0 respectively.

The simulated reflectance factor as a function of the *d/p* ratio (with *d* the thickness of the coating layer and *p* the period of the halftone screen) are displayed in Figure 44 for various surface coverages, *a*. When *d/p* = 0, the reflectance of the print is proportional to the surface coverage, as described by the Neugebauer model. In the case where *d/p* is high, the limit given by the Williams-Clapper model depend on the average intrinsic reflectance depend on the surface coverage in a non-linear manner. The prints of surface coverage around 0.5 are the most darkened by the addition of a coating layer. On the contrary, as the prints of surface coverage equal to 0 and 1 are uniform, the addition of a coating layer has no-impact on their reflectances.

3.7.2 Influence of the halftone pattern shape

To evaluate the influence of the halftone pattern on the color change caused by the halation phenomenon, simulations were performed with various monochrome binary halftone screens. The reflectance factors were described on two-dimensional cells of dimension $p \times p$ pixels. Each cell was repeated along the *x* and *y* axis to generate a halftone screen which had a surface coverage of 0.5. The reflectance factors of the non-coated print were arbitrarily set to 0.1 for the inked areas and 0.9 for the non-inked areas, for all wavelengths. These reflectance factor values were chosen to prevent total absorption of the light reaching the inked areas and have a global reflectance factor without coating of 0.5. Various shapes were selected, presented in Figure 45, among which a line pattern, a chess pattern, a "circle" pattern of shape quite similar to the halo PSF, and a random pattern of rather high spatial frequency.

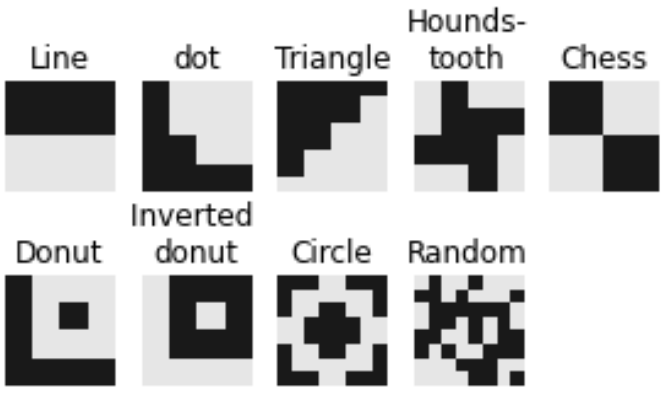

Figure 45. Simulated halftone patterns, dark areas have a reflectance of 0.1 and clear areas have a reflectance of 0.9, (p = 8).

The simulated global reflectance factors of the various halftone shapes presented in Figure 45, predicted with the multi-convolutive model, are displayed in Figure 46 as a function of *d/p*, for a measurement geometry 0°:0°, specular excluded, which corresponds to an apparatus described in the next chapter.

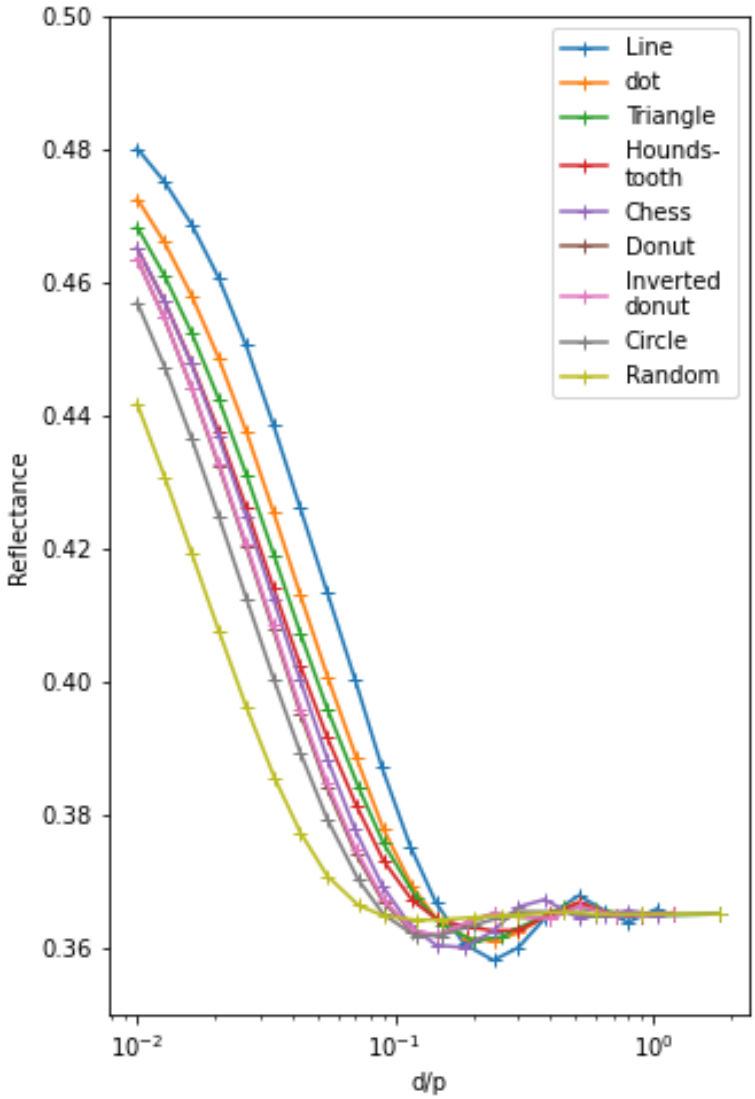

Figure 46. Average reflectance factor of various halftone patterns as a function of the ratio between the thickness of the coating layer d, and the period of the halftone screen p.

As expected, when the coating thickness tends to 0, i.e., $d/p \rightarrow 0$, the average reflectance factor gets closer to the bound of 0.5 for all patterns. Similarly, when $d/p \rightarrow +\infty$, the pattern period is so small with respect to the coating thickness that the halftone can be considered uniform and the halftone reflectance factors also reach the limit of 0.37 defined by the Williams-Clapper model. The results show that for $d/p < 0.1$, at a given d/p, patterns composed of small, dispersed dots are more darkened by the coating layer than patterns with few dot-dispersion. This is because light meeting patterns composed of small, dispersed dots can easily travel from one inked area to another one. For a small d/p, the overall halftone dot shape matters then less than the spatial frequency or perimeter of the small dots within it, this is particularly depicted by the fact that the curves of the donut and inverted donut are almost superimposed. Yet, the pattern presenting the overall strongest darkening is the line pattern. Indeed, for $d/p \approx 0.2$, it reaches a minimum below the reflectance factor limit given by the Williams-Clapper model which is due to the multiple convolutions between the halo shaped PSF and the line shapes.

In the simulations presented in Figures 45 and 46, the halftone screens have a binary reflectance distribution between inked and non-inked areas. In practice, light diffusion within the substrate can smoothen the spatial reflectance at the borders between inked and non-inked areas, making the intrinsic reflectance of the halftone, $\rho(x, y)$, vary continuously along the halftone profile. The second simulation was then designed to evaluate the impact of a coating layer on various halftone profiles, thus simulating various dot gains due to light scattering within the substrate.

3.7.3 Influence of halftone profiles

To simplify the problem, unidimensional line halftones have been selected, with different reflectance factor profiles displayed in Figures 47.a and 48.a. The first profile is a step, which would be observed with perfectly printed halftones not subject to dot gain, and the second profile is a sinusoidal one, which is a rough approximation of the profile observed on prints strongly impacted by the optical dot gain due to light scattering within the substrate. For comparison purposes, a triangular profile has also been considered in the simulations. The first set of profiles which were tested had all an identical range between the lowest reflectance factor value 0.1 and the highest value 0.9, as for the patterns shown in Figure 45. They are displayed in Figure 47 as well as the simulation results for the 0°:0° geometry, specular excluded.

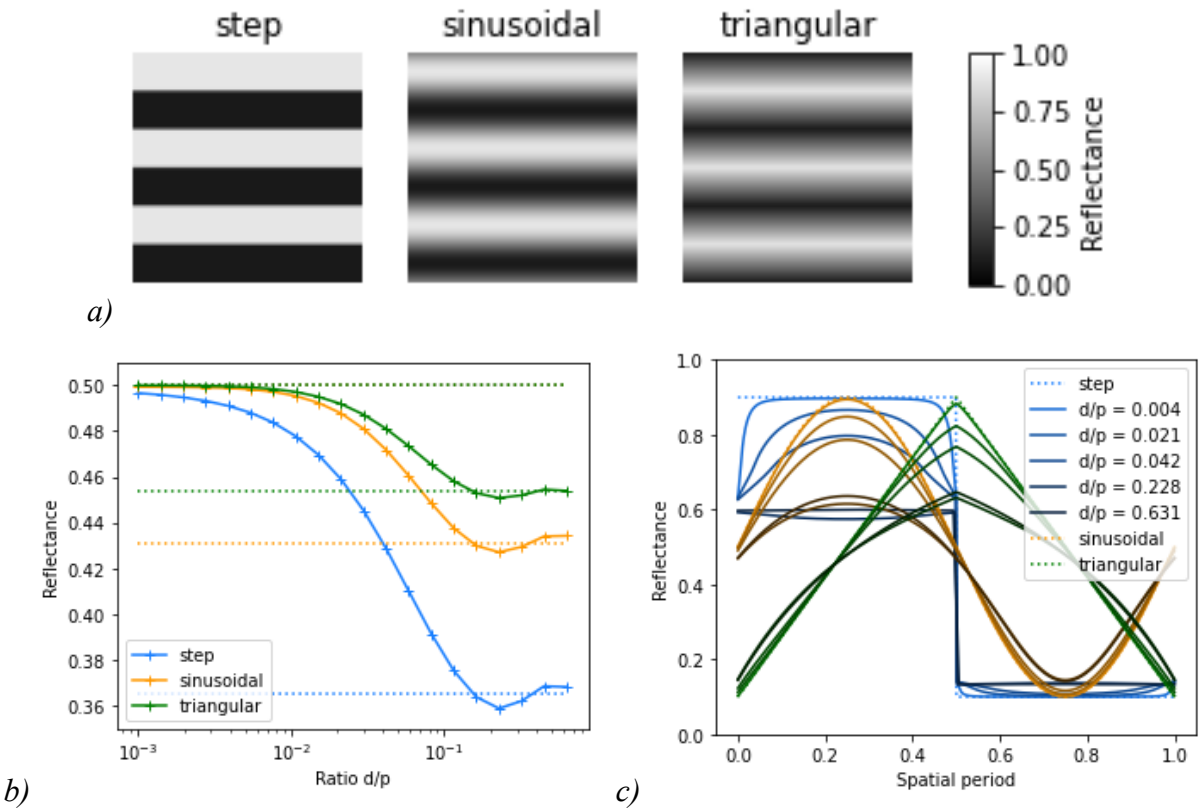

Figure 47. a) Simulated line profiles, step, sinusoidal, and triangular, of reflectance factor range]. b) Average reflectance of the line halftone of various profiles as a function of d/p, dotted lines show the limits when d/p→0 and when d/p→∞; c) Spatial reflectance profile of line halftones over one period for various d/p.

With this simulation, it can be seen in Figure 47.b that the limits when $d/p \to \infty$ are not the same for all the profiles. This is explained by the non-linearity of the Williams-Clapper model with the reflectance factor. Thus, the triangular and the sinusoidal profiles are less darkened than the sharp-edged profile.

To be able to compare the profiles, the ranges of the sinusoidal and of the step profiles have been manually fitted to get the same overall reflectance factor limit when d/p tends to infinity as the one obtained for the triangular profile. For the sinusoidal pattern, the reflectance factor range was set between 0.17 and 0.83, and for the step pattern, it was set between 0.27 and 0.74. Therefore, all profiles presented the same spatial average of the intrinsic reflectance, $\overline{p}$, equal to 0.67, and the same limit of R as d/p tends to zero. The adapted halftone profiles and the simulation results are presented in Figure 48.

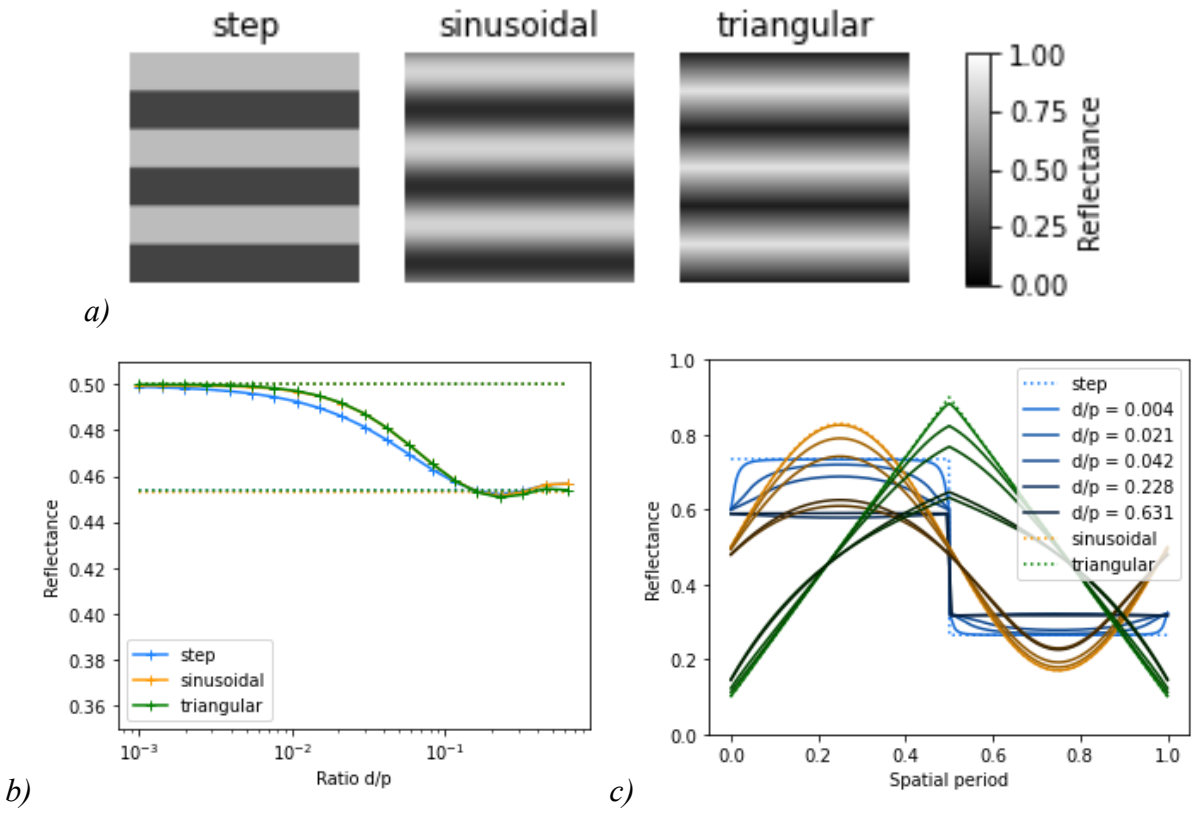

Figure 48. a) Simulated line profiles, step, sinusoidal, and triangular, of respective reflectance range [0.27; 0.74], [0.17; 0.83], and [0.10; 0.90]. b) Average reflectance of the line halftone of various profiles as a function of d/p; c) Spatial reflectance profile of line halftones over one period for various d/p.

These graphs enable to see the darkening effect caused by the halation phenomenon, both on the global reflectance factor and on the spatial reflectance factor of the print. It can be observed that the step profile is more impacted by the halation phenomenon than the other profiles: it intervenes for smaller d/p than for the triangular or sinusoidal profiles, Figures 48.b. The sharp edges of the step profile smoothen significantly as light propagates farther within the coating

layer, whereas the impact on the sinusoidal profile is mainly on the amplitude of the reflectance factor, Figure 48.c. The darkening of the clear areas is slightly compensated by an increase of reflectance of the dark areas as the coating enables light to propagate from inked areas to non-inked areas as well as the other way around. There is still yet a global darkening of the prints as light has more probability to reach an absorbing area when the print is coated than when it is not.

To conclude, these simulations showed that both the halftone shape and profile have an impact on the darkening caused by the addition of a coating layer, as well as the surface coverage. Line halftones can be the most impacted by the coating layer, and, at a given coating thickness, the color change is happening at a smaller period than the other shapes. It can also be concluded that a print subject to a lot of dot gain within its substrate will be less impacted by the halation phenomenon than the prints less subject to dot gain having a sharp profile, see Figures 48.b. The simulation results along with an application detailed in Section 5.1.2 were shared through a conference paper [155]. These simulations were performed on achromatic simulated prints but can be applied to colored prints by considering the spatial reflectance independently at each wavelength.

3.8 Rough interface

In the modelling, simulations, and experiments previously presented, the interface with air of the coating layer was assumed to be perfectly smooth. Therefore, light reflected at the interface propagated in directions completely defined by the incident direction on the interface, in a mirror-like manner. If the coating is matte, i.e. the air-coating interface is rough, the direction of the reflection at the interface can be modified which can have an impact on the halation phenomenon.

When the coating layer is matte, the color usually becomes lighter and less saturated than on the glossy coated print [156]. In the case of uncoated halftone prints, it has been shown that the air-print interface roughness has almost no impact on the flux transfers at the interface, therefore no impact on the print spectral reflectance, except light that can be externally scattered by the interface itself towards the observer, which explains the brightening observed for matte coatings, [156], [157].

The objective of this subsection is to model the impact of a rough interface on the halo-shaped internal reflections in order to be able to predict the darkening caused by a matte coating layer. A first paragraph is dedicated to simulations of the halation phenomenon for rough interfaces through a microfacet model, the simulation results are compared to an experiment in a second point. The third paragraph presents simulations of the effect of a matte coating on the appearance of printed halftones.

3.8.1 Modelling the halo with rough interfaces

Let us consider that the coating layer is matte, i.e. its interface with air is rough. This roughness can be modelled by considering the interface to be composed of small planar areas, microfacets, of various orientations compared to the normal of the mean surface (assumed to be flat). The direction and proportion of light internally reflected by the interface not only depends on the angle of incidence of light on the interface, but also on the orientation of the local microfacet. This can thus have an impact on the halo phenomenon which can be simulated using a bi-directional reflectance distribution function (BRDF) model [158].

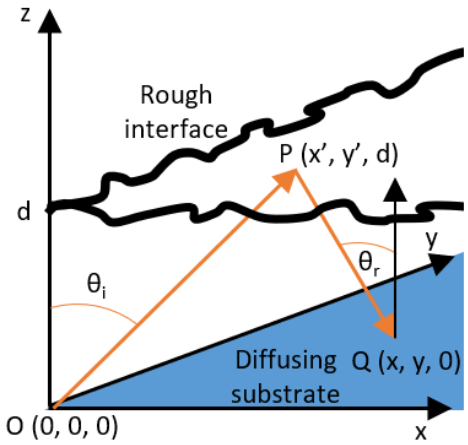

Figure 49. Scheme of the system. The diffusing substrate (in blue) is covered with a matte coating layer of average thickness d. *Its rough interface with air is represented by the bold crooked lines. Points* O *and* Q *belong to the substrate plane, and point* P *belongs to the interface between coating and air.*

We consider an orthonormal system (x, y, z) where $(x, y, z = 0)$ is the plane of the Lambertian substrate of normal parallel to the z axis, and $(x, y, z = d)$ is the average plane of the rough interface between the coating layer and air, see Figure 49. Supposing a small area A around a point O of the substrate, of coordinates (0, 0, 0), has an exitance M_0, it has a radiance $L_0 = M_0/\pi$ in every direction of the hemisphere. This produces an irradiance $h_{interface}(x', y')$ on a small area $dx'dy'$ of the rough interface around a point P of coordinates (x', y', d):

$$h_{interface}(x', y') = \frac{L_0 d^2 G(0, x', y')}{dx'dy'} \qquad 99$$

where $d^2G(x', y')$ is the geometrical extent between areas A and $dx'dy'$:

$$d^2G(x', y') = \frac{A dx' dy' \cos^4 \theta_i}{d^2} \qquad 100$$

where θ_i is the angle between $\overrightarrow{OP}$ and the normal of the substrate plane, $\cos\theta_i = \sqrt{d^2/(x'^2 + y'^2 + d^2)}$. The irradiance around P is then:

$$h_{interface}(x',y') = \frac{M_0 A \cos^4\theta_i}{\pi d^2} \quad 101$$

The radiance $L(x,y,x',y')$ from the small area around P reaching a small area *dxdy* around a point Q (x, y, 0) of the substrate can be described using a BRDF function f_r which depends on $\overrightarrow{\boldsymbol{OP}}$ and $\overrightarrow{\boldsymbol{PQ}}$, and on a roughness parameter m:

$$L(x,y,x',y') = f_r\left(\overrightarrow{\boldsymbol{OP}},\overrightarrow{\boldsymbol{PQ}},m\right)h_{interface}(x',y') \quad 102$$

Function f_r, described in [64] pp.190-192, accounts for a gaussian microfacet slope distribution, and a roughness parameter $m = \sigma/\tau$ where σ is the r.m.s. height of the rough interface, and τ is its correlation length.

The irradiance around Q due to light reflected around P is:

$$d^2 h_{rough}(x,y) = \frac{L(x,y,x',y')\cos^4\theta_r}{d^2}\,dxdy \quad 103$$

where θ_r is the angle between $\overrightarrow{\boldsymbol{PQ}}$ and the normal of the substrate plane:

$$\cos\theta_r = \sqrt{\frac{d^2}{(x'-x)^2+(y'-y)^2+d^2}}.$$

The total irradiance in Q coming from all points of the rough interface is then:

$$h_{rough}(x,y) = \int_{y=-\infty}^{\infty}\int_{x=-\infty}^{\infty}\frac{L(x,y,x',y')\,cos^4\theta_r}{d^2}dx'dy'$$

$$= \frac{M_0 A}{\pi d^4}\int_{y=-\infty}^{\infty}\int_{x=-\infty}^{\infty} f_r\left(\overrightarrow{\boldsymbol{OP}},\overrightarrow{\boldsymbol{PQ}},m\right)\,cos^4\theta_i\,cos^4\theta_r\,dx'dy' \quad 104$$

From this equation can be modelled the halos of rough interfaces. The irradiance profiles at the center of the halos for different roughness parameters, m, are displayed in Figure 50.

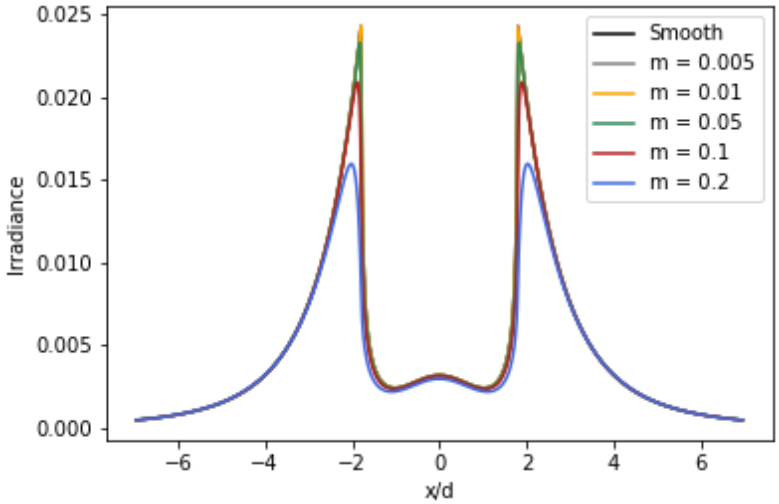

Figure 50. Profiles of the modelled halos, with an initial exitance at the central point equal to unity.

The striking information lays in the fact that the profile of the halo is very similar whether the interface is smooth or rough, the curves are almost superimposed for $m < 0.01$. The roughness of the interface tends to decrease the sharpness of the profile, but a halo is still clearly visible. However, the profiles described by the model for high roughness are in fact inexact as the BRDF model does not take into account multiple reflections between neighboring microfacets, which tend to artificially reduce the total fraction of light reflected by the interface (fraction often denoted r_i in classical print reflectance models, around 0.6 for $n_1 = 1.5$). This limitation has already been described and quantified in [159].

Equation (104) describes the ring-like irradiance on the substrate caused by one reflection at the coating-interface. This light is scattered again by the substrate, generating another ring-shaped irradiance pattern on the substrate, and so on, in a similar way as described in Section 3.2, where h is replaced with h_{rough}.

3.8.2 Experimental observation of the halo with a matte coating

The objective of this section is to observe experimentally the impact of a rough interface on the halo and to compare it to the modelled results described in the first part. An experiment was performed at the macroscale, where a laser beam illuminated a white diffuser alternately coated with a layer of smooth and rough interface with air. The resulting halos were captured with a camera. The scheme of the setup is displayed in Figure 51.a.

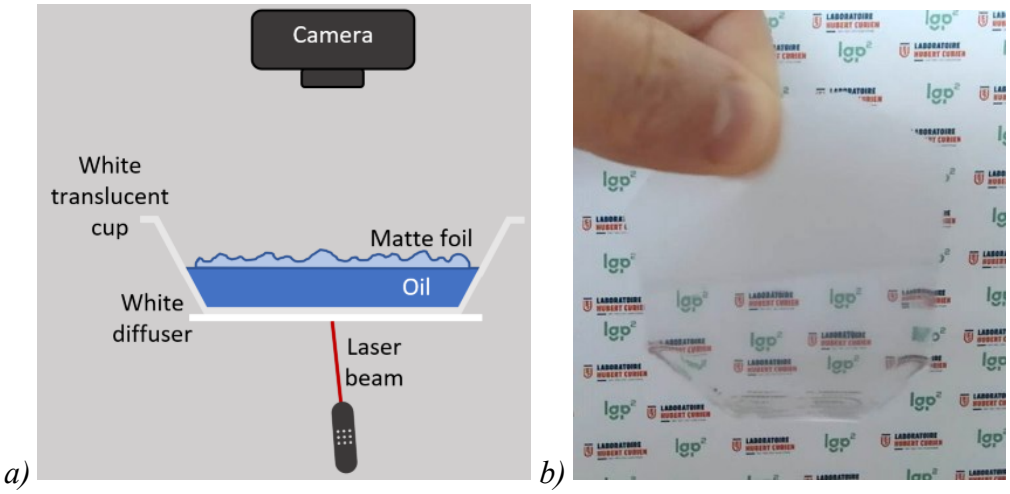

Figure 51. a) Scheme of the setup. b) Picture of the matte lamination foil, the bottom part is covered by oil.

The camera was a Sony ILCE-6000, identical to the one used for the experiment in Section 3.4, capturing images in RAW format, with an exposure time of 1/3 s, an ISO of 400, and an aperture F/5.6. The laser was a red pointer illuminating the white diffuser from beneath to prevent disruptions due to the coating interface. The diffuser was a uniform white paper stuck to the external surface of the flat bottom of a white translucent cup. The coating layer consisted in an oil layer, of optical index close to 1.5, which had a smooth interface with air. The rough

interface with air was generated by floating a matte lamination layer on the oil surface. The lamination layer was 27 µm thick, measured with a micrometer from Adamel Lhomargy, which is negligible in comparison to the thickness of the oil layer which was millimetric. Since the optical index of the lamination layer is close to the one of oil, the two layers are in optical contact, i.e. the interface between them is optically neutral. This optical index matching and the transparency of the lamination layer were checked by dipping the lamination layer in oil: the lamination layer then became transparent as its interface with air became smooth, as shown in Figure 51.b.

For both rough and smooth interfaces, the experiment was performed with two different oil thicknesses. The pictures, issued from the red channel of the camera, are displayed in Figure 52. The thicknesses were retrieved from the position of the maximal digital count of the halo of the smooth interfaces, taking into account the diameter of the laser spot [143] p.92:

$$\mathrm{d} = \left(\frac{\Phi_i}{2} - 0.4\Phi_{laser}\right)\left(\sqrt{n_1^2 - 1}/2\right) \tag{8}$$

where Φ_{laser} is the diameter of the laser spot, which was around 2 mm, and where Φ_i is the diameter of the ring of maximal digital count. The thicknesses were found to be respectively 3.4 mm and 6.8 mm.

The pictures show that even though the interface with air is rough, there is still a ring-like halo. It only appears blurrier than the one with a smooth interface. This confirms the conclusions from the modelling of the first section: rough interfaces induce a similar halo phenomenon as smooth interfaces.

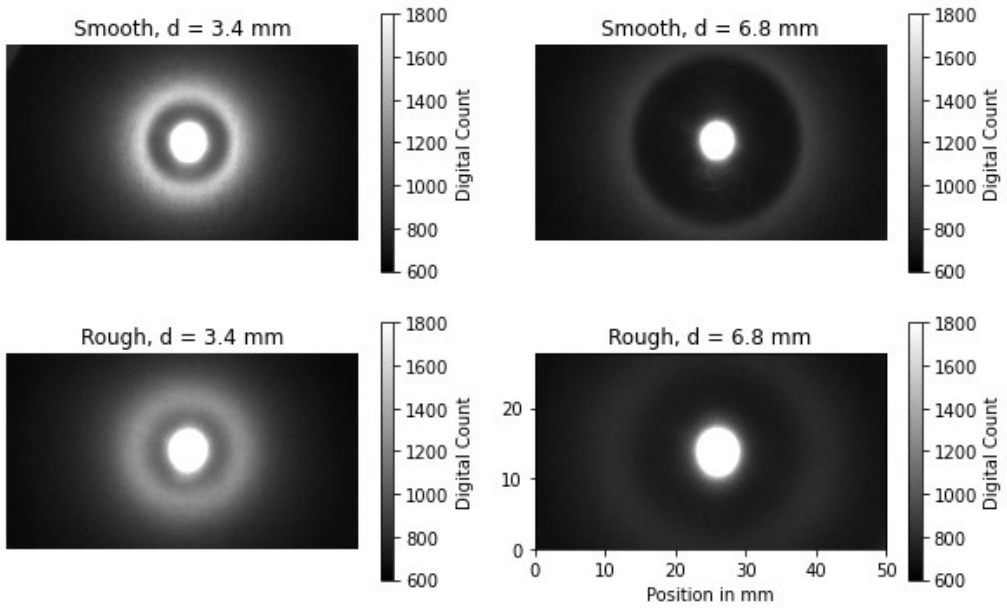

Figure 52. Pictures of the halo induced by a smooth and a rough interface with air for two different coating thicknesses.

From this experiment and the modelling, we can try to deduce the roughness parameter of the matte coating. Knowing the layer thicknesses, the theoretical function *h* related to the smooth interface can be retrieved for each thickness from Equation (68). Amplitude factor and offset were manually fitted to get values comparable to the digital counts: the amplitude coefficient was set to $5.2 \cdot 10^5$, and the offset, linked to light diffusion on the substrate, was set to 645 (in pixel value). Knowing these parameters and the thickness of the two layers, the halo induced by a rough interface can be calculated through the model presented in the previous section. The roughness parameter, *m*, was then fitted to the experimental curve; *m* was found to be around 0.22, the resulting experimental and theoretical curves are displayed in Figure 53.

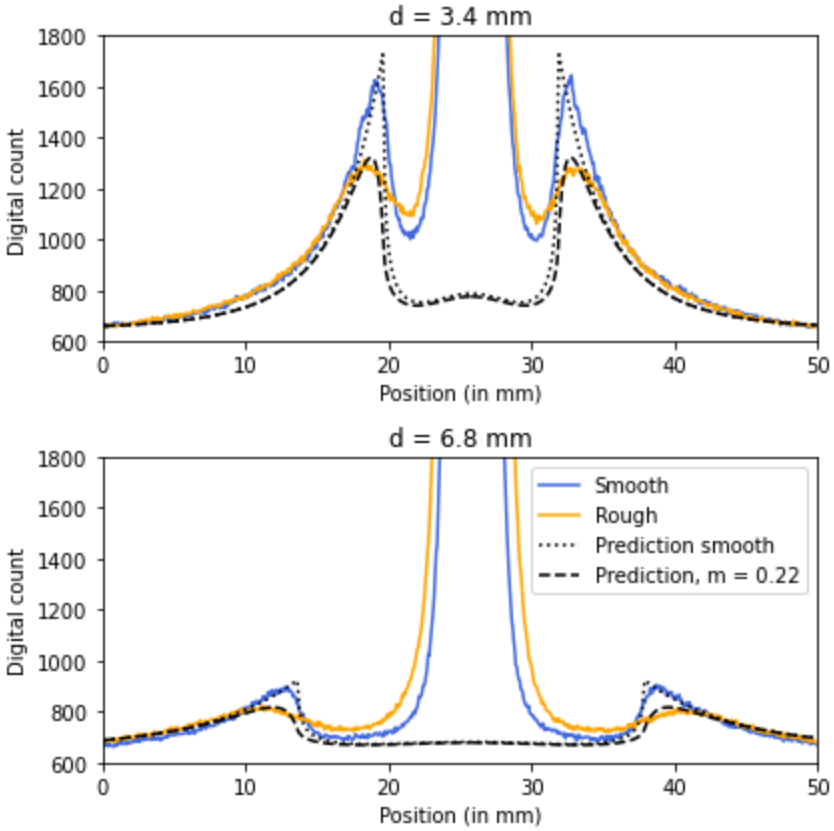

Figure 53. Profiles for each thickness, the black lines are modelled respectively through Equation (68) for the smooth interface, and Equation (104) for the rough one.

This is a rough estimation which could be better evaluated by considering the actual laser beam diameter in the multi-convolutive model, in place of a punctual illumination. The halos in the images also result from multiple interreflections between the substrate and the interface and are imaged through the interface which, in the case of the rough interface, can increase the blur of the halo (Figures 52 and 53). It is then likely that the roughness of the foil was overestimated. In any case, it has been shown that the halo phenomenon is similar whichever the roughness of the transparent coating. The previous studies on glossy finishing, presented in Sections 3.4, 3.5, 3.6, and 3.7, show that the color change of a print which is coated is mainly dependent on the

ratio between the halo diameter and the halftone period. In the case of a rough coating, simulation and experiment show that the halo overall shape and diameter is unchanged as for a rough coating, similar color prediction methods can then be used for both surface finishing.

3.8.3 Simulation of appearance of coated halftones

The objective of this part is to extend the appearance prediction of coated prints to rough interfaces. The simulation and experiments detailed in this section were the object of a conference paper [160]. Concerning the light fluxes at the interface with air, displayed in Figure 12, it has been shown that T_{in} and T_{out} are almost identical whether the interface is rough or smooth, [157]. The rough interface only has an impact on r_s (i.e., the light portion externally reflected by the interface towards the sensor), and, to a lesser extent, on the sharpness of the halo PSF. For these simulations, it has been considered that the roughness parameter was m = 0.2, which corresponds to a high roughness, a limit roughness value for a matte finishing, that the thickness of the coating layer was d = 20 µm, and that the error on r_i mentioned in the first part was equally compensated on each pixel of the rough halo image. The appearance for a smooth interface was also simulated with the same coating thickness for comparison purposes. The spatial and spectral reflectance factors of the non-coated prints chosen as inputs for the simulations were the one of a fulltone magenta patch and the one of a line magenta halftone patch of period 0.337 mm. The method used to estimate them is explained in Section 4.1.

Even though the situation where r_s = 0 is usual for prints with a glossy coating by looking at them in the non-specular direction, it is far less usual for a print coated with a matte foil as light is scattered externally in every direction by the coating surface and eventually reaches the sensor. To evaluate r_s in the case of a matte coating for a d:8° geometry, the reflectance factors of both a glossy and of a matte coating were measured with the spectrophotometer CM-2600d from Konica Minolta specular component excluded, with an aperture of 8 mm diameter. To prevent the influence of the bottom interface of the coating layers, it was colored in black with multiple layers and set in optical contact with a black paper. The measured reflectance factors are displayed in Figure 54. The parameter r_s was calculated as the average difference between the reflectance factors of the rough and of the smooth interfaces. It was found to be equal to 0.03 over the whole spectrum. The measurements with a di:8° geometry are also displayed, it can be noted that for the glossy coating, the difference between the specular included and excluded measurements is rather high and corresponds roughly to 0.04, which can be verified theoretically with Fresnel's formula. For the matte coating, the difference between the specular included and excluded measurements is small, which tends to show that the surface reflection on the matte coating is mostly diffuse. This method to evaluate the r_s parameter might be dependent on the spectrophotometer sensor and secondary light source geometry, as well as on automatic data treatment by the spectrophotometer, it thus only serves to get a rough estimation of this parameter.

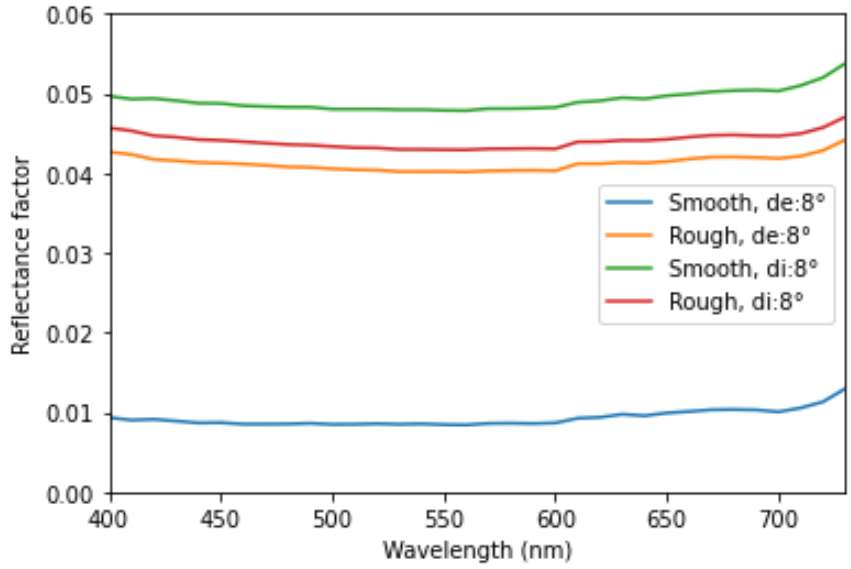

Figure 54. Reflectance factor of matte and glossy coatings over a black substrate, used to estimate the r_s parameter in the case of a matte coating.

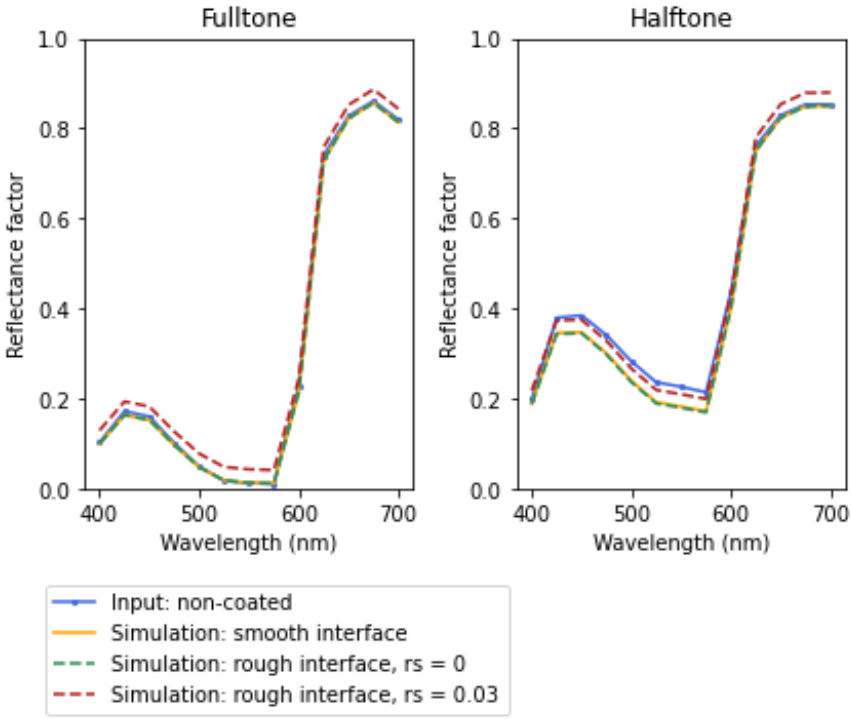

Figure 55. Modelling of the effect of matte and glossy coatings on the reflectance factor of magenta prints.

Figure 55 displays the resulting spatially averaged reflectance factor of the tested patches for the different interfaces and, in the case of the rough interface, for $r_s = 0$ and for $r_s = 0.03$. The blue lines correspond to the spectral reflectance factor of the non-coated prints. The yellow lines describe the simulated spectral reflectance factor of the prints coated with a glossy finishing layer. The reflectance factor of the halftone decreases at the spectral bands at which

ink absorbs the most, which results in a darkening and saturation of the color visually perceptible. The green lines correspond to the spectral reflectance factor of the prints predicted by the multi-convolutive model by considering a very rough interface with air. It is shown that the prediction for the smooth and the rough interfaces are almost similar, which is explained by the fact that the prints are subject to similar ring-like interreflections within the coating layer. The red lines present the same prediction and includes the surface reflection component, r_s = 0.03. This increases the spectral reflectance factor uniformly over the whole spectrum, which lightens colors, making them comparable to the ones of the non-coated prints with a slight loss of saturation.

3.9 Conclusion

In this chapter, an optical multi-convolutive model has been proposed to predict the impact of the addition of a coating layer on the reflectance of a halftone print. It is based on reflection of diffuse light at a distance from the substrate, that provokes lateral propagation of light within the layer and illuminates back the substrate according to a ring around each point of the substrate from which light emerges. This phenomenon was first observed in astronomical photographs and put into equations by Simonot and co-workers [6]. This phenomenon enables light to propagate between differently colored areas of the print. It increases the probability for light to meet an absorbing area and thus induces a darkening and saturation of the print color, even though the transparent coating layer is perfectly clear. This color change depends on the thickness of the coating layer, and on the spatial distribution of the reflectance factor of the print. If the variations of the reflectance factor distribution are small in comparison with the coating thickness, a reflectance limit is reached, described by the Neugebauer model. On the contrary, if the variations are large with respect to the coating thickness, another limit is reached, described by the Williams-Clapper model extended to halftone colors. The multi-convolutive model enables to predict the reflectance of prints of period and coating thickness such that the print reflectance is between the two limits. The multi-convolutive model has been verified in two experiments where the halo-phenomenon was the only physical phenomenon at stake; the optical dot gain due to the substrate was negligible in these experiments. The two experiments were performed with completely different materials, which shows that the multi-convolutive model is rather robust.

Several simulations were performed to evaluate the impact of various parameters of the multi-convolutive model on the darkening induced by a clear layer. Increasing the optical index of the coating layer intensifies the halo phenomenon and increases the darkening it causes. Concerning the halftone patterns: line halftone patterns of surface coverage around 0.5 with a step profile seem to be the most subject to a darkening caused by the addition of a coating layer, especially at a ratio d/p around 0.23, with d the thickness of the coating layer, and p the period of the halftone pattern.

An optical model has been developed to predict the Point Spread Function of a diffusing substrate coated by a transparent layer with rough surface, whose shape is a ring-like halo. The simulations show that rough interfaces cause a similar ring-like interreflections as smooth interfaces. This was verified by an experiment where the halo induced by a laser beam was captured by a camera for a smooth and for a rough interface. Therefore, the multi-convolutive model previously developed for halftones with a glossy coating can be used with matte lamination layers without lack of accuracy. The main color change difference between a print coated with respectively matte and glossy lamination foils lays in the difference of light externally reflected by the interface. The matte laminated prints are subject to the same darkening effect caused by the halo interreflections for a rough as for a smooth coating, but they usually appear lighter with a rough coating due to the light externally reflected at the interface.

A limitation of the multi-convolutive model lays in the fact that it relies on the spatial distribution of the halftone print reflectance. In the case where the print is not subject to dot gain, this spatial distribution is identical to the nominal printing layout, and the multi-convolutive model can be rather easily applied. However, if the print is subject to deformations caused by mechanical or optical dot gain, which is rather common as explained in Sections 2.1.2 and 2.1.3, the spatial reflectance factor distribution of the print needs to be determined to apply the multi-convolutive model, which can be complex as prints usually have microscale distributions. Next chapter aims at providing a solution to cope with this issue.

Chapter 4. Effect due to a clear coating on microscale halftone prints

An optical multi-convolutive model has been presented in Chapter 1. Section 3.2, which predicts the color change caused by the addition of a coating layer on a halftone print. This multi-convolutive model relies mainly on the spatial and spectral reflectance factor of the halftone print and on the thickness of the coating layer. It has been validated through experiments performed at rather large scales (centimetric and millimetric scales). However, in the printing industry, the reflectance of the halftone prints usually varies at a micrometric scale which makes it complex to characterize these variations. Indeed, the spectrophotometers traditionally used in the printing industry perform average print reflectance measurements over large areas compared to the micrometric variations of the print reflectance.

Furthermore, at this scale the printed halftone patterns are subject to dot gain which makes it complex to predict the variations of the print reflectance both in the spatial and in the spectral dimensions. As described in Sections 2.1.2 and 2.1.3, the dot gain is an effect causing the inked patterns to appear larger or deformed with respect to the nominal halftone patterns. It can have a mechanical origin due to the printing process and the ink-substrate interactions (i.e., mechanical dot gain) and an optical origin due to light propagation within the substrate (i.e., optical dot gain). Dot gain has an impact on the shape of the halftone patterns, on the contrast between the differently colored areas, and it tends to blur the edges of the printed patterns, the printed halftone patterns are thus different from the nominal ones.

Therefore, to apply the multi-convolutive model on classical halftone prints, a device is required to characterise the halftone reflectance at the microscale, both spatially and spectrally. For this purpose, during this work, an optical microscope has been converted into a multispectral microscopic reflectance measurement device, it is presented in Section 4.1. Section 4.2 and 4.3 presents respectively the method to predict the color change of microscale halftone prints when they are coated with a transparent layer, and the performances of the multi-convolutive model which were evaluated in two experiments where the prints were subject to the dot gain effect. In Section 4.4 is described the impact of dot gain on the color change induced by the addition of a coating layer. If the coating layer is matte, its rough interface with air can induce a blurring in the images of the print captured with the developed microscope device. To prevent the additional optical effect a matte coating layer could induce, in this chapter we focused on a glossy surface finishing.

4.1 Multispectral microscopic measurements

To characterize the spatial and spectral reflectance of a print at the microscale, an optical microscope was turned into a multispectral imaging device. As the spatial resolution of the reflectance factor was the crucial point, the staring approach was selected, which consists in scanning the spectral dimension over time, one picture being taken for each wavelength bandpass, as explained in Section 2.3.2. The microscope components and characteristics are described in Section 4.1.1. The device calibration method and the equations on which it relies are detailed in Section 4.1.2. Section 4.1.3 shortly presents the softwares which were developed to enable the measurements. To verify the quality of the measurements by this multispectral microscope, they were compared to macroscopic ones performed with a classical spectrophotometer, which is detailed in Section 4.1.4.

4.1.1 Hardware

In order to characterize the spectral reflectances of halftone prints at the microscopic scale, a custom multispectral imaging microscope was developed. The hardware, described in [25], is composed of a microscope, colored optical filters mounted on a wheel, and a commercial digital camera. The camera captures an RGB image through each optical filter of a wheel. The filters are of rather small wavelength bandwidth, which allows to reconstruct the multispectral reflectance of the sample for various wavelengths. The scheme of the setup is displayed in Figure 56.

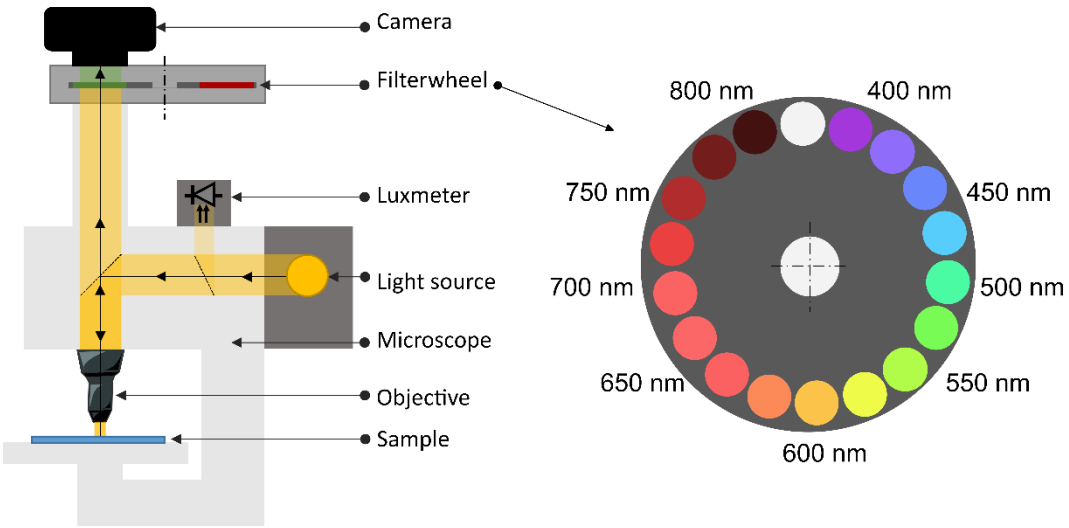

Figure 56. Scheme of the setup. (Imaging optics inside the microscope are not displayed).

The setup is composed of a microscope Zeiss Axio Imager M1 m mounted with the objective EC Epiplan Neofluar 5×/0.13 HD DIC [161]. To remove the specular reflections on the sample, a polarizer and an analyzer are used in a crossed configuration inside the microscope.

The light source within the microscope in reflection mode is a Zeiss HAL 100 tungsten-halogen lamp set at 3200 K; it was turned on at least 20 minutes before the experiments to reach the steady state. Its emission spectrum is stronger for large wavelengths than for small wavelengths. A luxmeter, Yocto-Light-V3 LIGHTMK3 from Yoctopuce, is inserted across the path of the incident light beam in order to calibrate the irradiance of the sample for each image capture. The photodiode, manufactured by Rhoms (reference BH1751FVI), can measure in the range of 0 to 100,000 lux with a resolution of 0.25 lux. As shown in Figure 57, the light source is rather stable over time, and the luxmeter helped to overcome small instabilities as it was taken into account during the measurement process.

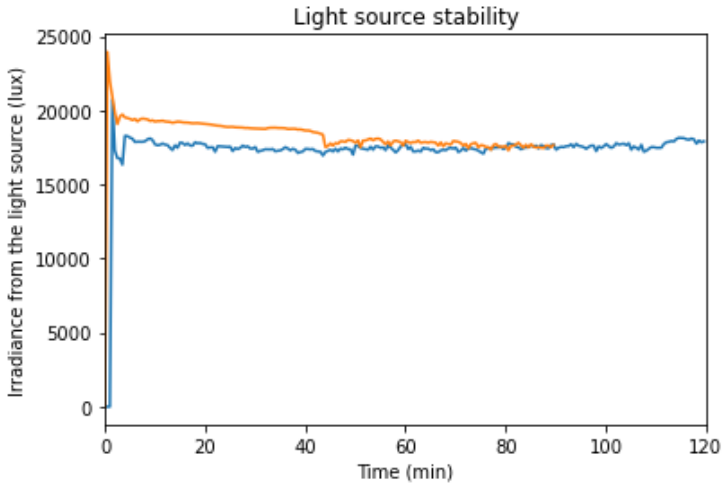

Figure 57. Stability of the light source 2 hours following its switching on, measured with the luxmeter.

The filterwheel is composed of 17 filters (Hard Coated OD 4.0 25 nm Bandpass Filters from Edmund Optics [162]) and driven by a motor. The camera captures at least one picture per filter with an adapted exposure time. The central wavelengths of the filters are in the range [400; 800 nm] with a 25 nm step. The filters have a 25 nm bandwidth. In practice, 13 filters are used in the range [400; 700 nm] corresponding to the spectral bandwidth of the light source.

The camera is a commercial reflex camera, Canon 1200D with a RGGB CMOS sensor [163]. The ISO was set to 800. The sensor, coded in 14 bits, has a dimension of 3516×5344 pixels, of approximate size 22.3×14.9 mm according to the manufacturer. As the response of the microscope was low for certain pixels of the Bayer matrix according to the studied wavelength (for instance for the red Bayer filter coupled with a blue optical filter), one pixel of the Bayer matrix was selected for each considered filter of the filterwheel, dividing the resolution of the pictures by 2 in each dimension. (For the green pixels of the Bayer matrix one of the two position was arbitrarily selected). Moreover, the non-imaging part of the sensor was cropped. In the end, the resulting pictures had a dimension 1728×2592 pixels.

A black light-shield was set around the sample plate of the microscope to prevent ambient light to disrupt measurements.

The linearity of the pixel values with exposure time was verified by capturing a white paper with all the exposure times available on the camera for various tensions of the light source. The average value in the dark of each pixel at each exposure time (i.e., the blackframe V_k, further detailed in Section 4.1.2) was subtracted from the captured images. The measurements were performed two times and the average pixel values of each color channel are displayed in Figure 58. It can be noted that the variations can be due to the variations of the light source, indeed, when the voltage of the light source is set at 3200 K, its tension is stabilised at 10.7 V, and for this tension, the results show smaller variations.

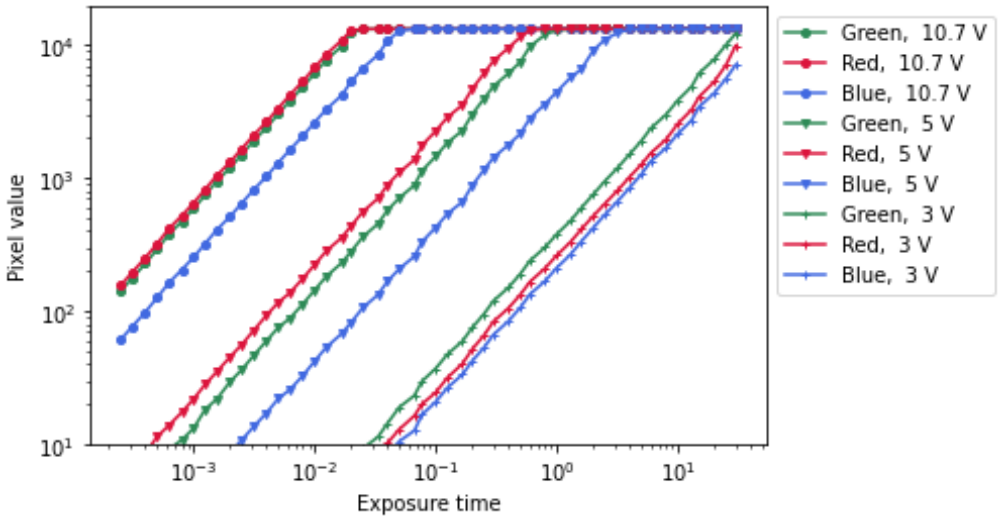

Figure 58. Linearity of the pixel value of the camera as a function of the exposure time for various light source tensions and for each color channel of the Bayer matrix.

The accuracy of the pixel values of the camera was evaluated by capturing six times a white sample for each exposure times. Once again, the average pixel value in the dark for each pixel location and each exposure time, V_k, described in the next section, was subtracted from the measurements. The pixel value coefficient of variation averaged over the pixel locations is displayed as a function of the pixel value in Figure 59. The overall pixel values ranged approximately between 0 and 14 000. The coefficient of variation was rather high for low pixel values, which can be caused by pixel noise and by the inaccuracy over the exposure time which might be stronger for low values. On the contrary, the coefficient decreased for high pixel values: as the sensor saturated, the pixel values were capped at the maximal value. In the measurements, to prevent sensor saturation, pixels outside the [100; 12 000] value range (figured by the grey dotted lines in the graph) were discarded; they were set as NaNs (Not a Number).

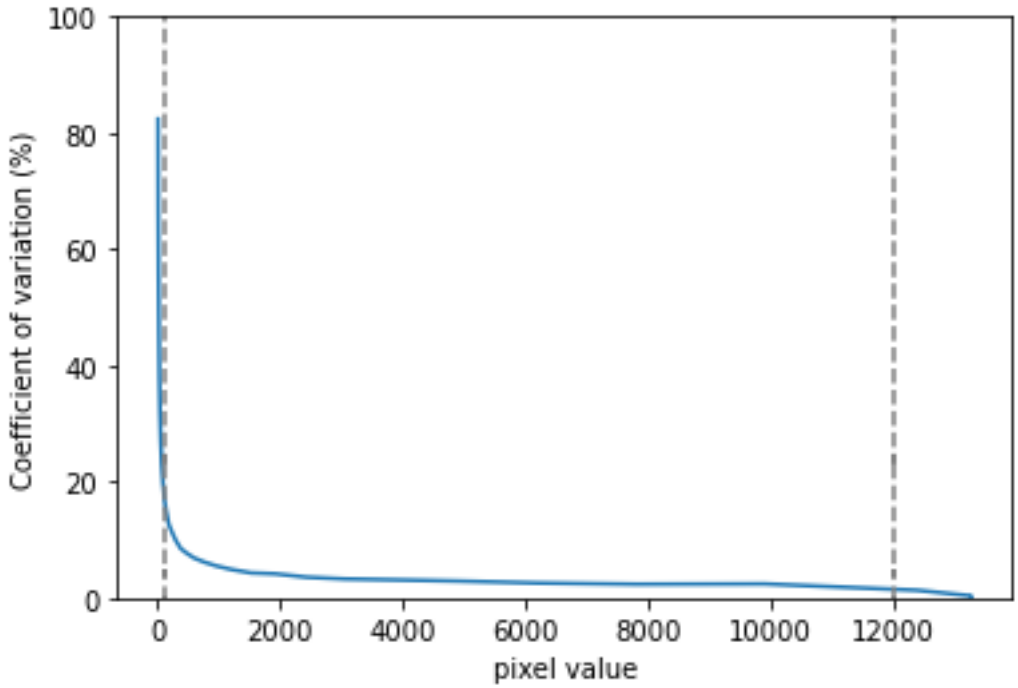

Figure 59. Coefficient of variation of the pixel values as a function of the pixel values.

The spatial resolution of the system was evaluated by capturing pictures of a graduated target of 1 mm length. Four pictures were captured with the target image located at the center of the sensor, and four at the corners of the sensor, the camera focus was made at the central part of the pictures. In average, the 1 mm target was imaged with 721.4 pixels. The resolution is 1.386 µm/pixel, (where one pixel is composed of four Bayer subpixels). This experimental resolution did not match with the theoretical resolution which can be calculated from the objective magnification, the size of the sensor and number of pixels of the sensor. Further additional experiments with the objectives $\times 10$ and $\times 20$ of the microscope confirmed that the system behaves as if an additional lens of magnification 1.21 is contained within the imaging system.

We identified two optical aberrations in the imaging system: Petzval field curvature and chromatic aberration. The corners of the pictures were slightly blurred, and items showed red edges at the centre side and blue edges in the outer side. Therefore, in the experiments, images were cropped to the centre of the pictures.

4.1.2 Calibration to retrieve reflectance factors from pixel values

To retrieve the spatial and spectral reflectances of a sample from the pixel values obtained through the camera, the apparatus is calibrated as follows. One pixel value is related to reflectance through [164]–[167]:

$$V = Te \int_{\lambda} E(\lambda)\, F(\lambda) B(\lambda) s(\lambda) R(\lambda) d\lambda + V_k \qquad 105$$

where V is the pixel value associated with one optical filter, T is the exposure time, e is proportional to the irradiance on the sample, measured with the photodiode, E is the spectral

power distribution of the light source, F is the spectral transmittance of the filter, B is the spectral transmittance of the Bayer filter, s is the spectral response of the sensor, R is the reflectance of the sample associated with the considered pixel, λ is the wavelength, and V_k is a constant corresponding to the pixel value in the dark. T is monitored by the computer and can be retrieved in the metadata of the pictures

E, F, B, and s are intrinsic to the device and complex to measure as they can depend on the spatial position of the pixel. If R is constant within the spectral bandwidth of the filter, Equation (105) becomes:

$$V = R(\lambda')TeQ + V_k \tag{106}$$

where $R(\lambda')$ is the reflectance of the sample at the central wavelength of the filter, λ', and Q is:

$$Q = \int_{\lambda} E(\lambda)\, F(\lambda)\, B(\lambda)\, s(\lambda)\, d\lambda \tag{107}$$

V_k and Q can be evaluated during the calibration of the system, the method is explained below.

The reflectance of any sample can then be determined from its pixel value V:

$$R(\lambda') = \frac{V - V_k}{TeQ} \tag{108}$$

To calibrate the system, the value of each pixel of the camera in the dark, V_k, was determined once for ever by capturing pictures in the dark for each exposure times. The results, for each exposure time and for each pixel, were averaged over 9 measurements and were used afterward to calibrate all measurements. The average pixel value in the dark was 2047 ± 11, the average pixel value for each exposure time is displayed in Figure 60.

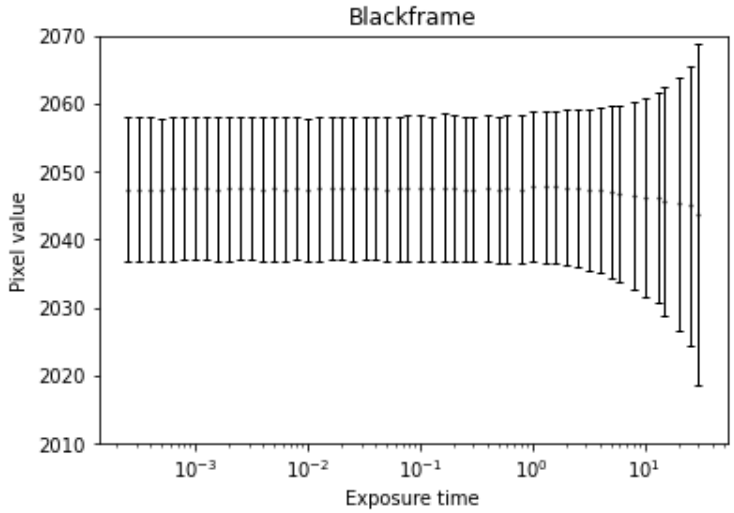

Figure 60. Average pixel value of the blackframe for each exposure time. The error bars are the average standard deviations of the 9 measurements over all the pixels.

The measurement of Q was made for each series of measurement through the capture of an opal glass spectralon (Commission of the European communities, community bureau of reference BCR, reference material number 406, individual identification number 0004), pictured in Figure 61.a [113]. Q was derived, for each filter and for each pixel position from:

$$Q = \frac{V_c - V_k}{R_c(\lambda')T_c e_c} \qquad 109$$

Where V_c is the pixel value of the captured spectralon, T_c the exposure time of this capture, e_c the value from the luxmeter for this capture, and $R_c(\lambda')$ is the spectral reflectance of the opal glass spectralon at the central wavelength of the considered filter, λ'. This reflectance was determined through a measurement with a spectrophotometer, CM-2600d from Konica Minolta, with a di:8° geometry, including a UV cutoff filter, and an aperture of 8 mm diameter. It was measured 10 times and showed negligible uncertainties. The resulting average reflectance spectrum is displayed in Figure 61.b. For one filter, the reflectance at the central wavelength, R_c, was the average reflectance over the 25 nm bandpass of the filter. The specular component of this spectrophotometric measurement (which is not included in the microscopic measurement) was removed by subtracting 0.04 to R_c. The entire process was repeated at least four times and the final Q value is the average of the four computed Q values for each pixel position.

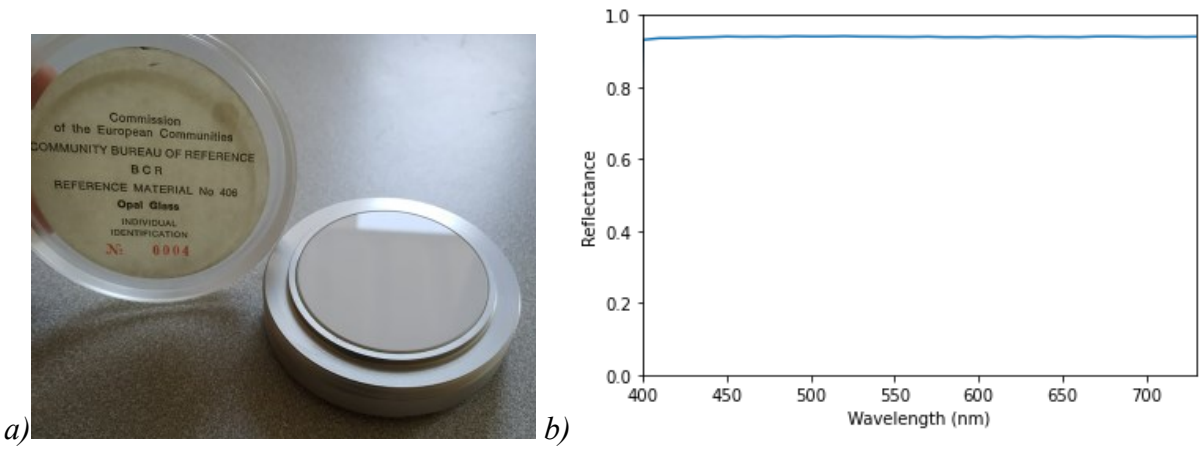

Figure 61. a) Picture of the glossy white spectralon used for calibration. b) Reflectance spectrum of the spectralon (d:8°), specular component included.

4.1.3 Software

Two Graphical User Interfaces (GUI) were developed in Python programming language to facilitate measurements and make them user friendly. The first one was designed to manage the hardware for the measurement and calibration processes, it is displayed in Figure 62 and the second one was designed to convert the captured images into spatial and spectral reflectance factors, displayed in Figure 63. These interfaces were initiated in a previous PhD project [25],

and were functionalised during this work, partly through a six-month internship project conducted by Léo Condamine.

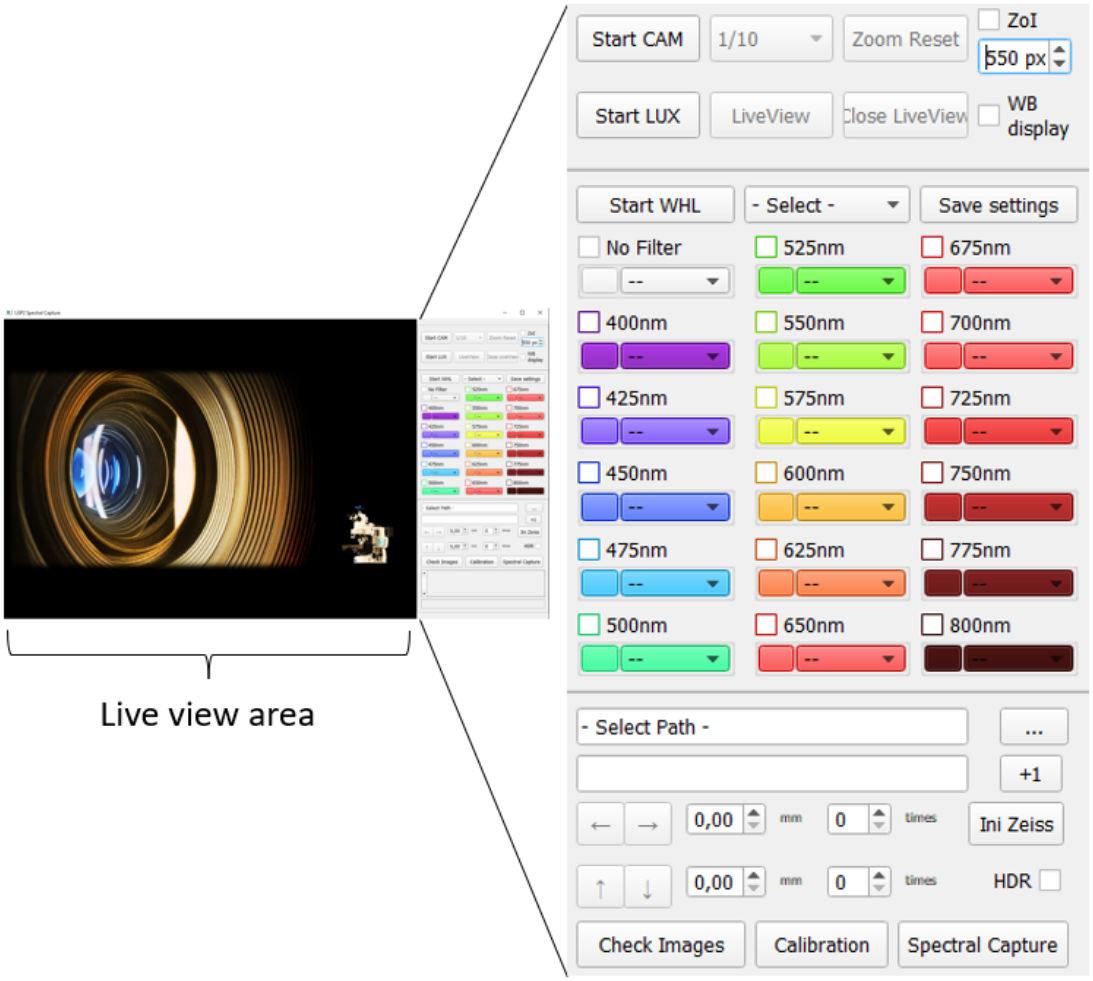

Figure 62. Graphical User Interface manage the hardware to capture images for the calibration and for the measurements.

The first interface aims at capturing and saving raw pictures of the samples and of the calibration spectralon through various optical filters and with one or two exposure times. It coordinates the different instruments and remotely control them.

Several buttons are dedicated to initiate communication between the computer and the hardware devices: *Start CAM* to start the communication with the camera, *Start Lux* to initiate the communication with the luxmeter, *Start WHL* to start the communication with the filterwheel and initialise its position, and *Ini Zeiss* to start the communication with the microscope plate and initialise its reference position (this starting button is optional, one can also manipulate by hand the sample-plate, in this case the microscope may not be plugged to the computer). The *LiveView* button can be pushed to display in real time what the camera detects on the display area on the left of the command panel. Live View must be closed to start measurements.

The middle panel allow to tick for the optical filters which are needed for the measurements, and a scrollable list allow, for each filter, to select an exposure time. These settings can be saved and uploaded with the -*Select*- list. If the *HDR* checkbox is selected, two exposure-time settings can be selected to capture each image with two different exposure times. The -*Select Path*- line and the line underneath it allow to select a saving folder path and give a name to the measurements, respectively. For each measurement session two folders should be created: one for the calibration pictures and one for the measurement pictures.

The *Calibration* button launches automatic calibration measurements: the spectralon need to be on the sample plate of the microscope, the light beam illuminating it close to its center, and the focus of the microscope must be set on its surface. The number of desired measurements can be entered, and the program automatically moves the sample plate between each measurement to capture a different area of the spectralon. This method prevents local calibration issues due to dusts on the spectralon.

If the microscope was unplugged for the measurements, which has been the case for the experiments in this work, the *Spectral Capture* button enables the picture captures of any sample, potentially in HDR mode. Previously, the focus needs to be manually set with the live view. If the microscope is connected, the focus can be performed automatically. Series of automatic measurements for several patches on a test form can also be performed by selecting the arrows according to the measurement direction, entering the spacing between the patches in the x and y axis in millimetre, and the number of patches on each axis. These two last options (automatic focus and automatic series of measurement) require further testing to be fully reliable. For each patch and each exposure-time setting, the filter wheel rotates to position the next optical filter, the exposure time is set on the camera, the value from the luxmeter is saved, the picture is captured, and it is saved. Afterwards, the wheel moves to its next position and the process repeat itself until all the selected optical filters have been used. This process is repeated two times if the HDR mode is selected and the pictures for each exposure time are saved.

Check images allow to display in the Python kernel the saved images, this function is useful to verify that the exposure time was well adapted and to see where the sensor saturates.

The second interface, displayed in Figure 63, aims at doing the calculations to get, for each measured patch, a 3D dataset containing the spatial and spectral reflectance factor values, from the data saved using the first interface. The two interfaces were not merged into one to make the program as transparent as possible and get independently the raw data, and the final reflectance measurements. Firstly, the calibration can be performed to estimate and save the average matrix Q, calculated with Equation (109), over all the calibration measurements. Secondly, the calculation of the reflectance factors of the measured patches can be performed, according to Equation (108). All reflectance factors outside the [0; 1] range were discarded by setting them to NaNs (Not a Number).

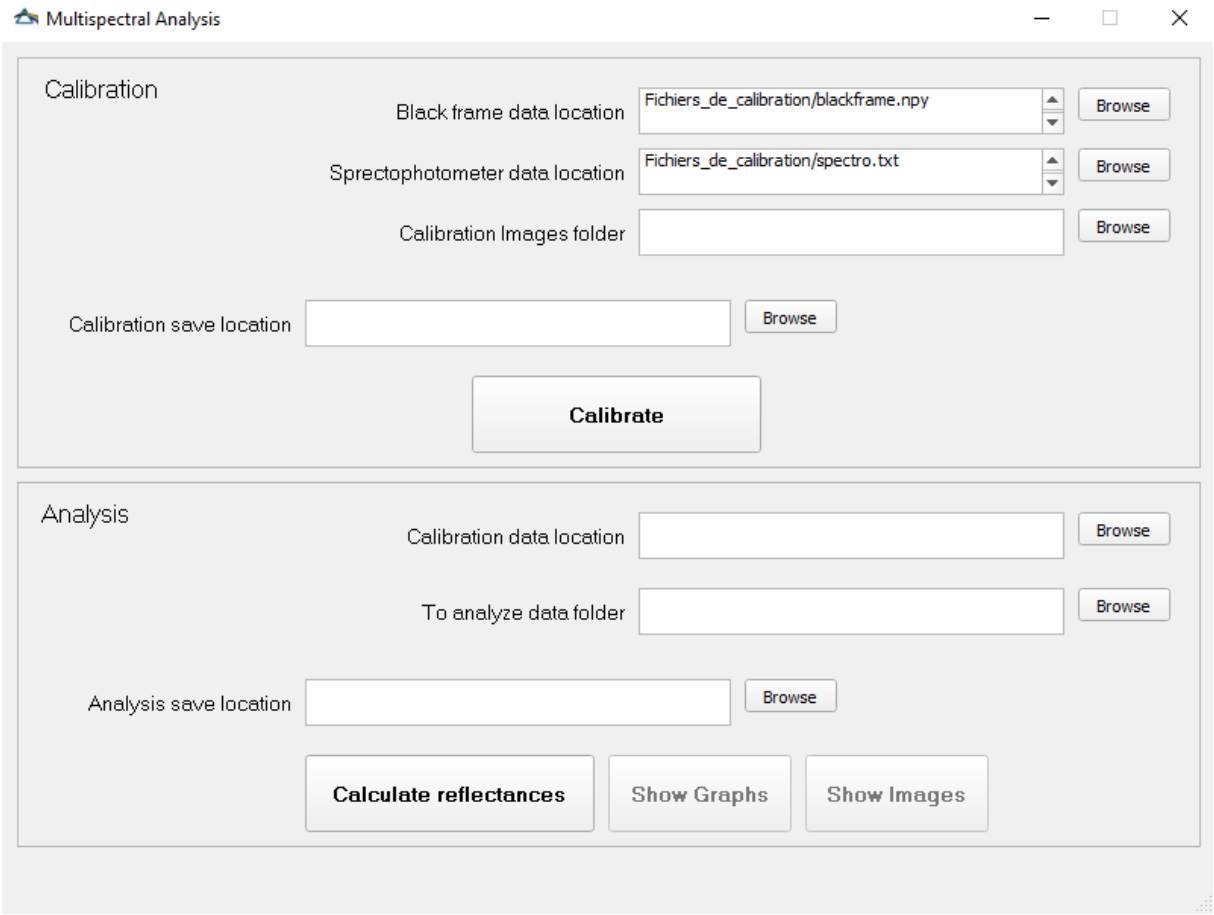

Figure 63. Graphical User Interface for calculations of the calibration data and of the measured reflectance (Analysis tab).

Concerning the processing of HDR measurements, where images are captured twice with different exposure times to prevent sensor saturation, the reflectance factor data for each exposure-time setting are calculated. In this process, all pixel locations where the sensor saturated (pixel values outside the [100, 12 000] range once V_k removed) were set to NaNs. The two measurements were combined by replacing all the NaNs from one of the calculated reflectance factor data by the values from the second measurement. A pixel location where both measurements showed a NaN value remained a NaN after the recombination.

4.1.4 Microscale-macroscale reflectance factor comparison

Using the spectrophotometer in the calibration process enables to compare the microscopic measurements from the custom apparatus (of resolution 1.386 µm per pixel) with the macroscopic ones from the spectrophotometer (measuring on an area of 8 mm diameter). Various halftone colors were designed and printed with an electrophotographic printer according to the protocol detailed in the Subsection 4.3.1, and their reflectances were captured with the two systems. The average spectra of the images were calculated and compared with the spectrophotometric measurements, displayed in Figure 64. A contribution of 0.04 was added

to all reflectances which were measured with the microscope to account for the specular reflection included in the spectrophotometric measurement [12].

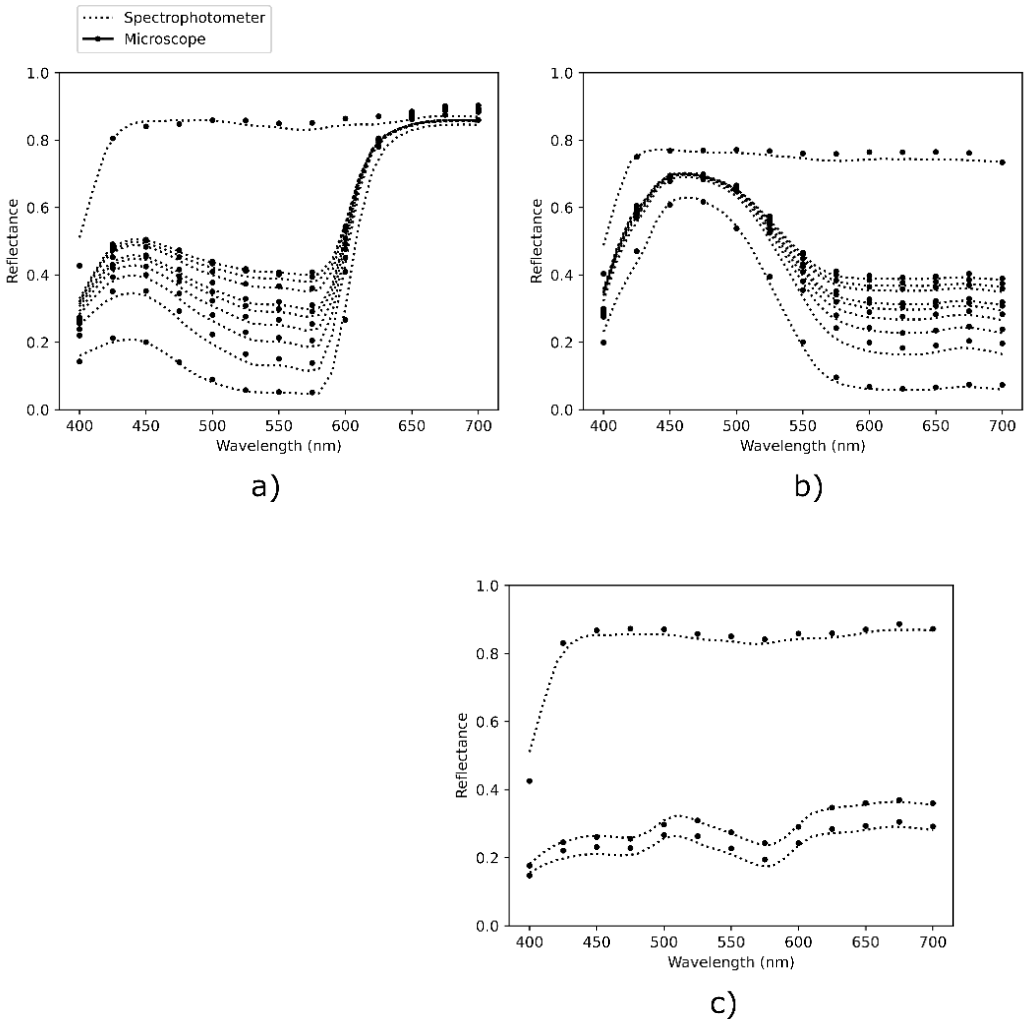

Figure 64. Average reflectance of the multispectral microscope images, compared with macroscale reflectance measurement with a spectrophotometer. a) Magenta line halftones, b) cyan line halftones, c) multicolored dot halftones.

The results showed a rather good agreement between the two measuring methods. The color difference between spectrophotometric and microscopic measurement was calculated with the ΔE_{00}^{*} determined with the 2° observer, illuminant D65, and a perfect reflector as white reference. It is in average equal to $\Delta E_{00}^{*} = 1.02 \pm 0.49$ unit, which shows the uncommonly good agreement between the spectrophotometric and the microscopic measurements, in particular as they have different measurement geometries. Detailed performances are summarized in Table 4.

Small fluctuations in the reflectance measurements with the microscope were observed, but we were unable to fully understand their origin. They can be due to optical aberrations, light source fluctuations, camera sensor temperature variations, imprecisions in the filter positions, or

mispositioned ambient light shield. Yet the microscale/macroscale agreement is usually hard to reach, and the results obtained with this setup are particularly compliant in this regard.

patch #	Magenta Sample	Cyan Sample	Multicolored Sample
Fulltone	0,44	1,27	1,21
1	2,01	1,82	1,08
2	1,24	0,86	
3	1,19	0,92	
4	0,68	0,85	
5	0,75	0,93	
6	0,44	1,24	
7	0,89	0,94	
8	0,28	0,73	
Substrate	1,51	1,57	0,50
Average	0,94	1,11	0,93
Standard deviation	0,55	0,35	0,37

Table 4. Color difference ΔE_{00}^{*} between the spectrophotometric measurements and the ones performed with the multispectral microscope on non-coated samples printed in electrophotography.

The microscale-macroscale agreement was less accurate for the second experiment detailed in Subsection 4.3.2 which was performed at least 10 months later with inkjet prints. This inaccuracy could be due to an ageing of the system (especially of the microscope light source), or due to the difference of substrates between the electrophotographic and inkjet experiments. It could in particular be due to differences in the BRDF of the two substrates. The results are detailed in Appendix VII.

4.2 Prediction of the halation phenomenon on microscale halftones

The objective of this section is to describe the method used to predict the color change of a microscale halftone print when it is coated with a clear layer, using the multispectral microscopic measurements. To predict the reflectance of the print after the addition of a glossy coating layer, three main parameters need to be implemented in the multi-convolutive model: the spatial and spectral intrinsic reflectance of the print, the thickness of the coating layer, and the measurement geometry.

As the print is subject to optical and mechanical dot gains, it spatial and spectral intrinsic reflectance of the print cannot be easily estimated from models, we chose to deduce it from reflectance factor measurements performed with the multispectral microscope presented in Section 4.1. The setup needed first to be calibrated with a glossy spectralon; the exposure times are displayed in Table 5. The pattern of the halftone print was aligned with the x and y axis of the microscope to prevent edge issues during the convolution steps in the computation, as described in Section 3.3.2. This alignment was verified for line patterns by translating the microscope plate on which the sample is placed and verifying that the line was aligned according to one of the two horizontal directions. For small halftone patterns, this alignment step was less necessary as the reflectance factor at the edges can be considered statistically independent of the position on the print. The samples were usually set over a white support, except for the cyan electrophotographic prints presented in 4.3.1 which were set over a black support. Even if the support had an impact on the reflectance measurement due to the transparency of the paper, it did not seem to impact the quality of the predictions. The corners of the sample were simply pasted to the sample plate with tape, outside of the measurement area. No microscope glass slide was used to avoid the optical effects they can induce. The samples were not perfectly flat and the focus of the microscope had to be adjusted for each patch.

The spatial microscopic reflectances of the halftones were captured with the custom-built multispectral microscope through 13 optical filters, from 400 nm to 700 nm. To ensure that both inked and non-inked areas were non-saturated, halftone prints are captured in HDR mode. The typical exposure times ranged from 0.4 s to 30 s depending on the optical filter, they are detailed in Table 5 for a general case, but they can be adapted to the color of the halftone print by decreasing the long exposure time at wavelengths for which the ink is not absorbing. The measurements lasted approximately ten minutes per patch. During this time, the microscope plate must not move to keep a good focus. Therefore, all movements inducing vibrations around the microscope were avoided as much as possible, (such as walking around the microscope or using the microscope table). This was a rather sensitive and constraining element during the experiments. A light shield set around the microscope plate also proved to be indispensable to prevent any light pollution from the rooms ambient light.

λ (nm)	400	425	450	475	500	525	550	575	600	625	650	675	700
T_c	10	3.2	1	0.8	0.8	0.5	0.5	0.5	0.4	0.5	0.5	0.5	6
T_1 (s)	20	3.2	1	0.8	0.8	0.5	0.5	0.5	0.4	0.5	0.5	0.5	6
T_2 (s)	30	25	20	10	6	5	5	5	6	4	4	5	13

Table 5. Exposure time settings for each optical filter of the filterwheel at wavelength λ, T_c, for the calibration, T_1 and T_2, for the halftone prints in HDR mode.

During the conversion from pixel values to reflectance factors, some pixels were set as NaNs due to imprecisions, as explained in Section 4.1, especially for highly absorbing inks which can absorb all light. During experiments, NaNs were largely avoided through HDR measurements and showed negligible impacts on the results. In practice, in all calculations, they were considered as Not a Number (NaN), except when displayed in pictures where they were set equal to 1 to outline them, and in convolution operations where they were set equal to the average spectral and spatial reflectance of the sample.

The print reflectance factor pictures were usually cropped to an integer number of periods at the centre of the pictures to avoid the blur caused by optical aberrations at the corners of the pictures. The image sizes were in the range of 1728 × 302 pixels and 1728 × 1533 pixels for the electrophotographic prints, and 892 × 700 pixels and 1250 × 700 pixels for inkjet prints, with 13 wavelengths. For line patterns, the cropping limits were determined by evaluating the reflectance profile of the prints, selecting an arbitrary threshold in the reflectance range and finding the pixel position corresponding to this threshold value. This ensured to have an integer number of period. It was afterwards verified that these pixel positions were in adequation with the nominal halftone period.

These 3D reflectance factor data of the non-coated prints were used as input in the multi-convolutive model. The first dimension was the spectral one, the two others were the spatial dimensions. In the computation of the optical model, the convolutions were performed on the spatial dimensions simultaneously for all wavelengths.

To determine the thickness of the coated foil, thickness measurements were conducted on the prints before and after coating. The measurements were made with a micrometer from Adamel Lhomargy (m120, 15 mm diameter probe). In the electrophotographic experiment, presented in section 4.3.1, the same prints were measured with and without coatings. Each patch was measured 3 times, the average thickness over each patch was used to initialize the optical multi-convolutive model. In the inkjet experiment, presented in Section 4.3.2, the measurements were performed on two different prints coming from the same printed batch. Six measurements were performed on a non-inked area and the average coating thickness was implemented in the multi-convolutive model.

The microscope has a geometry 0°:0°, specular component excluded. This specular component is excluded by using a polarizer and an analyser in crossed configuration. As the measurement geometry is 0°:0°, the light polarisation has no impact on the Fresnel reflectance at the interface. Therefore, the parameters r_i, T_{in}, and T_{out} describing the flux at the interface remain identical with and without the polarizers, they are detailed in Table 1. As the light specularly reflected at the interface is polarized and cut off by the analyser, r_s is equal to 0. The light transmitted at the interface with air is scattered within the print and becomes depolarized. It is then transmitted through the analyser to an equivalent amount as for the spectralon used in the calibration step.

During the computations, the halo function h of the multi-convolutive model was implemented through a 501 × 501 matrix of pixel pitch equal to the pixel pitch of the microscope images, it is presented in Section 3.3.2. It was calculated for each patch with the same coating thickness as the measured one, which was around 20-25 µm. For this range of thicknesses, the halo was rather well resolved at the pixel pitch of the setup. For small thicknesses, thus for small halos, one may need to subsample h and the measured reflectance factors of the prints to maintain a good resolution for h.

Parameter γ was fitted with experimental values of the magenta electrophotographic halftones presented in Section 4.3.1, with a multi-convolutive model accounting for 1 spatial dimension giving similar results as the 2D multi-convolutive model on line halftones. γ was found to be 1.23. The same value was used for the other electrophotographic prints, and was tested for inkjet prints. To use this parameter, the reflectance factor of the substrate needed to be measured.

The computation to predict the spectral reflectance factor of the coated prints lasted approximately 70 seconds per patch.

To verify the predictions given by the multi-convolutive model, multispectral microscopic measurements of the coated prints were also performed, with the same protocol as described in this section.

4.3 Experimental validation

The objective of this section is to validate experimentally the multi-convolutive model presented in Section 3.2 for halftone prints at the microscale. Two experiments with different printers and substrates were performed. The first one, presented in Section 4.3.1, dealt with electrophotographic prints and the second one with inkjet prints, presented in Section 4.3.2. In both experiments, the spectral reflectance of the halftone samples was measured before and after applying the coating layer, and the thickness of the coating layer was evaluated. From the non-coated halftone reflectances and the layer thickness, the multi-convolutive model was calibrated to predict the reflectances of the coated halftones, which was then compared to the experimental ones. The objective was to evaluate both the spectral and the spatial performances of the multi-convolutive model. In both experiments line halftone patterns were preferred as

they allow to compare the average spatial profile of the predicted and measured line halftones, as well as the measured and predicted average spectral reflectance factors.

4.3.1 Electrophotography

A first experiment was performed with an electrophotographic printer. This printing process was first selected to ensure that the colorant, i.e., the toner, did not penetrate the substrate, which could lead to complex light-matter interactions. The sample design is first described, the comparison between the experience and the multi-convolutive model is then presented.

Halftone print design

Various halftones were designed with Adobe Photoshop®: two samples were composed of 8 patches of various periods made of an alternance of white and colored lines, respectively, magenta and cyan, displayed in Figure 65. The nominal periods of the lines were: 0.169, 0.254, 0.339, 0.423, 0.508, 0.847, 1.270 and 2.117 mm (corresponding to, respectively, 150, 100, 75, 60, 50, 30, 20, and 12 lpi), and the nominal ink surface coverage was 0.5. Two additional patches were designed and measured, corresponding to the substrate without ink and the substrate fully covered by ink (surface coverage 0, respectively, 1). The first one is needed to calibrate the multi-convolutive model. Afterwards, the same experiment was enlarged to more complex halftones: a third sample was designed, composed of cyan, magenta, yellow and black inked dots arranged in a rosette pattern. Each ink had a nominal surface coverage of 0.25. Two patches were made with this pattern with different periods.

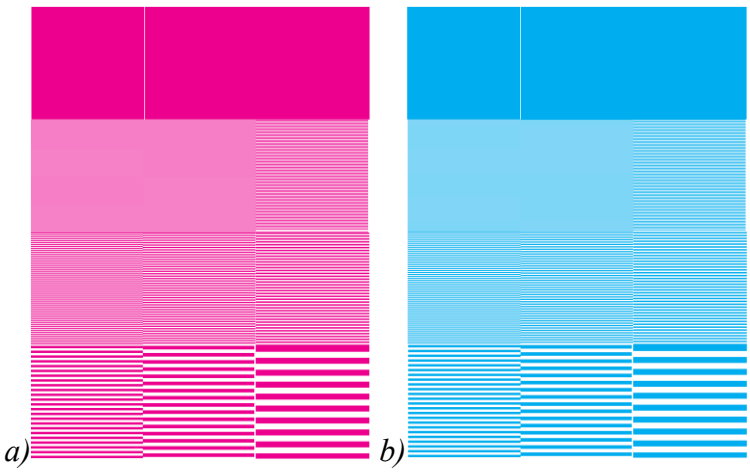

Figure 65. Test forms of the line halftones, a) in magenta, b) in cyan. The first halftone patch of the test form (second row, first column) was discarded from the measurements as, once printed, it was almost a fulltone due to the optical and mechanical dot gains.

The samples were printed on white coated paper (90 g/m^2, Bekk smoothness ~2000 s) with an electrophotographic printer (Xerox Versant 180, toner references 006R01643 for cyan and 006R01644 for magenta). The coated paper had the L*a*b* coordinates: $L^* = 95$, $a^* = 1.4$, $b^* = -4.5$, measured on a white background with a 45°:0° spectrophotometer in M1 condition

with D50 illuminant, which corresponds to the PS1 (Premium coated) of ISO 12647-2: 2013. The printer resolution was 1200 dpi, and the print resolution was 600 dpi. The halftone generation on Adobe Photoshop® was perfomed using the bitmap mode and a line threshold matrix. This method was sometimes inaccurate as some lines contained an incorrect number of pixels. These errors were manually fixed by counting the pixels, and for further experiments detailed in Section 5.1 a Python code was created to generate accurate test forms and avoid this manual step. Any automatic color management was disabled. The halftones were printed through the Xerox Freeflow Software in direct CMJN printing mode.

For the coating process, the samples were laminated with a bright transparent foil theoretically 25 µm thick, with the laminator DRY 350 W from RBS. The lamination foil was composed of OPP and was considered perfectly transparent (its intrinsic transmittance was above 0.993). The temperature of the laminator was 110°C and a coating speed of approximately 0.9 m/min was chosen. The silicon lamination rollers were 0.04 mm apart. After the coating step, reflectances of the samples were measured again with the microscope.

As mentioned in Section 4.2, in the computation, microscope images of the line halftones were cropped to an integer number of periods at the centre of the image to avoid the blur caused by optical aberrations at the corners. One image was the exception, the coated magenta 1.270 mm-period line halftone (patch 7), which was cropped to the edge of the image due to experimental difficulties: the Xerox printer that we used generates some yellow dots which cannot be avoided as they are a signature of the printer (one is visible on the patch 6 of the non-coated cyan halftones in Figure 72). Most of the time, we could take the microscopic pictures in areas without these yellow dots. For this patch 7, however, due to the presence of theses yellow dots at the center of the image, we had to analyse the border of the image impacted by the chromatic aberration (a slight violet tint can be seen at the frontier between inked and non-inked areas in this patch 7 of the coated magenta halftones). The images of the multicolored halftone prints were also cropped to the center of the images with a size 1728×700 pixels, such that they contained enough printed dots so that cropping had no impact on the average reflectance.

Pixels discarded during calculations because they were saturated or had an outranged reflectance represented an average of 0.12% of the pixels in the images, with high variations according to the samples and to the optical filters. The value reached an average of 1.3% for the worst sample, and 7.0×10^{-5}% for the best sample.

Each patch, coated and non-coated, was also measured twice with the spectrophotometer CM-2600d from Konica Minolta, 8 mm aperture, with a di:8° geometry and with a UV filter to prevent fluorescence. This measurement was performed to ensure that the microscope response was in adequation with spectrophotometric measurements. They led to the results presented in Section 4.1.

Prediction and observation of dot gain in coated prints

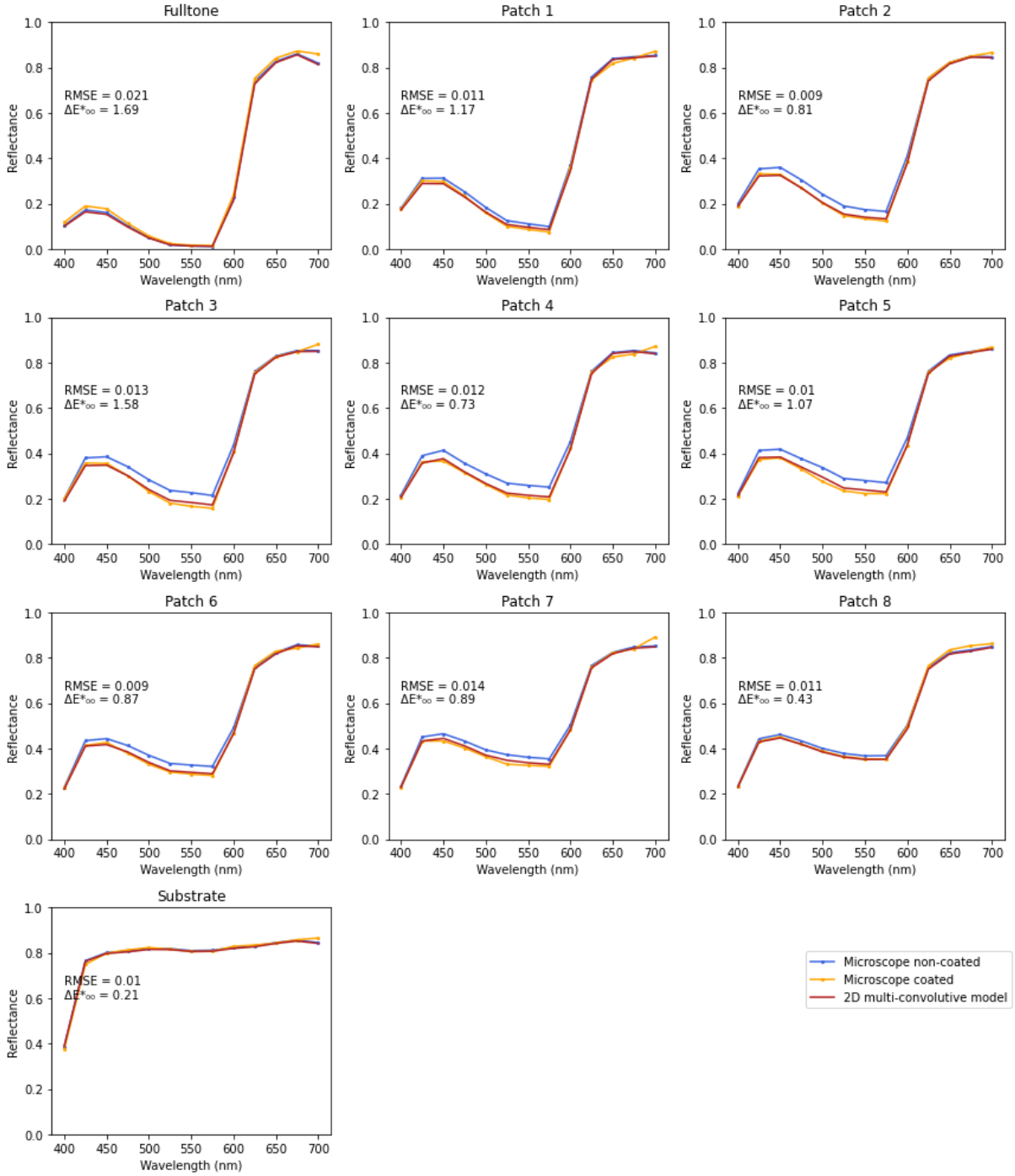

Figure 66. Spectra of the magenta line halftones, averaged over the spatial dimension. Patch 1 to 8 have a period of respectively: 0.168, 0.252, 0.337, 0.421, 0.505, 0.839, 1.263, and 2.104 mm. A specular component of 0.04 is added to all spectra.

Figure 66 presents the average spectral reflectances of the magenta line halftones over the area of the pictures. Experimental coated and non-coated spectra show differences due to the coating

layer, especially for halftones of medium period. For these halftones, the coating layer enables light to transit from non-inked areas to magenta areas and be absorbed by them, which darkens the macroscopic reflectance of the coated copies.

The fulltone and bare substrate have the same reflectance whether coated or not as their color is uniform at the microscopic scale; the convolution of a constant spatial function with the halo pattern still gives a constant spatial function, which means that the halation phenomenon has no impact on the print reflectance. The smallest-period halftone, patch 1, also shows small differences between coated and non-coated halftone reflectances. A hypothesis, which can be confirmed through the spatial characterization, is that it undergoes high optical and mechanical dot gains, leading to a high effective surface coverage, less distinct white lines, and a more uniformly colored halftone than patch 2 for instance. As the color is more uniform and the edges less sharp, the coating layer has less effect on the halftone, as shown through the simulations in Section 3.7.3. The thickest-period halftone, patch 8, is composed of lines so large that light can almost not transit from one colored area to another one at the given coating thickness, thus the coating layer has few impacts on its reflectance.

The multi-convolutive optical model gives a prediction of the reflectance of the coated halftones. On each graph are displayed the root mean square error between the predicted spectrum and the experimental one, as well as the color difference with the ΔE_{00}^{*} determined with the 2° observer, illuminant D65, and a perfect reflector as white reference, they are also detailed in Table 6. There is a good match between the predictions given by the multi-convolutive model and the experimental coated-halftone reflectances, which validates the model in the spectral dimension.

The experiment on cyan line halftones displays similar results, presented in Appendix VI, in Figure 98.

As the multi-convolutive model and the multispectral microscope both yield spectral and spatial reflectances, the spatial dimension of the results can also be studied. The spatial reflectance are presented in Figure 67 for various magenta halftones and in Appendix VI: in Figure 99 for cyan halftones, and in Figure 100 for all the magenta halftones. In these figures, the average profiles of the halftone lines over the reflectance images, averaged in the spectral dimension, are displayed. The corresponding sRGB pictures are displayed at their side, the non-coated halftone images on the left, the predictions given by the multi-convolutive model in the middle, and coated halftone images on the right. sRGB were calculated with the norm described in [168] and the displayed pictures were cropped to zoom in the centre of the images. These pictures allow to visually assess the measurements and predictions of spatial and spectral reflectances. Small bright yellow dots in the magenta fulltone reveal that some pixels of this image were saturated during the measurement.

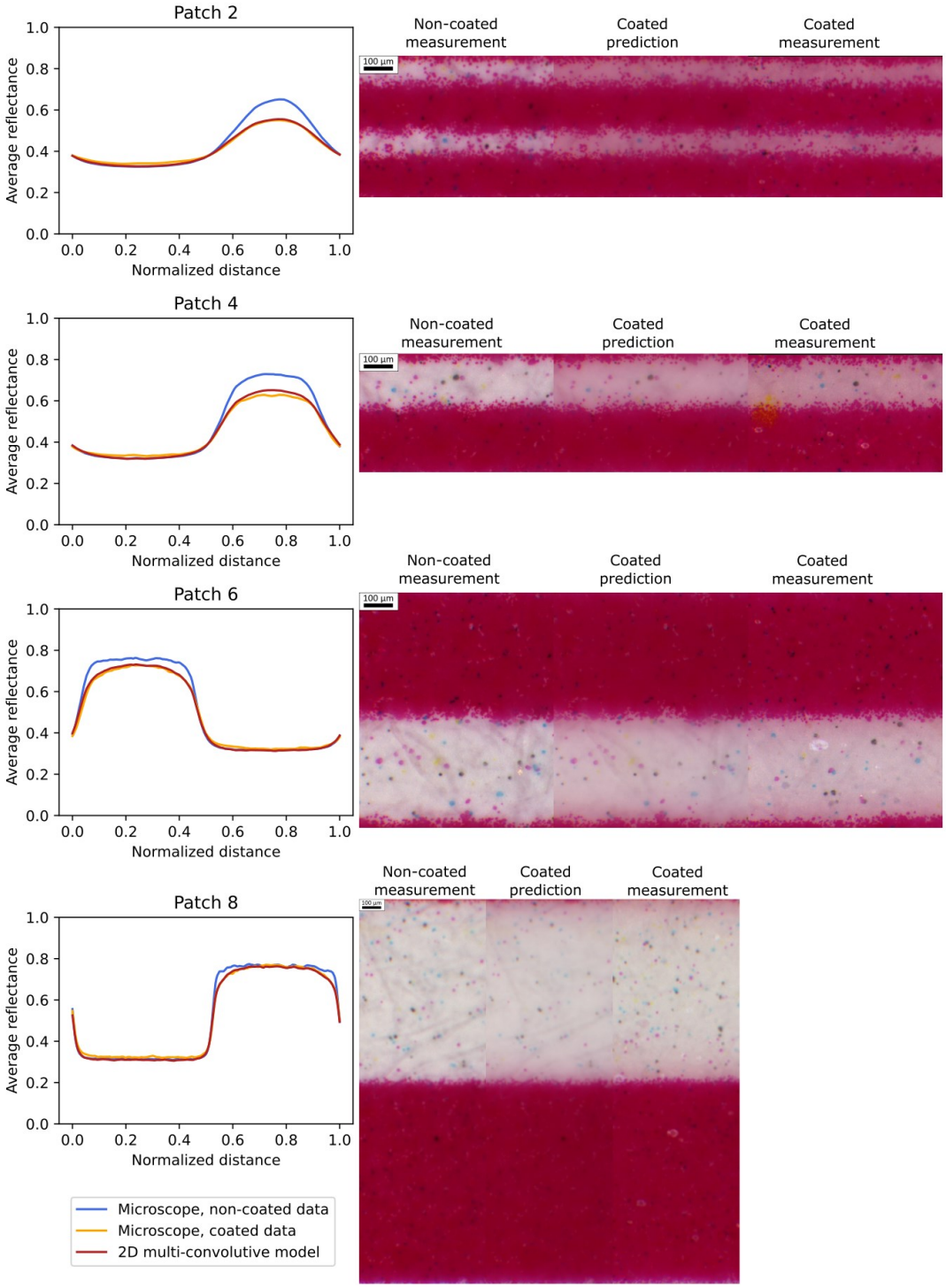

Figure 67. Magenta halftone reflectance profiles averaged over the spectral dimension. On their right, corresponding sRGB pictures of the non-coated, predicted, and coated halftones. Patch 2,4,6,and 8 have a period of 0.252, 0.421, 0.839, and 2.104 mm, respectively.

In the figures displaying the reflectance profiles, Figures 67, 99 and 100, the low reflectance values correspond to the inked areas, and the high ones to the non-inked areas. The profiles are computed from the microscopic image, by taking all the profile attached to all the vertical lines

and averaging them. Since the printed lines are composed of small ink dots also called 'satellites' (see the microscopic pictures in Figures 67, 99 and 100), the average profile is not perfectly crenel-shaped but a little smoothened. Moreover, the well-known phenomenon of optical dot gain due to light scattering by the support behind the ink patterns also contributes to blur the boundaries of the inked area, and thereby to smoothen the profile discontinuities. It is particularly emphasized with high frequency halftones (i.e., thin lines, e.g., patches 1 and 2) where non-inked lines appear slightly magenta as light can easily travel from the inked lines to the non-inked ones. This results in halftone patterns looking more homogeneous, less contrasted, and reflectance profiles having a lower amplitude. With low frequency halftone (i.e., large lines, e.g., patches 7 and 8), the optical dot gain is visible through the subtle color gradient next to the border of the inked area.

All these effects are much more pronounced when the halftones are coated, since the coating layer induces an additional optical dot gain. For high frequency halftones (patches 1 and 2), the microscopic pictures look even more homogeneous, and the amplitude of reflectance profiles even reduced. For low frequency halftone (patches 7 and 8), the color gradient next to the border of the ink areas is magnified; the discontinuities in the reflectance profiles are more smoothened than in absence of coating. The change of amplitude of the reflectance profiles due to the coating varies according to the profile and contrast of the non-coated halftone patterns and, therefore, to the halftone frequency; with high frequency halftones, whose contrast before coating is lower (consequence of the optical dot gain induced by the diffusing support) and whose profile before coating is less sharp, the effect of the halation phenomenon is less pronounced.

Figures 67, 99 and 100 also show the reflectance profiles predicted by the optical multi-convolutive model (from images of the non-coated patches), which can be compared with the ones measured with the microscope (images of the coated patches). The agreement between the predicted and measured profiles is fairly good. This is particularly remarkable as the non-coated and coated measurements were not done in the same area of the halftones, which proves the robustness of the method. There remains for some patches a small difference in the amplitudes of the predicted and measured profiles: an error of 5% is observed in the brightest areas of patch 4 and 5, whereas the error is less than 2% for patches 2 or 6. This might be due to the heterogeneities of the printed lines, or to differences between the properties of the real materials and the ones assumed by the multi-convolutive model, for instance scattering inks or a not perfectly smooth coating layer.

The performance of the multi-convolutive model can also be visually assessed in the sRGB pictures. The color difference between the non-coated and coated patches is striking, whereas the predicted and measured images of the coated patches look very similar. A closer look simply shows that the predicted images are more blurred, as a consequence of the multiple convolution process operated on the images of the non-coated patches, than the measured images of the coated patches.

The case of the single-ink line halftones that we have developed in detail above was useful to analyse the predictive performance and the imperfections of the multi-convolutive model, both spectrally and spatially, in the simplest cases. However, the method applies with any kind of halftone pattern. We propose to illustrate its capacities through the example of two grey color patches, printed with four-ink clustered dot halftones. The average spectra are presented in Figure 68, and the sRGB pictures in Figure 69. In these figures can be seen the good agreement between experiment and predictions, especially with patch 2 for which the ΔE^*_{00} is only 0.32 unit, and the color appearance in the predicted and measured images for the coated patch look very similar.

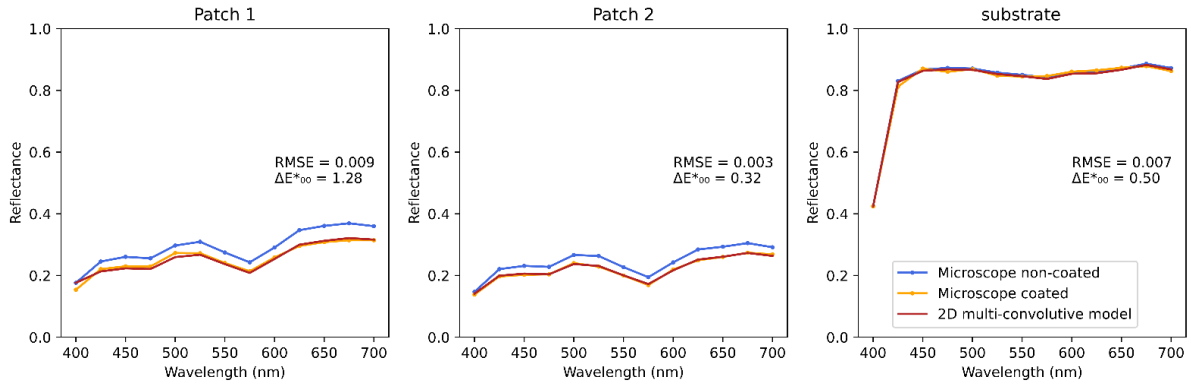

Figure 68. Average spectra of the multi-ink dot halftones, and of the bare substrate.

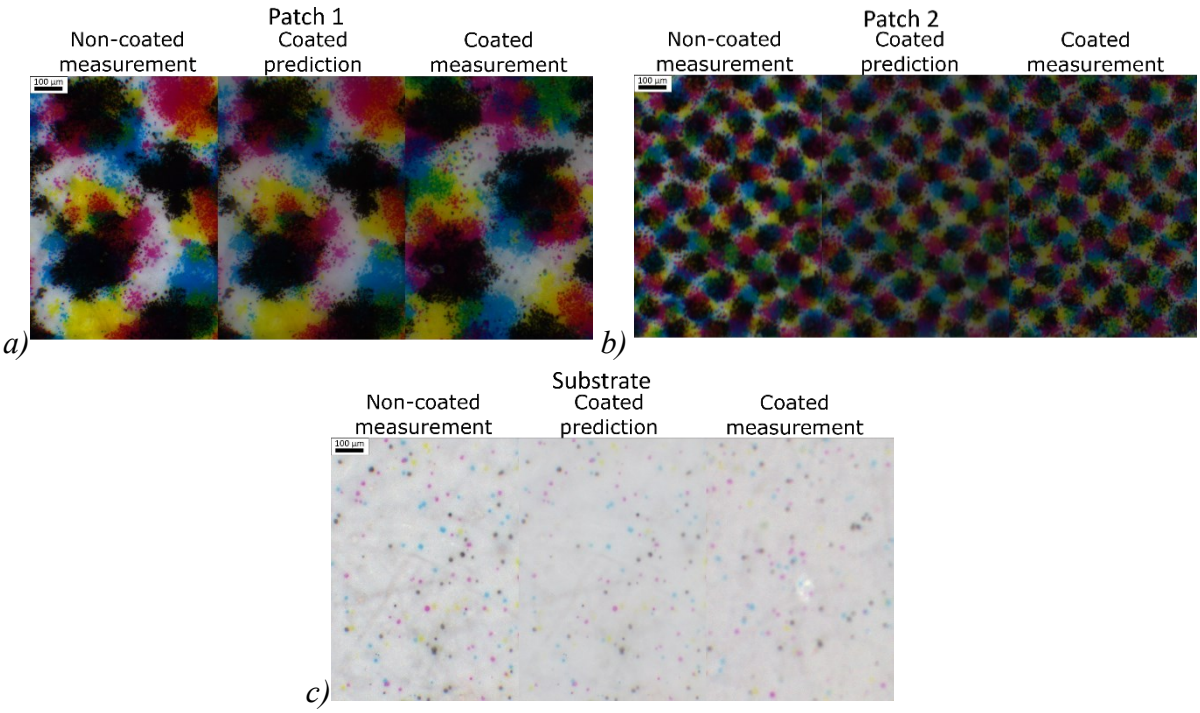

Figure 69. sRGB pictures of the multi-ink dot halftones: non coated on the left, predicted in the middle, and coated on the right.

Magenta Sample				
patch #	Coating Thickness (µm)	Period (mm)	ΔE_{00}^{*} Model vs. Experiment Coated Samples, with $\gamma = 1.23$	ΔE_{00}^{*} Model vs. Experiment Coated Samples, with $\gamma = 1$
Fulltone	20,3		1,69	1,20
1	21,0	0,168	1,17	1,40
2	19,7	0,252	0,81	1,14
3	19,7	0,337	1,58	1,81
4	19,3	0,421	0,73	1,16
5	19,7	0,505	1,07	1,43
6	19,7	0,839	0,87	0,95
7	20,3	1,263	0,89	1,00
8	21,0	2,104	0,43	0,33
Substrate	20,0		0,21	0,21
Average	20,1		0,94	1,06
Standard deviation	0,6		0,46	0,48

Cyan Sample				
patch #	Coating Thickness (µm)	Period (mm)	ΔE_{00}^{*} Model vs. Experiment Coated Samples, with $\gamma = 1.23$	ΔE_{00}^{*} Model vs. Experiment Coated Samples, with $\gamma = 1$
Fulltone	23,3		1,35	0,45
1	23,0	0,168	0,75	1,12
2	23,3	0,250	0,76	0,48
3	24,7	0,334	1,46	1,31
4	23,0	0,420	1,00	1,40
5	23,3	0,504	0,61	1,01
6	24,7	0,841	1,15	1,24
7	23,0	1,259	0,88	0,95
8	24,0	2,104	1,01	0,80
Substrate	23,7		1,36	1,36
Average	23,6		1,03	1,01
Standard deviation	0,6		0,29	0,34

Multicolored Sample			
		ΔE_{00}^{*}	
patch #	Coating Thickness (µm)	Model vs. Experiment Coated Samples, with $\gamma = 1.23$	Model vs. Experiment Coated Samples, with $\gamma = 1$
1	22,3	1,28	1,21
2	23,7	0,32	1,08
Substrate	25,3	0,50	0,50
Average	23,8	0,70	0,93
Standard deviation	1,5	0,51	0,37

Overall			
		ΔE_{00}^{*}	
	Coating Thickness (µm)	Model vs. Experiment Coated Samples, with $\gamma = 1.23$	Model vs. Experiment Coated Samples, with $\gamma = 1$
Average	22,1	0,95	1,02
Standard deviation	1,9	0,39	0,40

Table 6. Performances of the measurement system and of the optical multi-convolutive model.

The performances of the multi-convolutive model are summarized in table 6. The performances of the model are also displayed when the parameter γ is not fitted, i.e., equal to 1.

This experiment allowed to observe the effects of the mechanical dot gain, the optical dot gain caused by light diffusion within the substrate and the optical dot gain caused by the halation phenomenon. For the first time, we could predict the spectral reflectance of multi-ink microscale halftone prints after coating, by taking a microscopic spectral image of the prints before coating and applying an optical model describing the multi-convolutive optical process. The color prediction accuracy is rather good, with an average color difference: $\Delta E_{00}^{*} = 0.95 \pm 0.39$, and we could also render rather well the blurring effect induced by the coating on the

contours of the ink areas. The robustness of this prediction method was tested by applying it to another printing process: inkjet.

4.3.2 Inkjet

The results obtained with the electrophotographic process were published in a paper [169] which has drawn the attention of color scientists from GMG Color, a company specialised in color management for the printing industry. The study presented in this section, performed in collaboration with GMG Color, aimed at evaluating the performance of the multi-convolutive model for inkjet prints. The inkjet printing process is different from the electrophotographic as it relies on liquid inks dropped on a substrate, where the electrophotographic process rely on solid inks applied on the substrate with a roller. Both the optical and mechanical dot gains induced by the inkjet process are different from the ones induced by the electrophotographic process, which has an impact on the microscale reflectance of the print and could impact the color change predictions when prints are coated.

Cyan and magenta inkjet prints, uncoated and coated, were provided by GMG Color to experimentally validate the multi-convolutive model. These test forms were printed by GMG Color with an Epson SC-P5000 inkjet printer of resolution 1440 × 720 dpi on the GMG premium glossy 250 proof paper (250 g/m², 260 µm thick, free of optical brightener agent, glossy finishing) with a light cyan and a light magenta ink from the original Epson Ultrachrome HDX ink set. They were laminated with the industrial thermo-laminator Komfi Delta 52 at a temperature of 110°C and at a speed of 34 m/min. It deposited a clear glossy layer of Ultralen TK25 GLOSS (465 mm width, oriented polypropylene) of theoretical thickness 25 µm. The uncoated and coated prints were issued from the same printed batch, they were then statistically identical. The thickness, d, of the clear layer was measured with the micrometer m120 from Adamel Lhomargy by evaluating the thickness difference between the uncoated and the coated prints. The thickness was $d = 28 \pm 2$ µm for the cyan print and $d = 30 \pm 2$ µm for the magenta print.

The cyan and magenta test forms were composed of lines of various periods and surface coverages. In each test form, 6 patches were selected to experimentally test the multi-convolutive model, including a fulltone and an unprinted-substrate patch. Their respective nominal surface coverage and period are displayed in Table 7.

The spatial and spectral reflectance factors of the uncoated and coated prints were measured with the multispectral microscope. According to the method detailed in Section 4.2, the reflectance factors of the uncoated prints were used to calibrate the multi-convolutive model, and the ones of the coated prints were used to compare the prediction given by the model and the measurements.

		Fulltone	Patch 1	Patch 2	Patch 3	Patch 4	Substrate
Cyan	Surface coverage	1	0.333	0.333	0.364	0.114	0
	Period (µm)	∞	106	211	388	1234	∞
	d/p	0	0.266	0.133	0.073	0.021	0
Magenta	Surface coverage	1	0.333	0.167	0.091	0.114	0
	Period (µm)	∞	106	211	388	1234	∞
	d/p	0	0.280	0.141	0.076	0.024	0

Table 7. Characteristics of the inkjet patches. d/p describes the ratio between the thickness, d, of the coating layer and the period p of the halftone upon which the darkening phenomenon due to the addition of a coating layer is highly dependent.

The γ parameter of the multi-convolutive model, accounting for the increase of light absorption by the inked areas when the light rays on the ink have a high angle of incidence was found to be around $\gamma = 1.23$ for electrophotographic prints. For the inkjet experiment, both $\gamma = 1.23$ and $\gamma = 1$ were tested. The predictions for the cyan prints were more accurate for $\gamma = 1$, with an average color difference $\Delta E_{00}^{*} = 0.64 \pm 0.21$, estimated with illuminant D65 and a 2° observer [170], than for $\gamma = 1.23$, for which the color difference between the prediction and the measurements was in average $\Delta E_{00}^{*} = 0.91 \pm 0.12$. On the contrary, the predictions for the magenta prints were slightly more accurate for $\gamma = 1.23$, with an average $\Delta E_{00}^{*} = 0.63 \pm 0.11$, than for $\gamma = 1$, with in average $\Delta E_{00}^{*} = 0.73 \pm 0.37$. For the magenta prints, the measurement of the uncoated patch 4 at the wavelength $\lambda = 625$ nm was inaccurate, the ΔE_{00}^{*} results for this patch were then discarded from the overall results.

The prediction results are detailed here for the cyan prints, with $\gamma = 1$. The results for $\gamma = 1.23$ and for the magenta prints are displayed in Appendix VII, and the performances of the multi-convolutive model for the cyan and magenta inkjet prints are detailed in Table 8.

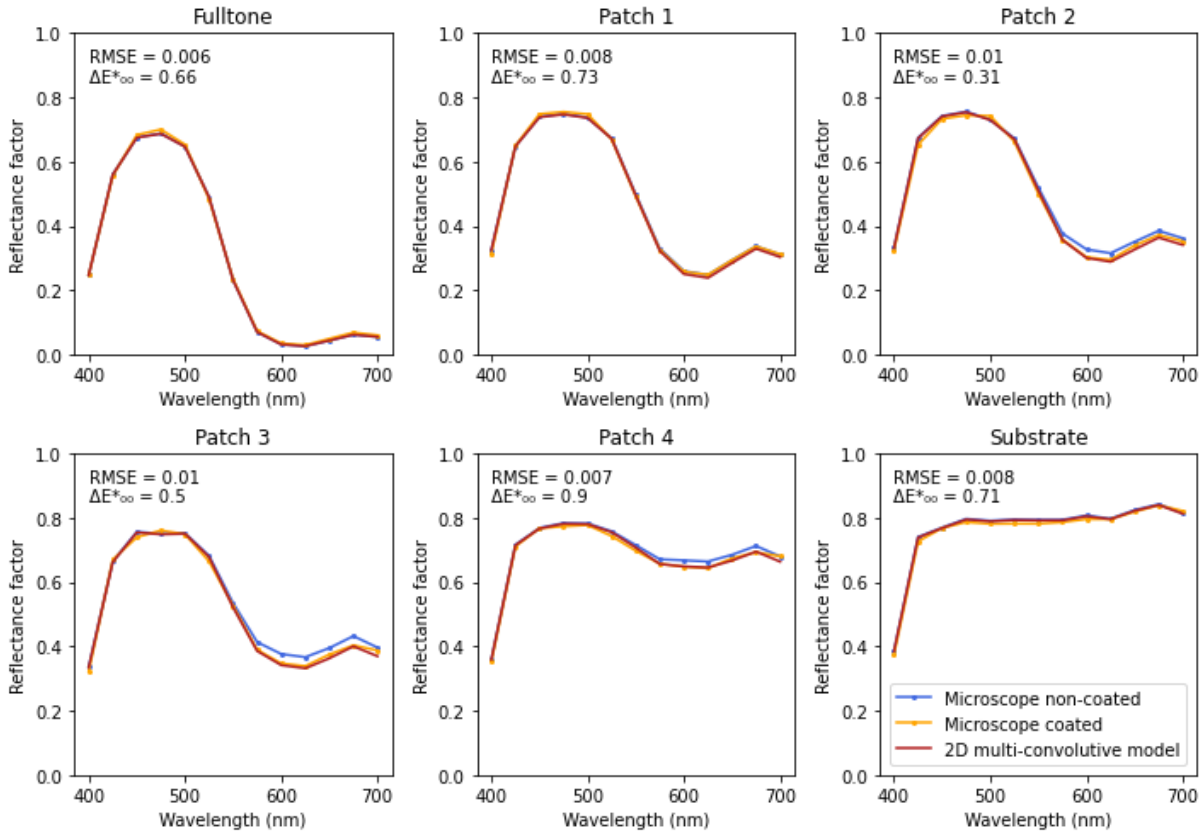

Figure 70. Reflectance factor of the cyan prints averaged over the spatial dimension. The predictions included $\gamma = 1$.

In Figure 70 are displayed the spectra of the various cyan halftone patches averaged on the spatial dimension. The blue lines correspond to the measured spectra of the uncoated prints, the yellow ones to the measured spectra of the coated prints, and the red ones to the spectra predicted by the multi-convolutive model simulating the effect of the coating layer. Similarly to the results obtained in electrophotography, the reflectance factors of the coated prints are rather well predicted by the multi-convolutive model.

This agreement is verified for various *d/p* ratios (ratio between the thickness of the coating layer, *d*, and the spatial period of the prints, *p*). It can be observed for the patch 4, which has a low *d/p* value: $d/p = 0.021$, that the reflectance factor is rather similar with and without coating: light propagates over a short distance inside the coating layer compared to the period of the lines, and can almost not propagate from an inked area to a non-inked area. The additional dot gain induced by the coating layer is then rather small. Furthermore, this patch also has a low surface coverage which contributes to decrease the impact of the coating layer compared to prints of surface coverages around 0.5, as presented in the simulations in Section 3.7.1.

It can also be observed that patch 1 has similar reflectance factors with and without the coating layer, yet this patch has an intermediate surface coverage and a high *d/p* ratio. The reflectance factor similarity is due to the optical dot gain already induced by substrate when the print is uncoated. This optical dot gain is visible in Figure 71 in which are displayed the spatial

reflectance factors of the various patches, averaged over the spatial dimension over all the lines. The dot gain decreases the amplitude of the reflectance factor profile of patch 1, and it smoothen its edges, compared to the profile of Patch 4 which is less impacted by the dot gain as it is thicker. As shown in Section 3.7.3, both the small reflectance amplitude and low profile sharpness tend to decrease the impact of the addition of a coating layer on the print, which explains why the reflectance factor of patch 1 is similar with and without coating.

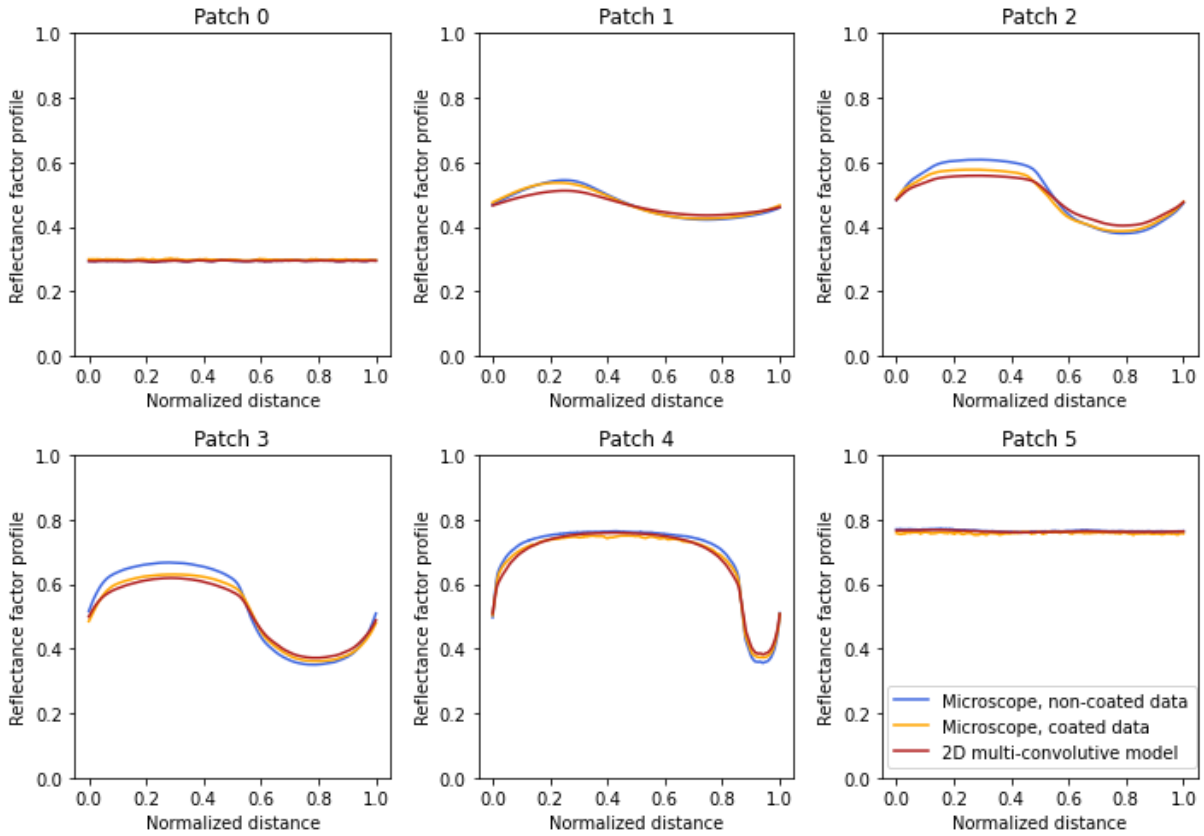

Figure 71. Reflectance factor profile of the cyan prints averaged over the spectral dimension; the profile was spatially averaged over all the lines. The predictions included $\gamma = 1$.

The profiles displayed in Figure 71 also show that the multi-convolutive model can rather well predict the spatial reflectance factor of the prints. This can be also visually observed in Figure 72 where the sRGB pictures of the prints, evaluated from their reflectance factors, are displayed.

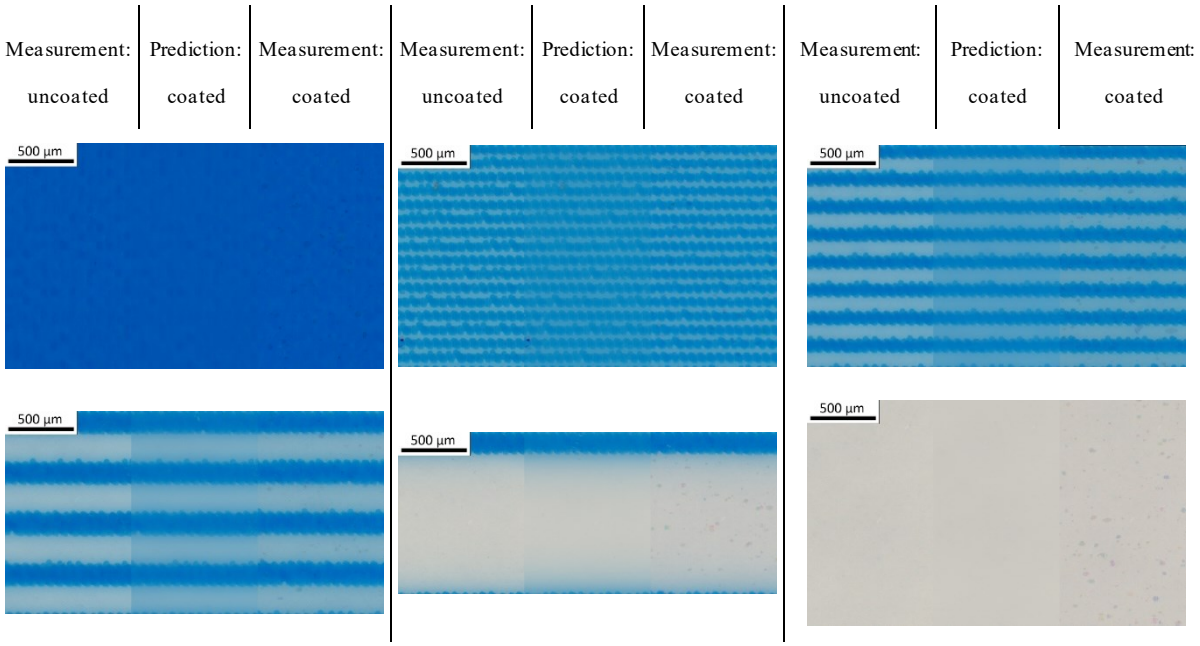

Figure 72. sRGB pictures of the results. The predictions included $\gamma = 1$.

	ΔE_{00}^{*} magenta samples		ΔE_{00}^{*} cyan samples	
patch #	Model vs. Experiment Coated Samples, with $\gamma = 1.23$	Model vs. Experiment Coated Samples, with $\gamma = 1$	Model vs. Experiment Coated Samples, with $\gamma = 1.23$	Model vs. Experiment Coated Samples, with $\gamma = 1$
Fulltone	0,77	0,23	0,98	0,66
1	0,68	0,65	0,95	0,73
2	0,48	0,91	1,05	0,31
3	0,57	1,21	0,88	0,50
4	22,24	21,81	0,86	0,90
Substrate	0,63	0,63	0,71	0,71
Average	0,63	0,73	0,91	0,64
standard deviation	0,11	0,37	0,12	0,21

Overall ΔE_{00}^{*}	Model vs. Experiment Coated Samples, with $\gamma = 1.23$	Model vs. Experiment Coated Samples, with $\gamma = 1$
Average	0,78	0,68
Standard deviation	0,18	0,28

Table 8. Performances of the multi-convolutive model for inkjet prints.

The overall performances of the multi-convolutive model, presented in Table 8, show that the model performs slightly better on inkjet prints than on the electrophotographic ones, with an overall color difference $\Delta E_{00}^{*} = 0.68 \pm 0.28$ when $\gamma = 1$. The microscope measurements were easier for the inkjet prints than for the electrophotographic ones as the inkjet inks were less absorbing than the toner used in electrophotography, but the substrate used in inkjet may require a different calibration method of the multispectral microscope to reach a microscale/macroscale agreement. Despite the substrate, ink, and dot gain differences between the electrophotographic and the inkjet prints, the accuracy of the results shows that the multi-convolutive model is rather resilient to a change in the printing process.

4.3.3 Discussion

The rather good agreements between the predictions and measurements obtained with our method throughout our experiments tend to confirm that we have well identified the optical phenomenon in play when a clear layer is coated on top of a halftone print, and well described it in our optical multi-convolutive model. We can also consider that the assumptions on which the model relies, regarding both the structure of the halftone print and the optical properties of the materials, reasonably meet the reality in rather conventional printing configurations. Some disadvantages and sources of errors, however, can be mentioned.

Spectral microscopic imaging is not usual in the printing domain, which often prefer spectral-only measurements with a spectrophotometer. Furthermore, spectral microscopes are not common instruments on the marketplace, especially with the spectral and spatial resolution that we have here. In our case, the microscope has been extended to spectra measurements by our own means. The spectral resolution is particularly critical for the optical multi-convolutive model to give a good accuracy: a minimum step size of 25 nm, consistent over the whole spectrum, is required. The calibration of the microscope is a delicate operation that requires special caution. Regarding the spectral aspect, the difficulty comes from the fact that the exposition time of the camera must be adapted to each filter in order to guarantee a good SNR and prevent saturation of the sensor in some pixels, despite the HDR algorithm used in the acquisition process. The homogeneity of the white standard used as reference should be

checked, and its spectral reflectance should be precisely known. We took care to verify that the average reflectance measured by the microscope and those measured by a spectrophotometer satisfying the recommendations by the CIE for colorimetric studies are consistent with each other, to ensure that the calibration was correctly performed. The difference in illumination and observation geometry between the two systems can cause large deviations with some types of surfaces, but the risk was limited with the surfaces studied here since the diffusing background was almost Lambertian and the specular component was excluded. It may be necessary to adapt the white standard reference to the type of surface which is studied, as might be the case for inkjet prints. We have achieved a color difference between the spectra from the two systems with electrophotographic prints of $\Delta E_{00}^{*} = 1.02 \pm 0.49$ on average, which is already a point of satisfaction.

On the spatial aspect, the main issue was the focus, since the overlay is transparent. The focusing operation was done separately on each measured sample. Since the acquisition was rather long, around 10 min for one sample due to the multiple acquisitions required by the HDR process, slight vibrations around the microscope could lead to a loss of focus, or a blurring effect. Note that microscopes may have some chromatic aberrations at the borders of the images, and the spectral values can be significantly impacted. It is, therefore, preferable to analyze the center of the images.

Regarding the printed samples, the Xerox printer that we used generates some yellow dots which cannot be avoided as they are a signature of the printer. One is visible on the patch 6 of the non-coated cyan halftones. Most of the time, we could take the microscopic pictures in areas without these yellow dots. In some cases, however, due to the presence of these yellow dots at the center of the image, we had to analyze the border of the image impacted by the chromatic aberration. The inkjet measurements were easier as there were no such dots and as the inks were less absorbing, which decreased the dynamic range compared to the electrophotographic prints.

In the multi-convolutive model, the value of the parameter γ, related to average path length of the light within the coating layer, can be discussed. For electrophotographic prints, it should be around 1.23, and all our predictions have been made with this value. However, we wanted to test the prediction accuracy when its value is 1 (or, equivalently, this parameter γ is removed from the equations). The results are almost as good as with $\gamma = 1.23$. The average ΔE_{00}^{*} between the predictions and the measurements for the electrophotographic process was 0.95 ± 0.39 with $\gamma = 1.23$, and 1.02 ± 0.40 with $\gamma = 1$. In inkjet, it was in average 0.78 ± 0.18 with $\gamma = 1.23$, *and* 0.68 ± 0.28 with $\gamma = 1$. The fitting of this parameter may account for complex interactions between the optical dot gain of the substrate and the interreflection inside the coating layer, two phenomena which are considered independent in the multi-convolutive model. It may also improve the predictions for inked areas which are too absorbing, which can truncate the spectra of these area at the lowest reflectance values. This may explain why the multi-convolutive model performed slightly better for inkjet prints: the inks were less absorbing than in electrophotography.

4.4 Impact of the microscale optical and mechanical dot gains on the color change

In Section 3.7 were presented simulations of the impact of various halftone pattern parameters such as the surface coverage, the ratio *d/p* between the coating thickness, *d*, and the period of the halftone, *p*, and the sharpness of the profile on the effect of the halation phenomenon. In the experiments presented in Sections 4.3.1 and 4.3.2 the parameters, considered separately in Section 3.7, are interdependent: as the period of the halftones decreases, the mechanical and optical dot gains impact more the prints, which therefore have smoother profiles and higher surface coverages. In the end, the color difference between the non-coated and coated areas are impacted by the different parameters all at the same time. In Figure 73 are displayed the ΔE^*_{00} between the non-coated and the coated patches as a function of the *d/p* ratio. It is displayed for both the electrophotographic and the inkjet processes, based on the multispectral microscopic measurements. It can be noted that for the electrophotographic process all halftone patterns had the same nominal surface coverage, which is not the case for inkjet halftones.

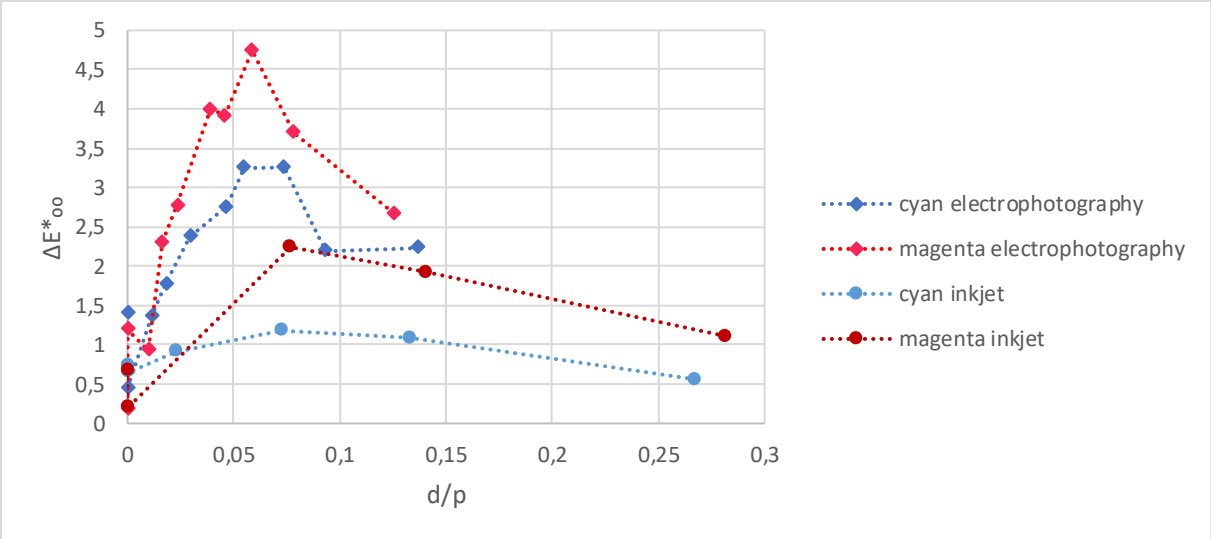

Figure 73. Color difference between the coated and the non-coated prints as a function of the ratio between the coating thickness, d, and the period of the halftones p.

In the various simulations, it was shown that the reflectances decreased as a function of the *d/p* ratio, which should lead to an increase of the color difference ΔE^*_{00} between the non-coated and the coated print as *d/p* increases. In Figure 73, it is rather clear that the color difference reaches a maximum for a *d/p* value, around 0.07 for the electrophotographic prints, and decreases for higher *d/p* values. Indeed, in the experiment we performed, the highest *d/p* values corresponded to the thinnest printed lines which are the most impacted by the optical and mechanical dot gains. As these dot gains tend to smoothen the halftone profiles, increase the effective surface coverage, which becomes higher than the ideal value of 0.5, and decrease the contrast between the non-inked and inked areas, the effect of the halation phenomenon is weaker at high *d/p*

values. Had these highest *d/p* values been obtained by increasing the thickness of the coating layer instead of decreasing the size of the halftone period, it is probable that the color difference would have been higher for the highest *d/p*, as was observed in the large scale experiment presented in Section 3.4.

It can be noted in Figure 73 that the ΔE_{00}^{*} was smaller for inkjet prints than for electrophotographic ones. This can have various origins, the first ones being that the nominal surface coverages were not identical for both processes and that the inkjet inks were less absorbing than the electrophotographic ones, leading to smaller contrasts between inked and non-inked areas. It is yet also very probable that the optical and mechanical dot gain differences between both processes also play a role. Depending on both dot gains, the impact of the halation phenomenon could be maximal for an inkjet *d/p* value different from the electrophotographic one.

4.5 Towards alternative calibration methods: Spectral reconstruction from RGB microscopic images

The multi-convolutive model presented in Section 3.2 can be calibrated through microscale spatial and spectral measurements of a non-coated halftone print. A major drawback of this method is that it requires a multispectral microscope able to measure the spatial and spectral reflectance factors of the uncoated prints. This device is rather rare, and the measurements are rather slow. The objective of this section is to determine, through simulations based on a dataset provided by GMG Color, whether a more common RGB microscope could be used to calibrate the model. The measurements would then be made simultaneously through the three filters of the Bayer matrix of microscope camera, i.e. the red, green, and blue filters (RGB), instead of the uncommon 13 optical filters which were used successively in the previous measurements.

The spectral reflectance factor of the prints needs to be reconstructed from the three RGB digital counts. This requires the print spectral reflectance factors to be fully described by only three values instead of 13, which corresponds to a dimensionality reduction. A method to get a dimensionality reduction is to perform a principal component analysis (PCA) (or equivalently a singular value decomposition, SVD) on a large set of spectral reflectance factors of prints. The PCA, the SVD, and the link between them, were explained by Hardeberg in [171] (especially in Section 6.4 and in Appendix A.2 and A.3 from [171]). Section 4.5.1 describes the PCA which was performed on a large dataset of reflectance factors of prints from GMG Color, as well as the performance of the spectral reconstruction it allowed through a dimensionality reduction. Section 4.5.2 describes the method and performances of a reconstruction of the dataset from simulated RGB values. Section 4.5.3 presents the performances of the multi-

convolutive model on reconstructed spectra from RGB values simulated from the multispectral microscopic measurements which were detailed in Section 4.3.2.

4.5.1 Principal component analysis and spectral reconstruction

For this analysis we focussed on the spectral reflectance factors of inkjet prints, printed with the Epson SC-P5000 inkjet printer of resolution 1440x720 dpi bidirectional mode, on the GMG premium glossy 250 proof paper, identically to Section 4.3.2. The test forms were printed in an uncalibrated CMYKOGV mode with GMG ColorProof, with a stochastic dithering. The ink set was composed of 10 inks from the original Epson Ultrachrome HDX ink set (without light black and matte black inks), including light cyan, light magenta and light black inks. The test forms were printed and measured by GMG color with the spectrophotometer CM-2600D from Konica Minolta of geometry di:8°, UV included on 39 wavelengths: [360 nm, 740 nm] with a 10 nm step. The dataset, provided by GMG color, was composed of 2170 reflectance factors issued from the Idealliance ECG (2019) test chart, visible in Figure 10.b, pages 1 and 2. To perform the PCA, the dataset was centred: the average spectrum on all the dataset was retrieved from each dataset spectrum.

The results from the PCA and SVD are displayed in Figure 74. In Figure 74.a are displayed the relative magnitude of the singular values from the SVD (each singular value is divided by the sum of singular values). This curve is not very steep compared to literature [171], therefore the prints have a rather high dimensionality, which was to be expected as there are 10 inks in the printing set. The accumulated energy ϵ_a of each eigenvector is displayed in Figure 74.b and the residual energy ϵ_r in Figure 74.c. For the k^{th} eigenvector out of $\xi = 39$, they are respectively defined as:

$$\epsilon_a(\mathrm{k}) = \frac{\sum_{i=1}^{k} \omega_i}{\sum_{i=1}^{\xi} \omega_i} \qquad 110$$

$$\epsilon_r(\mathrm{k}) = 1 - \epsilon_a(\mathrm{k}) \qquad 111$$

where ω_i is the singular value associated with the i^{th} eigenvector. These quantities enable to characterize the dimension of the dataset by evaluating the energy which is retrieved and respectively lost when only the k-first eigenvectors are taken into account [171]. If at least 90% of the reflectance variance are required to be retrieved, this dataset would require at least 6 eigenvectors. It is rather similar to the Munsell dataset which was analysed in [171].

A first step was to evaluate the accuracy of a spectral reconstruction using only the first three eigenvectors from the PCA, which are displayed in Figure 74.d, which corresponds to an accumulated energy of 75.5%. The method is to evaluate for each spectrum the scalar projection of this spectrum on the first three eigenvectors given by the PCA and reconstruct each spectrum of the dataset only from these three values and the corresponding eigenvectors. The difference between the reconstructed dataset and the original one is then estimated to evaluate the accuracy of the reconstruction from these three values.

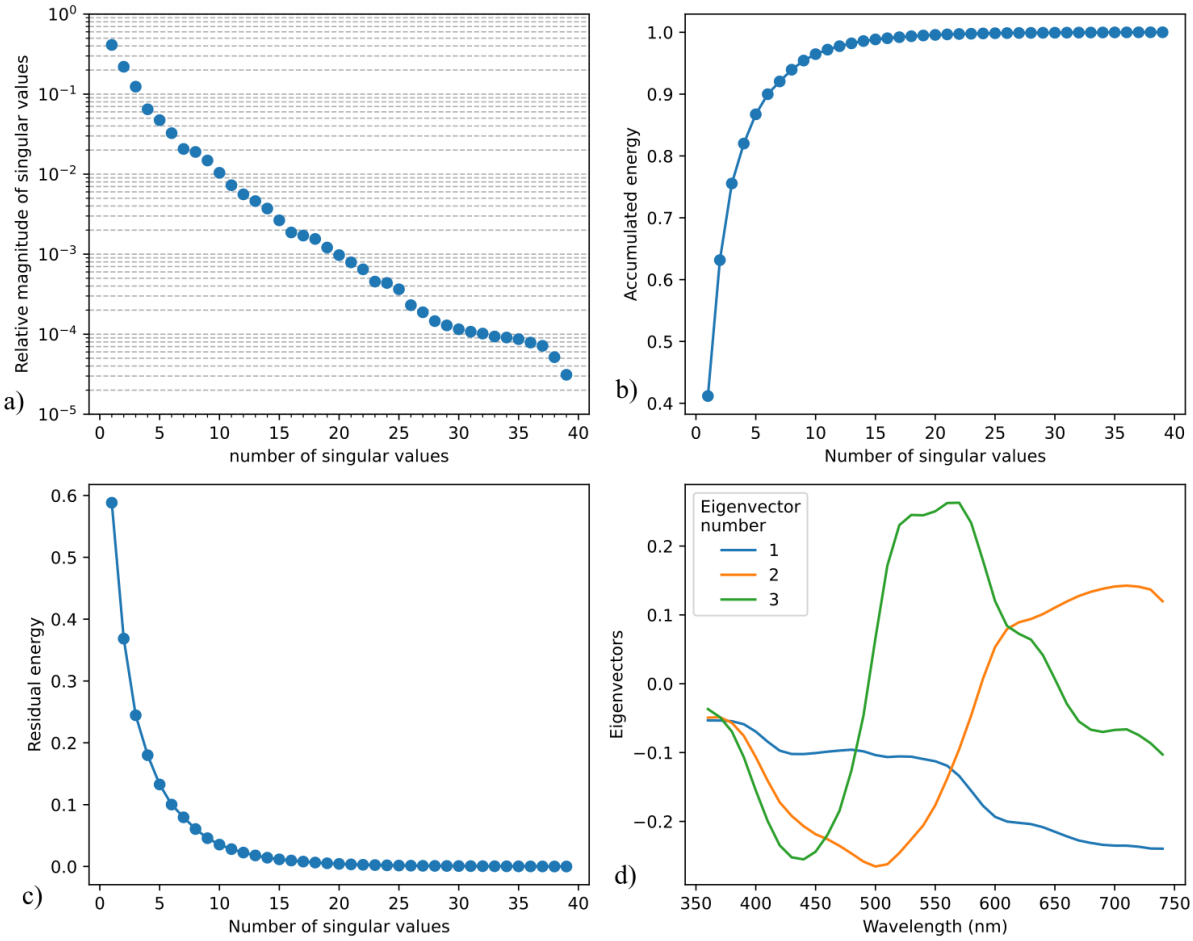

Figure 74. Results of the PCA. a) Relative singular values; b) Relative cumulative contribution of each singular value; d) The three first eigenvectors.

The projection matrix $\boldsymbol{T}$ is estimated with:

$$\boldsymbol{T} = \boldsymbol{XV} \tag{112}$$

where $\boldsymbol{X}$ denotes the matrix containing the dataset, of dimension $\nu \times \xi$ where the number of spectra is $\nu = 2170$, and where ξ is the number of wavelengths, ($\xi = 39$). $\boldsymbol{V}$ is the matrix containing the first three eigenvectors from the PCA, of dimension $\xi \times 3$. $\boldsymbol{T}$ contains three values for each spectrum, from which a spectral reconstruction of the original dataset can be performed:

$$\boldsymbol{X_3} = \boldsymbol{TV}^T \tag{113}$$

where $\boldsymbol{X_3}$ is the reconstructed dataset from the projection matrix and from the first three eigenvectors. ^{T} denotes the matrix transpose. All values of $\boldsymbol{X_3}$ were truncated to the [0, 1] range.

The average root mean square error between the original dataset, $\boldsymbol{X}$, and the reconstructed one, $\boldsymbol{X_3}$, was: $rmse = 0.034 \pm 0.026$, and the color difference between the two dataset was $\Delta E^*_{00} = 5.42 \pm 6.21$, with a maximal value $\Delta E^*_{00\,max} = 64.14$. This spectral reconstruction is then rather inaccurate.

4.5.2 Reconstruction from simulated RGB values

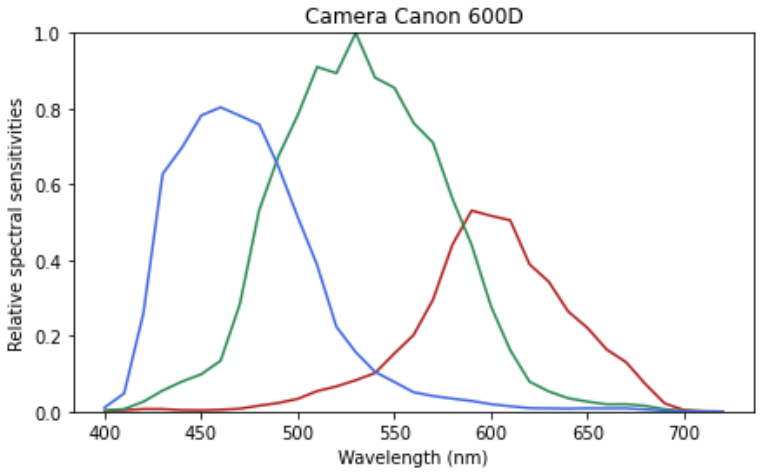

Figure 75. Spectral sensitivities of the camera.

In a second step, the accuracy of the spectral reconstruction was estimated using simulated RGB values. These values were simulated for each spectrum of the dataset by considering illuminant E (equal energy illuminant) and the spectral sensitivity of the Bayer filters of a commercial camera. These sensitivities came from [172], [173], the sensitivities of the camera Canon 600D were selected, they are displayed Figure 75. The RGB value matrix, denoted $\boldsymbol{U}$ is:

$$\boldsymbol{U} = \boldsymbol{X}\boldsymbol{Q}_{\boldsymbol{RGB}}^{T} \qquad 114$$

where $\boldsymbol{Q}_{\boldsymbol{RGB}}$ is the matrix containing the spectral sensitivities, of dimension $3 \times \xi$. In this Section, ξ, the number of wavelengths, is $\xi = 33$ as the spectral sensitivities are defined on a smaller range of wavelengths: [400 nm, 720 nm] with a 10 nm step. The spectral dimension of every other matrix is cropped accordingly.

The objective is to evaluate the accuracy of the reconstruction of $\boldsymbol{X}$, knowing the eigen vector matrix $\boldsymbol{V}$ and the spectral sensitivity matrix $\boldsymbol{Q}_{\boldsymbol{RGB}}$ of the camera. The reconstructed matrix, $\boldsymbol{X}_{\boldsymbol{RGB}}$, is:

$$\boldsymbol{X}_{\boldsymbol{RGB}} = \boldsymbol{U}\left(\boldsymbol{T}_{\boldsymbol{Q}}^{T}\right)^{-1}\boldsymbol{V}^{T} \qquad 115$$

where $\boldsymbol{T}_{\boldsymbol{Q}}$ is the projection matrix: $\boldsymbol{T}_{\boldsymbol{Q}} = \boldsymbol{Q}_{\boldsymbol{RGB}}\boldsymbol{V}$, of dimension 3×3, which is intrinsic to the print and camera system. All values of $\boldsymbol{X}_{\boldsymbol{RGB}}$ were truncated to the [0,1] range.

The difference between the original dataset matrix, $\boldsymbol{X}$, and the reconstructed one, $\boldsymbol{X}_{\boldsymbol{RGB}}$, was estimated: the root mean square error was $rmse = 0.036 \pm 0.036$, which is rather similar to the one previously obtained from the projection of the spectra on the first three eigenvectors. The color difference was: $\Delta E_{00}^{*} = 1.09 \pm 2.3$, with a maximal value $\Delta E_{00\ max}^{*} = 45.27$. The reconstruction is then far more accurate from a colorimetric point of view if it is performed

from RGB values, the filters of the camera may add spectral information and improve the reconstruction for wavebands at which the human vision is highly sensitive. Random original and reconstructed spectra of the database are displayed in Figure 76. It can be seen that the reconstructed spectra from the RGB values are closer to the original ones for small wavelengths.

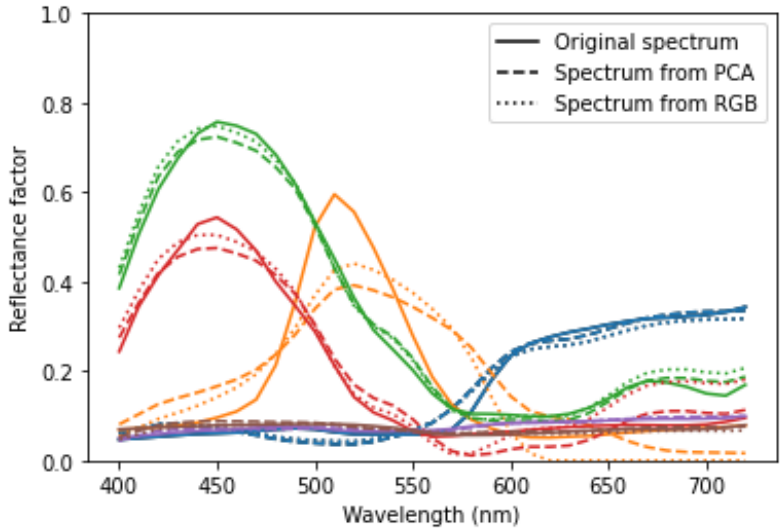

Figure 76. Random original and reconstructed spectra, the continuous lines correspond to the original spectra from the dataset, $\boldsymbol{X}$, the dashed lines correspond to the reconstructed spectra from their projection on the first three eigenvectors from the PCA, from $\boldsymbol{X_3}$, and the dotted lines correspond to the reconstructed spectra from the simulated RGB values, from $\boldsymbol{X_{RGB}}$.

4.5.3 Performance of the multi-convolutive model on reconstructed data

The objective of this section was to evaluate the accuracy of the multi-convolutive model on reconstructed spectral images from simulated RGB images. A scheme of the pipeline is presented in Figure 77.

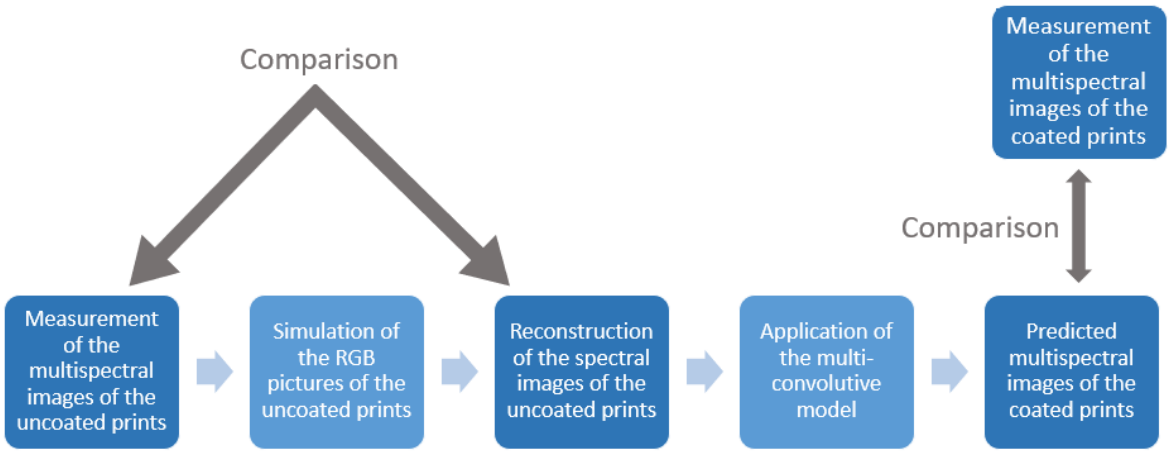

Figure 77. Scheme of the simulation pipeline.

Both the magenta and the cyan line halftones presented in Section 4.3.2 were tested: RGB images were simulated from the multispectral images of the uncoated prints which were captured with the multispectral microscope. The spectral sensitivities of the simulated RGB camera were the same as the ones displayed in Figure 75. From these RGB images, the spectral reconstruction was performed using the eigenvectors of the PCA, as detailed in section 4.5.2. The only difference lays in the fact that the eigenvectors were linearly interpolated to be described at the same wavelengths as the multispectral images. The multi-convolutive model was then applied to the reconstructed multispectral images, and the predicted multispectral images of the coated prints were compared to the experimental ones, measured with the microscope.

The color difference between the spatially averaged reflectance factor spectra from the reconstruction compared to the original multispectral images of the uncoated prints was in average $\Delta E_{00}^{*} = 1.30 \pm 0.83$ for the six cyan patches, and $\Delta E_{00}^{*} = 0.56 \pm 0.2$ for the magenta ones. The color difference between the multi-convolutive model predictions and the measurements of the coated prints was in average $\Delta E_{00}^{*} = 1.13 \pm 0.47$ for the cyan patches, and $\Delta E_{00}^{*} = 0.68 \pm 0.17$ for the magenta ones (patch 4 excluded). The measured, reconstructed, and modelled spectra are displayed in Appendix VIII. It can be noted that the PCA was performed on a dataset constituted in different conditions from the data which was tested here: the halftone pattern was different, as well as the measurement conditions. It is likely that if the PCA had been performed on prints more similar to the ones tested in this last part, the predictions would have been more accurate. In the current state, the accuracy of this method seems rather promising. In these simulations the illuminant was the equal energy one, in practice the spectrum of the illuminant would also need to be perfectly known and taken into account in matrix $\boldsymbol{Q_{RGB}}$.

4.5.4 Perspectives

The spectral reconstruction from RGB values presented in this section seems rather promising and would require testing through experiments. If the results prove to be not accurate enough, other calibration methods could be envisioned to measure the reflectance of prints both spectrally and spatially.

First, the RGB microscopic measurement of a halftone-printed patch could be linked with macroscale spectrophotometric ones of the printed patch and of the Neugebauer primaries composing it: the microscopic images yielding the spatial distribution and intensity of the Neugebauer primaries and the spectrophotometric measurements yielding the reflectance values of these Neugebauer primaries.

Secondly, a more thorough method could be to use an optical and statistical model to derive the spatial and spectral reflectance of halftone prints from the nominal halftone screen, as was performed on black and white prints in [25].The calibration of such a model for color prints

would yet demand a great number of hyperspectral microscopic measurements to characterize the printer, especially if the number of inks is large. This would require the microscopic measurement to be automated. A step towards this was made during this work but it still requires further testing and characterization. A common issue for the calibration of such models as presented in [25] and [80] is to accurately separate spatially the variously inked areas, as optical dot gain tends to blur the edges. Numerical methods have been used to try to reach such a separation. We further suggest two optical methods: the first one would be to rely on microscopic white light interferometry to capture the structure of the halftone print; and the second one would rely on measurements of the light specularly reflected by inked areas and paper. If the paper is rather matte and the inked areas rather smooth, the amount of light specularly reflected towards the sensor should be different for inked areas as for paper. The light specularly reflected by inked areas can also be colored, due to the bronzing effect [28], [174], which could also increase the difference between inked and non-inked areas and help to identify the ink. Such specular measurements could be performed by capturing the reflectance factor of prints both with the analyser and polarizer in crossed configuration (diffuse light) and in parallel configuration (specular and diffuse light). The specular component could be retrieved by subtracting the first measurement from the second one.

Thirdly, in Section 3.5, it was shown that the Yule-Nielsen model predicted rather accurately the reflectance factor of coated large-patterned halftone prints. It remains to be tested for prints subject to optical dot gain. A broader study could enable to find a fitting curve for the Yule-Nielsen parameter, n_{YN}, which would enable us to use the Yule–Nielsen model to predict the coated halftone reflectances in an easier manner than with the multi-convolutive model.

4.6 Conclusion

In order to predict the color change induced by the addition of a coating layer on microscale halftone prints impacted by the optical and mechanical dot gain, a multispectral microscope has been developed. This device enables to characterize the spatial and spectral reflectance of prints at a microscale. Its spatial resolution is 1.386 µm/pixel and its spectral resolution is 25 nm, with a geometry 0°:0°, specular excluded. Its calibration, originally performed for electrophotographic prints, was the most delicate step in our protocol. Its was checked by comparing the average spectral reflectance computed over a spectral image and the spectral reflectance measured with a standard spectrophotometer for color applications satisfying the recommendations by the CIE. To obtain comparable reflectance factor measurements between the spectrophotometric ones, with a geometry di:8°, and the microscopic ones averaged over the spatial dimension (with the addition of a specular component of 0.04), a calibration of the microscope was performed, using a glossy spectralon. The average color difference between

the spectrophotometric and the microscopic measurement systems on electrophotographic prints was $\Delta E_{00}^{*} = 1.02 \pm 0.49$. The rather good agreement between the two measurement systems enabled to validate the microscopic measurements (of resolution 1.386 µm per pixel), and to overcome the challenge of linking microscale measurements with macroscale measurements.

The microscale spatial and spectral measurements captured with this device were used in the calibration of the multi-convolutive model presented in Section 3.2. This allows, for any type of halftone, to predict its spatial and spectral reflectance once coated. The predictions were compared to measurements in two experiments, one with electrophotographic prints and one with inkjet prints, in collaboration with GMG Color. In the electrophotographic experiment, the predictions had an accuracy of $\Delta E_{00}^{*} = 0.95 \pm 0.39$ compared to the measurements, it was $\Delta E_{00}^{*} = 0.68 \pm 0.28$ in inkjet. These experiments allowed to validate the multi-convolutive model and its calibration device for microscopic prints. These experiments to validate the model at a microscale were performed only on glossy coatings as using matte ones would have been complex: the share of light specularly reflected by the interface towards the spectrophotometer sensor is difficult to estimate, and the pictures of the coated prints by the multispectral microscope could have been blurred by this interface, making the comparison with the prediction results complex. Yet, as detailed in Section 3.8, now that the multi-convolutive model has been validated, it can be used to predict the color change induced by coatings of both surface finishing, as long as the light portion externally reflected by the interface towards the sensor is known.

In these experiments, the effects of the dot gain of the prints as well as the additional one caused by the coating layer were visible both spectrally and spatially on the different halftones. For the large patterns, the coating layer further blurred the edges between inked and non-inked areas, visible both in the pictures and in the profiles. For thin patterns, the dot gain already within the non-coated prints decreased the amplitude range between inked and non-inked areas compared to large pattern, and completely blurred the edges between these two areas. Therefore, the addition of a coating layer had few impacts on the print reflectance. It is as if light could already propagate long distances within the substrate, and the addition of a transparent layer offered almost no additional light propagation. Consequently, the color difference between non-coated and coated prints reached a maximum for a period around 0.381 mm and a coating thickness around 22.1 µm, for which the period was small enough so that the addition of a coating layer enabled light to travel from an inked area to another one, and large enough so that this effect was not already enabled by the optical dot gain of the non-coated print.

As the multispectral microscope required to calibrate the multi-convolutive model is a rather rare instrument, simulations were performed to test another calibration method. This alternative method would require an RGB microscope and is performed through spectral reconstruction thanks to a base of eigenvectors issued from the principal component analysis of the printing system. The simulations showed rather promising results for this method. It yet requires the spectral sensitivity of the microscope as well as the illuminant spectrum to be known.

In practice, the multi-convolutive model, its calibration with the multi-spectral microscope, and the knowledge acquired on the interactions between dot gain within the prints and the additional one caused by the coating layer, could lead to various applications, some of them are presented in the next chapter.

Chapter 5. Applications and conclusions

This Chapter first presents applications of the halation phenomenon and of its prediction in Section 5.1. Section 5.2 is an overall conclusion of this work.

5.1 Applications

The knowledge and prediction of the halation phenomenon could find two main application fields in the printing industry: for the color management and for the security printing domains. The multi-convolutive model allows to predict the change of prints coated with a transparent layer; a method for an inverse approach for color management is presented in Section 5.1.1. Section 5.1.2 presents printed test forms playing on the halation phenomenon to hide and reveal images, which is a step towards anticounterfeiting applications.

5.1.1 Inverse approach: How to print a target color when the print is coated?

The optical model presented in Section 3.2 has been tested for halftone prints in Chapter 1. It has been shown that the reflectance factor of coated prints can be predicted from the spatial and spectral reflectance factor of uncoated prints. In fixed printing conditions, how can a desired color be rendered when the print is coated? If the printing conditions are set (set lpi, halftoning technique, printing materials, known coating thickness, …), the underlying question is: which nominal surface coverages of each color channel should be implemented to produce a target color once the print is coated?

A first approach would be to print a great number of color patches, coat them, measure their reflectance factor with a spectrophotometer, and use interpolation to find an accurate set of nominal surface coverages. This approach can be tedious, especially if the ink set is large, as explained in Section 2.1.5.

The optical approach we suggest, would be to print calibration patches and measure their spatial and spectral reflectance factor with a hyperspectral microscope. These calibrations patches would have ink surface coverages of: 0, 0.25, 0.5, 0.75, and 1, potentially with ink superimpositions, similarly to the calibration of the halftone color prediction models detailed in [64] (Section 7.5). In each picture, the average spatial and spectral intrinsic reflectance factor would be estimated over all the halftone patterns in the picture. This would produce a statistical map of the intrinsic reflectance factor of the prints taking into account the mechanical and optical dot gains. The multi-convolutive model can be applied on them to retrieve the spatial reflectance of the coated calibration patches. Interpolation on the spatial and spectral intrinsic reflectance factors can be performed to predict with the multi-convolutive model the reflectance

factor of any coated patch of intermediate surface coverages. This predicted database could be used to retrieve the nominal surface coverages minimizing the difference between the target color and the predicted ones.

In the future, experiments would be needed to compare these two approaches of color management on coated prints.

5.1.2 Exploiting the coating-induced color changes: hidden image

The Sections 3.7.3 and 4.4 showed that the halftone pattern and the dot gain due to scattering within the substrate can have a strong impact on the color change caused by the addition of a coating layer. The objective in this section is to use the dot gain within the substrate and the halation phenomena to find two halftone patterns, one for the image and one for the background, such that under one clear coating layer they appear the same, whereas by adding or removing a clear coating layer, they appear differently, revealing a hidden image. Such a system could find applications in the anticounterfeiting domain.

To generate such a hidden image, one of the halftone patterns should be only slightly impacted by the darkening caused by the halation phenomenon (denoted *pattern 1*) whereas the other one should be significantly impacted (denoted *pattern 2*). We then chose two halftones consisting of line patterns with different periods. The choice of periods was the crucial element for this application as the halation phenomenon fundamentally depends on it. They were comprised between two limits: the smallest printable period is limited by the resolution of the printer, and the largest period is limited by the eye perception: if the periods are too large, the pattern lines become perceptible by the naked eye.

For *pattern 1*, the period was one of the smallest ones we could accurately print, it was p_1 = 0.180 mm, such that this pattern was highly impacted by the optical dot gain within the substrate, leading to small color differences by addition of clear coating layers, as presented in the simulations in 3.7.3 and in the experiments in Section 4.4, (the results are reproduced in Figure 78.b). Furthermore, for a coating thickness around $d = 24$ µm that we used, having a small period enabled to reach a rather high *d/p* ratio, $d/p_1 = 1.3 \cdot 10^{-1}$, above which the increase of the coating thickness has a small impact on the print reflectance factor, as shown in the simulation results in Section 3.7.2 (also reproduced in Figure 78.a). Indeed, adding a second coating layer results in a *d/p* ratio of $2d/p_1 = 2.6 \cdot 10^{-1}$ for which the reflectance factor is rather similar to the one obtained with only one layer. It can be also noted that the shape of *pattern 1* does not really matter as long as the period is small enough for the reflectance factor to be relatively unaffected by addition of coating layers, one could also have chosen an FM halftoning technique.

On the contrary, for *pattern 2*, which was designed such that it is highly impacted by the halation phenomenon, a line pattern was specifically chosen as it is the pattern shape for which the reflectance values have the highest range, and as, at a given coating thickness, its low

reflectance factor limit is reached for smaller halftone periods than for any other shape. The period of *pattern 2* was rather high, p_2 = 0.479 mm, which yields $d/p_2 = 5.0 \cdot 10^{-2}$ for a coating thickness around d = *24* µm, so that the reflectance factor of the halftone print varies significantly by adding a second coating layer ($2d/p_2 = 1.0 \cdot 10^{-1}$) and by removing one, as can be seen in Figure 78.a. Furthermore, with this period, the print and the halation phenomenon are rather unaffected by the optical dot gain within the substrate, as shown in Figure 78.b. In Section 3.7.1, in Figure 44, it was shown that the surface coverage optimizing the halation phenomenon is 0.5, therefore, the surface coverages of *pattern 1* and *pattern 2* were selected so that the effective surface coverage of *pattern 2* was around 0.5 and so that the two patterns had the same appearance under one coating layer.

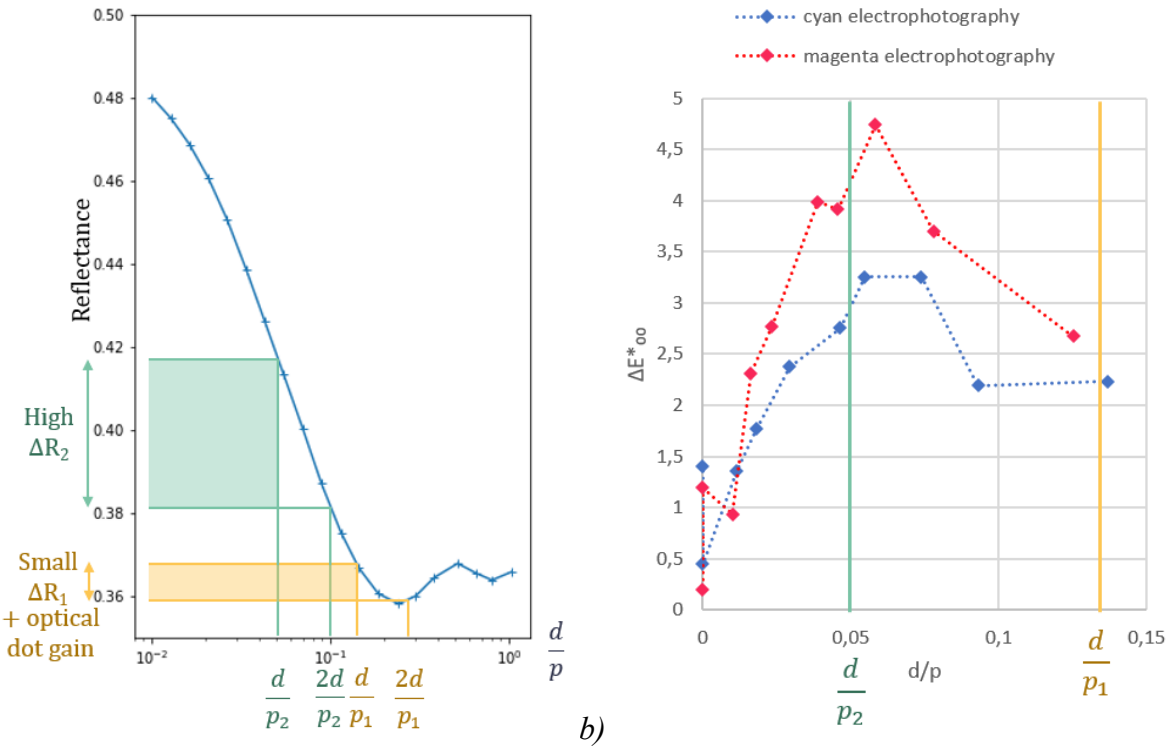

Figure 78. a) Simulation of the reflectance factor differences, ΔR1 and ΔR2, respectively of the thin line halftone (pattern 1) and the large line halftone (pattern 2), which would be obtained by addition of a coating layer if the printed patterns were identical to the line pattern simulated in Section 3.7.2. b) Color change due to the addition of a coating layer for electrophotographic prints of various periods, extracted from Section 4.4. For high d/p *the color change is reduced due to dot gain (both optical and mechanical).*

Based on the observations above, the thin pattern, *pattern 1*, was designed with a 6 × 6-pixel threshold matrix displayed in Figure 79.a. The large pattern was designed with a 16 × 16-pixel threshold matrix displayed in Figure 79.b. The lines were inclined by a 45° angle to be less detectable by the naked eye than horizontal or vertical lines. The printer was a Xerox Versant 180, printing at 600 dpi. The substrate was a white glossy-coated paper (the same as in Section

4.3.1). The coater was the laminator DRY 350 from RBS, coating a smooth transparent foil composed of OPP of thickness approximately equal to 24 µm.

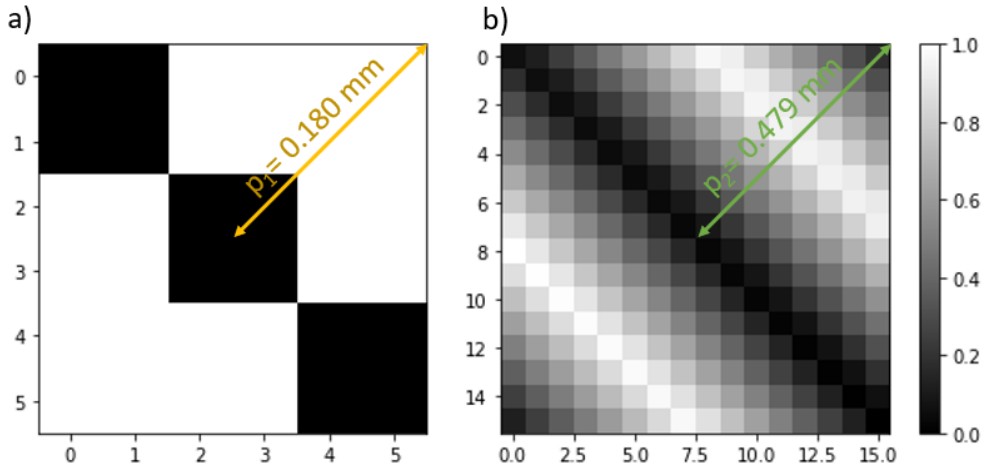

Figure 79. a) Threshold matrix of the thin pattern, pattern 1*; b) threshold matrix of the large pattern,* pattern 2*. For a given halftone surface coverage, all the pixels of the threshold matrix having a grey value inferior to this surface coverage are inked.*

The nominal surface coverage of the thin pattern, *pattern 1*, was set to 33.3%, which results in an effective surface coverage around 50% due to mechanical and optical dot gain within the substrate. As the *pattern 1* is more subject to mechanical and optical dot gain within the substrate than *pattern 2*, the nominal surface coverage of *pattern 2* should be higher for the two halftones to have the same appearance. The surface coverage of *pattern 2* was evaluated experimentally through spectral measurements of lookup tables of prints coated with one clear layer. The spectral measurements were performed with the spectrophotometer CM 2600d from Konica Minolta (di:8°, 8 mm aperture, UV included). The selected surface coverages of the large lines were the ones minimizing the color difference ΔE_{00} under D65 illuminant between the image and the background, coated with one layer.

Two test forms were designed on this basis: one composed of black lines printed on a white paper with a QR-code image, presented in top position in Figure 80, the other one mainly composed of superimposed cyan and magenta lines of different periods with an elephant image, displayed at the bottom position in Figure 80. In this cyan and magenta test form, to better adjust the appearance match of the two halftones areas (image and background), yellow dots were added to the image area. Cyan and magenta lines had different orientations to prevent Moiré effects. The nominal surface coverage of the large black lines was found to be 54%, the one of the large magenta lines was 52%, the one of the large cyan lines was 53%, and the one of the yellow dots was 3%. The difference of nominal surface coverage compared to *pattern 1* (which was set to 33.3%) is significant and visible in the nominal halftones presented in Figure 80, yet the difference is much less visible on the prints due to dot gains. It can be noted that as

the prints involved only one or two inks, it was easier to estimate these surface coverages through lookup tables by measuring printed patches of various surface coverages and not through an optical approach using the multi-convolutive model. The performance and predictions of the multi-convolutive model on these prints were nonetheless estimated, the results are displayed in Appendix IX.

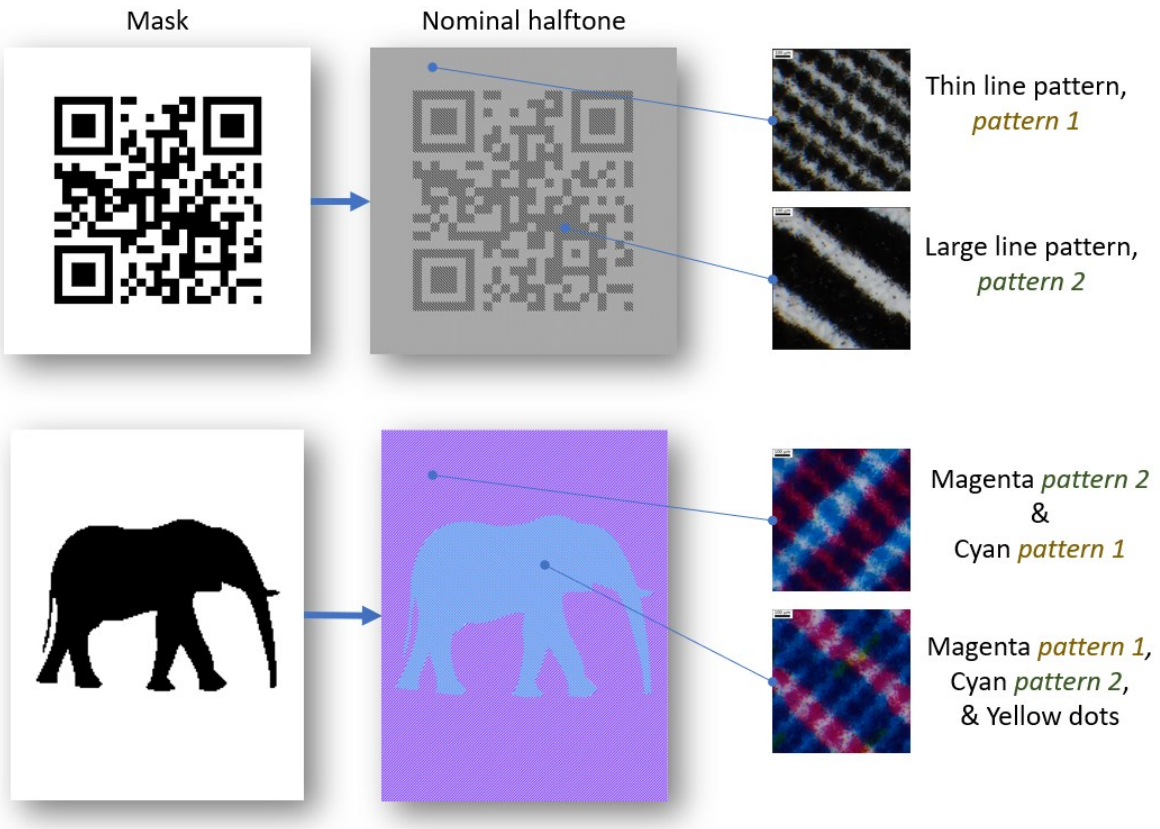

Figure 80. Top: design of the test form composed of black lines with a QR-code mask, bottom: design of the test form mainly composed of cyan and magenta lines, with an elephant mask.

Three identical test forms were printed for each image: one was not coated, the second was coated with one layer, and the third was coated with two layers. The objective was to have the smallest possible color difference between the image and the background for one coating layer, and a visible color difference for other coating thicknesses.

The color changes between the image and the background for the different coating thicknesses can be characterized with macroscale spectrophotometric reflectance factor measurements. The reflectance factor around the blue disks in Figure 80 was measured on each test form with the spectrophotometer i7 from X-Rite (di:8°, 6 mm measurement aperture, 17 mm illumination

aperture, UV excluded, average on 7 consecutive measurements). The differences of reflectance factor between the background and the image are displayed in Figure 81 for each coating layer. The CIE1976 L*a*b* values, estimated for the D65 illuminant and a perfect white as reference, are displayed in the a*b* plane and the L*C* plane in Figure 82.

In this figure, a negative reflectance factor difference implies that the background has a smaller reflectance than the image, thus that it appears darker than the image. In the QR-code picture, the background is darker than the image when the print is non-coated, they have a similar reflectance factor when the print is coated with one layer (the reflectance factor difference is near 0), and the image is darker than the background when the print is laminated two times. This is also visible in the L*C* plane in Figure 82. This is due to the fact that the large lines composing the image are more impacted by the darkening caused by the halation phenomenon than the thin lines composing the background. In terms of color difference between the QR-code image and its background, estimated with ΔE_{00}^* under D65 illuminant [170], there is a difference of ΔE_{00}^* = 1.38 without coating, ΔE_{00}^* = 0.99 with one coating layer, and ΔE_{00}^* = 1.25 with two coating layers. The image can then be rather successfully hidden with one coating layer and revealed by adding or removing a coating layer.

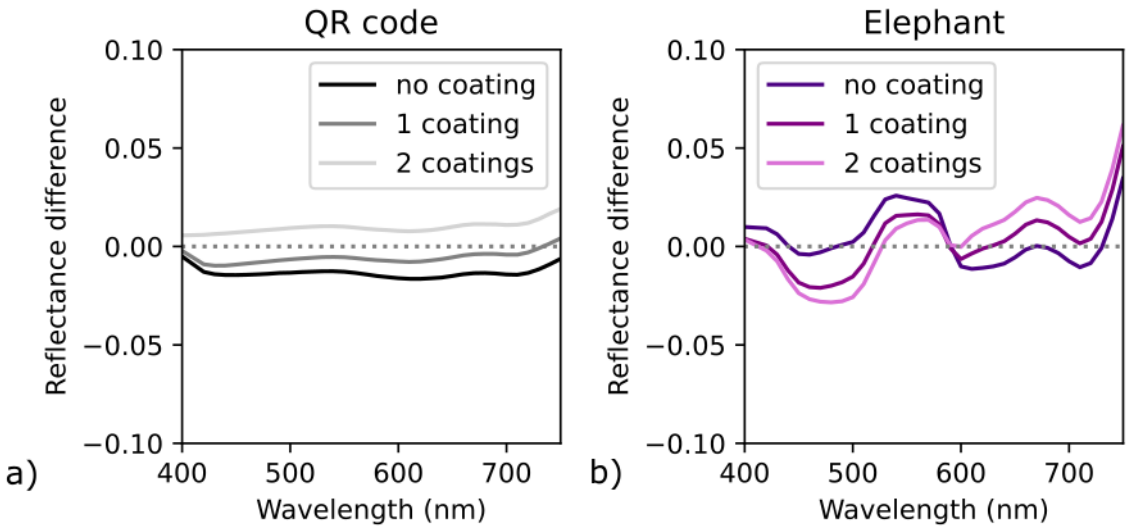

Figure 81. Difference of reflectance measurements between the background and the image for each coating layer. a) black and white QR-code picture; b) color elephant picture.

For the color elephant test form, the color matching with one coating layer was more difficult to obtain. The difference of reflectance factors between the background and the image is farther to zero than the one of the QR code. Metamerism between the elephant and the background was observed both for the non-coated test form and for the one coated with one layer, depending on the illumination. As the elephant image is composed of large cyan lines, its reflectance factor

at long wavelengths tends to decrease by addition of coating layers. Similarly, the background, composed of large magenta lines, absorbs more light at short wavelengths as the coating thickness increases. As a result, the reflectance factor difference shown in Figure 81.b decreases by addition of coating layers at short wavelengths and increases at long wavelengths. The hue shift of the image is visible in the a*b* plane in Figure 82, but it is less visible for the background. The color difference between the elephant image and the background under D65 illuminant is $\Delta E_{00}^{*} = 3.02$ without coating, $\Delta E_{00}^{*} = 1.73$ with one coating layer, and $\Delta E_{00}^{*} = 2.32$ with two coating layers.

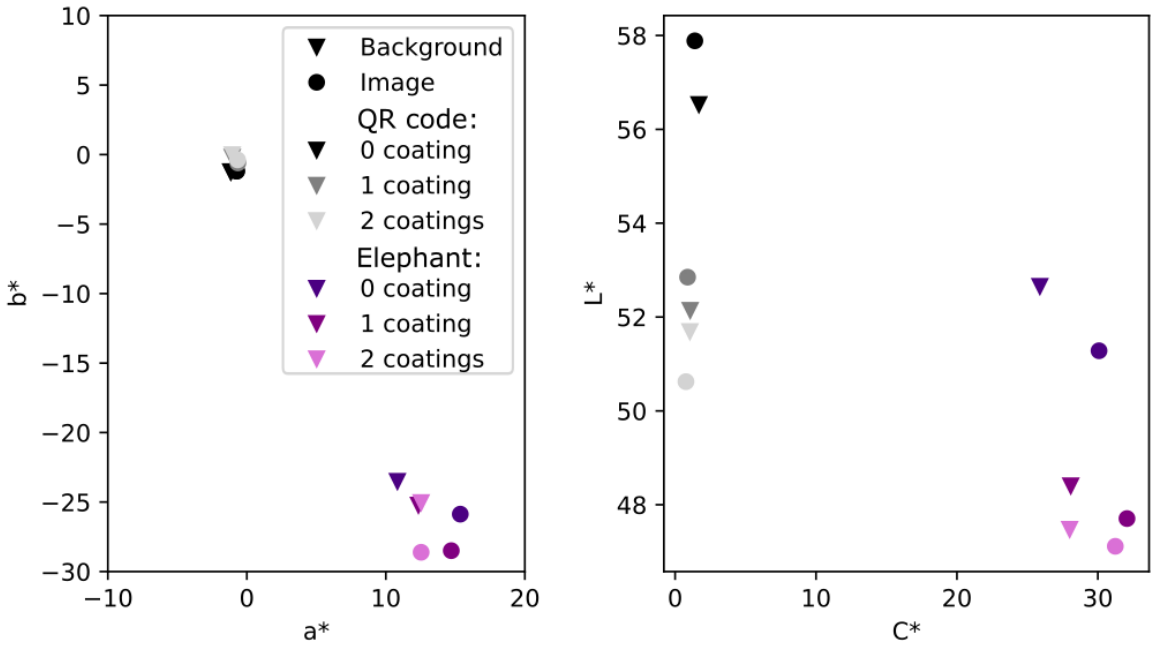

*Figure 82. CIE1976 L*a*b* values of the image and the background for the different test forms and the various coating layers.*

The generated color shifts are visible in the pictures displayed in Figure 83. It can be noticed that the pictures do not perfectly reflect the visual appearance of the prints, especially as the printed lines tend to interfere with the anti-aliasing filter of the camera. The middle pictures appear less contrasted than the others, the image hiding is then rather successful for the pictures with one coating layer. For the QR-code picture, the images appear lighter than the background on the image without coating, and darker than the background with two coating layers. The image is then rather well revealed by addition or removal of a coating layer. For the elephant pictures, the elephant image shifts from pinkish on a bluish background for the test form without coating, to a blue elephant on a pinker background with two coating layers, revealing also the image hidden under one coating layer.

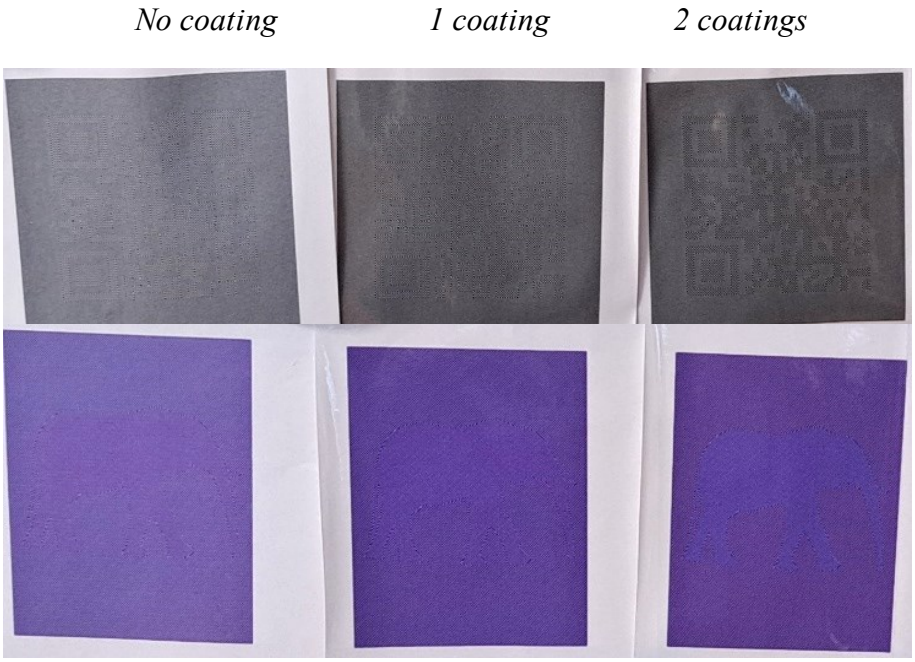

Figure 83. Pictures of the test forms. Top: black and white QR code test form, bottom: color elephant test form. Left: no coating layer, middle: one coating layer, right: two coating layers. The surface coverages were adjusted to have a color match between the image and the background with one coating layer.

Lastly, it was observed that the hidden image could also be revealed by illuminating the test forms from the backside (in transmission mode) as displayed in Figure 84. With this illumination mode, light rays transit in the substrate before being possibly absorbed by ink or reaching the eye. This significantly reduces optical dot gain within the print due to light diffusion inside the substrate. In reflection mode, thin lines (i.e., *pattern 1*) were more impacted by optical dot gain from the substrate than large lines (i.e., *pattern 2*) as thin lines have a longer perimeter. Thus, in transmission mode, as there is less optical dot gain, thin lines appear significantly lighter than large lines, revealing the hidden image. The effect is even more pronounced when the print is coated due to the halation phenomenon.

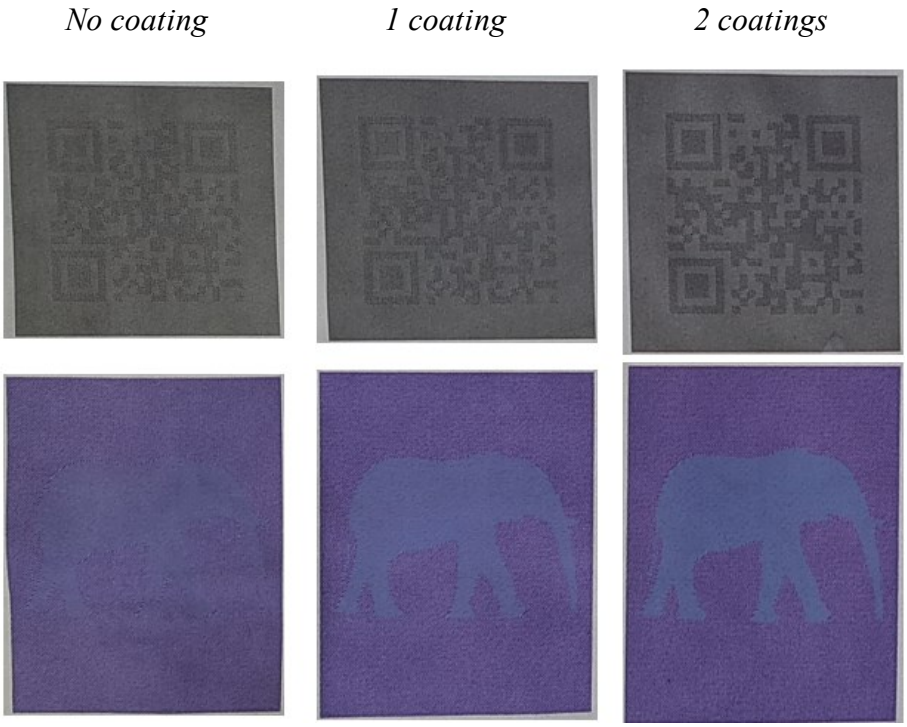

Figure 84. Pictures of the test forms in transmission mode (the pictures of one test form with the various coatings were extracted from one picture, all pictures of one test form were subject to the same color management by the camera).

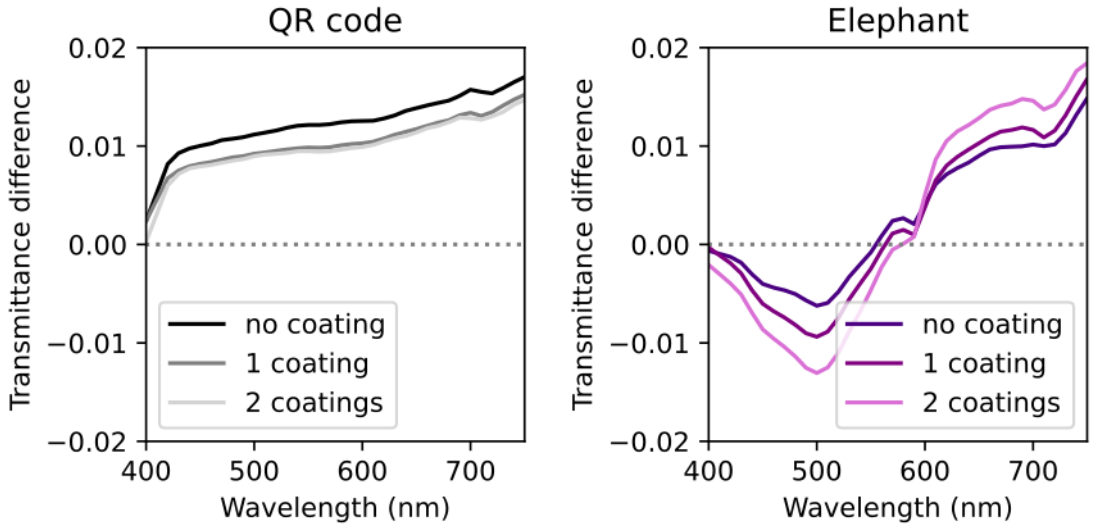

Figure 85. Difference of transmittance measurements between the background and the image for each coaating layer. a)QR-code image; b)colored elephant image.

This phenomenon was also characterized by spectrophotometric measurements in transmission mode (with the same apparatus and in the same conditions as in reflection mode) and the difference of measurement between the background and the image are displayed in Figure 85. The results were not really conclusive for the black and white QR code test form: visually, for each additional test form, the difference between the background and the image increases. Yet the transmittance differences displayed in Figure 85.a show that the measured difference decreases when layers are added. This might be due to heterogeneities in the paper, especially as the measurement area of the image is rather small. Further testing is needed to fully understand this difference. For the elephant test form, the measured transmittance differences are coherent with the observations: when adding a coating layer, the background becomes redder while the image becomes bluer.

The observations on the influence of the halftone shape and profiles on the darkening caused by the coating layer enabled to design pictures containing a hidden image. The image was hidden when coated with one lamination layer and could be revealed by adding or removing a coating layer, or by observing the picture in transmission mode. To hide this image, two halftone patterns were designed, one for the image and one for the background, so that the reflectance of one of the halftones was noticeably impacted by the halation phenomenon and the other one much less impacted. We could rather successfully adjust the period and surface coverage of line halftones to obtain the desired results, both in terms of darkening with the QR-code picture, and in terms of hue, with the Elephant picture. Adjusting the period allowed to act both on the halation phenomenon, which depends on the d/p ratio, and on the dot gain effect due to light scattering within the substrate, which tends to impact more halftones having a small period. This could be used towards anti-counterfeiting applications in the future.

Other systems playing on the halation phenomenon can be envisioned: if a thick transparent layer with lines printed on its lower side is set in optical contact with a white diffuser also printed with lines, changing the angle between the two foils would generate a moiré pattern of period depending on the angle between the two foils. As the halation phenomenon depends on the period of the printed pattern, the reflectance of the system and its darkening would undoubtedly depend on the angle between the two foils. Similarly, if lines are printed on a stretchy white diffuser in optical contact with a stretchy transparent layer, different colors should be obtained be stretching the system, as the period of the lines becomes longer and as the coating becomes thinner.

The halation phenomenon could also be used to measure the thickness of thin transparent layers, by depositing it on a known halftone pattern of various periods (similar to the 1951 USAF resolution test chart) and analyzing the color variations.

5.2 Conclusions

From the early age of photography to nowadays coated prints, the halo-shaped internal reflection within coating layers continues to modify the appearance of reproduced images. Indeed, for a halftone print, it increases the probability for light to be absorbed by inked areas. This halation phenomenon can darken the print colors and make them more saturated as the light absorption occurs at wavelengths at which the ink absorbs.

The halo-shaped propagation phenomenon, originally put into equations by Simonot and co-workers for a uniform substrate [6], was the foundation for an optical model we developed to predict the reflectance factor of coated prints, Section 3.2. This model relies on multiple convolutions between the spatial and spectral intrinsic reflectance factor of the print and the halo-shaped point spread function caused by one internal reflection on the upper interface of the coating layer.

The impact of the halation phenomenon on the color of a non-uniform substrate and the predictions by the multi-convolutive model were evaluated experimentally in conditions where the halation phenomenon was the main optical phenomenon at stake, in Sections 3.4 and 3.5. It was shown that the halation phenomenon did impact the color of coated non-uniform substrate. It was particularly shown in Section 3.4 that increasing the thickness of a clear coating layer over a line-halftoned substrate did darken its color, and this even if the layer was perfectly clear and even if the interface with air was perfectly smooth and identical for the different coating thicknesses. The predictions by the multi-convolutive model matched rather well with the measurements, both in the spatial dimension with an optical blur of the halftone pattern (Section 3.4) and in the spectral dimension (Section 3.5).

The impact of various parameters on the color change predicted by the multi-convolutive model was evaluated, namely the optical indices of the coating layer and of the printed substrate (Section 3.6), the surface coverage, the shape of the halftone patterns, and their reflectance profile (Section 3.7). It was shown that the halation phenomenon was stronger for high optical indices, for surface coverages around 0.5, for line patterns, and for a sharp-edged profile. In Section 3.8, it was shown through simulations and experiment that the halation phenomenon also occurred with matte coating layers (i.e. rough interface with air), with a similar halo-shaped internal reflection as for glossy coating layers (i.e. smooth interface with air). Therefore, as long as the light externally reflected by the interface towards the sensor is known, the multi-convolutive model can also be applied to matte-coated prints.

There were however two entangled issues with the multi-convolutive model: first, it relies on the spatial and spectral intrinsic reflectance factor of the non-uniform substrate, which, in the case of a print varies at the microscale and cannot be measured with a spectrophotometer; secondly, prints are usually subject to optical dot gain due to light diffusion within the substrate, an optical phenomenon which may interact with the halation phenomenon. It was then required

to test the multi-convolutive model for prints subject to optical dot gain. Furthermore, both optical and mechanical dot gains have an impact on the print spatial and spectral intrinsic reflectance factor at the microscale, making it complex to simulate this intrinsic reflectance. To address all these issues, a multispectral microscope was developed to enable a direct measurement of the spatial and spectral reflectance factors of prints. It has a spectral resolution of 25 nm, and a spatial resolution of 1.386 µm/pixel.

The measurements performed by this multispectral microscope at the microscale were calibrated and compared to spectrophotometric ones at the macroscale. Both devices showed a rather good agreement for the electrophotographic prints it was originally designed for, with an average color difference between the two devices of $\Delta E_{00}^{*} = 1.02 \pm 0.49$ (Section 4.1). This microscale/macroscale agreement was less performing for inkjet prints which were tested afterwards. This might be caused by a BRDF difference between the spectralon used for calibration and the substrate of the inkjet prints and would require further testing.

The experiments detailed in Sections 4.3 showed that the predictions of the multi-convolutive model for prints subject to dot gain were fairly accurate both for electrophotographic and for inkjet prints, with an average color difference $\Delta E_{00}^{*} = 0.95 \pm 0.39$ for electrophotographic prints and $\Delta E_{00}^{*} = 0.68 \pm 0.28$ in inkjet. It also showed that the approximation in the model consisting in considering independently the halation and the optical dot gain phenomena was a rather reasonable approach. These experiments proved that the halation phenomenon was at the origin of a color change in coated microscale prints and that it could be optically predicted both spatially and spectrally. The multispectral microscope used for the calibration of the multi-convolutive model is an uncommon measurement tool. Other calibration methods were suggested as perspectives in Section 4.5.

This work provided theoretical and experimental tools to better understand the color change occurring when a print is coated with a transparent layer. The optical multi-convolutive model we developed could be used for color management purposes in the printing industry. Furthermore, the knowledge acquired on the phenomenon and the impact of various parameter (among which the optical dot gain) led to a curious application where images can be hidden or revealed only by adding a clear layer on them. This could find perspectives as an anticounterfeiting solution.

Communications

Journal articles

F. Dailliez, M. Hébert, A. Blayo, L. Chagas, and T. Fournel, 'Impact of a Transparent Coating on the Reflectance of a Line Halftone Pattern', *Coatings*, vol. 11, p. 1465, Nov. 2021, doi: 10.3390/coatings11121465.

F. Dailliez, M. Hébert, L. Chagas, T. Fournel, and A. Blayo, 'Use of Multispectral Microscopy in the Prediction of Coated Halftone Reflectance', *Journal of Imaging*, vol. 8, no. 9, Art. no. 9, Sep. 2022, doi: 10.3390/jimaging8090243.

Conferences with proceedings

M. Hébert, F. Dailliez, and L. Simonot, 'Why a clear coating modifies halftone color prints', presented at the Material Appearance, IS&T Electronic Imaging Symposium, Online, Jan. 2021.

F. Dailliez *et al.*, 'Impact of a coating layer on the appearance of various halftone patterns', in *Electronic Imaging*, Society for Imaging Science and Technology, Jan. 2023, pp. 1–7. doi: 10.2352/EI.2023.35.15.COLOR-204. (with an oral presentation)

F. Dailliez, M. Hébert, L. Simonot, L. Chagas, A. Blayo, and T. Fournel, 'Color change of printed surfaces due to a clear coating with matte finishing', presented at the London Imaging Meeting 2023, Jun. 2023. Accessed: Jul. 10, 2023. [Online]. Available: https://hal.science/hal-04146250 (with a poster)

Book chapters

F. Dailliez, M. Hébert, L. Simonot, L. Chagas, A. Blayo, and T. Fournel, 'Impact of a Transparent Layer on the Color of a Non-Homogeneous Colored Support', in *Radiometry of wet surfaces: When Water Matters*, in Institut d'Optique Graduate School Advanced Textbook. EDP Sciences, 2023.

L. Dolin, F. Dailliez, and L. Simonot, 'Determination of Water Layer Thickness from Laser Halo', in *Radiometry of Wet Surfaces: When Water Matters*, Science Press, EDP Sciences.in Institut d'Optique Graduate School Advanced Textbook. 2023, pp. 85–102.

Oral presentations

F. Dailliez, M. Hébert, L. Chagas, T. Fournel, and A. Blayo, 'Effet et modélisation d'une couche transparente sur un imprimé en demi-ton', University of Poitier and GDR Appamat, Optique des matériaux, 9th April 2021.

F. Dailliez, M. Hébert, L. Chagas, T. Fournel, and A. Blayo, 'How does a clear layer modify the appearance of a halftone print?', EUR – MANUTECH SLEIGHT, SLEIGHT Science Event #6, 6th July 2021.

F. Dailliez, M. Hébert, L. Chagas, T. Fournel, and A. Blayo, 'Verifying the optical effect of a clear coating on the halftone patterns of printed surfaces by using multispectral spectroscopy', GDR Appamat, CCIW (Computational Color Imaging Workshop), 9th June 2022.

F. Dailliez, M. Hébert, L. Chagas, T. Fournel, and A. Blayo, 'Halo à l'eau : la recette d'un mystérieux effet visuel', GDR Appamat, Webinaire: Radiométrie des surfaces mouillées, 1st June 2023.

References

[1] H. Kipphan, *Handbook of Print Media*. Springer, 2001.

[2] G. Rogers, 'Optical dot gain in a halftone print', *Journal of Imaging Science and Technology*, vol. 41, no. 6, pp. 643–656, Nov. 1997.

[3] 'The Future of European Printing to 2027 | Market Reports & Research', Smithers. Accessed: Apr. 04, 2023. [Online]. Available: https://www.smithers.com/services/market-reports/printing/the-future-of-european-printing-to-2027

[4] J. Hoffstadt, 'Simulating color changes due to coating of offset prints', *Conference on Colour in Graphics, Imaging, and Vision*, vol. 2004, no. 1, pp. 489–493, Jan. 2004.

[5] 'The Astrographic Telescope: a story of restoration- Part One', Inside the Collection. Accessed: Aug. 26, 2022. [Online]. Available: https://www.maas.museum/inside-the-collection/2014/12/10/the-astrographic-telescope-a-story-of-restoration-part-one/

[6] L. Simonot, M. Hébert, M. Gerardin, C. Monpeurt, and T. Fournel, 'Halo and subsurface scattering in the transparent coating on top of a diffusing material', *Journal of the Optical Society of America A*, vol. 35, no. 7, pp. 1192–12, Jun. 2018, doi: 10.1364/JOSAA.35.001192.

[7] A. Cornu, 'Sur le halo des lames épaisses, ou halo photographique, et les moyens de le faire disparaitre', *J. Phys. Theor. Appl.*, vol. 9, no. 1, pp. 270–277, 1890.

[8] M. Elias and P. Cotte, 'Multispectral camera and radiative transfer equation used to depict Leonardo's sfumato in *Mona Lisa*', *Appl. Opt., AO*, vol. 47, no. 12, pp. 2146–2154, Apr. 2008, doi: 10.1364/AO.47.002146.

[9] 'The Future of Package Printing to 2027 | Market Reports & Research', Smithers. Accessed: Apr. 04, 2023. [Online]. Available: https://www.smithers.com/services/market-reports/printing/the-future-of-package-printing-to-2027

[10] G. Sharma and R. Bala, *Digital Color Imaging Handbook*. CRC Press, 2017.

[11] P. Thirkell and S. Hoskins, 'Continuous Tone Digital Output, Using Archivally Proven Printing Methods and Materials', Jan. 2003.

[12] M. Kriss, *Handbook of Digital Imaging*. John Wiley & Sons, 2015.

[13] J. Sugita and T. Takahashi, '[Paper] A Method for Generating Pointillism Based on Seurat's Color Theory', *MTA*, vol. 1, no. 4, pp. 317–327, 2013, doi: 10.3169/mta.1.317.

[14] L. Simonot and M. Hébert, 'Between additive and subtractive color mixings: intermediate mixing models', *J. Opt. Soc. Am. A, JOSAA*, vol. 31, no. 1, pp. 58–66, Jan. 2014, doi: 10.1364/JOSAA.31.000058.

[15] F. Zhang and X. Zhang, 'Image inverse halftoning and descreening: a review', *Multimed Tools Appl*, vol. 78, no. 15, pp. 21021–21039, Aug. 2019, doi: 10.1007/s11042-019-7458-y.

[16] Daniel L. Lau and Gonzalo R. Arce, *Modern Digital Halftoning*, Second edition. Taylor & Francis Group, 2008.

[17] T. Frank, O. Haik, A. Jumabayeva, J. P. Allebach, and Y. Yitzhaky, 'New Design for Compact Color Screen Sets for High-End Digital Color Press', *IEEE Transactions on Image Processing*, vol. 29, pp. 3023–3038, 2020, doi: 10.1109/TIP.2019.2955295.

[18] Y. Ito and K. Nakano, 'A new fm screening method to generate cluster-dot binary images using the local exhaustive search with fpga acceleration', *Int. J. Found. Comput. Sci.*, vol. 19, no. 06, pp. 1373–1386, Dec. 2008, doi: 10.1142/S0129054108006339.

[19] B. Oztan, G. Sharma, and R. P. Loce, 'Quantitative evaluation of misregistration-induced color shifts in color halftones', in *Color Imaging X: Processing, Hardcopy, and Applications*, SPIE, Jan. 2005, pp. 501–512. doi: 10.1117/12.585072.

[20] J. A. C. Yule, *Principles of Color Reproduction, Applied to Photomechanical Reproduction, Color Photography, and the Ink, Paper, and Other Related Industries*. Wiley, 1967.

[21] I. Amidror, 'Unified approach for the explanation of stochastic and periodic moirés', *JEI*, vol. 12, no. 4, pp. 669–681, Oct. 2003, doi: 10.1117/1.1604785.

[22] R. Ulichney, *Digital Halftoning*. MIT Press, 1987.

[23] T. Q. Nguyen, Y. Delignon, L. Chagas, and F. Septier, 'Printer identification from micro-metric scale printing', in *2014 IEEE International Conference on Acoustics, Speech and Signal Processing (ICASSP)*, May 2014, pp. 6236–6239. doi: 10.1109/ICASSP.2014.6854803.

[24] D. S. Rimai, D. S. Weiss, M. Cristina de Jesus, and D. J. Quesnel, 'Electrophotography as a means of microfabrication: the role of electrodynamic and electrostatic forces', *Comptes Rendus Chimie*, vol. 9, no. 1, pp. 3–12, Jan. 2006, doi: 10.1016/j.crci.2004.10.030.

[25] L. Vallat-Evrard, 'Mesure,analyse et modélisation à l'échelle microscopique de points imprimés pour améliorer les solutions de lutte anti-contrefaçon', Communauté Université Grenoble Alpes, LGP2, 2019.

[26] 'Spot color vs. process color | Adobe'. Accessed: Apr. 12, 2023. [Online]. Available: https://www.adobe.com/creativecloud/design/discover/spot-vs-process-color.html

[27] E. Galić, I. Ljevak, and I. Zjakić, 'The Influence of UV Varnish on Colorimetric Properties of Spot Colors', *Procedia Engineering*, vol. 100, pp. 1532–1538, Jan. 2015, doi: 10.1016/j.proeng.2015.01.525.

[28] M. Hébert *et al.*, 'Exploring the bronzing effect at the surface of ink layers', presented at the SPIE/IS&T Electronic Imaging, San Francisco, United States: Proceedings of SPIE - The International Society for Optical Engineering, 2015.

[29] S. Gustavson, 'Dot Gain in Colour Halftones', Linköping University, Image Processing Laboratory, Department of Electrical Engineering, 1997.

[30] R. Hersch and M. Hébert, 'Interaction between Light, Paper and and Color Halftones: Challenges and Modelization Approaches', presented at the Computer Graphics, Imaging and Visualization, 2006. Accessed: Apr. 28, 2023. [Online]. Available: https://www.semanticscholar.org/paper/Interaction-between-Light%2C-Paper-and-

and-Color-and-Hersch-H%C3%A9bert/dd78800c3843912a26580d7ce4fd06438cf46541

[31] F. Österberg, *The visual impact of lamination*. 2005. Accessed: Apr. 17, 2023. [Online]. Available: http://urn.kb.se/resolve?urn=urn:nbn:se:liu:diva-97777

[32] J. H. Schott, 'Optical security features for plastic card documents', in *Optical Security and Counterfeit Deterrence Techniques II*, San Jose, United States: SPIE, Apr. 1998, pp. 294–298. doi: 10.1117/12.304698.

[33] J. K. Kucharska, 'Technical and technological analysis of modern methods of printing lamination', Instytut Mechaniki i Poligrafii, 2021. Accessed: Nov. 18, 2021. [Online]. Available: https://repo.pw.edu.pl/info/bachelor/WUTc95ed9f526c843c88004ea9d0ca2aa70/

[34] C. G. Roffey, *Photogeneration of reactive species for UV curing*, Wiley. 1997.

[35] Z. W. Wicks, F. N. Jones, and S. P. Pappas, *Organic Coatings, Science and technology*, Wiley., vol. 1: Film formation, components and appearance. 1992.

[36] M. Lindner, N. Rodler, M. Jesdinszki, M. Schmid, and S. Sängerlaub, 'Surface energy of corona treated PP, PE and PET films, its alteration as function of storage time and the effect of various corona dosages on their bond strength after lamination', *Journal of Applied Polymer Science*, vol. 135, no. 11, p. 45842, 2018, doi: 10.1002/app.45842.

[37] K. Czimbalmos and Á. Borbély, 'Color changes during the production of laminated flexographic prints', in *Scientific, Technical and Art Releases - 2020*, Media Technology and Light Industry Institute of Rejtő Sándor Faculty of Light Industry and Environmental Engineering Óbuda University., Budapest, 2020, pp. 11–15.

[38] I. Car, I. Majnarić, and B. Lozo, 'Colorimetric Changes Caused by UV Varnishing', presented at the Proceedings of 8th Conference On Information And Graphic Arts Technology, 2018, pp. 37–40.

[39] A. Childers, A. Etheredge, S. Flannery, and J. Freeman, 'Effects of Varnish on Printed Material', *FlexoGlobal, Salmon Creek Publishing*, 2008.

[40] B. Sakovic, 'Effect of different types of lamination on colour gamut and tone value increase of digital prints', presented at the Printing Future Days, Chemnitz, Germany: Proceedings, 2007, pp. 199–203.

[41] E. R. de la Rie, 'The influence of varnishes on the appearance of paintings', *Studies in Conservation*, vol. 32, no. 1, pp. 1–13, Feb. 1987, doi: 10.1179/sic.1987.32.1.1.

[42] R. S. Berns and E. R. de la Rie, 'The relative importance of surface roughness and refractive index in the effects of varnishes on the appearance of paintings', *13thTriennal Meeting of ICOM Commitee for Conser-vation, Rio de Janeiro*, pp. 211–2016, 2002.

[43] L. Simonot and M. Elias, 'Color change due to a varnish layer', *Color Research & Application*, vol. 29, pp. 196–204, Jun. 2004, doi: 10.1002/col.20008.

[44] I. Karlovits, I. Tomić, I. Rilovski, D. Novaković, M. Vucinic Vasic, and U. Kozmidis-Luburić, 'The Influence of the Surface Roughness of Aqueous Coated Samples and the Particle Size of the Coatings on the Reflection and Colourimetric Values of Offset Printed Samples', *Journal of the International Circle*, vol. 5, pp. 18–29, Jan. 2012.

[45] T. Hudika, I. Majnarić, and T. Cigula, 'Influence of the Varnishing "Surface" Coverage on Optical Print Characteristics', *Tehnički Glasnik*, vol. 14, no. 4, pp. 428–433, doi: 10.31803/tg-20191129104559.

[46] T. Aida, 'Glossiness of colored papers and its application to specular glossiness measuring instruments', *Systems and Computers in Japan*, vol. 28, no. 1, pp. 95–112, 1997, doi: 10.1002/(SICI)1520-684X(199701)28:1<95::AID-SCJ10>3.0.CO;2-N.

[47] M. Mikula, M. Čeppan, and K. Vaško, 'Gloss and goniocolorimetry of printed materials', *Color Research & Application*, vol. 28, no. 5, pp. 335–342, 2003, doi: 10.1002/col.10177.

[48] I. Majnarić, I. Bolanča Mirković, and K. Golubović, 'Influence of UV curing varnish coating on surface properties of paper', *Tehnički vjesnik*, vol. 19, no. 1, pp. 51–56, Mar. 2012.

[49] J. Dolić, J. Pibernik, and I. Majnarić, 'Influence of UV Varnish Pattern Effect on Print Quality', in *Journal of Imaging Science and Technology*, Nov. 2014, pp. 60501-1-60501–9. doi: 10.2352/J.ImagingSci.Technol.2014.58.6.060501.

[50] B. Jiang, Y. D. Huang, and Y. P. Bai, 'Noncontact and rapid analysis of the quality of the recording coating on ink jet printing by near-infrared spectroscopy', *Analyst*, vol. 136, no. 24, pp. 5157–5161, 2011, doi: 10.1039/C1AN15676D.

[51] D. P. Zhao, X. F. Wei, and P. Q. Huang, 'Influence of Promoter on the Glossiness of Water-Soluble Varnish', *Advanced Materials Research*, vol. 174, pp. 441–444, 2011, doi: 10.4028/www.scientific.net/AMR.174.441.

[52] J. J. Hastreiter and W. H. Simpson, 'Matte Finish on Thermal Prints', *NIP & Digital Fabrication Conference*, vol. 2004, no. 2, pp. 976–979, Jan. 2004.

[53] T. Cigula, T. Hudika, and D. Donevski, 'Color reproduction on varnished cardboard packaging by using lower ink coverages due to the gray component replacement image processing', *Color Res Appl*, pp. 1–10, Jul. 2021, doi: 10.1002/col.22704.

[54] S. Horita, 'Printed color prediction method and device, profile generation method and device, color conversion method and device, and color conversion system', US9723178B2, Aug. 01, 2017 Accessed: Apr. 11, 2023. [Online]. Available: https://patents.google.com/patent/US9723178B2/en

[55] 'INTERNATIONAL COLOR CONSORTIUM'. Accessed: Apr. 20, 2023. [Online]. Available: https://color.org/index.xalter

[56] A. Sharma, *Understanding Color Management*. Chichester, UK: John Wiley & Sons, Ltd, 2018. doi: 10.1002/9781119223702.

[57] 'Print houses can save A LOT of time and paper with Colorsource press-setting applications'. Accessed: Apr. 20, 2023. [Online]. Available: https://www.iso12647solution.com/

[58] 'ICC Profile Registry'. Accessed: Apr. 20, 2023. [Online]. Available: https://color.org/registry/index.xalter

[59] 'en:downloads [ECI European Color Initiative]'. Accessed: Apr. 21, 2023. [Online]. Available: http://www.eci.org/doku.php?id=en:downloads

[60] 'Idealliance Releases Updated Expanded Color Gamut (ECG) Characterization Target and Kit', Idealliance. Accessed: Apr. 21, 2023. [Online]. Available:

https://idealliance.org/idealliance-releases-updated-expanded-color-gamut-ecg-characterization-target-and-kit/

[61] 'Printing standard for packaging printing (32.176) | Fogra'. Accessed: Apr. 21, 2023. [Online]. Available: https://fogra.org/en/research/offset-printing/printing-standard-for-packaging-printing-32176

[62] 'CMYK Characterization Data'. Accessed: Apr. 21, 2023. [Online]. Available: https://www.color.org/chardata/drsection1.xalter

[63] 'en:colorstandards:offset [ECI European Color Initiative]'. Accessed: Apr. 20, 2023. [Online]. Available: http://www.eci.org/doku.php?id=en:colorstandards:offset

[64] M. Hébert, *Optical Models for Material Appearance*. EDP sciences, 2022. doi: 10.1051/978-2-7598-2647-6.

[65] F. E. Nicodemus, J. C. Richmond, J. J. Hsia, I. W. Ginsberg, and T. Limperis, 'Geometrical considerations and nomenclature for reflectance', National Bureau of Standards, Gaithersburg, MD, NBS MONO 160, 1977. doi: 10.6028/NBS.MONO.160.

[66] D. J. Schneider, B. L. Myers, and B. N. Altay, 'Investigating the agreement between polarized and unpolarized densitometry in offset lithography printing', *Color Research & Application*, vol. n/a, no. n/a, doi: 10.1002/col.22840.

[67] L. Simonot and P. Boulenguez, *Quand la matière diffuse la lumière*, Presses des Mines. in Sciences de la matière. Paris, 2019.

[68] P. Kubelka and F. Munk, 'Ein Beitrag zur Optik der Farbanstriche (Contribution to the optic of paint)', *Zeitschrift fur Technische Physik*, vol. 12, pp. 593–601, 1931.

[69] P. Kubelka, 'New Contributions to the Optics of Intensely Light-Scattering Materials. Part I', *J. Opt. Soc. Am., JOSA*, vol. 38, no. 5, pp. 448–457, May 1948, doi: 10.1364/JOSA.38.000448.

[70] R. McDonald, 'Computer match prediction-dyes', in *Colour physics for industry*, Society of Dyers and Colourists, 1997, pp. 116–185.

[71] J. L. Saunderson, 'Calculation of the Color of Pigmented Plastics*', *J. Opt. Soc. Am., JOSA*, vol. 32, no. 12, pp. 727–736, Dec. 1942, doi: 10.1364/JOSA.32.000727.

[72] A. Murray, 'Monochrome reproduction in photoengraving', *Journal of the Franklin Institute*, vol. 221, no. 6, pp. 721–744, Jun. 1936, doi: 10.1016/S0016-0032(36)90524-0.

[73] Neugebauer H.E.J., 'Die Theoretischen Grundlagen des Mehrfarbenbuchdrucks', *Zeitschrift fur Wissenschaftliche Photographie. Photophysik und Photochemie*, vol. 36, no. 4, pp. 73–89, 1937.

[74] D. Wyble and A. Kraushaar, 'The theoretical basis of multicolor letterpress printing, Hans E. J. Neugebauer', *Color Research & Application*, vol. 30, no. 5, pp. 322–331, 2005, doi: 10.1002/col.20135.

[75] J. Morovic, P. Morovic, and J. Arnabat, 'HANS – A New Color Separation and Halftoning Paradigm', in *Final Program and Proceedings - IS and T/SID Color Imaging Conference*, Nov. 2010.

[76] E. Demichel, 'Le procédé', *Société Française de Photographie*, vol. 26, pp. 17–21, 1924.

[77] J. A. C. Yule and W. J. Nielsen, 'The penetration of light into paper and its effect on halftone reproduction', *Proc. TAGA*, vol. 3, pp. 65–76, 1951.

[78] J. A. Stephen Viggiano, 'The Color Of Halftone Tints', *TAGA Proceedings*, pp. 647–661, 1985.

[79] J.A. Stephen Viggiano, 'Modeling the Color of Multi-Colored Halftones', *TAGA Proceedings*, pp. 44–62, 1990.

[80] G. Rogers, 'A generalized Clapper–Yule model of halftone reflectance', *Color Research & Application*, vol. 25, no. 6, pp. 402–407, 2000, doi: 10.1002/1520-6378(200012)25:6<402::AID-COL4>3.0.CO;2-6.

[81] A. Lewandowski, M. Ludl, G. Byrne, and G. Dorffner, 'Applying the Yule-Nielsen equation with negative n', *J. Opt. Soc. Am. A, JOSAA*, vol. 23, no. 8, pp. 1827–1834, Aug. 2006, doi: 10.1364/JOSAA.23.001827.

[82] J. S. Arney, P. G. Engeldrum, and Z. Huanzhao, 'An expanded Murray-Davies model of tone reproduction in halftone imaging', *J Imag Sci Tech*, vol. 39, Nov. 1995.

[83] M. Hébert and R. D. Hersch, 'Analyzing halftone dot blurring by extended spectral prediction models', *Journal of the Optical Society of America. A, Optics, image science, and vision*, vol. 27, pp. 6–12, Jan. 2010, doi: 10.1364/JOSAA.27.000006.

[84] R. D. Hersch and F. Crete, 'Improving the Yule-Nielsen modified Neugebauer model by dot surface coverages depending on the ink superposition conditions', in *Color Imaging X: Processing, Hardcopy, and Applications*, SPIE, Jan. 2005, pp. 434–447. doi: 10.1117/12.588907.

[85] M. Hébert and R. D. Hersch, 'Yule–Nielsen based recto–verso color halftone transmittance prediction model', *Appl. Opt., AO*, vol. 50, no. 4, pp. 519–525, Feb. 2011, doi: 10.1364/AO.50.000519.

[86] R. Balasubramanian, 'Optimization of the spectral Neugebauer model for printer characterization', *JEI*, vol. 8, no. 2, pp. 156–166, Apr. 1999, doi: 10.1117/1.482694.

[87] M. Hébert and R. D. Hersch, 'Review of spectral reflectance prediction models for halftone prints: calibration, prediction and performance', *Color Research & Application*, no. 21907, 2014.

[88] F. P. Callahan, 'Light Scattering in Halftone Prints', *J. Opt. Soc. Am., JOSA*, vol. 42, no. 2, pp. 104–105, Feb. 1952, doi: 10.1364/JOSA.42.000104.

[89] F. R. Clapper and J. a. C. Yule, 'The Effect of Multiple Internal Reflections on the Densities of Half-tone Prints on Paper', *J. Opt. Soc. Am., JOSA*, vol. 43, no. 7, pp. 600–603, Jul. 1953, doi: 10.1364/JOSA.43.000600.

[90] R. D. Hersch, P. Emmel, F. Collaud, and F. Crete, 'Spectral reflection and dot surface prediction models for color halftone prints', *JEI*, vol. 14, no. 3, p. 033001, Jul. 2005, doi: 10.1117/1.1989987.

[91] F. C. Williams and F. R. Clapper, 'Multiple Internal Reflections in Photographic Color Prints', *Journal of the Optical Society of America*, vol. 43, pp. 595–599, 1953.

[92] J. D. Shore and J. P. Spoonhower, 'Reflection Density in Photographic Color Prints: Generalizations of the Williams–Clapper Transform', *Journal of Imaging Science and Technology*, vol. 45, no. 5, pp. 484–488, 2001.

[93] M. Elias, L. Simonot, and M. Menu, 'Bidirectional reflectance of a diffuse background covered by a partly absorbing layer', *Optics Communications*, vol. 191, no. 1, pp. 1–7, May 2001, doi: 10.1016/S0030-4018(01)01087-2.

[94] R. D. Hersch and M. Hébert, 'Base Models for Color Halftone Reproduction', in *Handbook of digital imaging*, vol. 2: image display and reproduction, Wiley, 2015.

[95] R. S. Berns, 'Spectral modeling of a dye diffusion thermal transfer printer', *JEI*, vol. 2, no. 4, pp. 359–370, Oct. 1993, doi: 10.1117/12.153030.

[96] J. A. C. Yule, D. Howe, and J. Altman, 'The effect of the spread-function of paper on halftone reproduction', presented at the TAPPI J., 1967, pp. 337–344.

[97] F. R. Ruckdeschel and O. G. Hauser, 'Yule-Nielsen effect in printing: a physical analysis', *Appl. Opt., AO*, vol. 17, no. 21, pp. 3376–3383, Nov. 1978, doi: 10.1364/AO.17.003376.

[98] H. Wakeshima, T. Kunishi, and S. Kaneko, 'Light Scattering in Paper and Its Effect on Halftone Reproduction', *J. Opt. Soc. Am., JOSA*, vol. 58, no. 2, pp. 272–273, Feb. 1968, doi: 10.1364/JOSA.58.000272.

[99] M. Ukishima, 'Prediction and evaluation of color halftone print quality based on microscopic measurement', University of Eastern Finland, 2010.

[100] J. R. Huntsman, 'A New Model of Dot Gain and its Application to a Multilayer Color Proof', *Journal of Printing Science and Technology*, vol. 24, no. 3, pp. 189–202, 1987, doi: 10.11413/nig1987.24.189.

[101] J. S. Arney, 'A Probability Description of the Yule-Nielsen Effect', p. 5.

[102] J. S. Arney and M. Kutsube, 'A Probability Description of the Yule-Nielsen Effect II: The Impact of Halftone Geometry', p. 6.

[103] J. S. Arney, C. D. Arnay, and P. G. Engeldrum, 'Modeling the Yule–Nielsen halftone effect.', *Journal of Imaging Science and Technology*, vol. 40, no. 3, pp. 233–238, 1996.

[104] L. Yang, 'Spectral model of halftone on a fluorescent substrate.', *Journal of Imaging Science and Technology*, vol. 49, no. 2, pp. 179–184, 2005.

[105] L. Yang, R. Lenz, and B. Kruse, 'Light scattering and ink penetration effects on tone reproduction', *J. Opt. Soc. Am. A, JOSAA*, vol. 18, no. 2, pp. 360–366, Feb. 2001, doi: 10.1364/JOSAA.18.000360.

[106] L. Yang, 'Probabilistic spectral model of color halftone incorporating substrate fluorescence and interface reflections', *J. Opt. Soc. Am. A, JOSAA*, vol. 27, no. 10, pp. 2115–2122, Oct. 2010, doi: 10.1364/JOSAA.27.002115.

[107] 'Manuel d'instructions Spectrophotometer CM-2600d/2500d'. Konica Minolta.

[108] G. de Vaucouleurs, J. Dragesco, and P. Selme, *Manuel de Photographie Scientifique (Sciences physiques et biologiques)*. La Revue Optique, 1956.

[109] Y. Garini, I. T. Young, and G. McNamara, 'Spectral imaging: Principles and applications', *Cytometry Part A*, vol. 69A, no. 8, pp. 735–747, 2006, doi: 10.1002/cyto.a.20311.

[110] G. Lu and B. Fei, 'Medical hyperspectral imaging: a review', *JBO*, vol. 19, no. 1, p. 010901, Jan. 2014, doi: 10.1117/1.JBO.19.1.010901.

[111] L. Gevaux, '3D-hyperspectral imaging and optical analysis of skin for the human face', Theses, Université de Lyon, 2019. Accessed: Dec. 17, 2021. [Online]. Available: https://tel.archives-ouvertes.fr/tel-02881115

[112] M. Hébert *et al.*, 'Characterization by Hyperspectral Imaging and Hypercolor Gamut Estimation for Structural Color Prints', in *Computational Color Imaging*, S. Bianco, R. Schettini, A. Trémeau, and S. Tominaga, Eds., in Lecture Notes in Computer Science. Cham: Springer International Publishing, 2017, pp. 211–222. doi: 10.1007/978-3-319-56010-6_18.

[113] M. Brydegaard, A. Merdasa, H. Jayaweera, J. Ålebring, and S. Svanberg, 'Versatile multispectral microscope based on light emitting diodes', *Review of Scientific Instruments*, vol. 82, no. 12, p. 123106, Dec. 2011, doi: 10.1063/1.3660810.

[114] M. Namedanian, D. Nyström, P. Z. Elias, and S. Gooran, 'Physical and optical dot gain: characterization and relation to dot shape and paper properties', in *Color Imaging XIX: Displaying, Processing, Hardcopy, and Applications*, SPIE, Feb. 2014, pp. 69–78. doi: 10.1117/12.2035713.

[115] Q.-T. Nguyen, A. Mai, L. Chagas, and N. Reverdy-Bruas, 'Microscopic printing analysis and application for classification of source printer', *Computers & Security*, vol. 108, p. 102320, Sep. 2021, doi: 10.1016/j.cose.2021.102320.

[116] D. Nyström, 'Microscopic Color Measurements of Halftone Prints', *NIP & Digital Fabrication Conference*, vol. 2010, no. 2, pp. 459–462, Jan. 2010.

[117] G. M. A. Rahaman, O. Norberg, and P. Edström, 'Microscale halftone color image analysis: perspective of spectral color prediction modeling', in *Color Imaging XIX: Displaying, Processing, Hardcopy, and Applications*, SPIE, Feb. 2014, pp. 34–48. doi: 10.1117/12.2037256.

[118] M. Lea Carey, *A manual of photography: intended as a text book for beginners and a book of reference for advanced photographers:*, Benerman&Wilson. 1868. [Online]. Available: http://name.umdl.umich.edu/ael5141.0001.001

[119] W. Crookes, *The Photographic News: A Weekly Record of the Progress of Photography*. Cassell, Petter and Galpin, 1887.

[120] *Revue photographique: recueil mensuel exclusivement consacré aux progrès de la photographie*. Remquet, 1865.

[121] W. Crookes, *The Photographic News: A Weekly Record of the Progress of Photography. Ed. by William Crookes, and by G. Wharton Simpson*. Cassell, 1864.

[122] E. E. Barnard, *The First Comet Discovered by Photography*. 1892. [Online]. Available: https://digitalcollections.library.ucsc.edu/concern/works/sj139496m?locale=en

[123] *Celestial objects: galaxy*. [Online]. Available: https://digitalcollections.library.ucsc.edu/concern/works/pz50h031q?locale=en

[124] J. W. Short, *Glass plate negative of Nebulae Minor*. 1890. Accessed: Aug. 30, 2022. [Glass plate]. Available: https://collection.maas.museum/object/328682

[125] H. C. Russel, *Albumen print of the Smaller Magellan Cloud*. 1890.

[126] H. C. Russel, *'Mapping the Stars' 817 photographic negatives*. 1984.

[127] 'Star'.

[128] H. C. Russel, *Photography of The Milky-Way & Nubeculae*. 1890. Accessed: Aug. 26, 2022. [Online]. Available: https://www.maas.museum/inside-the-collection/2014/12/10/the-astrographic-telescope-a-story-of-restoration-part-one/

[129] H. Baines, *The Science of Photography*. Wiley, 1967.

[130] A. C. Hardy, A. C. Hardy, and F. H. Perrin, *The Principles of Optics*. McGraw-Hill book Company, Incorporated, 1932.

[131] Corporation, *Popular Science*. Bonnier Corporation, 1907.

[132] R. M. Evans, W. T. Hanson, and W. L. Brewer, *Principles of Color Photography*, Eastman Kodak Company. John Wiley & Sons, 1953.

[133] J. Kormendy, 'Calibration of direct photographs using brightness profiles of field stars.', *The Astronomical Journal*, vol. 78, p. 255, Apr. 1973, doi: 10.1086/111412.

[134] L. Latacz and P. Nowak, 'Model examination of the reflex-halation in single-layer light-sensitive system', *Optica Applicata*, no. Vol. 31, nr 2, pp. 499–506, 2001.

[135] T. Satoh *et al.*, 'Performance of Akatsuki/IR2 in Venus orbit: the first year', *Earth, Planets and Space*, vol. 69, no. 1, p. 154, Nov. 2017, doi: 10.1186/s40623-017-0736-x.

[136] N. Sanduleak, 'A new planetary nebula in Puppis.', *PASP*, vol. 87, p. 705, Oct. 1975, doi: 10.1086/129831.

[137] R. J. Wallace, 'The Function of a Color-Filter and "isochromatic" Plate in Astronomical Photography', *The Astrophysical Journal*, vol. 27, p. 106, Mar. 1908, doi: 10.1086/141533.

[138] I. G. van Breda, 'Halation in image intensifiers', *Monthly Notices of the Royal Astronomical Society*, vol. 257, no. 3, pp. 415–418, Aug. 1992, doi: 10.1093/mnras/257.3.415.

[139] Q. Guo, H. Wang, and J. Yang, 'Adaptive Dark Channel Prior Enhancement Algorithm for Different Source Night Vision Halation Images', *IEEE Access*, pp. 1–1, 2022, doi: 10.1109/ACCESS.2022.3203183.

[140] J. A. Cobb, 'Halation', *Nature*, vol. 73, no. 1881, Art. no. 1881, Nov. 1905, doi: 10.1038/073054c0.

[141] W. Yi, L. Dong, M. Liu, M. Hui, L. Kong, and Y. Zhao, 'MFAF-Net: image dehazing with multi-level features and adaptive fusion', *Vis Comput*, Jul. 2023, doi: 10.1007/s00371-023-02917-8.

[142] L. S. Dolin, 'Laser bathymetry based on the halo effect', *Appl. Opt., AO*, vol. 58, no. 6, pp. 1555–1561, Feb. 2019, doi: 10.1364/AO.58.001555.

[143] L. Dolin, F. Dailliez, and L. Simonot, 'Determination of Water Layer Thickness from Laser Halo', in *Radiometry of Wet Surfaces: When Water Matters*, Science Press, EDP Sciences., in Institut d'Optique Graduate School Advanced Textbook. , 2023, pp. 85–102.

[144] F. E. Nicodemus, J. C. Richmond, J. J. Hsia, I. W. Ginsberg, and T. Limperis, 'Geometrical considerations and nomenclature for reflectance', National Bureau of Standards, Gaithersburg, MD, NBS Monograph 160, 1977. Accessed: Jun. 09, 2021. [Online]. Available: https://nvlpubs.nist.gov/nistpubs/Legacy/MONO/nbsmonograph160.pdf

[145] M. Hébert, F. Dailliez, and L. Simonot, ‘Why a clear coating modifies halftone color prints’, presented at the Material Appearance, IS&T Electronic Imaging Symposium, Online, Jan. 2021.

[146] M. D. Fairchild, *Color Appearance Models*, John Wiley&Sons,Ltd. 2005.

[147] G. Rogers, ‘Analysis of the Yule-Nielsen effect with the multiple-path point spread function in a frequency-modulated halftone’, *J. Opt. Soc. Am. A, JOSAA*, vol. 35, no. 6, pp. 916–922, Jun. 2018, doi: 10.1364/JOSAA.35.000916.

[148] G. L. Rogers, ‘Measurement of the modulation transfer function of paper’, *Appl. Opt., AO*, vol. 37, no. 31, pp. 7235–7240, Nov. 1998, doi: 10.1364/AO.37.007235.

[149] G. Rogers, O. Corblet, T. Fournel, and M. Hebert, ‘Measurement of the diffusion of light within paper’, *J. Opt. Soc. Am. A*, vol. 36, no. 4, p. 636, Apr. 2019, doi: 10.1364/JOSAA.36.000636.

[150] G. L. Rogers, ‘Effect of light scatter on halftone color’, *J. Opt. Soc. Am. A*, vol. 15, no. 7, p. 1813, Jul. 1998, doi: 10.1364/JOSAA.15.001813.

[151] G. L. Rogers, ‘Optical Dot Gain: Lateral Scattering Probabilities’, *Journal of Imaging Science and Technology*, vol. 42, no. 4, pp. 341–345, Jul. 1998.

[152] L. Yang and B. Kruse, ‘Ink penetration and its effects on printing’, in *Color Imaging: Device-Independent Color, Color Hardcopy, and Graphic Arts V*, SPIE, Dec. 1999, pp. 365–375. doi: 10.1117/12.373417.

[153] F. Dailliez, M. Hébert, A. Blayo, L. Chagas, and T. Fournel, ‘Impact of a Transparent Coating on the Reflectance of a Line Halftone Pattern’, *Coatings*, vol. 11, p. 1465, Nov. 2021, doi: 10.3390/coatings11121465.

[154] L. Simonot, *Radiometry of wet surfaces: When Water Matters*. in Institut d’Optique Graduate School Advanced Textbook. EDP Sciences, 2023. doi: 10.1051/978-2-7598-2931-6.

[155] F. Dailliez *et al.*, ‘Impact of a coating layer on the appearance of various halftone patterns’, in *Electronic Imaging*, Society for Imaging Science and Technology, Jan. 2023, pp. 1–7. doi: 10.2352/EI.2023.35.15.COLOR-204.

[156] M. Elias, P. Castiglione, and G. Elias, ‘Influence of interface roughness on surface and bulk scattering’, *Journal of the Optical Society of America. A, Optics, image science, and vision*, vol. 27, pp. 1265–73, Jun. 2010, doi: 10.1364/JOSAA.27.001265.

[157] M. Hébert and R. D. Hersch, ‘Extending the Clapper–Yule model to rough printing supports’, *J. Opt. Soc. Am. A, JOSAA*, vol. 22, no. 9, pp. 1952–1967, Sep. 2005, doi: 10.1364/JOSAA.22.001952.

[158] R. L. Cook and K. E. Torrance, ‘A Reflectance Model for Computer Graphics’, *ACM Transactions on Graphics*, vol. 1, no. 1, pp. 7–24, 1982.

[159] L. Simonot, R. D. Hersch, M. Hébert, and S. Mazauric, ‘Multilayer four-flux matrix model accounting for directional-diffuse light transfers’, *Applied optics*, 2016, doi: 10.1364/AO.99.099999.

[160] F. Dailliez, M. Hébert, L. Simonot, L. Chagas, A. Blayo, and T. Fournel, ‘Color change of printed surfaces due to a clear coating with matte finishing’, presented at the London Imaging Meeting 2023, Jun. 2023. Accessed: Jul. 10, 2023. [Online]. Available: https://hal.science/hal-04146250

[161] ‘Carl Zeiss Microscopy Deutschland GmbH - Assistant objectif - Objectif EC “Epiplan-Neofluar” 5x/0,13 HD DIC M27’. Accessed: Dec. 01, 2021. [Online]. Available: https://www.micro-shop.zeiss.com/fr/de/shop/objectives/000000-1156-514/Objectif-EC-Epiplan-Neofluar-5x-0,13-HD-DIC-M27

[162] ‘Filtres Passe-Bande OD 4; 25 nm à Traitement Dur | Edmund Optics’. Accessed: Oct. 12, 2021. [Online]. Available: https://www.edmundoptics.fr/f/hard-coated-od-4-25nm-bandpass-filters/14529/

[163] C. France, ‘Canon EOS 1200D -Caractéristiques - Appareils photo reflex et hybrides EOS’, Canon France. Accessed: Dec. 01, 2021. [Online]. Available: https://www.canon.fr/for_home/product_finder/cameras/digital_slr/eos_1200d/specification.html

[164] G. Finlayson and Y. Zhu, ‘An improved optimization method for finding a color filter to make a camera more colorimetric’, in *Electronic Imaging 2020*, USA, Oct. 2020, pp. 163–1. Accessed: May 11, 2022. [Online]. Available: https://ueaeprints.uea.ac.uk/id/eprint/73655/

[165] F. Imai, ‘Multispectral Image Acquisition and Spectral Reconstruction using a Trichromatic Digital Camera System associated with absorption filters’, Jan. 1998.

[166] M. Parmar, F. Imai, S. Ho, and J. Farrell, ‘A database of high dynamic range visible and near-infrared multispectral images’, *Proceedings of SPIE - The International Society for Optical Engineering*, vol. 6817, Mar. 2008, doi: 10.1117/12.767830.

[167] F. Imai and R. Berns, ‘Spectral Estimation Using Trichromatic Digital Cameras’, Jan. 1999.

[168] ‘sRGB’. Accessed: Feb. 24, 2022. [Online]. Available: https://www.color.org/chardata/rgb/srgb.xalter

[169] F. Dailliez, M. Hébert, L. Chagas, T. Fournel, and A. Blayo, ‘Use of Multispectral Microscopy in the Prediction of Coated Halftone Reflectance’, *Journal of Imaging*, vol. 8, no. 9, Art. no. 9, Sep. 2022, doi: 10.3390/jimaging8090243.

[170] G. Sharma, W. Wu, and E. N. Dalal, ‘The CIEDE2000 color-difference formula: Implementation notes, supplementary test data, and mathematical observations’, *Color Research & Application*, vol. 30, no. 1, pp. 21–30, 2005, doi: 10.1002/col.20070.

[171] J. Hardeberg, ‘Acquisition et reproduction d’images couleur: approches colorimétrique et multispectrale’, Télécom ParisTech, Paris, France, 1999.

[172] ‘Camera Spectral Sensitivity Database’. Accessed: Mar. 13, 2023. [Online]. Available: https://www.gujinwei.org/research/camspec/db.html

[173] J. Jiang, D. Liu, J. Gu, and S. Süsstrunk, ‘What is the space of spectral sensitivity functions for digital color cameras?’, in *2013 IEEE Workshop on Applications of Computer Vision (WACV)*, Jan. 2013, pp. 168–179. doi: 10.1109/WACV.2013.6475015.

[174] L. Simonot, T. Girardeau, and M. Hebert, ‘Bronzing effect: predicting the color shine of printed surfaces by estimating the refractive index of the inks’, *J. Opt. Soc. Am. A, JOSAA*, vol. 40, no. 7, pp. 1443–1450, Jul. 2023, doi: 10.1364/JOSAA.493319.

[175] S. V. Kravkov, ‘The Influence of Caffeine on the Color Sensitivity’, *Acta Ophthalmologica*, vol. 17, no. 1, pp. 89–94, 1939, doi: 10.1111/j.1755-3768.1939.tb04309.x.

[176] C. de J. Sousa, M. L. C. de Oliveira, and L. O. Gomes, 'Cataract and chromatic expression in Monet's work', *Rev. bras.oftalmol.*, vol. 78, pp. 304–309, Nov. 2019, doi: 10.5935/0034-7280.20190150.

[177] CIE publication, *A framework for the measurement of visual appearance | CIE*. 2006. Accessed: Jul. 15, 2021. [Online]. Available: http://cie.co.at/publications/framework-measurement-visual-appearance

[178] M. J. T. Milton, *New Frontiers for Metrology: From Biology and Chemistry to Quantum and Data Science*. IOS Press, 2021.

[179] M. Habekost, 'Which color differencing equation should be used?', *International Circular of Graphic Education and Research*, no. 6, 2013.

[180] M. R. Luo, G. Cui, and B. Rigg, 'The development of the CIE 2000 colour-difference formula: CIEDE2000', *Color Research & Application*, vol. 26, no. 5, pp. 340–350, 2001, doi: 10.1002/col.1049.

Résumé étendu en français

Contexte : gestion de la couleur en impression

La couleur d'une image imprimée est obtenue en appliquant à l'échelle microscopique des points d'encre sur le substrat (usuellement cyan, magenta, jaunes et noirs), un procédé appelé *impression en demi-tons*. Dans sa quête pour reproduire des couleurs fidèles, l'imprimeur est confronté à un problème d'accroissement de la taille des points imprimés (dot gain en anglais) : ceux-ci sont généralement plus gros que ceux commandés à l'imprimante, ce qui impacte la couleur observée à distance.

La première origine de ce phénomène est liée aux interactions encres-papier et au procédé d'impression : selon leurs propriétés (comme la viscosité de l'encre, la pression des rouleaux imprimeurs, la vitesse d'impression, …) l'encre s'étale sur le substrat et y pénètre de façons différentes. Les tailles et formes de points imprimés dépendent ainsi des propriétés d'impression et tendent à être plus gros que le motif nominal, ce qui assombrit la couleur de l'imprimé, un phénomène aussi appelé *dot gain mécanique*. La seconde origine du phénomène de dot gain est purement optique : la lumière se propageant dans le substrat par diffusion vient flouter les contours des points encrés ; cette propagation dans le substrat augmente la probabilité de la lumière d'être absorbée par de l'encre, ce qui assombrit et sature les couleurs et fait paraitre les points imprimés plus gros que ce qu'ils ne sont physiquement. Ce phénomène est appelé *dot gain optique*.

Pour imprimer les couleurs souhaitées, l'imprimeur doit faire de la gestion de la couleur : l'imprimante est calibrée, ses couleurs sont caractérisées et des conversions entre espaces colorimétriques des différents systèmes de reproduction utilisés sont effectuées. Il existe principalement deux approches en gestion de la couleur : une numérique qui consiste à caractériser le système d'impression en imprimant et mesurant un grand nombre de patches colorés et à utiliser des algorithmes d'interpolations pour en déduire les couleurs intermédiaires, et une optique qui consiste, à partir de quelques mesures, à prédire les couleurs en utilisant des modèles optiques.

Problème : changement de couleur induit par l'ajout d'une couche transparente

Les impressions sont régulièrement vernies ou laminées pour améliorer leurs propriétés mécaniques ou pour améliorer leur apparence, mais la gestion de la couleur en impression est généralement faite sur des impressions non-vernis et non-laminées. Néanmoins, l'ajout d'une couche transparente (même non-absorbante) sur une impression peut modifier significativement sa couleur. Ce changement de couleur par ajout de couche transparente est visible dans la Figure R.1 où la zone couverte d'une pellicule brillante est plus sombre et saturée

que la zone non-pelliculée. Il peut également être noté que la zone pelliculée matte parait moins saturée que la zone non pelliculée.

Figure R.1. Photo d'une impression jet d'encre non-pelliculée à gauche, pelliculée matte au milieu, et pelliculée brillante à droite.

Ce changement de couleur a été décrit à de multiples reprises dans la littérature et dépend non-seulement de la rugosité de surface de la couche transparente, mais également des paramètres d'impression. Hoffstadt en parle comme d'un dot gain additionnel causé par la propagation de la lumière dans la couche transparente.

Les travaux réalisés cherchent à répondre à un certain nombre de questions : quel est le phénomène optique à l'origine de ce changement de couleur ? Comment le modéliser et le prédire ? Quel est l'impact des différents paramètres d'impression sur le changement de couleur ? Comment l'exploiter ?

Phénomène optique et modélisation

En 2018, une étude menée par Simonot met en équation la propagation de la lumière au sein d'une couche transparente lisse en contact optique avec un substrat diffusant. Cette étude montre que la lumière se propage de façon très spécifique sous la forme d'un halo : la lumière atteignant le substrat est diffusé de façon lambertienne dans toutes les directions dans la couche transparente. Les rayons atteignant l'interface entre la couche transparente sont soit transmis par l'interface, ils peuvent alors atteindre le détecteur, soit réfléchis par l'interface, ils se propagent alors de nouveau vers le substrat où ils sont diffusés une nouvelle fois, comme montré dans la Figure R.2.b. Cette réflexion ou transmission par l'interface avec l'air dépend

uniquement de l'angle d'incidence des rayons lumineux et de l'indice optique de la couche, comme décrit par la réflectance et transmittance de Fresnel : les rayons ayant un faible angle d'incidence par rapport à la normale à l'interface sont majoritairement transmis, et ceux ayant un angle d'incidence supérieur à un angle critique sont totalement réfléchis vers le substrat où ils sont de nouveaux diffusés dans toutes les directions. Cet angle critique, décrit par la loi de Descartes, vaut approximativement 42° pour un indice optique de la couche transparente de 1.5. Ainsi, les rayons réfléchis à l'interface forment un anneau lumineux autour du point source du substrat, comme montré dans la Figure R.2.a. Ce phénomène avait déjà été observé et expliqué par des astronomes à la fin du XIXe alors que les sources de lumière ponctuelles comme les étoiles paraissaient, dans les photographies, entourées d'un halo. En effet les photographies étaient composées d'une couche photosensibles diffusante en contact avec une lame de verre. Les rayons réfléchis par l'interface entre le verre et l'air, sur la face arrière de la photographie, formaient un halo sur la couche photosensible.

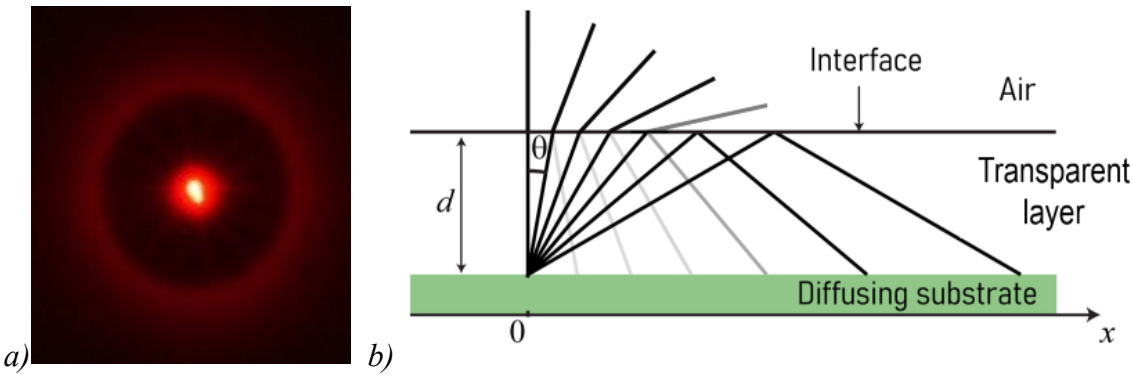

Figure R.2. a) Photographie du halo autour du point d'impact d'un laser éclairant une surface blanche couverte d'une couche transparente. b) schéma des rayons lumineux réfléchis et transmis à l'interface entre la couche transparente et l'air.

Dans le cas d'un substrat imprimé non-uniforme, cette réflexion interne à l'interface entre la couche transparente lisse et l'air augmente la probabilité qu'a la lumière d'être absorbée par un motif imprimé. Ce phénomène peut rendre les couleurs des impressions couvertes d'une couche transparente plus sombres et plus saturées que celles de l'imprimé non-pelliculé (ou non-vernis). Ce phénomène a été modélisé durant ces travaux de thèse, en se fondant sur les équations décrites par Simonot pour un substrat uniforme. Le modèle repose sur des convolutions multiples entre la carte d'éclairement de la réflexion en forme de halo, qui dépend principalement de l'épaisseur de la couche transparente, et la réflectance intrinsèque spatiale et spectrale du substrat imprimé, qui peut être déduite de la réflectance spatiale et spectrale de l'imprimé sans couche transparente.

Validation expérimentale

Deux expériences ont été réalisées pour tester l'hypothèse théorique, et pour évaluer la validité du modèle multi-convolutif. Ces expériences ont été réalisées à l'échelle macroscopique où le phénomène de halation était le principal phénomène optique. Dans la première expérience, un motif de demi-ton ligne noir et blanc de période 33.3 mm a été appliqué sur un support blanc diffusant au fond d'une cuve. Un liquide d'indice optique 1.5, similaire à l'indice optique d'une pellicule ou d'un vernis, a été graduellement versé au-dessus du demi-ton qui était éclairé avec une lumière rouge. Des photos de la cuve ont été prises pour chaque épaisseur de liquide. Comme la bande passante spectrale du système était faible, des valeurs de facteurs de réflectance spatiales du demi-ton pour chaque épaisseur ont pu être déduites des photos et comparées au modèle. Les résultats, présentés en Figure R.3 ont pour la première fois montré que lorsque l'épaisseur *d* de la couche transparente augmente par rapport à la période *p* du motif de demi-ton (p = 33.3 mm), il y a bien un phénomène d'assombrissement causé par l'augmentation d'épaisseur de la couche transparente, Figure R.3.a et Figure R.3.b. Ce phénomène de halation floute les bords des lignes blanches, visible dans la Figure R.3.c. Le modèle multi-convolutif permet de prédire cet assombrissement avec une assez bonne concordance spatiale.

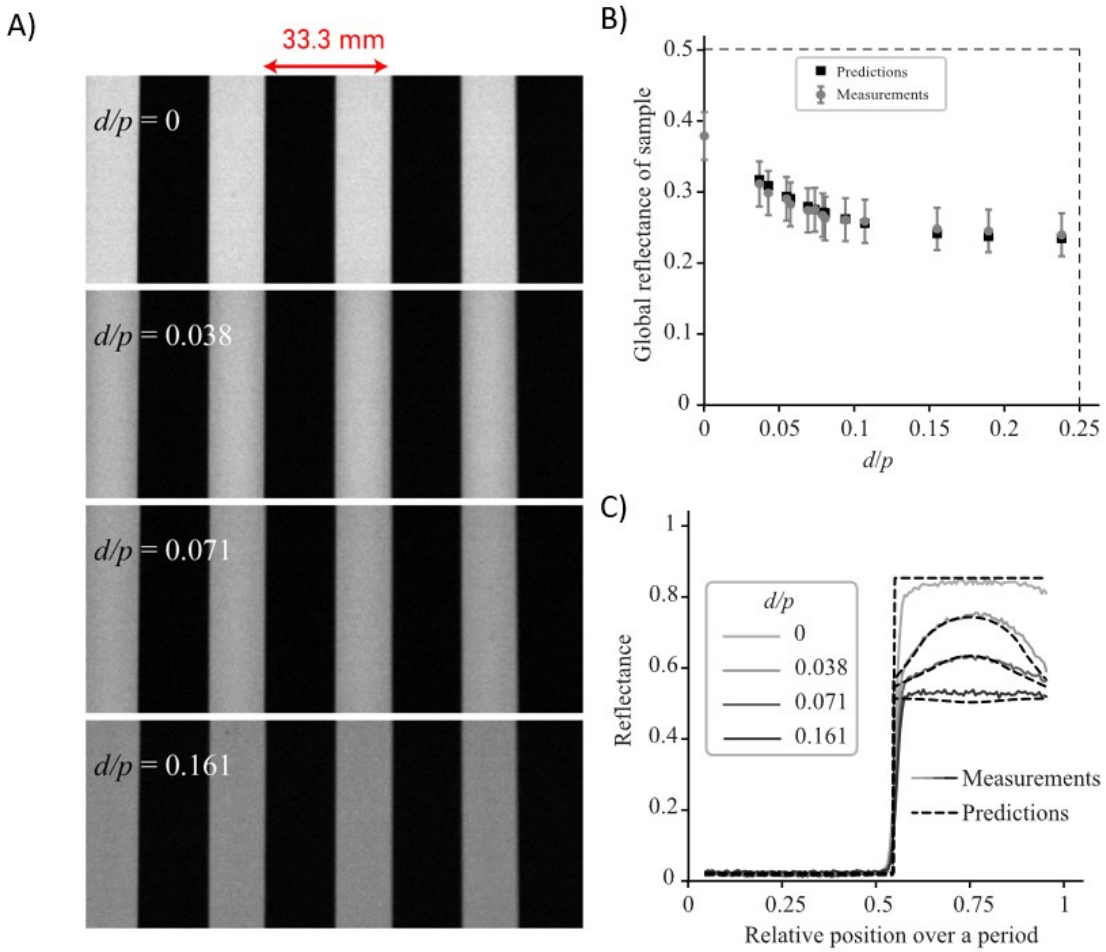

Figure R.3. a) Images des facteurs de réflectance spatiaux du demi-ton pour différentes épaisseurs de couche transparente. b) Facteur de réflectance moyenné sur la surface

pour différents ratios entre l'épaisseur de la couche transparente, d*, et la période* p *du motif de demi-ton. c) Profile du facteur de réflectance spatial pour différentes épaisseurs de couche transparente.*

Une seconde expérience a été réalisée à l'échelle millimétrique où des lignes imprimées magenta ont été couverts d'un vernis légèrement absorbant. Les prédictions du modèle multi-convolutif étaient plutôt en accord avec les mesures spectrophotométriques des impressions vernis, ce qui a permis de valider le modèle spectralement.

Effets de différents paramètres d'impression

Différentes simulations utilisant le modèle multi convolutif ont été réalisées pour déterminer l'influence sur le changement de couleur de différentes propriétés d'impression : l'indice optique de la couche et du substrat imprimé, le taux de couverture du demi-ton, la forme du motif de demi-ton et son profil (qui peut être impacté par le dot gain optique). Il a été observé que le changement de couleur était maximal pour des indices optiques élevés, un taux de couverture autour de 0.5, un motif en forme de ligne avec un profil en échelon.

Des simulations utilisant un modèle de BRDF à micro-facettes et une expérience ont permis de montrer que la propagation de la lumière sous forme de halo à l'intérieur de la couche transparente reste pratiquement identique quelle que soit la rugosité de surface de la couche transparente. Ainsi, le modèle multi-convolutif peut être appliqué aussi bien à des couches brillantes qu'à des couches mattes. Il faut simplement adapter un paramètre du modèle représentant la quantité de lumière réfléchie extérieurement par l'interface vers le capteur. En effet, cette quantité varie si la pellicule est matte ou brillante et explique la différence de couleur qui peut être observée entre un imprimé pelliculé mat et un brillant, comme montré dans la Figure 1.R.

Application pour la gestion de la couleur en impression

Les motifs de demi-tons classiquement imprimés ont des dimensions microscopiques. A cette échelle leur réflectance spatiale est fortement impactée par le dot gain optique et mécanique. Ceci rend la réflectance spatiale effective difficile à estimer à partir de mesures macroscopiques et du motif de demi-ton nominal. Ainsi, pour pouvoir calibrer le modèle multi-convolutif dans le cas d'impressions à l'échelle microscopique, un microscope multispectral a été développé. Celui-ci permet de prendre des photos d'un motif imprimé successivement à travers différents filtres optiques colorés laissant passer de faibles bandes spectrales (25 nm), ce qui permet de mesurer le facteur de réflectance spatial et spectral d'imprimés en demi-ton avec une résolution spatiale de 1.386 µm par pixel. Ce système de mesure a été calibré de façon à avoir un accord entre les mesures macroscopique réalisées avec un spectrophotomètre et les mesures

microscopiques spatialement moyennées réalisées avec le microscope. La différence de couleur moyenne entre ces deux types d'instruments sur des impressions électrophotographiques était de $\Delta E_{00}^{*} = 1.02 \pm 0.49$. L'accord était moins précis pour les impressions jet d'encre testées ultérieurement, ce qui pourrait être dû à une différence de BRDF entre les deux types d'impressions et nécessiterait plus de tests.

Le facteur de réflectance mesuré avec le microscope sur des impressions non pelliculées permet d'estimer la réflectance intrinsèque des impressions et de calibrer le modèle multi-convolutif pour prédire le facteur de réflectance spatial et spectral des impressions pelliculées. Pour évaluer la performance du modèle multi-convolutif à l'échelle microscopique, le facteur de réflectance prédit peut être comparé à la mesure par le microscope multispectral des impressions pelliculées. Cette expérience a été réalisée en premier lieu avec des impressions électrophotographiques puis avec des impressions jet d'encre dans le cadre d'une collaboration avec GMG Color. Le motif de demi-ton était en majorité un motif ligne imprimé à différentes périodes en cyan et magenta. Les résultats pour un des patches éléctrophotographiques cyans sont présentés dans la Figure R.4. Dans cette figure, on peut voir l'effet de l'ajout d'une couche transparente sur le facteur de réflectance spectral (Figure R.4.a) avec une réduction du facteur de réflectance aux longueurs d'ondes où l'encre absorbe, et sur les valeurs spatiales (Figure R.4.b) avec un assombrissement et floutage du profil des lignes blanches. L'impact de l'ajout de couche transparente est également visible dans la Figure R.4.c où sont affichées les images en sRGB de l'impression non-pelliculée à gauche, pelliculée à droite, et prédite par le modèle multi-convolutif au centre. Le modèle parvient à prédire le changement de couleur dû au phénomène de halation de façon assez précise. En électrophotographie, la différence de couleur moyenne entre mesure et prédiction était $\Delta E_{00}^{*} = 0.95 \pm 0.39$, et en jet d'encre elle était $\Delta E_{00}^{*} = 0.68 \pm 0.28$.

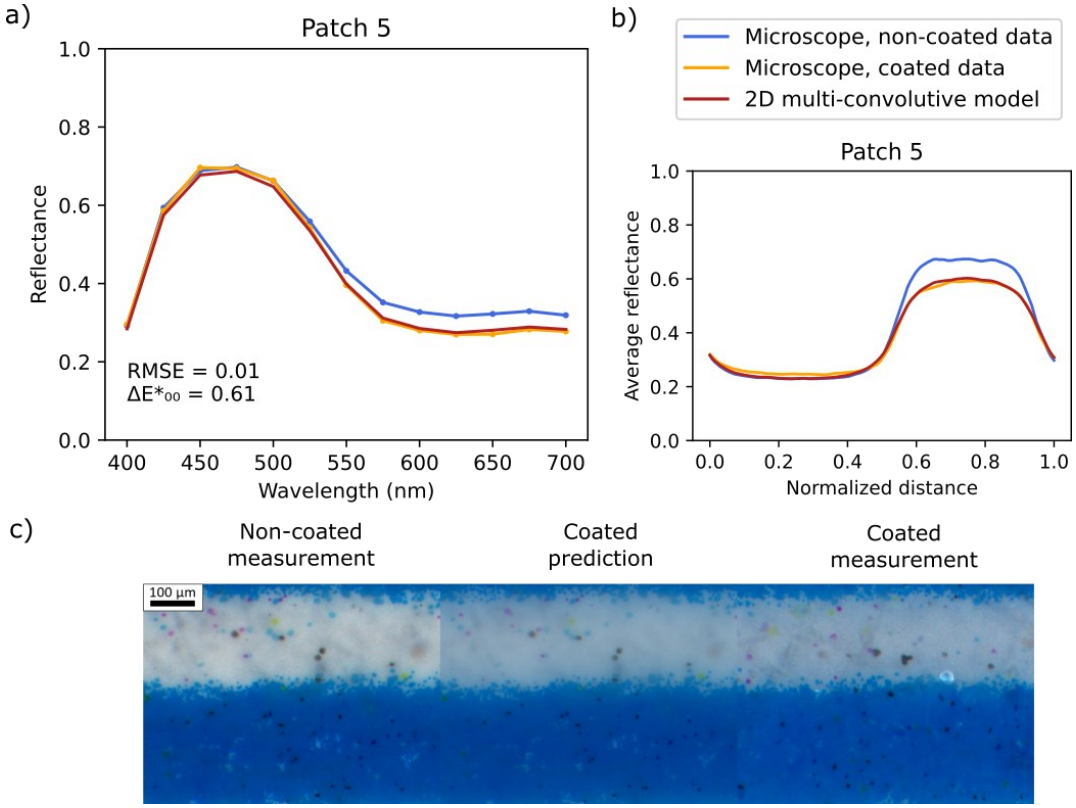

Figure R.4. a) Facteur de réflectance spectrale d'une impression en demi-ton cyan avec un motif ligne, le facteur de réflectance est moyenné spatialement sur une période de l'impression ; b) Profil du facteur de réflectance spatial sur une période du demi ton, moyenné spectralement ; c) Images sRGB du demi-ton non-pelliculé à gauche, pelliculé à droite et prédit par le modèle multi-convolutif au milieu.

Le modèle permet donc d'avoir une plutôt bonne prédiction de la couleur d'impressions couvertes d'une couche transparente, ce qui peut s'avérer utile pour la gestion de la couleur en impression. Néanmoins, en pratique, le microscope multispectral utilisé pour la calibration du modèle est un instrument assez rare. Des simulations préliminaires ont été réalisés pour tester si des mesures de microscope RGB classiques pourraient être utilisées pour reconstruire le facteur de réflectance spatial et spectral d'impressions en demi-tons et pouvoir calibrer le modèle. Cette méthode repose sur l'utilisation de l'analyse en composantes principales d'un système d'impression et a montré des premiers résultats plutôt prometteurs.

Application : images cachées

Enfin, à partir des connaissances sur le phénomène de halation et sur les paramètres l'impactant, une application a été réalisée. Elle consiste à cacher et révéler une image dans une impression en ajoutant ou en retirant une couche transparente en contact avec l'impression. Cette application repose sur l'utilisation de deux motifs de demi-ton différents pour l'image et pour le fond qui sont impactés différemment par le phénomène de halation. Ainsi, l'image peut être confondue avec le fond pour une épaisseur de couche transparente donnée et ressortir lorsque

cette épaisseur change. Deux formes tests ont été réalisées suivant ce principe, une en nuances de gris, l'autre en couleur. Il a été observé que les images, indiscernables sous une couche de pellicule devenaient visibles lorsque la pellicule était retirée ou lorsqu'une deuxième pellicule était ajoutée. Cette application pourrait ouvrir la voie à un nouveau système anti-contrefaçon.

Conclusion

Il a été montré que la propagation de la lumière à l'intérieur d'une couche transparente au-dessus d'une impression est à l'origine d'un changement de couleur, que ce changement peut être modélisé en prenant en compte la forme annulaire de la propagation de la lumière dans la couche transparente. Ce modèle a été vérifié expérimentalement à l'échelle macroscopique et à l'échelle microscopique. Il a permis de mieux comprendre l'impact de différents facteurs sur le changement de couleur ce qui a mené à une curieuse application où des images peuvent être cachées simplement en jouant sur l'épaisseur d'une couche transparente au-dessus d'une impression. Un futur objectif serait de faciliter la calibration du modèle pour pouvoir l' intégrer plus facilement dans le processus de gestion de la couleur.

Appendix I. Color and colorimetry

The light emitted by a source (such as the sun) interacts with objects, which can absorb, reflect, transmit or scatter it. The share of light issued from this interaction reaching our eyes can be captured by the retina and processed by our eyes and brains to generate internal appearance of the objects around us.

The appearance of a material is characterised by each individual perception. It cannot be measured or completely described by physics for it depends on each brain interpretation of what is seen. For instance, age or even drinking a cup of coffee can have an influence on color perception [175], [176]. Only psychophysical tests allow comparing perceptions of different persons and try to link them with the physics of the materials. The appearance of a material is usually described thanks to four attributes: color, texture, translucency and gloss [177], to which can be added sparkle, shape, fluorescence, etc [178]. They are illustrated in Figure 86.

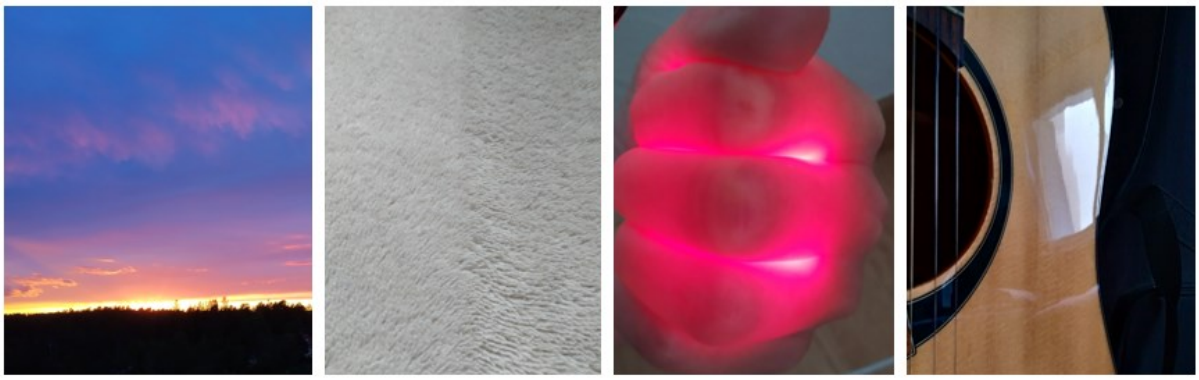

Figure 86. Appearance attributes: color, texture, translucency, gloss.

Even if material appearance cannot be described by physics, the luminous signal reaching the eyes can still be characterized thanks to optical measurements with, for instance reflectance factor measurements. A model of perception was established to link in a simple manner the reflectance and the perceived color. Having usually three different types of cones in the retina to detect color, color is usually described in a three-dimensional space, for instance with hue, chroma and lightness. One of the best established colorspace is the CIE1931 XYZ colorspace. This colorspace associates to a reflectance spectrum a triplet *X, Y, Z* which characterizes color without considering the viewing conditions:

$$X = \int I(\lambda)\, R(\lambda)\, \overline{x}(\lambda) d\lambda \qquad 116$$

$$Y = \int I(\lambda)\, R(\lambda)\bar{y}(\lambda)d\lambda \quad 117$$

$$Z = \int I(\lambda)\, R(\lambda)\bar{z}(\lambda)d\lambda \quad 118$$

with $\bar{x}$, $\bar{y}$, $\bar{z}$ the color matching functions, $R(\lambda)$ and $I(\lambda)$ the amplitude of the spectrum respectively of reflectance and of illumination at the wavelength λ.

The CIE1931 XYZ tristimulus values do not account for the viewing conditions. Yet, as shown in Figure 87, viewing conditions can have an important impact on color perception. The CIE1976 L*a*b* colorspace was then introduced to better account for the viewing conditions [146]. In this colorspace, color is described by L* the lightness, b* the blue – yellow hue, a* the green-red hue.

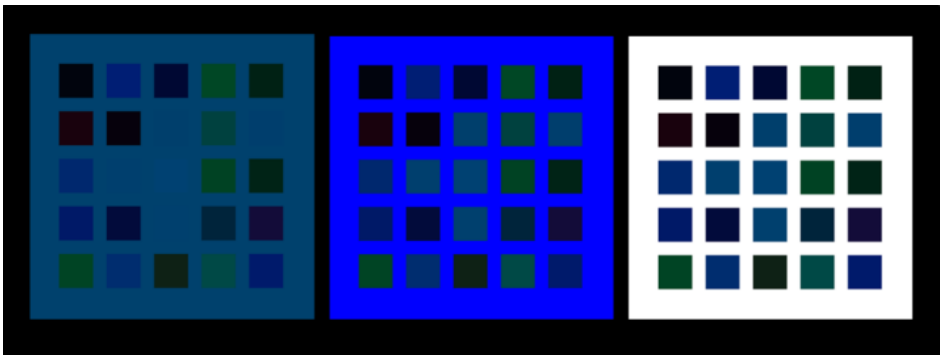

Figure 87. Influence of the viewing conditions in color perception. Each colored patch has the same RVB values in the three colorcharts. Yet, the colorcharts have different backgrounds. Simultaneous contrast makes the patch color appear differently according to the background.

This colorspace takes into account a particular viewing condition called chromatic adaptation. Chromatic adaptation describes the principle that every color is perceived by the brain with respect to a white reference (white point): the brightest point in the field of view.

The L*, a*, b* values are calculated from the CIE1931 XYZ tristimulus values thanks to the following formulas:

$$L^* = 116 \times f\left(\frac{Y}{Y_w}\right) - 16$$

$$a^* = 500 \times \left[f\left(\frac{X}{X_w}\right) - f\left(\frac{Y}{Y_w}\right)\right] \quad 119$$

$$b^* = 200 \times \left[f\left(\frac{Y}{Y_w}\right) - f\left(\frac{Z}{Z_w}\right)\right]$$

with X_w, Y_w, Z_w the CIE1931 tristimulus values of the white reference and f a function:

$$f(u) = \begin{cases} u^{\frac{1}{3}} & \text{if } u > 0.008856 \\ 7.787 \times u + \dfrac{16}{116} & \text{if } u \leq 0.008856 \end{cases} \quad 120$$

The L*, a*, b* values of the white reference are $L^* = 100$, $a^* = 0$, $b^* = 0$, and the L*a*b* values of the black are $L^* = 0$, $a^* = 0$, and $b^* = 0$.

The results in the L*a*b* space are usually shown in the a*b* plan which describes the colors without considering the lightness, and in the L*C* plan, with C* the chroma (color saturation):

$$C^* = \sqrt{a^{*2} + b^{*2}} \quad 121$$

The color difference between two elements can be estimated through a numerical value. In the CIEL*a*b* colorspace, it can be calculated as the Euclidian distance ΔE^*_{ab} in this colorspace:

$$\Delta E^*_{ab} = \sqrt{L^{*2} + a^{*2} + b^{*2}} \quad 122$$

The color difference under which the eye is unable to detect the difference corresponds to $\Delta E^*_{ab} = 2.2$ (just noticeable difference).

The estimations of color differences gradually evolved, in 1994 the CIE suggested the formula of ΔE_{94} [179]. Currently it is rather estimated from the CIE2000, described in [180], this color difference estimation was preferred in this work.

Another colorspace which was helpful during this work is the sRGB colorspace as it allows to reproduce the color of an object on a calibrated screen from its coordinates in another colorspace. The way we performed this conversion is presented here:

The CIE1931 tristimulus values, *X, Y, Z* of a color patch, estimated with the D65 illuminant, were normalized with the Y_w value of the white reference (estimated with D65 illuminant too), and converted to *R, G, B* values from the sRGB colorspace (respectively, red, green and blue components of the color to display on a screen) with the conversion [168]:

$$\begin{bmatrix} R \\ G \\ B \end{bmatrix} = \begin{bmatrix} 3.2404542 & -1.5371385 & -0.4985314 \\ -0.9692660 & 1.8760108 & 0.0415560 \\ 0.0556434 & -0.2040259 & 1.0572252 \end{bmatrix} \times \begin{bmatrix} X/Y_w \\ Y/Y_w \\ Z/Y_w \end{bmatrix} \quad 123$$

The R,G,B values were then cropped to fit between 0 and 1.

This method allows to display the color to assess them visually, but it is limited by the capacity of the screen to display a range of colors wide enough to contain the targeted color. Furthermore, it does not reproduce the original viewing conditions of the object, which can have an influence on color perception.

Appendix II. Electrophotography and inkjet

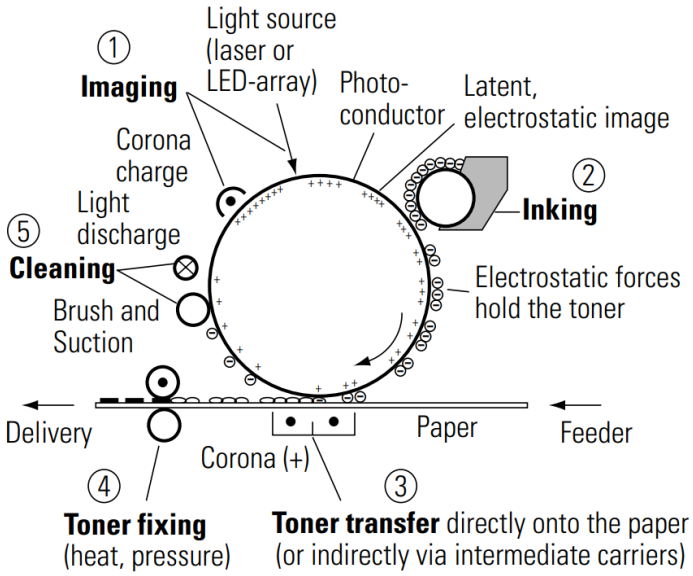

Figure 88. Scheme of an electophotographic printer, extracted from [1].

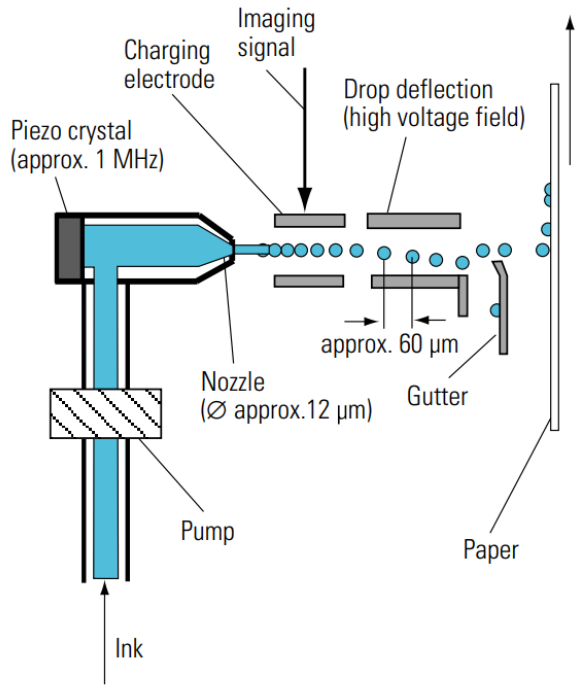

Specifications (example):
Drop frequency: approx. 1 MHz
Drop diameter: approx. 20 µm
Drop speed: approx. 40 m/s

Figure 89. Scheme of a continuous inkjet printer, extracted from [1].

Appendix III. Theoretical evaluation of the γ parameter of the multi-convolutive model

The optical model describing the halation phenomenon over a print subject to optical dot gain contains a parameter γ. This parameter describes the increase of the ink intrinsic transmittance when the light rays are inclined with respect to the normal of the surface, see Figure 90. This is the case for the rays reflected at the interface. The ink transmittance is then t^{γ}, where t is the intrinsic transmittance of the ink at normal incidence. In previous studies, the parameter γ was fitted to the experimental data. The objective here is to calculate its theoretical value. A scheme of the system is displayed in Figure 90.

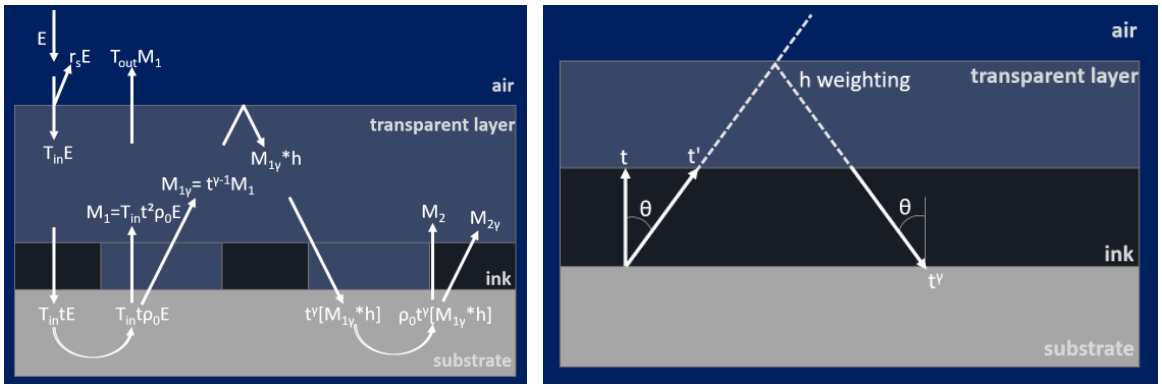

Figure 90. Left: scheme of the optical model. Right: parameters of the calculation of the theoretical γ.

A matrix **Θ** composed of incidence angles on the substrate is defined, with the same size and pixel pitch as the matrix **h** defining the halo point spread function. For a position (i, j) in the matrix, the corresponding position (x, y) is calculated, knowing the pixel pitch. The angle θ at the position (i, j) of matrix Θ is calculated with $\theta = arctan\left(\frac{\sqrt{x^2+y^2}}{2d}\right)$, with d the coating thickness.

A matrix of intrinsic transmittances is defined in three dimensions: two dimensions for the spatial dimension, the same as the dimensions of $\boldsymbol{\Theta}$ and $\boldsymbol{h}$. The last dimension is used to make the ink intrinsic transmittance along the normal, t, vary from 0 to 1 with a step of 0.01.

The matrix containing the intrinsic transmittance for each incident angle is calculated, **T'**. At position (i, j), it is equal to: $t'(\theta) = t(k)^{1/\cos(\theta)}$, where t(k) is the kth intrinsic transmittance along the normal, between 0 and 1.

To find the γ parameter for each *t(k)*, the average intrinsic transmittance taking into account the various angle of incidence is estimated, t_γ, by averaging matrix ***T'*** weighted by the halo matrix ***h***:

$$t_\gamma(k) = \frac{\sum_i \sum_j h(i,j) \times T'(i,j,k)}{\sum_i \sum_j h(i,j)} \quad 124$$

By definition of the γ parameter, this value corresponds to:

$$t_\gamma(k) = t^\gamma(k) \quad 125$$

From this follows:

$$\gamma = \frac{\ln\left(t_\gamma(k)\right)}{\ln\left(t(k)\right)} \quad 126$$

Which allow to estimate the γ parameter for each *t*. The results are displayed in Figure 91:

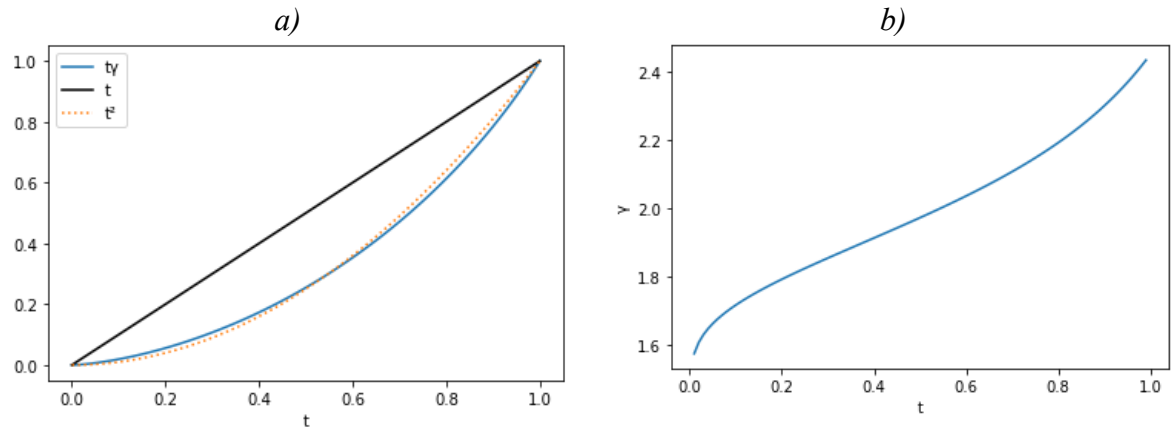

Figure 91. a) Theoretical intrinsic transmittance encountered by the light rays reflected by the halo-shaped internal reflection as a function of the intrinsic transmittance at normal incidence. b) γ parameter as a function of the intrinsic transmittance at normal incidence.

For $d = 10\ \mu m$, the average value of γ over all intrinsic transmittances is 1.99. It can be noted that this value does not theoretically depend on the coating thickness *d* (the critical angle at the coating-air interface is the same whatever *d)* but the simulations show slight variations, probably because the matrices have a finite spatial dimension (when $d = 10\ \mu m$, the angles of incidence higher than 88° are not considered, this limit decreases as *d* increases).

It can also be noted that this parameter does not depend on the thickness ratio between the ink thickness and the coating thickness. Even if the coating thickness is high with respect to the ink thickness, this parameter should influence the results. It can be noted that the theoretical value is far from the experimental fit presented in Section 4.3.1 (the fitted value was 1.23, and the results from the model are highly dependent on the value of γ). Furthermore, experimental

results showed that fulltones were better modelled with $\gamma = 1$ than with higher values. These different points can lead to two conclusions:

- In the experiment presented in Section 4.3.1 the intrinsic transmittances of the inks at normal incidence were probably misevaluated: they were evaluated from the Williams-Clapper model and Berns approximation. Yet, in these models, light is also subject to the halo-shaped internal reflection at the ink-air interface and light reflected by the interface also propagates a longer distance inside the ink layer. Thus, t may have been overestimated, taking a share of γ.
- In the experiment presented in Chapter 3, the $\gamma = 1.23$ which was found helps to model optical dot gain to a certain extent: it tends to underestimate the modelled reflectance of the inked part, while the modelled reflectance of the non-inked parts is still above the measured one.

Appendix IV. Simulations of the approximation of the model with a reduced number of convolutions

The simulations presented in Figures 92 and 93 rely on the reflectance factor prediction of a line halftone pattern of surface coverage 0.5, of period p and covered by a clear layer of thickness d and optical index $n_1 = 1.5$, identically to the simulations presented in Section 3.6. The blue continuous lines show the reflectance factors predicted by the multi-convolutive model described in Section 3.2.2 and the dashed and dotted lines rely on the approximation presented in Section 3.2.3, with i, the number of reflection on the substrate after which the convolutions are no-longer taken into account. Figure 92 shows the spatially averaged reflectance factor, and Figure 93 displays the spatial reflectance factor profiles along one period of the halftone pattern.

It can be observed that the convolutions need to be accounted for in at least the four or five first reflections on the substrate. After which, the approximation seems to be rather sufficient.

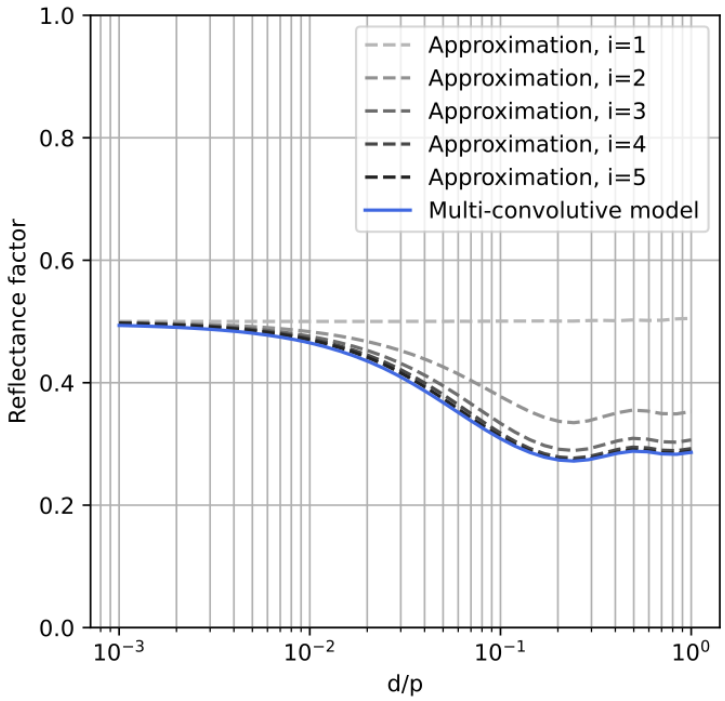

Figure 92. Overall reflectance factor of a halftone pattern predicted by the multi-convolutive model and by its approximation with various i-values.

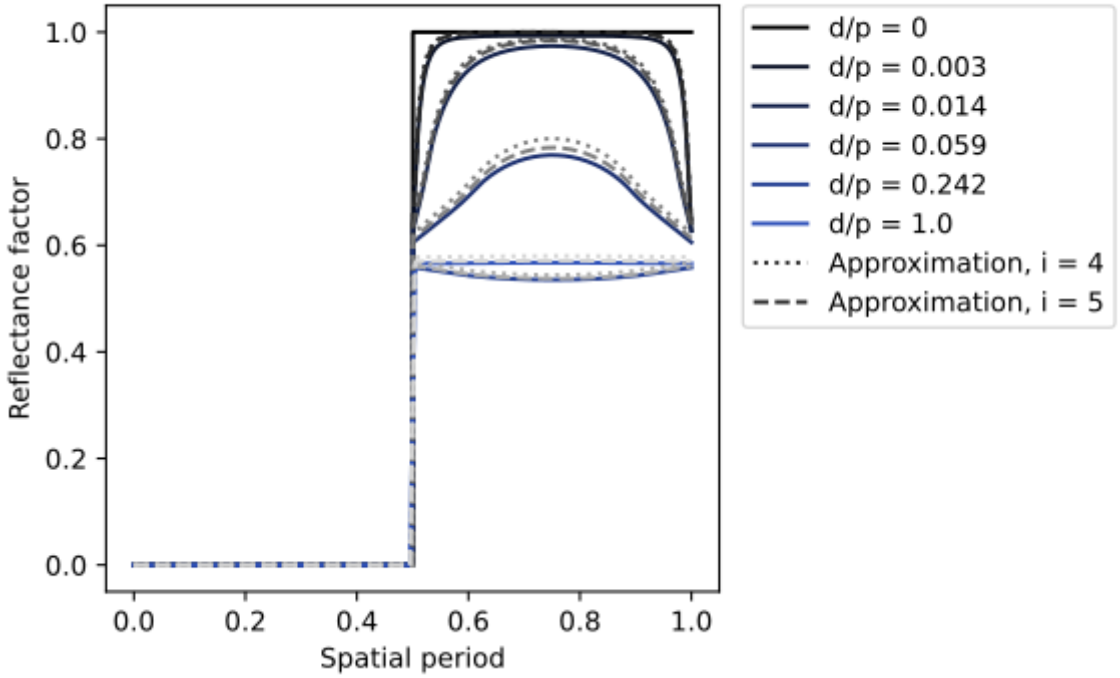

Figure 93. Spatial reflectance factor along one period predicted by the multi-convolutive model (continuous lines) and by its approximation (dotted lines for $i = 4$ and dashed lines for $i = 5$).

Appendix V. Small-scale experiment : resulting reflectance factor curves for each halftone screens

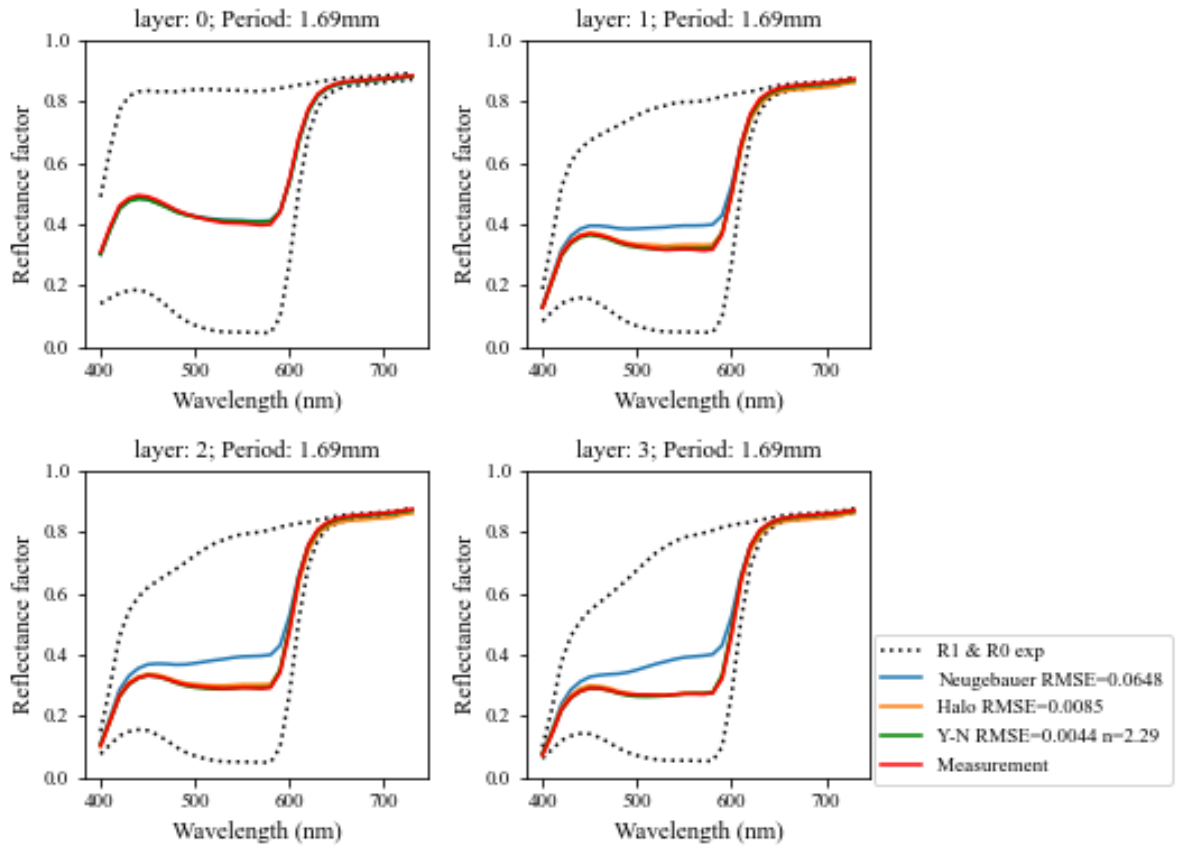

Figure 94. Spectral reflectance factors of the 1.69 mm-period halftone pattern.

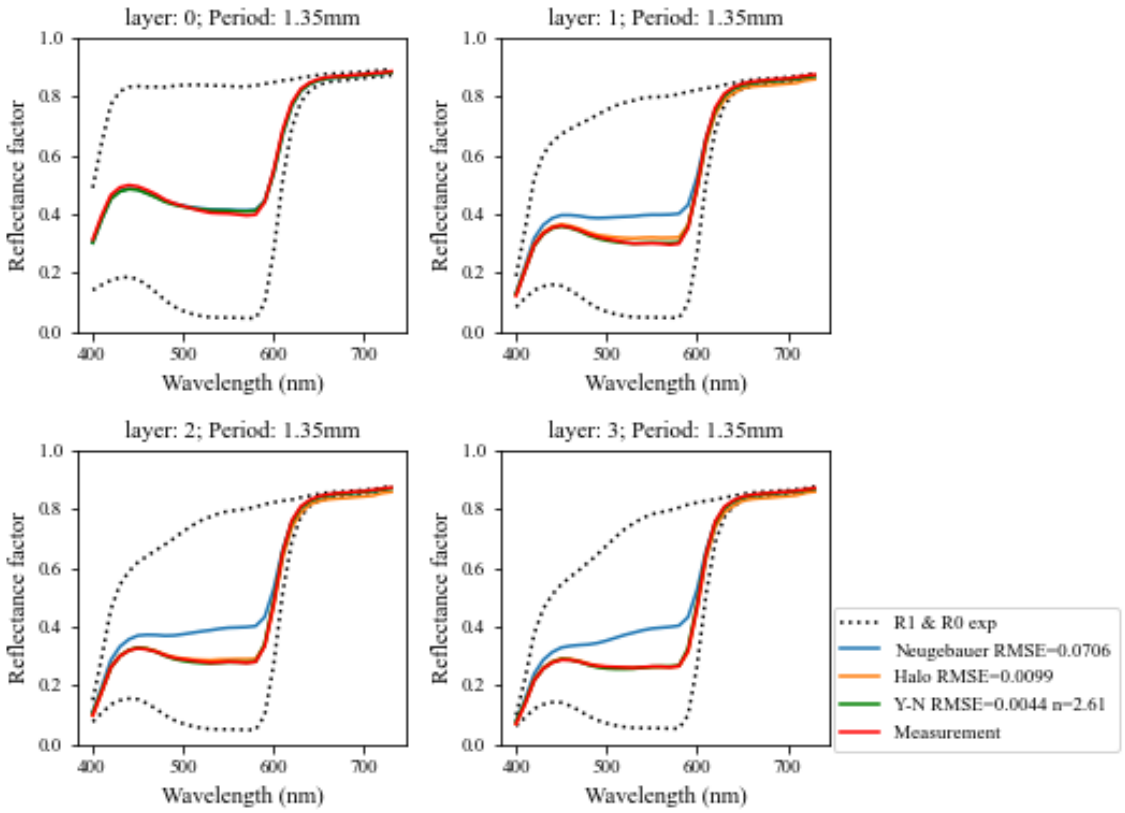

Figure 95. Spectral reflectance factors of the 1.35 mm-period halftone pattern.

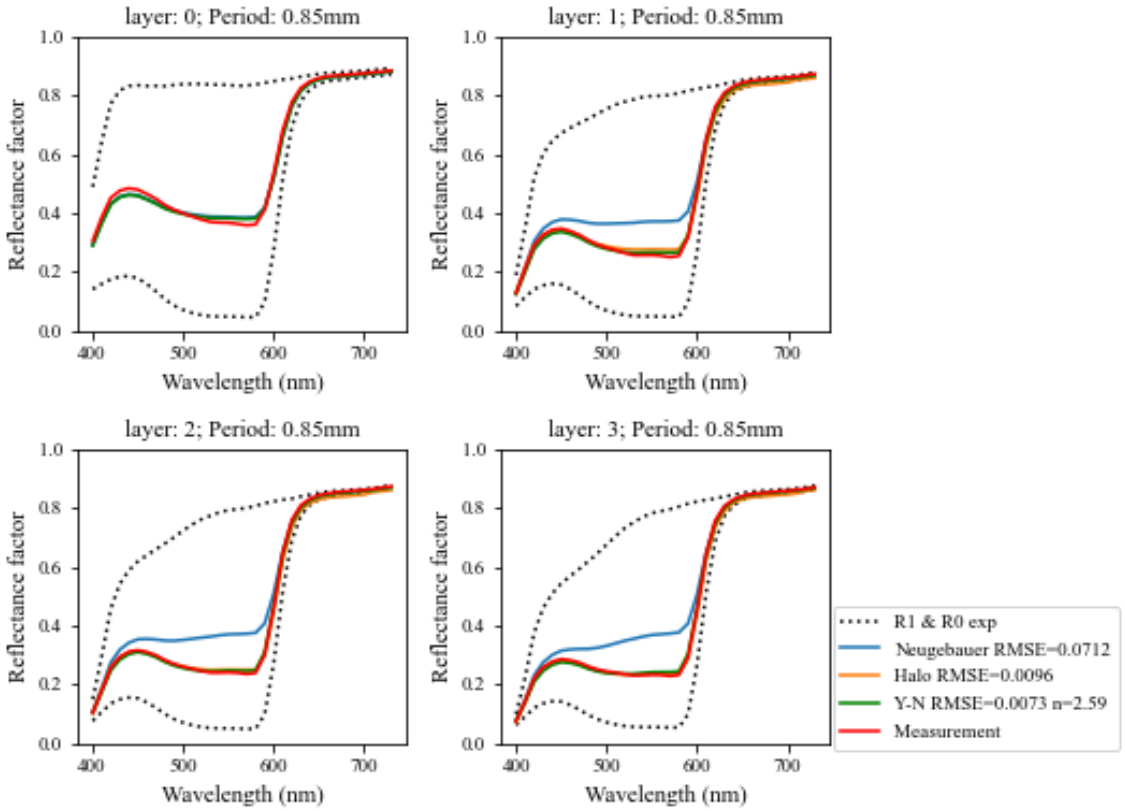

Figure 96. Spectral reflectance factors of the 0.85 mm-period halftone pattern.

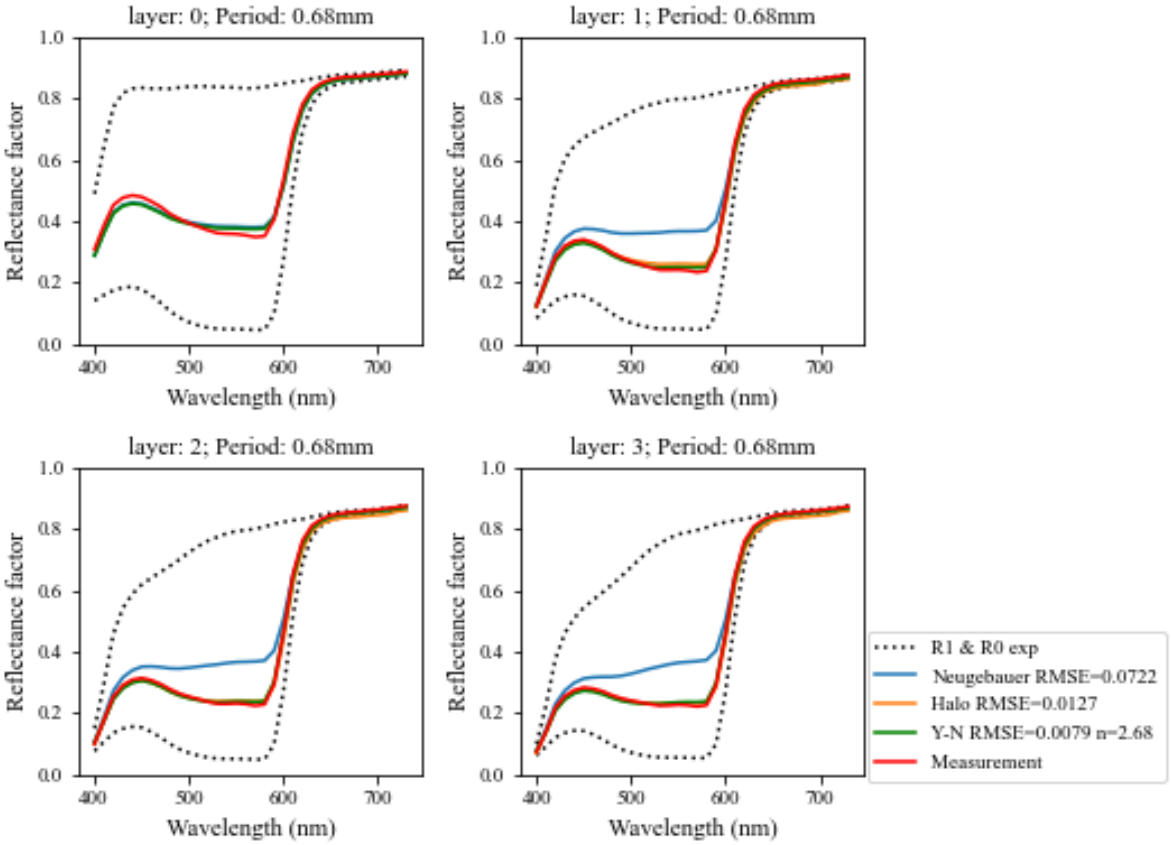

Figure 97. Spectral reflectance factors of the 0.68 mm-period halftone pattern.

Appendix VI. Microscopic measurements: results for the electrophotographic process

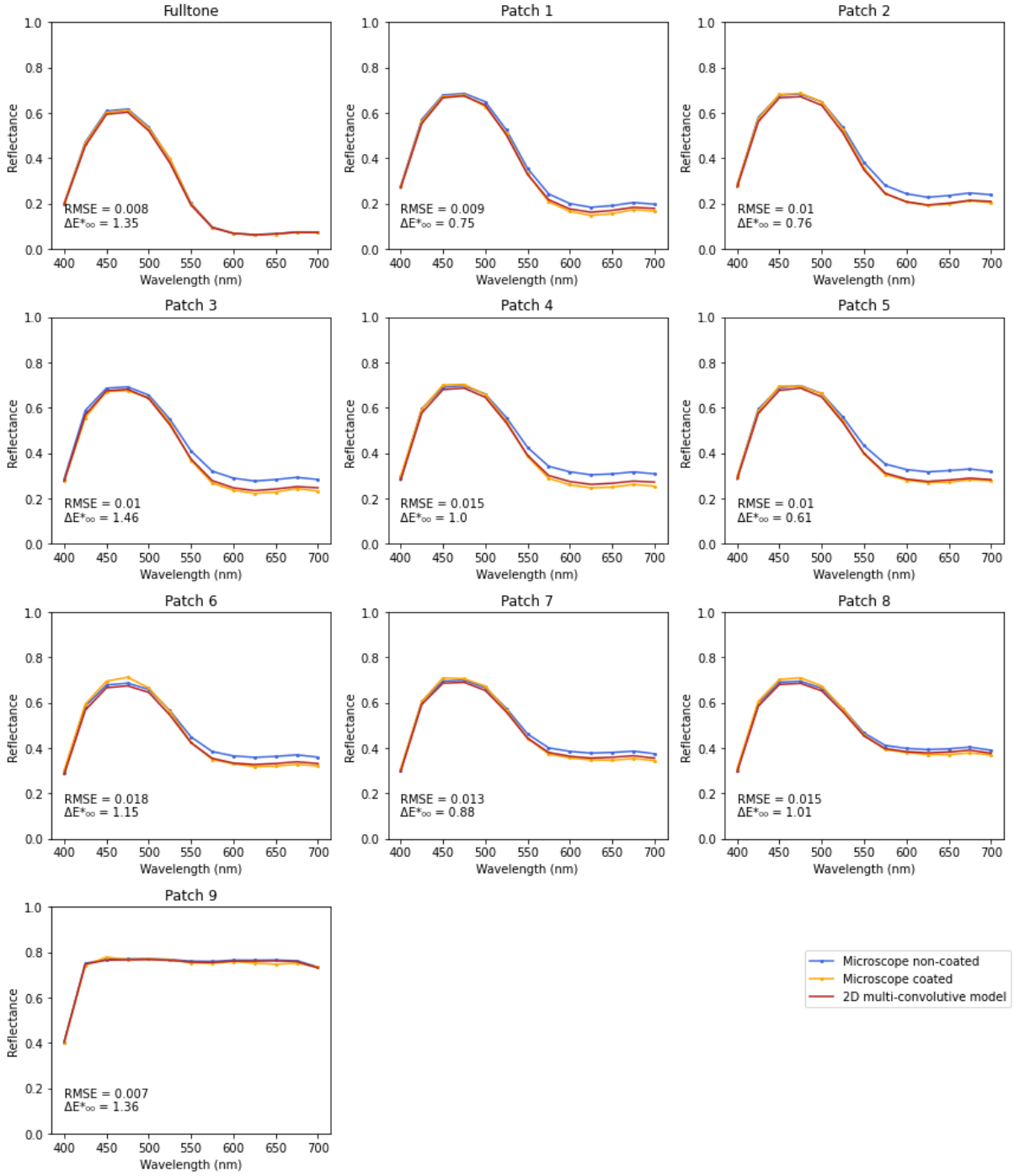

Figure 98. Line cyan halftone reflectance spectra, averaged over the spatial dimension. Patch 1 to 8 have a period of 0.168, 0.250, 0.334, 0.420, 0.504, 0.841, 1.259, and 2.104 mm, respectively. A specular component of 0.04 is added to all spectra.

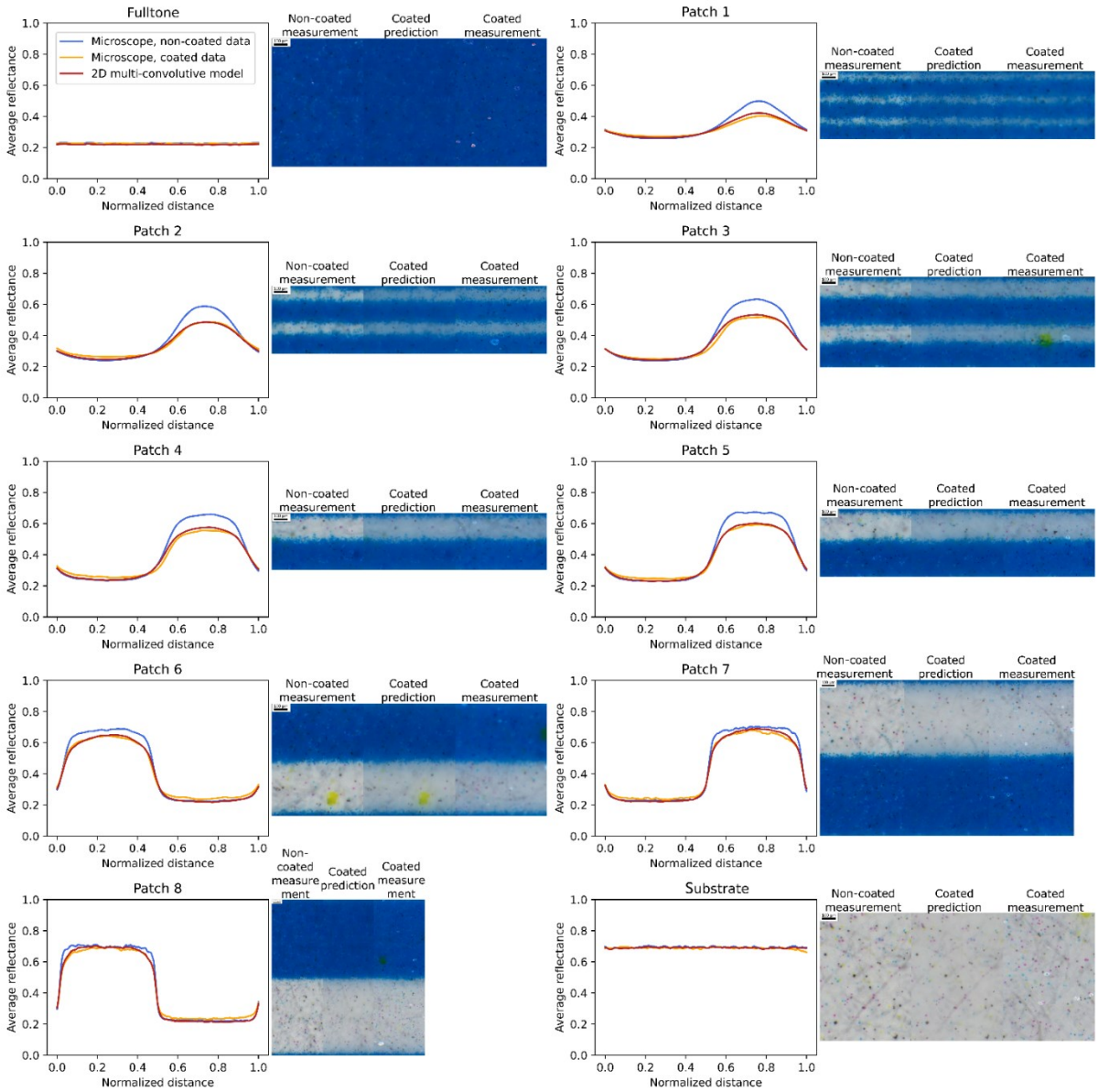

Figure 99. Cyan halftone reflectance profiles averaged over the spectral dimension. On their right, corresponding sRGB pictures of the non-coated, predicted, and coated halftones. Patch 1 to 8 have a period of 0.168, 0.250, 0.334, 0.420, 0.504, 0.841, 1.259, and 2.104 mm, respectively.

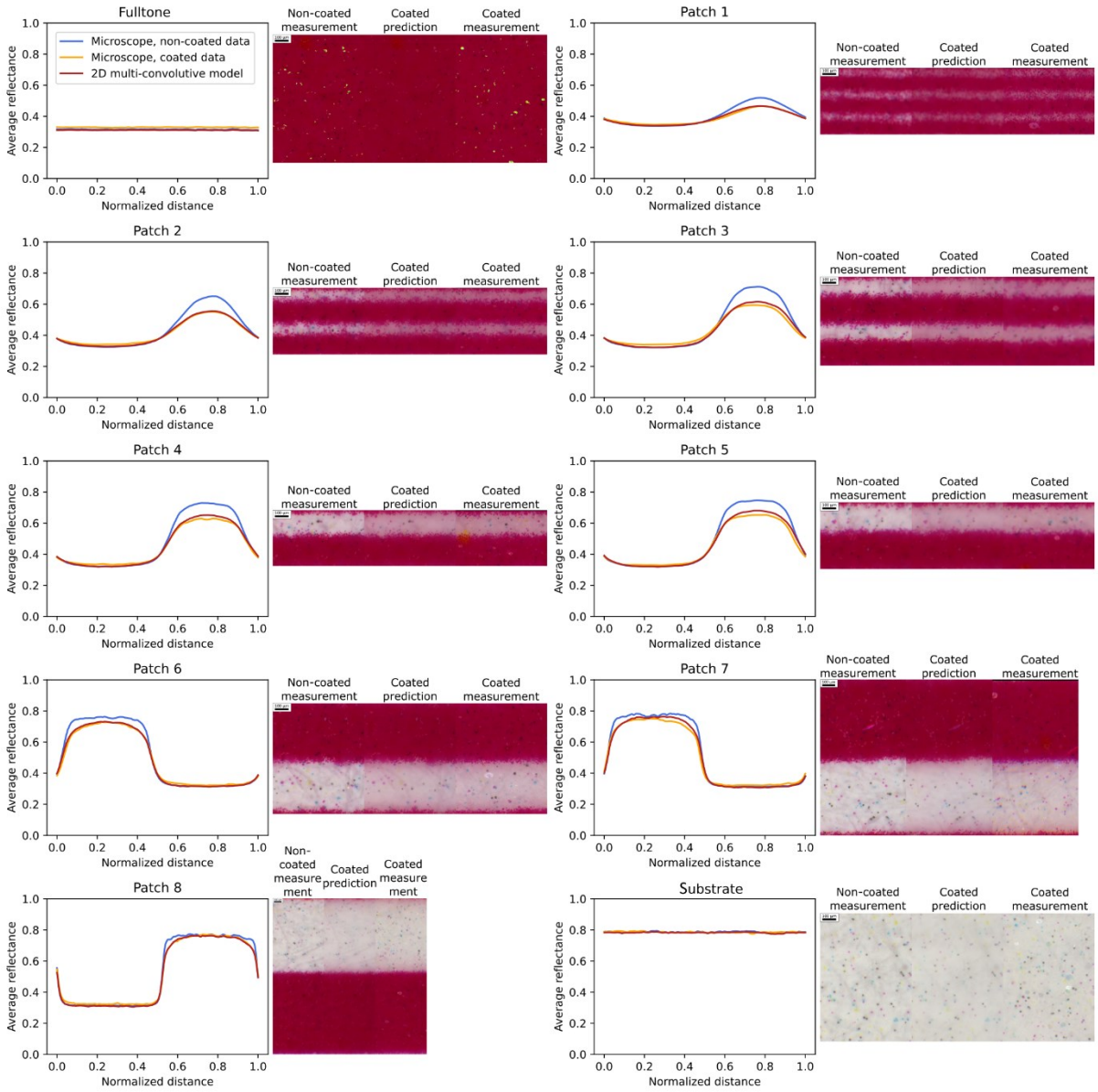

Figure 100. Magenta halftone reflectance profiles averaged over the spectral dimension. On their right, corresponding sRGB pictures of the non-coated, predicted, and coated halftones. Patch 1 to 8 have a period of 0.168, 0.252, 0.337, 0.421, 0.505, 0.839, 1.263, and 2.104 mm, respectively.

Appendix VII. Microscopic measurements: results for the inkjet process

The agreement between the measurements at the microscale performed with the multispectral microscope and the ones at the macroscale performed by GMG with the spectrophotometer CM2600D from Konica Minolta (di:8°) was evaluated. The microscale reflectance factor measurements were averaged on the spatial dimension over an integer number of period and compared to the microscale measurements. It was observed that dividing the microscope measurements by a correction factor of 0.92 and adding to them the specular component 0.04 allowed to have comparable measurements at the micro and at the macro scales, displayed Figure 101. The factor 0.92 can be caused by the difference of BRDF between the calibration spectralon and the inkjet substrate. It is possible that this substrate is less Lambertian than the spectralon, leading to an increase of the reflectance factor measured with the microscope. The detailed performances are detailed with and without correction in Table 9.

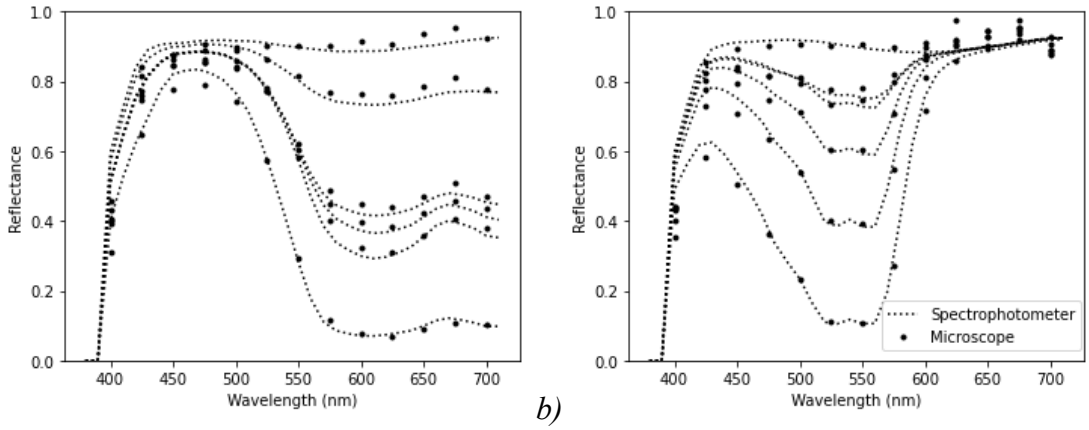

Figure 101. Microscale and macroscale reflectance factor measurements; a) on cyan samples, b)on magenta samples. The microscope measurements were multiplied by 1/0.92, and 0.04 was added to account for the specular component which is included in the spectrophotometric measurements.

	ΔE_{00}^{*} magenta samples		ΔE_{00}^{*} cyan samples	
patch #	Spectrophotometer vs. Microscope Non-Coated Samples without correction	Spectrophotometer vs. Microscope Non-Coated Samples with correction	Spectrophotometer vs. Microscope Non-Coated Samples without correction	Spectrophotometer vs. Microscope Non-Coated Samples with correction
Fulltone	2,56	0,98	2,32	1,57
1	2,55	1,40	2,32	1,68
2	2,52	1,73	2,22	1,24
3	2,31	1,72	2,16	1,51
4	18,56	18,78	2,54	1,99
Substrate	2,75	2,28	2,81	2,35
Average	2,54	1,62	2,40	1,72
standard deviation	0,16	0,48	0,24	0,39
Overall	Spectrophotometer vs. Microscope Non-Coated Samples without correction		Spectrophotometer vs. Microscope Non-Coated Samples with correction	
Average	2,46		1,68	
Standard deviation	0,21		0,41	

Table 9. Color difference ΔE_{00}^{*} between the spectrophotometric measurements and the ones performed with the multispectral microscope on non-coated samples printed in inkjet.

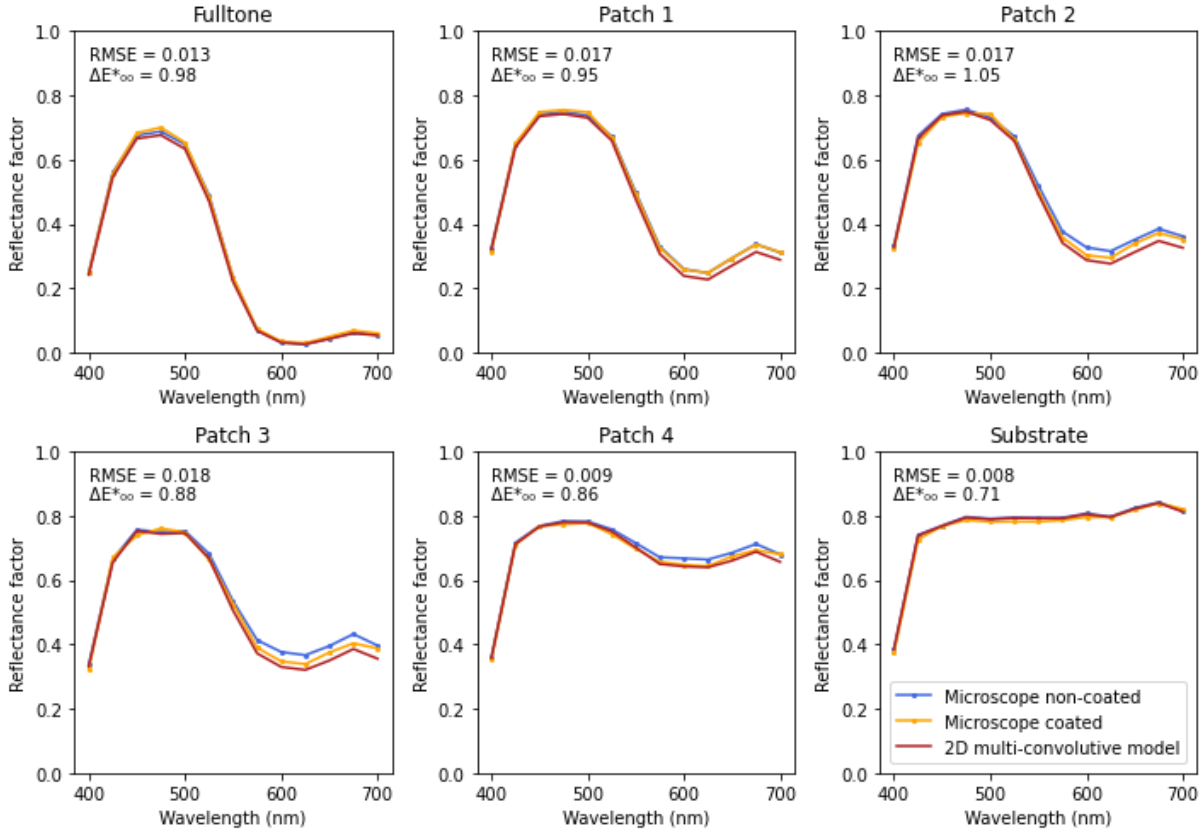

Figure 102. Reflectance factor of the cyan prints averaged over the spatial dimension. The predictions included $\gamma = 1.23$.

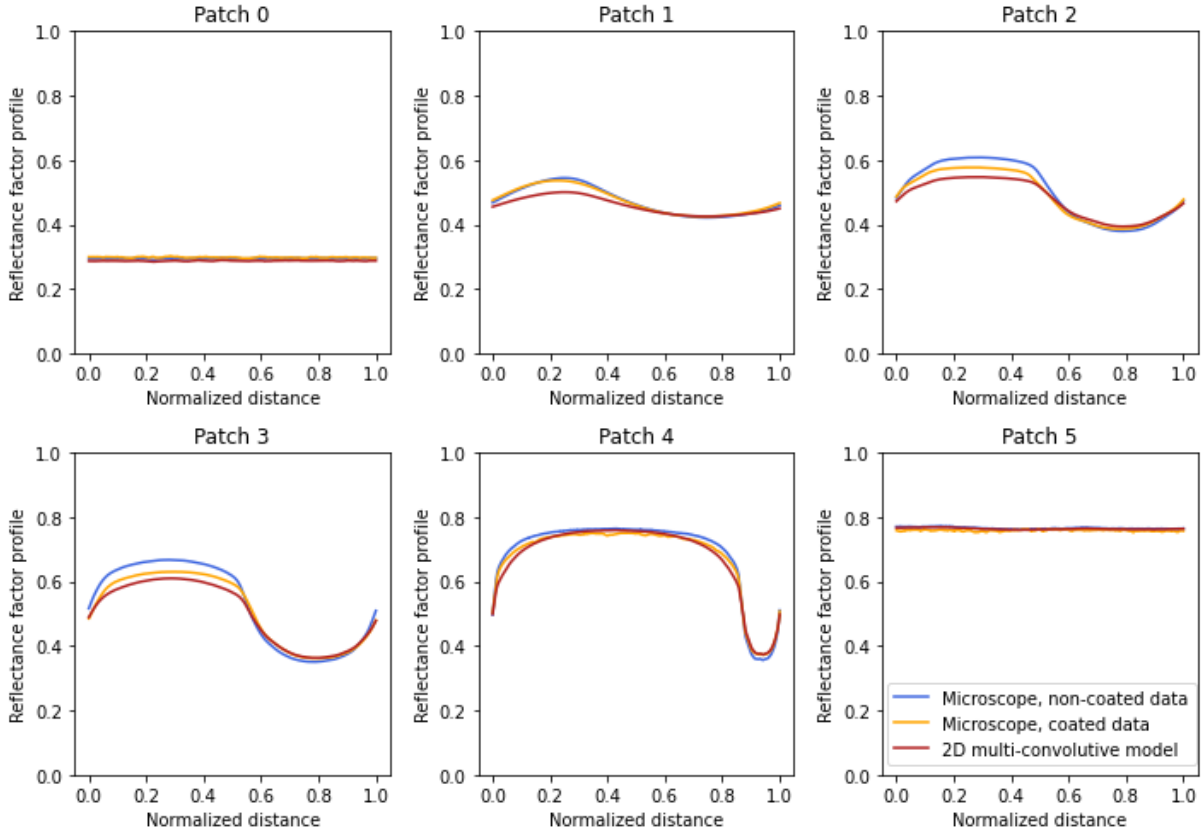

Figure 103. Reflectance factor profile of the cyan prints averaged over the spectral dimension; the profile was spatially averaged over all the lines. The predictions included $\gamma = 1.23$.

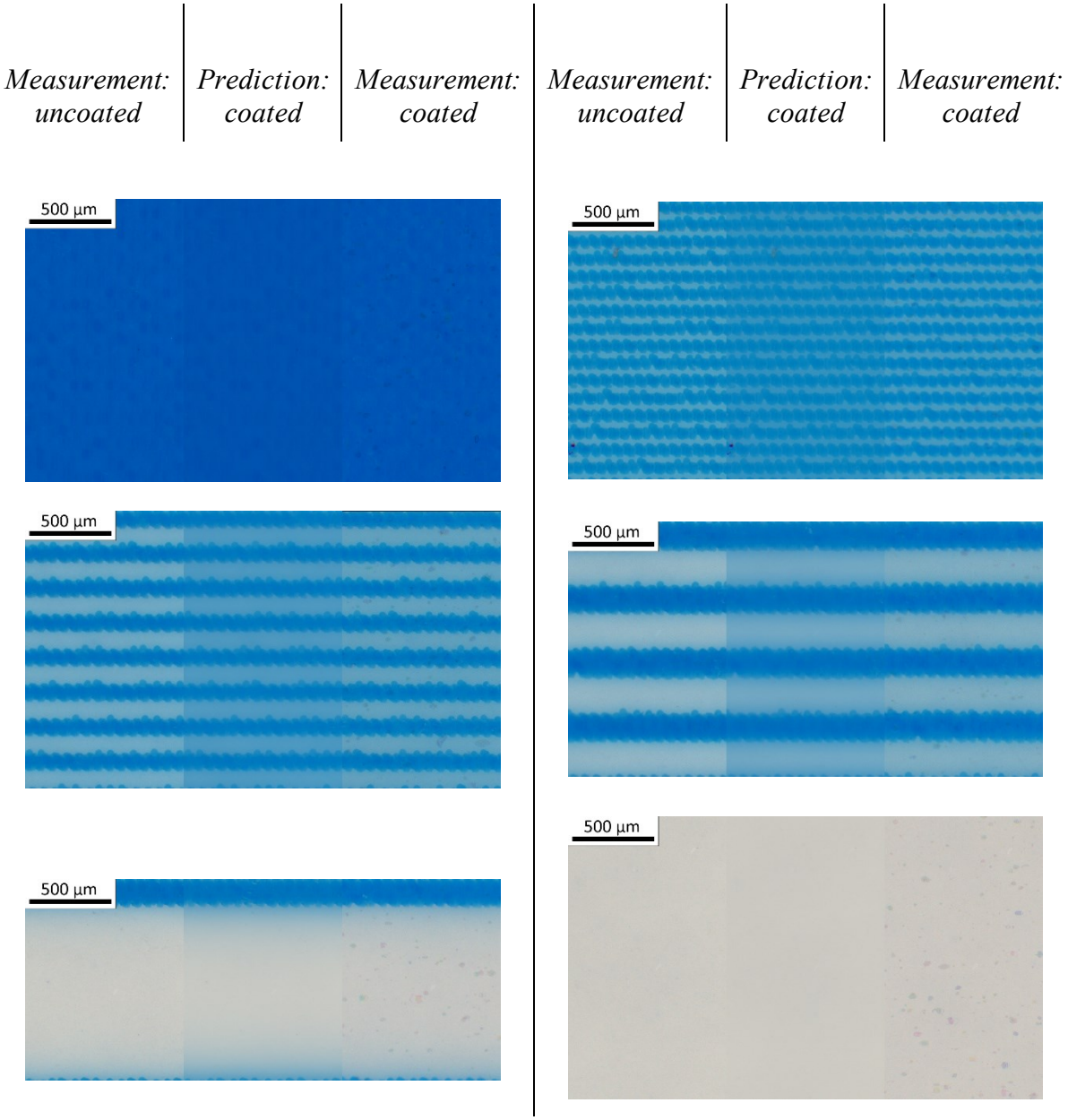

Figure 104. sRGB pictures of the results. The predictions included $\gamma = 1.23$.

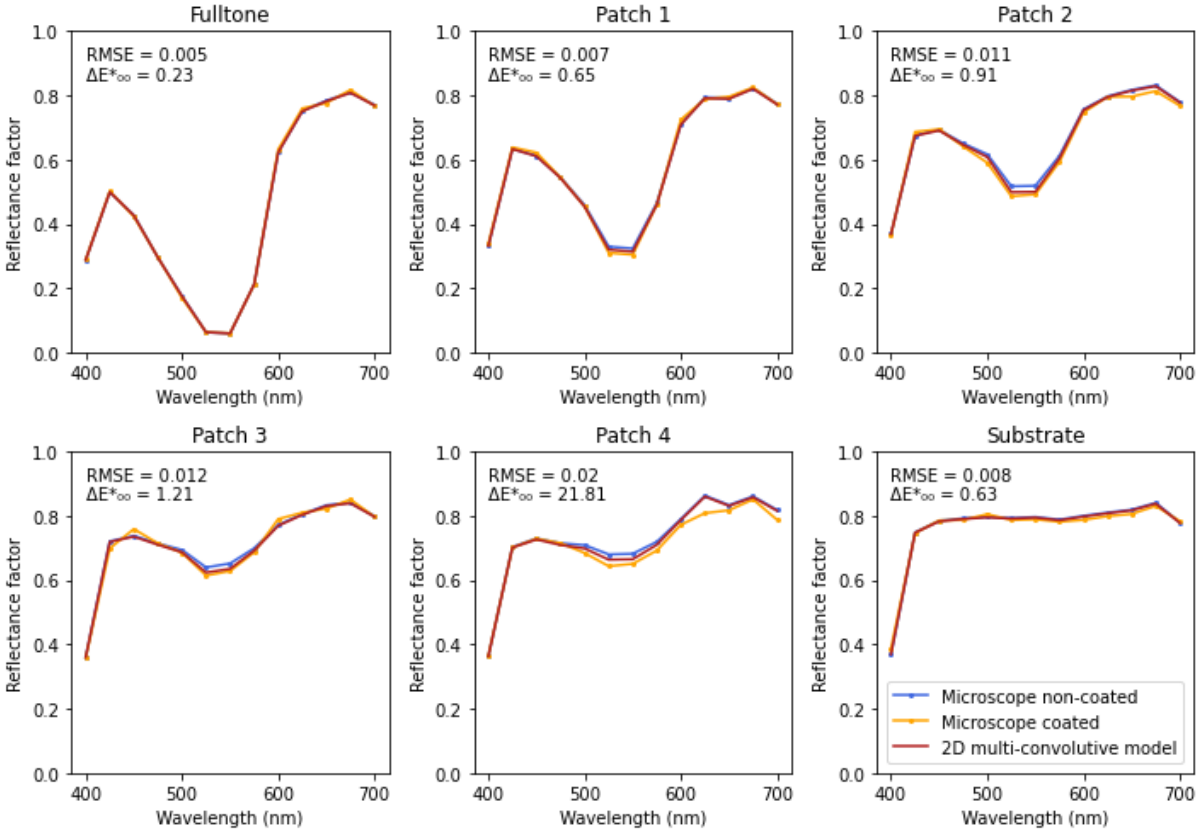

Figure 105. Reflectance factor of the magenta prints averaged over the spatial dimension. The predictions included $\gamma = 1$.

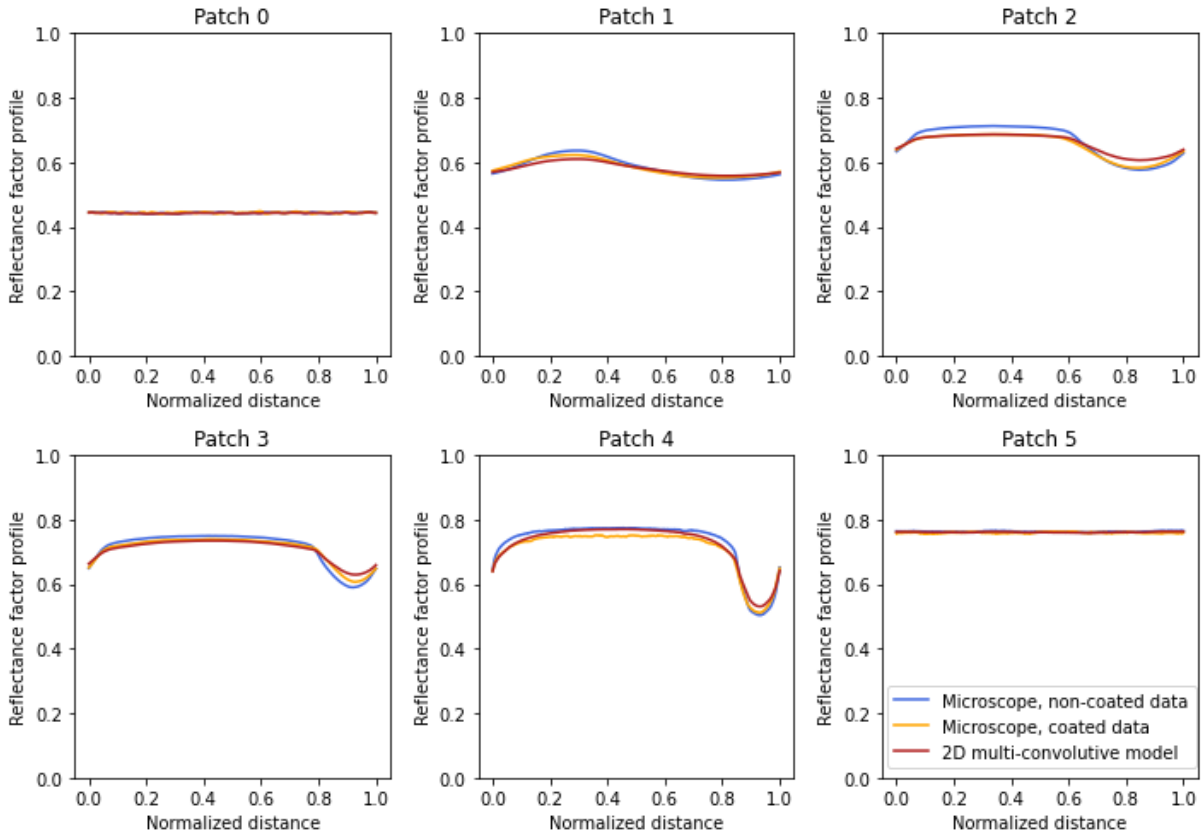

Figure 106. Reflectance factor profile of the magenta prints averaged over the spectral dimension; the profile was spatially averaged over all the lines. The predictions included $\gamma = 1$.

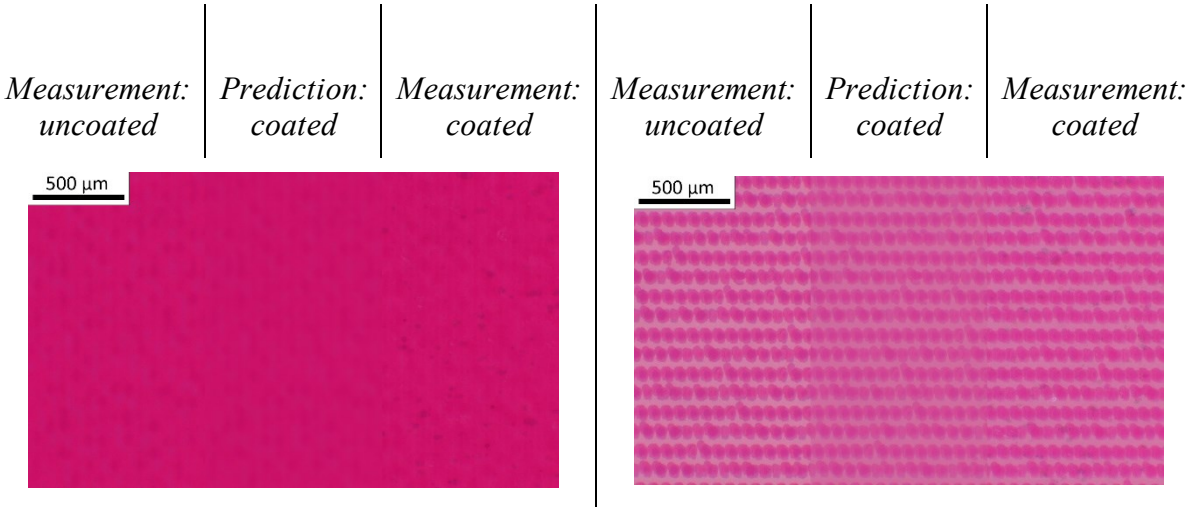

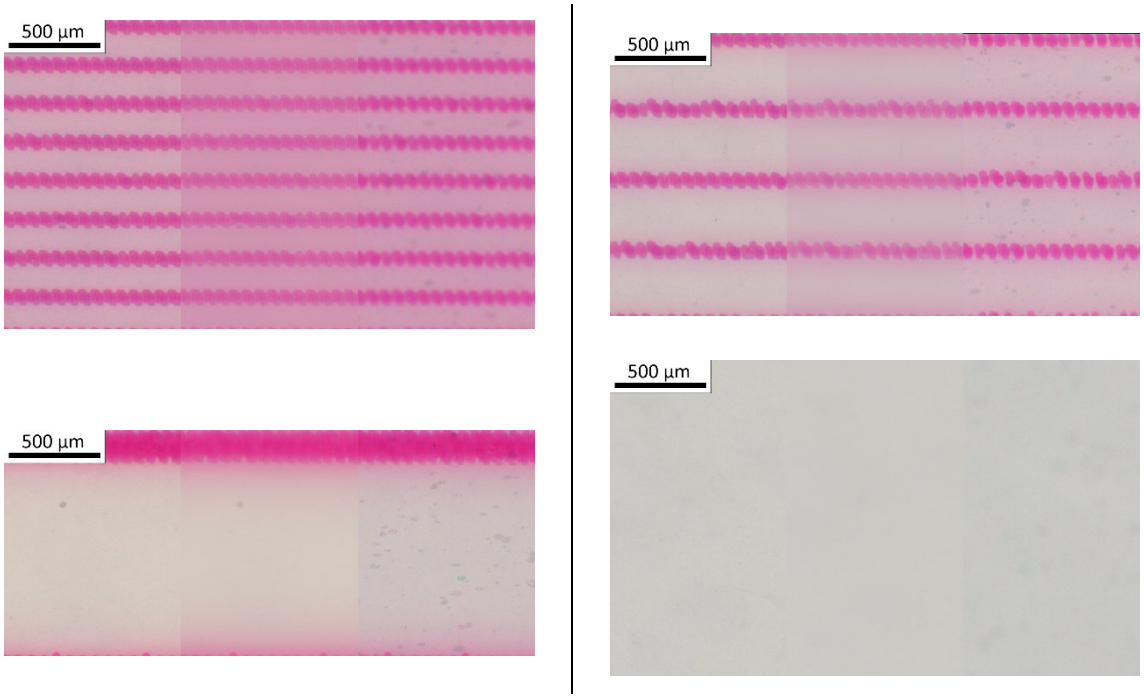

Figure 107. sRGB pictures of the results. The predictions included $\gamma = 1$.

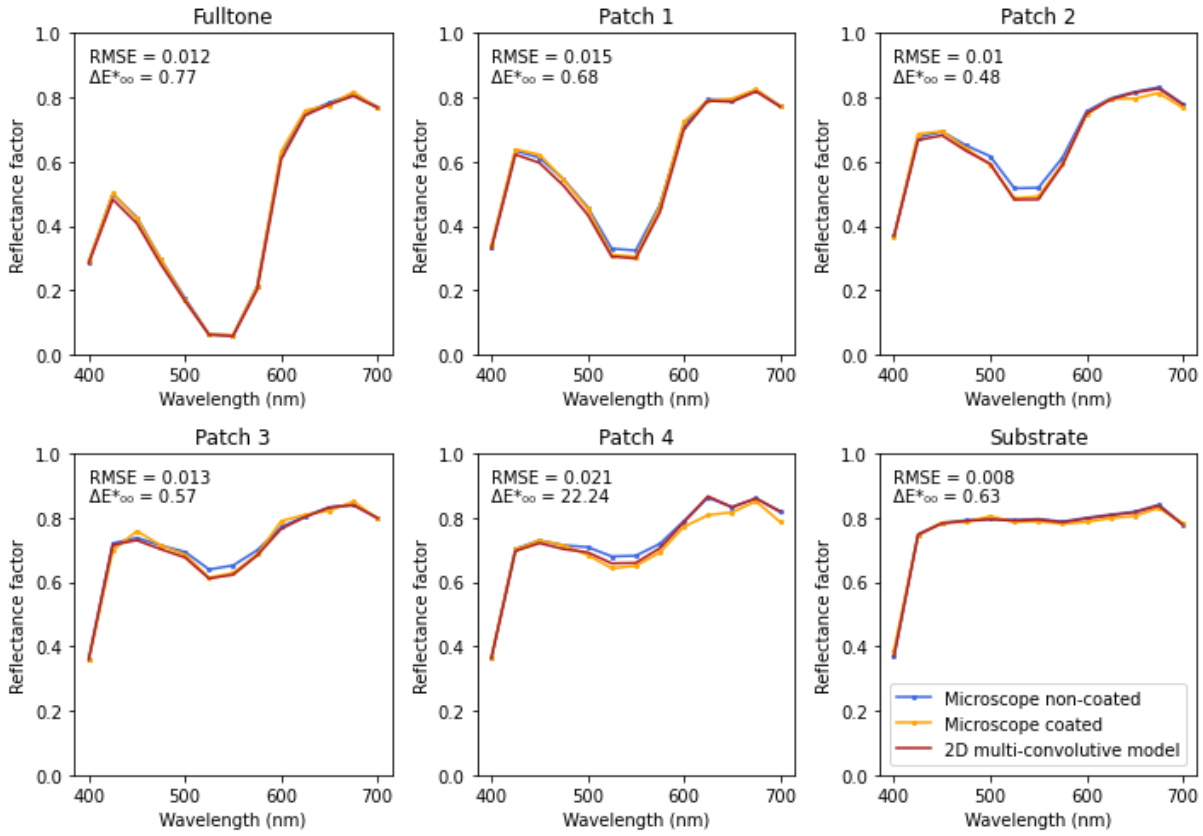

Figure 108. Reflectance factor of the magenta prints averaged over the spatial dimension. The predictions included $\gamma = 1.23$.

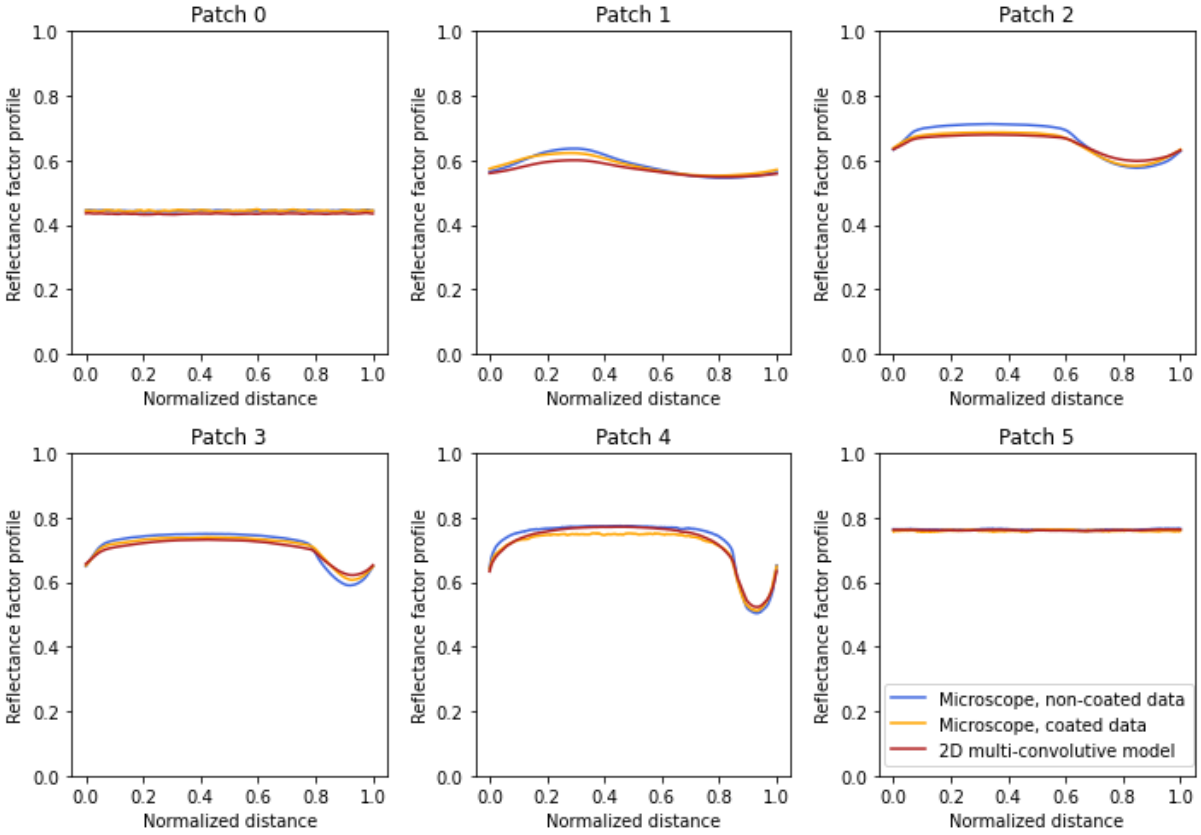

Figure 109. Reflectance factor profile of the magenta prints averaged over the spectral dimension; the profile was spatially averaged over all the lines. The predictions included $\gamma = 1.23$.

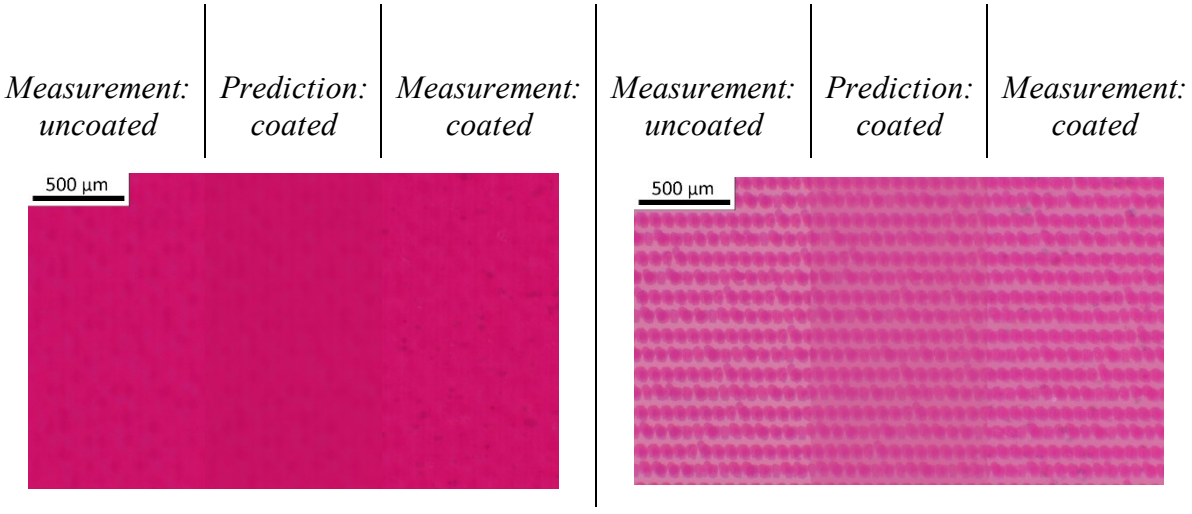

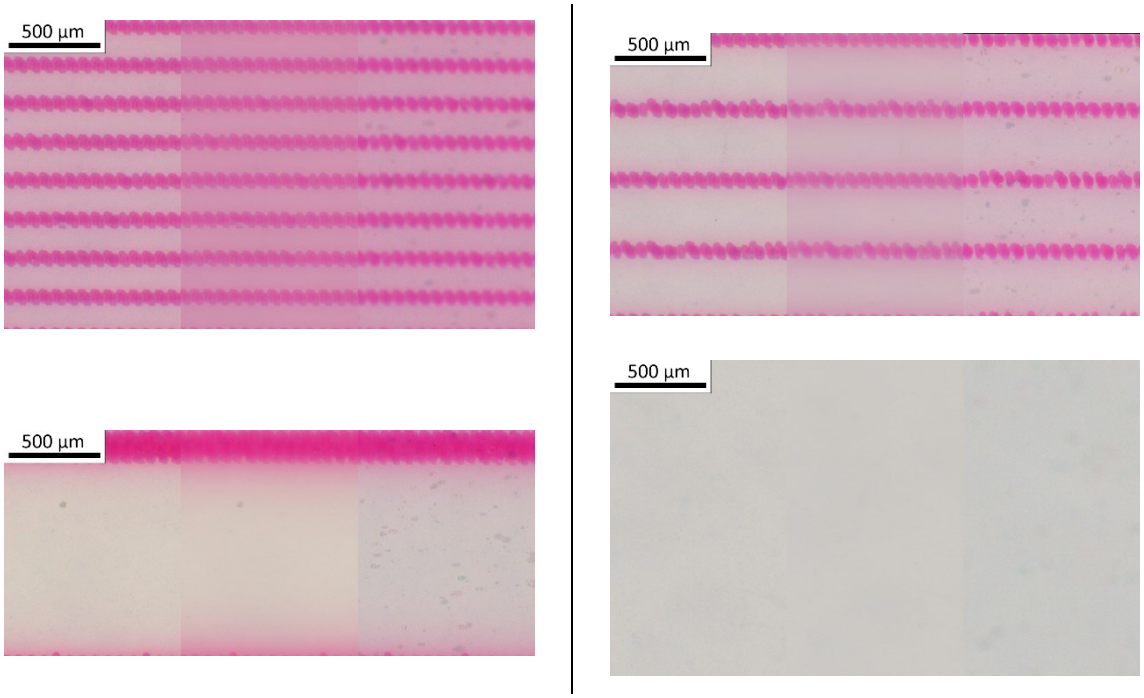

Figure 110. sRGB pictures of the results. The predictions included $\gamma = 1.23$.

Appendix VIII. Accuracy of the multi-convolutive model on reconstructed spectra from simulated RGB values

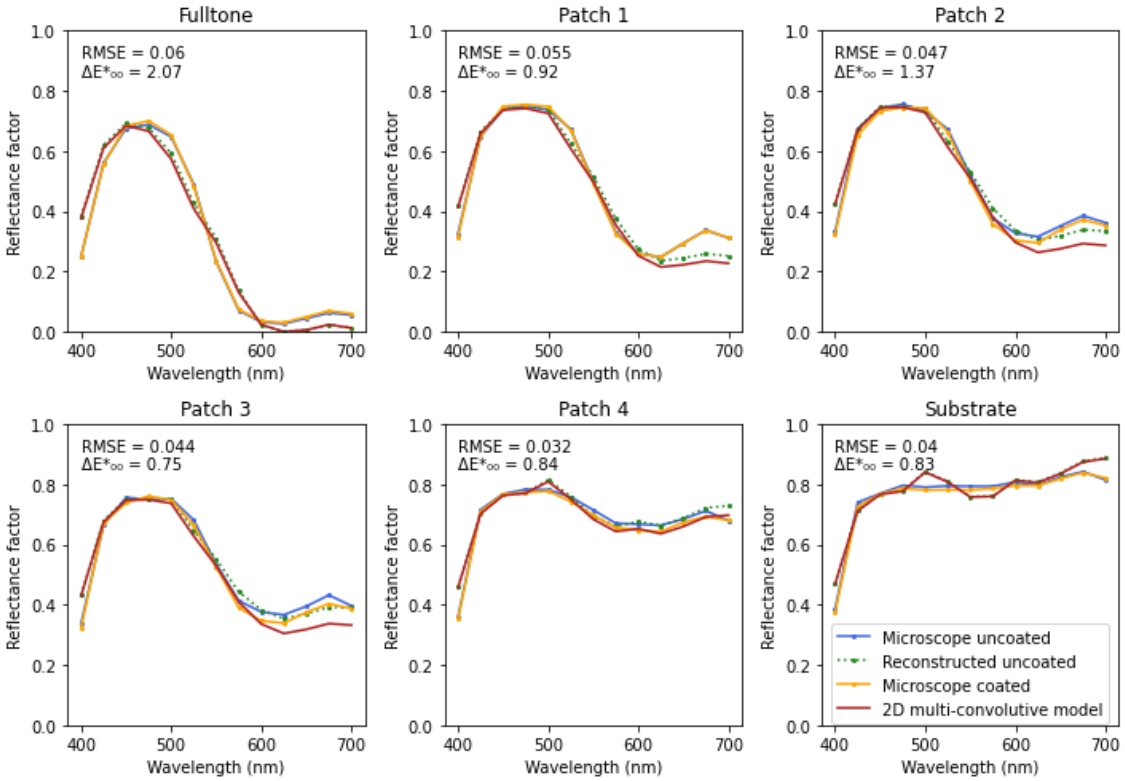

Figure 111. Reflectance factor of the cyan prints averaged over the spatial dimension. The green dotted lines describe the reconstructed reflectance factor from simulated RGB values of the uncoated prints. The predictions included $\gamma = 1.23$.

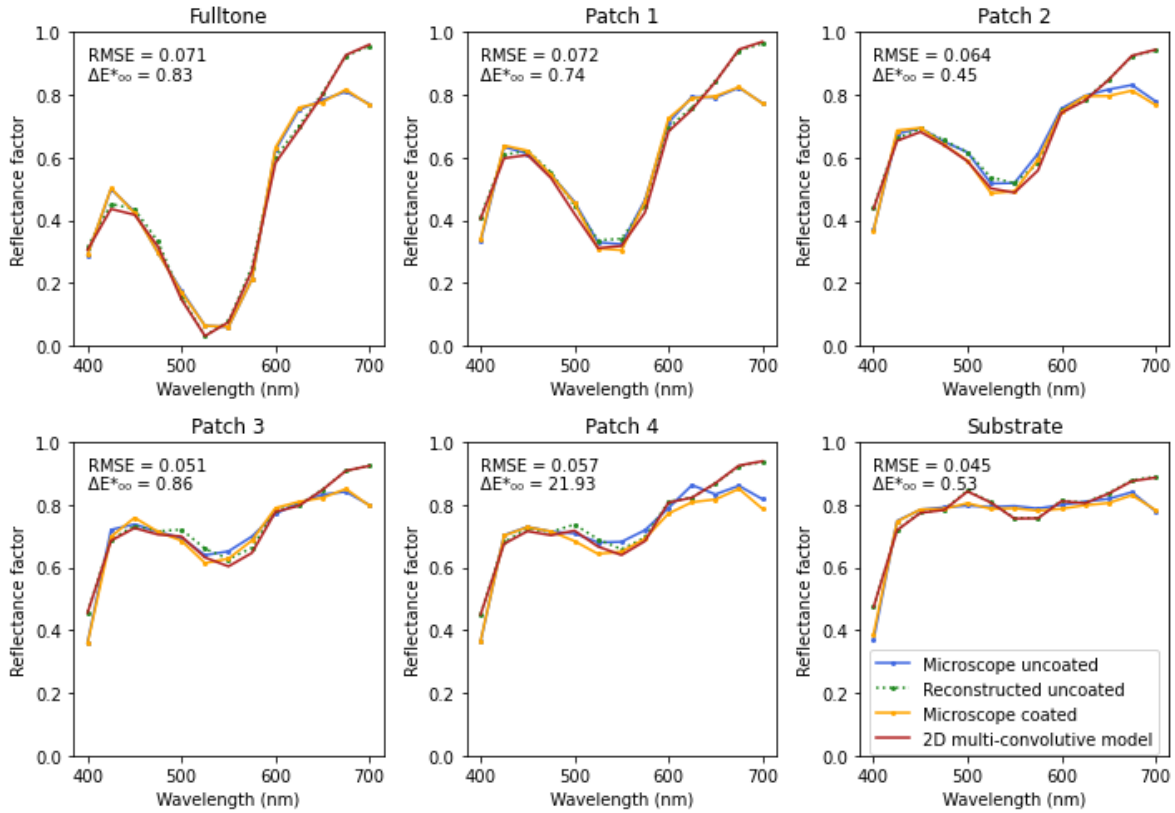

Figure 112. Reflectance factor of the magenta prints averaged over the spatial dimension. The green dotted lines describe the reconstructed reflectance factor from simulated RGB values of the uncoated prints. The predictions included $\gamma = 1.23$.

Appendix IX. Predictions of the multi-convolutive model on the hidden images

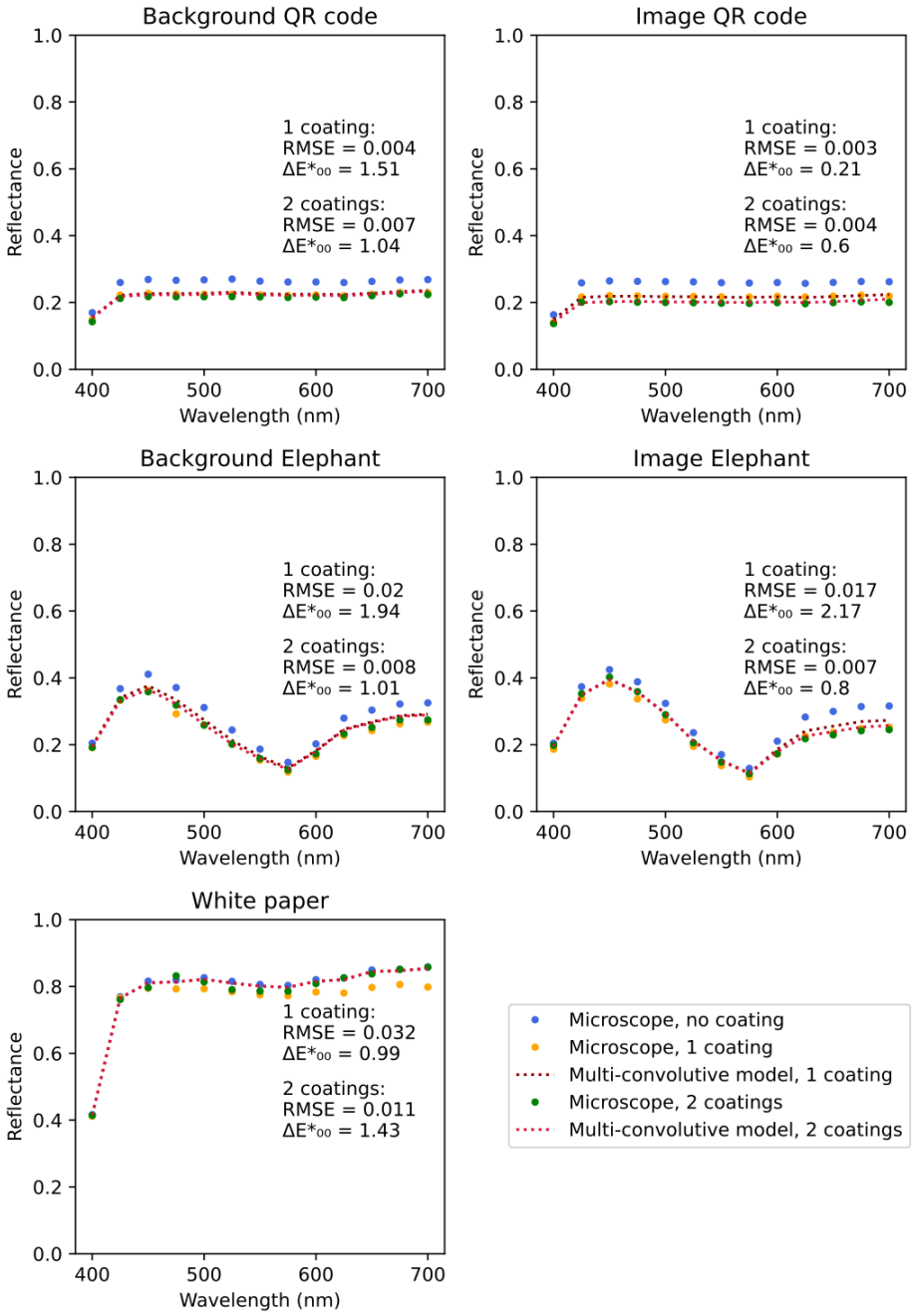

Figure 113. Predicted and measured spectral reflectance factors of the test forms containing hidden images. (In the multi-convolutive model, the γ-parameter was $\gamma = 1.23$*).*

a)

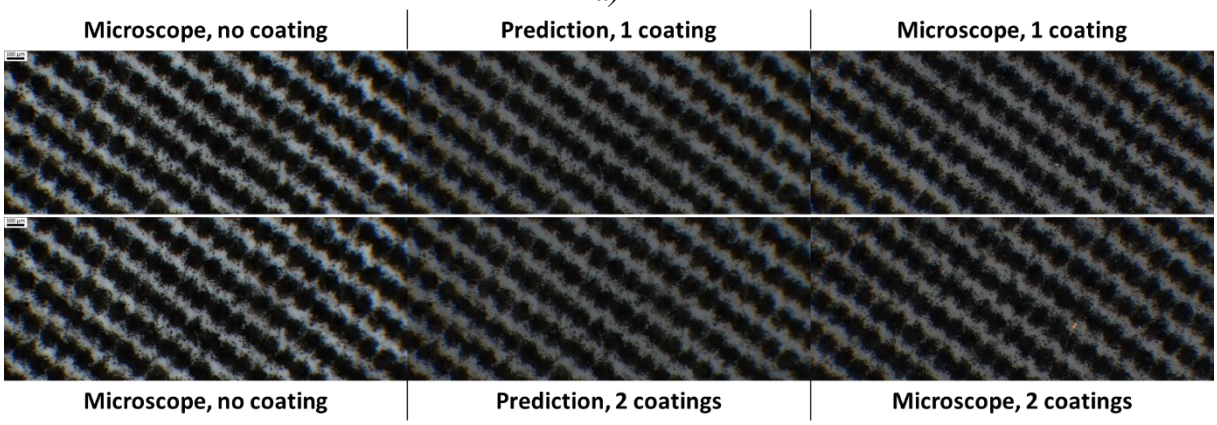

b)

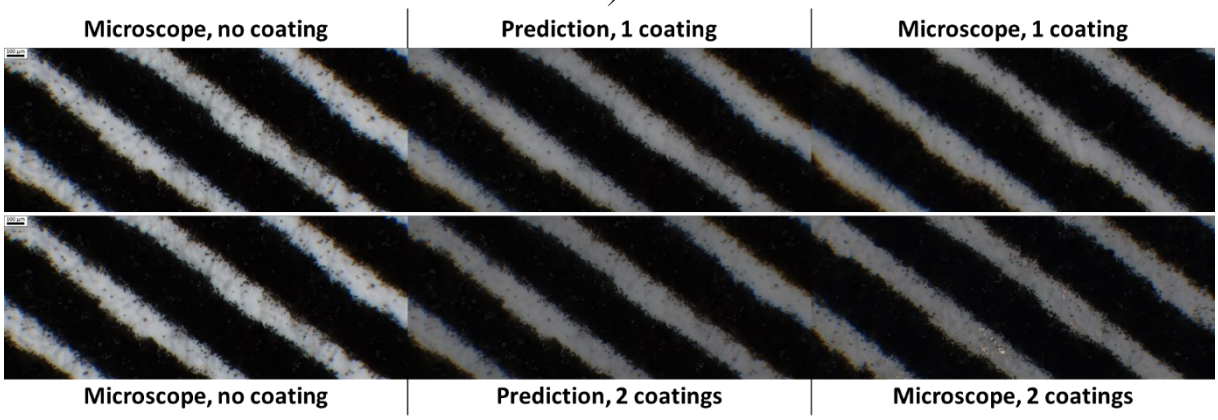

c)

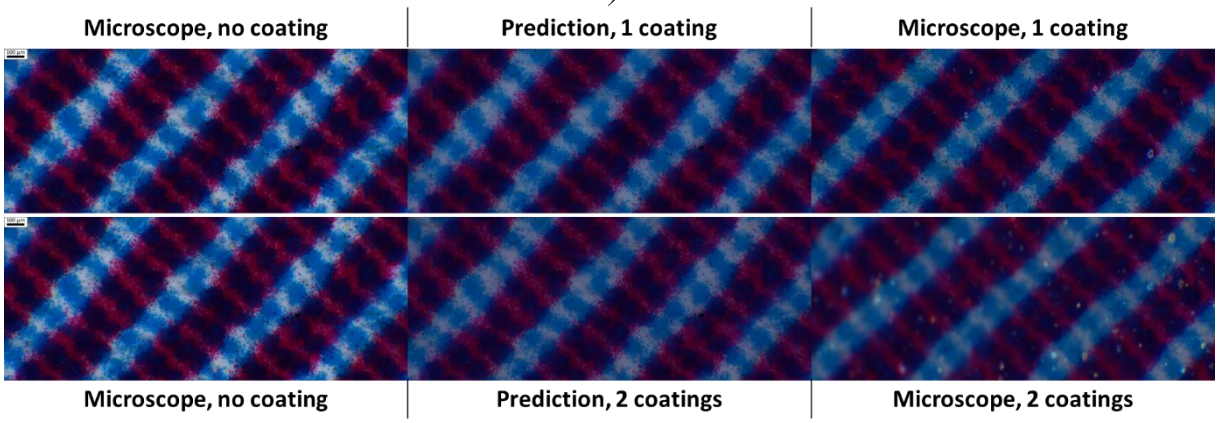

d)

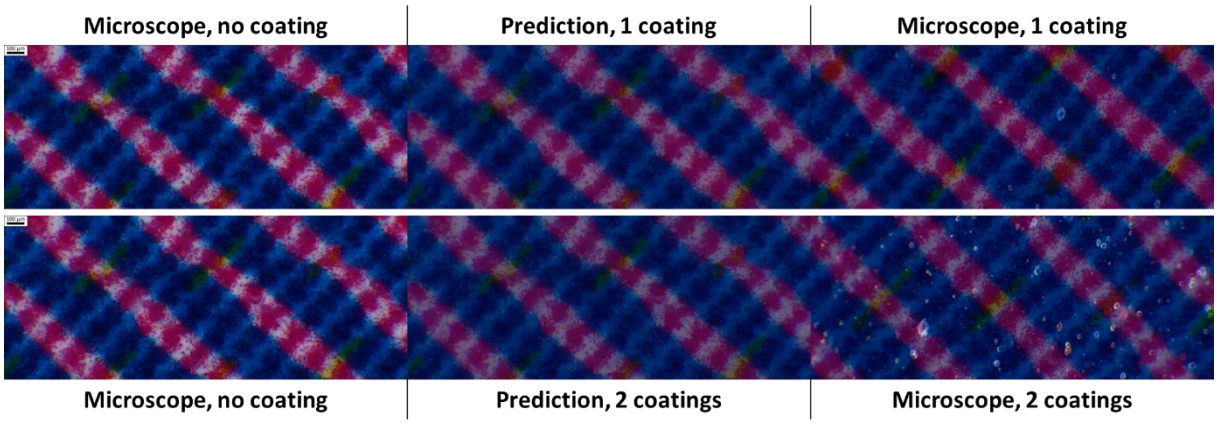

Figure 114. sRGB pictures of the measured and predicted test forms.

Appendix X. Notations

a	Surface coverage of a single printed ink
a_i	Surface coverage of a Neugebauer primary i
d	Thickness of a transparent coating layer
E_1	Irradiance at the print surface after one internal reflection at the coating-air interface
E_i	Initial irradiance of a surface
H	Substrate point spread function
h	Irradiance map on the printed surface after one internal reflection at a smooth coating-air interface
$h_{integrated}$	Irradiance map on the printed surface after one internal reflection at the coating-air interface integrated along one direction
h_{rough}	Irradiance map on the printed surface after one internal reflection at a rough coating-air interface
K	Absorption coefficient in the Kubelka-Munk model
L	Total radiance observed from a certain direction, after crossing the coating-air interface
L_{k}	Radiance of the light reflected by the print surface after the k^{th} reflection on this surface.
M_{k}	Exitance of the print surface after the k^{th} reflection on the surface
n_0	Optical index of air
n_1	Optical index of the print
R	Halftone print reflectance
R_0	Substrate reflectance

R_{01}	Fresnel reflectance at an interface between a medium 0 and a medium 1
R_1	Fulltone reflectance
R_m	measured halftone spectral reflectance factor
R_{NC}	Reflectance of a non-coated halftone print
r_i	Light portion internally reflected within the medium at an interface
r_s	Light portion externally reflected toward the sensor at an interface
S	Scattering coefficient in the Kubelka-Munk model
t	Intrinsic transmittance of a transparent layer
T_{01}	Fresnel transmittance at an interface between medium 0 and medium 1
t_i	Intrinsic transmittance of an ink layer (for instance of a Neugebauer primary i)
T_{in}	Light portion transmitted through an interface
T_{out}	Light portion transmitted through an interface towards the sensor
T	Ink transmittance
α	Absorption coefficient of a transparent medium
γ	Ratio between the path length in the ink layer for high angles of incidence and the one along the normal of the print
λ	Wavelength
ρ	Intrinsic reflectance of a system
$\bar{\rho}$	Spatially averaged intrinsic reflectance
ρ_0	Intrinsic reflectance of a bare substrate
ρ_i	Intrinsic reflectance of a substrate printed with a Neugebauer primary i